4)

Three-Dimensional Ultrasound Power Deposition Modeling, Thermal Field Visualization, and Clinical Integration for Hyperthermia Therapy

by

Daniel Alan Sidney

B.A., Yale University (1988)
M.S., Massachusetts Institute of Technology (1992)
Submitted to the Division of Health Sciences and Technology
Medical Engineering/Medical Physics Program
in partial fulfillment of the requirements for the degree of
Doctor of Philosophy in Medical Engineering
at the
MASSACHUSETTS INSTITUTE OF TECHNOLOGY
June 1997

Author ....
Division of Health Sciences and Technology
Medical Engineering/Medical Physics Program
June 2, 1997

Certified by ....
Dr. William H. Newman
Research Scientist, Division of Health Sciences and Technology
Thesis Supervisor

Certified by ....
Dr. H. Frederick Bowman
Director, Hyperthermia Program, Division of Health Sciences and Technology
Thesis Supervisor

Accepted by ....
Dr. Martha L. Gray
Chairman, Departmental Committee on Graduate Students
J. W. Kieckhefer Assoc. Prof. of Electrical Engineering and Computer Science
Co-Director, Division of Health Sciences and Technology

Three-Dimensional Ultrasound Power Deposition Modeling, Thermal Field Visualization, and Clinical Integration for Hyperthermia Therapy

by

Daniel Alan Sidney

Submitted to the Division of Health Sciences and Technology
Medical Engineering/Medical Physics Program on June 2, 1997,
in partial fulfillment of the requirements for the degree of
Doctor of Philosophy in Medical Engineering

Abstract

This thesis describes the development and implementation of an interactive, integrated clinical system for 3-D visualization of thermal fields on patient anatomy to aid in hyperthermia cancer treatment planning and evaluation in the hyperthermia clinic at DFCI. Hyperthermia is an adjunctive treatment modality based on the preferential temperature elevation of tumor tissue, creating a tumor environment that synergistically enhances the efficacy of radiotherapy and chemotherapy. Prior to hyperthermia treatment administration, power deposition and heat transfer models can be used to estimate the 3-D thermal fields that will be produced in the target volume by the power applicator. Following treatment these predicted fields can be modified, using thermometric data obtained from thermal probes during treatment, to estimate the 3-D thermal fields that occurred during treatment.

This project comprised two broad objectives: to develop a model for rapid calculation of the power deposition field from an ultrasound power applicator; and to combine this model with an existing rapid model for bioheat transfer and an existing geometric treatment planner to produce an integrated clinical system. For the first objective, a general method was developed for rapid calculation of the acoustic pressure field from a non-uniformly vibrating rectangular acoustic source. Comparisons between simulated and measured acoustic fields in a water bath indicated that acoustic beams from the applicator transducers could be modeled by a modified Gaussian parametric description, accelerating pressure field calculations by two orders of magnitude (compared with the conventional method of solving the Rayleigh-Sommerfeld diffraction integral). In addition, a new technique was developed to modify the pressure field from an acoustic source insonating a non-attenuating medium to account for acoustic absorption, and this method was validated by acoustic simulations with the transducer geometry. For the second objective, the power deposition and bioheat transfer models were incorporated into the environment of the geometric planner. This integrated system was used to perform thermal treatment planning predictions and therapy reconstructions using patient geometric models and thermometric data taken from a real treatment. Further work must now integrate the system's treatment predictive and reconstructive capabilities with clinical practice to provide maximal patient benefit.

Thesis Supervisors:
Dr. William H. Newman, Research Scientist, Division of HST
Dr. H. Frederick Bowman, Director, Hyperthermia Program, Division of HST
Doctoral Committee:
Drs. Newman, Bowman, Borivoje Mikić, Göran K. Svensson, and Hanne Kooy

Acknowledgements

The Celsius temperature scale was originally defined by two points: the freezing and boiling points of water at standard pressure. In much the same way, the importance of an endeavor is generally measured on a scale defined by two points: saving the universe and curing cancer. It has been singularly satisfying doing the second most important work in the world—especially when one considers the only person doing more important work wears pajamas and a red cape. This work was not performed in a vacuum, however, and there are many whom I wish to thank for their contributions to my thesis and to my personal and professional growth. I hope they recognize that my acknowledgement here of the help and support I received from them is a mere symbol of the appreciation I feel.

I have been an increasingly demanding little doctoral candidate as time has marched relentlessly toward the graduation deadline, and I thank my committee members for the accommodation they showed me in this difficult time. Bill Newman conceived this project, and he was also largely responsible for getting it funded; he helped me learn acoustic physics, suggested relevant course work and reading material, and providing focus to the project, and he took a personal interest in seeing me succeed in this work. Fred Bowman was a frequent source of moral support—and one of my interviewers way back when I was a prospective MEMP student. He strived to understand how different parts of my work related to each other and to the work of others, and this had the effect of helping me improve my own understanding. (Perhaps it was a Socratic trick on his part.) I have become a clearer thinker and communicator under his guidance, and I also appreciate the personal interactions we've had. Bora Mikić taught me almost everything I know in the field of heat transfer, and I am definitely richer for the association. He is an inspiring instructor and a gifted engineer. I owe thanks to Göran Svensson for making it so easy for me to collaborate with DFCI and JCRT people, and also for his interest and comments on my work. I also thank Hanne Kooy for his tutelage in radiation physics and his support of my clinical preceptorship.

In my immediate lab/office environment, I first thank Ken Szajda. He helped me with any number of computer and software issues, including getting my thesis footnote spacing correct on the eve of thesis submission. Greg Martin was a constant source of information on most aspects of this project, and in particular thermal modeling. A research group is as fun and pleasant as the individuals who comprise it, so I am grateful that mine was rounded out by Myev Bodenhofer, Bryce Greenhalgh, and Jialun He. Everybody has been especially supportive in my time of need.

This project brought me into contact with a number of individuals in the Longwood Medical Area. Jørgen Hansen patiently and endlessly (at my initiation) discussed power applicators and a variety of treatment issues. Jamie Pelagatti helped me learn AVS, from the perspective of a user and a developer. Bruce Bornstein was only too happy to show me around the radiation clinic in my preceptorship. Kullervo Hynynen and his protégé Erin Hutchinson were both helpful in addressing my acoustic modeling questions.

And, of course, my friends and family have been "there" for me. In terms of motivating me to finish this project, I owe thanks to Ken Szajda, Dan Sodickson, and Naomi Chesler. Their support was continual, but there were two dramatic junctures: one with Dan on March 10th, and another with Naomi on May 6th. Without both of these critical sessions, yes, I would have finished this thesis; but no, not now. I only recently met Valerie Sandler, but her intense support has more than compensated for the short duration of our special relationship. My brother Ray served as my math consultant in general, and in the eleventh hour as thesis editor. My parents believed in me, and they have derived even more delight in my accomplishment than I have. They love me, and I love them.

Contents

List of Figures

List of Tables

Glossary of Symbols and Abbreviations

Variables

A		second-order term coefficient
A	cm^2	area
B	cm^{-1}	inverse space constant
c	$\mathrm{J/g}$–°C	specific heat capacity
c	$\mathrm{cm/s}$	speed of sound
d	cm	heating margin without heating oscillations
$\overline{d}$	cm	heating margin with heating oscillations
d	cm	distance from differential surface to field point
d	cm	fan line offset distance
d_i	cm	distance from center of subelement to field point
D	EQ43	thermal dose (equivalent minutes at 43°C)
$\dot{D}$	EQ43/min	thermal dose rate (constant temperature)
$\overline{\dot{D}}$	EQ43/min	time-averaged thermal dose rate (varying temperature)
e		2.7182818284...
F		constraint factor
$F_{\mathrm{O\&F}}$		constraint factor from [79]
G		general transformation matrix
h	cm	height of rectangle or cylindrical wedge
I		identity matrix
I	$\mathrm{mW/cm}^2$	acoustic intensity
j		$\sqrt{-1}$
k	$\mathrm{mW/cm}$–°C	thermal conductivity
k	cm^{-1}	wave number ($k \equiv 2\pi/\lambda$)
k'	cm^{-1}	complex wave number ($k' = k - j\alpha$)
$\mathcal{M}$	%	comparative dose metric

Variables (continued)

n		number
N		number
p	$\mathrm{N/m^2}$	acoustic pressure
$\dot{q}$	mW	power
$\dot{q}''$	$\mathrm{mW/cm^2}$	heat flux
Q	$\mathrm{J/cm^3}$	volumetric thermal energy
$\dot{Q}$	$\mathrm{mW/cm^3}$	SAR (specific absorption rate)
r	cm	distance
r	cm	radial coordinate (spherical or cylindrical geometry)
$\vec{r}$	cm	vector or vertex coordinates
r'_p	cm	$R/\cos(\lvert\theta_p\rvert - \sigma_\theta/2)$
R	cm	radius, radius of curvature
R		base in the exponential temperature-thermal dose relation
R		rotation matrix
$\rlap{-}R$		rotation and scaling matrix (combined)
$\mathcal{R}$		ratio of normalized time-averaged dose rates ($\mathcal{R} = \frac{\overline{\dot{D}}_n/\overline{\dot{D}}_t}{\dot{D}_n/\dot{D}_t}$)
s	cm	length (or arc length) of side of source
S	$\mathrm{cm^2}$	surface of source
S		scaling matrix
t	s	time
$\vec{t}$		translation vector
T	°C	temperature
T		translation matrix
u		velocity
w	cm	width of rectangle
w	ml blood/s–ml tissue	tissue perfusion (volumetric blood flow)
W	ml/min–100g	tissue perfusion ($\rho W = w \times 60\mathrm{s/min} \times 100\mathrm{g}/100\mathrm{g}$)
x	cm	x coordinate of vector or vertex (Cartesian)
$\vec{x}$	cm	vector or vertex coordinates
y	cm	y coordinate of vector or vertex (Cartesian)
z	cm	z coordinate of vector or vertex (Cartesian or cylindrical)
Z	$\mathrm{kg/m^2{-}s}$	acoustic impedance

Variables (continued)

α	$\mathrm{cm^2/s}$	thermal diffusivity
α	dB/cm	ultrasound attenuation coefficient
β	$\mathrm{cm^{-1}}$	inverse space constant
β	rad	fan reference frame coordinate
γ		projection factor; $\gamma\{\beta_x, \beta_y\} = \sqrt{\tan^2\beta_x + \tan^2\beta_y + 1}$
θ	°C	temperature elevation
θ	rad	angle
ϑ	rad	arc of cylindrical wedge subsection
λ	$\mathrm{cm^{-1}}$	inverse perfusion length; $\lambda^2 \equiv w\rho_{\mathrm{bl}}c_{\mathrm{bl}}/k$
λ	cm	wavelength
μ	dB/cm	ultrasound absorption coefficient
ξ		dummy variable
π		3.1415926535...
ρ	$\mathrm{g/cm^3}$	density
σ_{b}	cm	Gaussian beam width
σ'_{b}	cm	analytical Gaussian beam width; $\sigma'_{\mathrm{b}} \equiv \sigma_{\mathrm{s}}\sqrt{1 + (z/k\sigma_{\mathrm{s}}^2)^2}$
σ''_{b}	cm	modified Gaussian beam width; $\sigma''_{\mathrm{b}} = f_1\sigma'_{\mathrm{b}}\{f_2 z\}$
σ_{s}	cm	Gaussian source width
σ_θ	rad	aperture of cylindrical wedge source
ϕ	cm–°C	substitution variable for $r\theta$
φ	rad	phase angle
ω	rad/s	angular velocity

Subscripts

a	amplitude
ap	applicator
b	boundary
bl	blood
br	breast
C	Cartesian geometry
FAM	Fanned Absorption Method
foc	focus
gr	graph
h	homogeneous
i	source subelement
I	initial (temperature elevation)
max	maximum
min	minimum
n	normal direction (*i.e.* in $\hat{n}$ direction), usually implies boundary
n	normal tissue
nh	non-homogeneous
pl	plane
pt	patient
pt	point
r	r coordinate, r derivative
RMS	root mean square
S	isentropic
S	spherical geometry
sq	square
sph	sphere
t	tumor tissue
T	isothermal
TX	therapeutic (thermal dose)
w	water
wob	wobulation mode of FSUM
x	x coordinate, x derivative
xd	transducer
y	y coordinate, y derivative
z	z coordinate, z derivative
θ	θ coordinate, θ derivative

Superscripts and Mathematical Symbols

$'$	transformed vector or vertex, modified quantity
$\vec{x}$	vector notation
$\hat{x}$	unit vector notation; $\hat{x} \equiv \vec{x}/\lVert\vec{x}\rVert$
x^*	critical x value (defines a constraint)
$\overline{AB}$	line segment between A and B
$\triangle$	triangle
$\angle$	angle, phase
Δ	difference, increment
^{T}	transpose of vector or matrix
$\overline{x}$	average value
$\langle x \rangle$	expected value, time-averaged value
$\lvert x \rvert$	absolute value
$\lVert\vec{x}\rVert$	magnitude; $\lVert\vec{x}\rVert \equiv \sqrt{\vec{x} \cdot \vec{x}}$
$f(x)$	function f evaluated at parameter x
$p\{x\}$	variable p evaluated at parameter x

Functions

$\mathrm{Gauss}(x, \sigma)$	$\exp(-x^2/2\sigma^2)$, Gaussian
$\mathrm{ginc}\, x$	$(\mathrm{sinc}\, x - \cos x)/x$
$\mathrm{Im}(a + jb)$	b, the imaginary part of the complex number $a + jb$
$\mathrm{lin}(x_0, x_1, t)$	$x_0 + (x_1 - x_0)t$, linear interpolation
$\max(x, y)$	greater of x and y
$\min(x, y)$	lesser of x and y
$\mathcal{O}(x)$	order of x, approximate size of x
$\mathrm{Re}(a + jb)$	a, the real part of the complex number $a + jb$
$\mathrm{sinc}\, x$	$(\sin x)/x$

Abbreviations

AVS	Application Visualization System
DFCI	Dana-Farber Cancer Institute (Boston)
FAM	Fanned Absorption Method
FBEM	Finite Basis Element Method
FSUM	Focused Segmented Ultrasound Machine
JCRT	Joint Center for Radiation Therapy (Boston)
LS	least squares
RMS	root mean square
SAR	specific absorption rate (volumetric power deposition)

Chapter 1

Introduction

> *Those who cannot be cured by medicine can be cured by surgery. Those who cannot be cured by surgery can be cured by heat. Those who cannot be cured by heat, they are indeed incurable.*
>
> — Hippocrates, 400 B.C.

Hyperthermia is an adjunctive treatment modality based on the preferential temperature elevation of tumor tissue, creating a tumor environment that synergistically enhances the efficacy of radiotherapy [91] and chemotherapy [42, 97]. In Asia and Europe many groups are actively practicing hyperthermia and achieving impressive clinical results; Harima *et al.* [39] in Japan and van der Zee *et al.* [99] in the Netherlands, for example, recently reported on the use of hyperthermia with radiotherapy in cervical stage IIIb tumors and assorted inoperable pelvic tumors, respectively; both studies indicated an approximate doubling in complete response rate, compared to radiotherapy alone.

Tissues, both normal and cancerous, are susceptible to thermal injury [57, 58]; the extent of the injury is correlated with the thermal dose, which is related to the magnitude and duration of the temperature elevation [12]. The technical aim of hyperthermia cancer therapy is to deliver a therapeutic thermal dose to tumor tissue while delivering a sub-therapeutic dose to the surrounding normal tissue.

To perform quantitative hyperthermia, it is necessary to have knowledge of the 3-D temperature field for the duration of treatment. Thermal modeling is used to obtain this knowledge, and thermal modeling in turn requires knowledge of the 3-D power deposition field (specific absorption rate SAR), as well as tissue thermal properties. Power deposition modeling requires a model of the power applicator used to heat the target volume, and accurate location of the applicator relative to the patient. For treatment thermal planning, patient and applicator geometric modeling, power deposition modeling and heat transfer modeling are necessary; for treatment thermal reconstruction, all these are required, plus thermometric data taken during heating. In both cases—treatment planning and treatment reconstruction—a 3-D visualization system is desirable to relate the calculated thermal fields to the patient geometry.

1.1 Project History

The Dana-Farber Cancer Institute (DFCI) and the MIT hyperthermia groups recognize the need to bring patient anatomic visualization and thermal and ultrasound modeling to bear to improve clinical hyperthermia dosimetry and in turn hyperthermia treatments. These two institutions joined together in a hyperthermia National Institutes of Health (NIH) Program Project Grant (PPG). This PPG traces its roots to the MIT Hyperthermia Center, directed throughout the 1980's by Dr. Padmakar P. Lele. At that time, the focus of work under the grant was in the areas of ultrasound device development and physics, and in particular in the development of the Steered, Intensity Modulated, Focused Ultrasound (SIMFU) system [58]. In the late 1980's Dr. H. Frederick Bowman became the principal investigator (PI) of the PPG, and under his tenure the Focused Segmented Ultrasound Machine (FSUM) [14, 38], designed to heat deep tumors, was commissioned. Dr. Terrance S. Herman followed as PI, and the base of operations moved from MIT to DFCI. In addition, the focus of the PPG changed to a more clinical orientation as the FSUM received a Food and Drug Administration (FDA) Investigational Device Exemption (IDE) for a phase I trial. Today Dr. C. Norman Coleman is the principal investigator of the PPG, and he heads a group comprising physicists, radiation therapists, and computer programmers at the Joint Center for Radiation Therapy (JCRT). Dr. Göran K. Svensson directs the physics group and is responsible for developments in ultrasound applicators and associated physics. Formerly in this group, Mark Dopheide performed early work in developing Xknife [55] and HYPER/Plan [38], a stereotactic radiosurgery and radiotherapy planning system and a hyperthermia therapy geometric planning system, respectively. Radionics Software Applications, Inc., (RSA) was established to maintain and develop Xknife, and it enjoys a close association with the JCRT. Within the DFCI group, Jørgen L. Hansen and James M. Pelagatti have maintained and developed HYPER/Plan. Both planning systems are built on the AVS scientific graphics and visualization commercial platform (Advanced Visual Systems, Inc.). On the MIT side of the collaboration, the Hyperthermia and Bioheat Transfer Group headed by Dr. H. Frederick Bowman has pursued thermal dosimetry via thermal modeling and dense thermometry for site-specific applications in hyperthermia. Dr. William H. Newman conceived and jointly developed with Dr. Gregory T. Martin a rapid computational model for bioheat transfer, the Finite Basis Element Method (FBEM) [65, 66, 73, 75]. With the geometric and heat transfer models in place, what remains for an integrated, clinical treatment modeling system is a power deposition model, and its integration with the other two models.

1.2 Document Organization

The task at hand, then, is to integrate rapid models of power deposition and heat transfer into an existing geometric planning system to create an integrated, interactive hyperthermia treatment planning and evaluation system. A brief outline of the tasks necessary to achieve this goal, and how they are broken down into chapters, follows.

Chapter 2 includes a discussion of object hierarchies and coordinate transformation in the context of computer graphics. These concepts, particularly coordinate transformation, recur repeatedly in this document, so a solid grounding early on is advisable. In addition, this chapter contains a detailed development of Volumizer, which is used to generate a patient volumetric model from a patient surface model. This volumetric representation of the patient is critical for power deposition and thermal calculations, so this chapter also briefly describes the steps to obtain the volumetric representation from the original 3-D patient image.

Chapters 3 and 4 concern ultrasound power deposition modeling. The former chapter provides background in acoustic physics, and the latter presents developments in acoustic calculation and modeling made in the course of this dissertation. These developments include a technique for rapid calculation of the acoustic pressure field from a non-uniformly vibrating rectangular or cylindrical wedge acoustic source; models of the acoustic pressure field from a single FSUM transducer and multiple FSUM transducers radiating into a water bath; and the description and theoretical validation of the Fanned Absorption Method (FAM) for modifying the acoustic pressure field from a source radiating into a non-attenuating medium to approximate the pressure field in an absorptive medium.

Chapter 5 represents the confluence of several lines of work by a number of individuals. It is here that the geometric, power deposition, and thermal modeling efforts join together to form an integrated treatment modeling and thermal visualization system. Included in this chapter is an overview of the system (depicted in a flow chart in Figure 5-1 on page 172, for impatient readers); a theoretical description of the Finite Basis Element Method (FBEM) thermal model; an inventory of thermal visualization tools; and an explanation of how predicted thermal fields can be modified by thermal measurements (in particular, SAR and temperature) into reconstructed thermal fields that more accurately reflect the heating that occurred during hyperthermia treatment administration. (The tissue perfusion field is critically important in the thermal model, although its characterization is beyond the scope of this thesis.) Chapter 6 applies the models to the clinical case of a patient who received hyperthermia treatment with the FSUM at DFCI, and in whom thermal measurements were taken during treatment. Thermal field predictions and reconstructions are presented using thermal visualization tools.

The final chapter, Chapter 7, contains a short discussion of the potential clinical utility of the integrated treatment system. In addition, directions for future work within the scope of this project are considered.

An ancillary chapter, relegated to Appendix A, presents material only peripherally related to the focus of this thesis. This self-contained appendix analyzes a theoretical strategy for concentrating thermal dose deposition in the target volume by temporally oscillating the power deposition field. Appendix B includes derivations that are not critical for understanding material presented or developed in the main chapters, but they may be welcome to the reader who desires supplemental details. These appendicular derivations are cited in the main chapters when relevant. Appendix C contains a tabulation of tissue power deposition and thermal properties, and another tabulation of various geometric and power specifications of the FSUM device. Finally, Appendix D provides a short list of clinical ultrasound hyperthermia systems.

1.2.1 Document Contributions

When reading a document like this one it is not always obvious which contributions are the author's, and which ones belong to others. This is all the more true when a number people from various disciplines are all involved in the work. As a service to the reader, then, the author's contributions are briefly itemized: the Volumizer algorithm and implementation (Chapter 2); the rapid diffraction integral solution for the acoustic pressure field from a non-uniformly vibrating rectangular or cylindrical wedge acoustic source; the models of the acoustic pressure field from an individual and multiple FSUM transducers; the FAM (Chapter 4); integration of the geometric, power deposition, and heat transfer models in AVS (Chapter 5); and the presented visualization tools (Chapter 6).

Chapter 2

Computer Graphics

> *When correctly viewed,*
> *Ev'rything is lewd.*
> *I can tell you things about Peter Pan*
> *And the Wizard of Oz*—there*'s a dirty old man!*
>
> — Tom Lehrer, verse in the song "Smut" on the album
> *That Was the Year that Was*, 1965

Computer graphics are obviously integral to visualization. (For more background in computer graphics, the reader is referred to Foley and van Dam [31] or its condensed, more readable brother Foley *et al.* [32].) In addition, computer graphic techniques for transforming coordinate systems can be used in power deposition and heat transfer modeling. In a hyperthermia treatment system designed for power deposition and thermal modeling on the one hand, and thermal field visualization on the other, computer graphics and thermal modeling are very closely related indeed. In a sense, such a treatment system starts with visualization, in which the patient and applicator geometries are established; proceeds to power deposition and heat transfer modeling, in which calculations are performed to compute the resulting thermal fields (such as SAR, temperature, and thermal dose fields); and finally returns to visualization, in which the calculated thermal fields are displayed on the patient anatomy.

First the patient is imaged, *e.g.* via CT. Relevant anatomic structures are contoured in each CT slice using IMEX, and the contours from adjacent slices are joined to form 2-D anatomic surfaces using Mosaic. These anatomic surfaces, along with the treatment applicator, are displayed using HYPER/Plan to specify the geometry of treatment. The 2-D anatomic surfaces are then transformed into a 3-D, volumetric patient representation using Volumizer, on which thermal calculations are performed. After the 3-D thermal fields are calculated, they are displayed on the patient anatomy. IMEX, Mosaic, HYPER/Plan, and Volumizer were all developed to function on the AVS platform, a scientific graphics and data visualization program.

This chapter begins with a general background of computer graphics, especially as it relates to coordinate transformation. This is followed by brief descriptions of AVS, IMEX, and Mosaic, and an extended description of Volumizer.

2.1 Computer Graphics Primer

Complex geometries composed of multiple parts are often organized into hierarchical structures called **trees**, although in schematic drawings they typically look like upside-down trees. The tree concept is illustrated in Figure 2-1. In HYPER/Plan the **root** of this tree is called *graph*. (AVS has an even more fundamental level to this tree structure called *top*.) *graph* has two important graphical structures underneath it, *patient* and *applicator*. The relationship of *patient* (or equivalently *applicator*) to *graph* is that of a **child** to a **parent**. *patient* typically has a number of children, corresponding to various organs, the tumor, thermometric sensors, and surface markers. *applicator* also has children, corresponding to its constituent transducers (*xducers*); and each *xducer* has a child of its own, *beam*, which is a graphical structure designed to show in which direction *xducer* radiates ultrasound waves, and does not correspond to a physical object in the conventional sense. The structure of the tree is that it has only one root, every child has one and only one parent, and a parent can have an arbitrary number of children.

The reason for organizing a structure in this hierarchical scheme is that geometric transformations (rotations, translations, *etc.*) of subsets of the total structure are easy to orchestrate. To give a specific example: The *patient* and *applicator* can be rotated independently. This is important for changing the treatment portal, for example, in which case *applicator* is moved relative to *patient*. But if it is desired to rotate *patient* and *applicator* together, which would occur if the user wanted to change his viewing position of *patient* and *applicator*, this rotation would take place by rotating *graph*, and not rotating *patient* or *applicator* directly at all. A subtle result arises if one applies the same rotation to *patient* and *applicator*, instead of rotating *graph*. Although the end effect on the orientations of *patient* and *applicator* are the same in both cases,

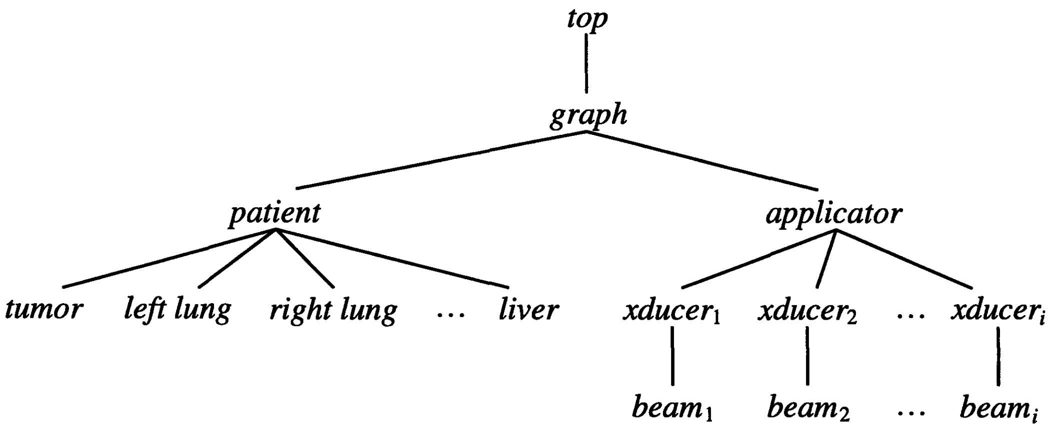

Figure 2-1: A typical tree hierarchical structure from HYPER/Plan.

their relative positions may change in the second case because the axis[1] about which rotation occurs is not necessarily clearly defined, and may be different for *patient* and *applicator*. Thus it is best and simplest to geometrically manipulate the highest (*i.e.* closest to the root) relevant structure in the tree to accomplish a geometric transformation.

Some common geometric transformations that can be performed are translation, rotation, reflection, shearing, scaling, and any combination of the above. In addition, changes in object projection (*i.e.* parallel projection vs. perspective projection) are easily accommodated by geometric transformations. For the scope of this thesis, however, only translation, rotation, uniform scaling, and combinations thereof will be discussed.

A geometric object, for present purposes, consists of a number of vertices. The geometric transformation of the object as a whole is in some sense equivalent to the simultaneous transformation of all its constituent vertices. A 3-D vector (or a point in 3-D space) will be denoted variously and equivalently by $\vec{p}$, (p_x, p_y, p_z), $|p_x \; p_y \; p_z|$, and $|p_x \; p_y \; p_z \; 1|$. A point in 3-D space may also be denoted by any of these conventions, or by P. A prime ($'$) will denote a transformed vector, which means the vector was multiplied by a transformation matrix. T, R, S, and G will denote matrices for the translation, rotation, scaling, and general (combination) transformations, respectively.

By convention in the field of computer graphics, vectors are row vectors (*i.e.* horizontal)

---

[1] In AVS the *default* axis of rotation for an object intersects the origin of the object's local reference frame, but the default can easily be changed.

that pre-multiply matrices. In other words, if G transforms $\vec{p}$ to $\vec{p}'$, then $\vec{p}' = \vec{p}G$.[2] This pre-multiplication scheme has the conceptual advantage that sequential transformations that occur appear as consecutive (*i.e.* left to right) matrix multiplications in matrix equations. That is, if $\vec{p}$ is transformed by G_A to $\vec{p}'$ (*i.e.* $\vec{p}' = \vec{p}G_A$), and $\vec{p}'$ is then transformed by G_B to $\vec{p}''$ (*i.e.* $\vec{p}'' = \vec{p}'G_B$), then $\vec{p}'' = \vec{p}G_AG_B$.[3] In general, transformations are not commutative, so $G_AG_B \neq G_BG_A$.

Translation can be performed by simple vector addition, $\vec{p}' = \vec{p} + \vec{t}$, where $\vec{t}$ is the translation vector. Alternatively, translation can be performed through matrix multiplication, $\vec{p}' = \vec{p}T$, or:

$$\left| \begin{array}{cccc} p'_x & p'_y & p'_z & 1 \end{array} \right| = \left| \begin{array}{cccc} p_x & p_y & p_z & 1 \end{array} \right| \left| \begin{array}{cccc} 1 & 0 & 0 & 0 \\ 0 & 1 & 0 & 0 \\ 0 & 0 & 1 & 0 \\ t_x & t_y & t_z & 1 \end{array} \right| = \left| \begin{array}{cccc} p_x + t_x & p_y + t_y & p_z + t_z & 1 \end{array} \right| \tag{2.1}$$

The translation matrix T can equivalently be represented by:

$$T = \left| \begin{array}{ccc|c} 1 & 0 & 0 & 0 \\ 0 & 1 & 0 & 0 \\ 0 & 0 & 1 & 0 \\ \hline t_x & t_y & t_z & 1 \end{array} \right| = \left| \begin{array}{cc} I_3 & \vec{0}^T \\ \vec{t} & 1 \end{array} \right| \tag{2.2}$$

where I_3 is the 3×3 identity matrix and $\vec{0}^T$ is the transpose of the zero-vector.

It turns out all relevant geometric transformations can fit into this paradigm of transforming a vector by a 4×4 matrix multiplication, so conceptually it is simplest to perform transformations in this fashion. This also explains why it is desirable to represent a 3-D vector by four components ($\left| p_x \; p_y \; p_z \; 1 \right|$).

The rotation transformation matrix is given by:

$$R = \left| \begin{array}{cc} R_3 & \vec{0}^T \\ \vec{0} & 1 \end{array} \right| \tag{2.3}$$

where R_3 is a 3×3 matrix with a determinant of one (*i.e.* $\det R_3 = 1$). To determine R_3, the rotational transformation from one reference frame to another is not a difficult task. Let the

---

[2] This equation is compared to the case where vectors are column vectors (*i.e.* vertical) that post-multiply matrices, in which case the equation would read $\vec{p}' = G\vec{p}$.

[3] If post-multiplication were the convention, then the equation would read $\vec{p}'' = G_BG_A\vec{p}$. This equation is confusing because the transformation G_A was applied prior to G_B, but G_B precedes G_A in the equation.

orientation of the first reference frame be defined by the orthogonal unit vectors $\hat{\imath}$, $\hat{\jmath}$, and $\hat{k}$ ($|1\ 0\ 0|$, $|0\ 1\ 0|$, and $|0\ 0\ 1|$, respectively), and let the orientation of the second reference frame be defined by orthogonal unit vectors that in the first reference frame are $\hat{e}_1$, $\hat{e}_2$, and $\hat{e}_3$. Then $\hat{e}_1 R_3 = \hat{\imath}$, $\hat{e}_2 R_3 = \hat{\jmath}$, and $\hat{e}_3 R_3 = \hat{k}$, or as a matrix equation:

$$\begin{vmatrix} \hat{e}_1 \\ \hat{e}_2 \\ \hat{e}_3 \end{vmatrix} R_3 = \begin{vmatrix} \hat{\imath} \\ \hat{\jmath} \\ \hat{k} \end{vmatrix} = I_3 \tag{2.4}$$

Interestingly:

$$\begin{vmatrix} \hat{e}_1 \\ \hat{e}_2 \\ \hat{e}_3 \end{vmatrix} \begin{vmatrix} \hat{e}_1 \\ \hat{e}_2 \\ \hat{e}_3 \end{vmatrix}^T = \begin{vmatrix} \hat{e}_1 \\ \hat{e}_2 \\ \hat{e}_3 \end{vmatrix} \begin{vmatrix} \hat{e}_1^T & \hat{e}_2^T & \hat{e}_3^T \end{vmatrix} = \begin{vmatrix} \hat{e}_1 \cdot \hat{e}_1 & \hat{e}_1 \cdot \hat{e}_2 & \hat{e}_1 \cdot \hat{e}_3 \\ \hat{e}_2 \cdot \hat{e}_1 & \hat{e}_2 \cdot \hat{e}_2 & \hat{e}_2 \cdot \hat{e}_3 \\ \hat{e}_3 \cdot \hat{e}_1 & \hat{e}_3 \cdot \hat{e}_2 & \hat{e}_3 \cdot \hat{e}_3 \end{vmatrix} = I_3 \tag{2.5}$$

Equations 2.4 and 2.5 can be combined to yield:

$$R_3 = \begin{vmatrix} \hat{e}_1 \\ \hat{e}_2 \\ \hat{e}_3 \end{vmatrix}^{-1} = \begin{vmatrix} \hat{e}_1 \\ \hat{e}_2 \\ \hat{e}_3 \end{vmatrix}^T \tag{2.6}$$

The scaling transformation matrix is given by:

$$S = \begin{vmatrix} S_3 & \vec{0}^T \\ \vec{0} & 1 \end{vmatrix} \tag{2.7}$$

where S_3 is a 3×3 diagonal matrix, and $S_3 = sI_3$ for uniform scaling (s being the scalar scaling factor).

The general transformation matrix, which can include multiple translation, rotation, and uniform scaling operations, has the form:

$$G = \begin{vmatrix} \mathcal{R}_3 & \vec{0}^T \\ \vec{t} & 1 \end{vmatrix} \tag{2.8}$$

where $\mathcal{R}_3$ denotes the combination of rotation and uniform scaling operations. In the tree hierarchical structure, each child has an associated transformation matrix by which it is spatially related to its parent. A meaningful way of looking at this transformation matrix is that it converts a point in the child's reference frame to the parent's reference frame, *i.e.* the transformation matrix corresponds to a transformation of reference frame.

For SAR field prediction, it is critical to know how transducers of the applicator spatially relate to the patient. More specifically, it is necessary to go from the reference frame of each transducer to that of the patient, and *vice versa*. Before going further it is necessary to define some notation. $G_{A \to B}$ denotes the transformation matrix from reference frame A to B. Also, as before, $\vec{p}$ refers to a vertex, and subscripts refer to reference frames. For example, $\vec{p}_{\mathrm{pt}}$ and $\vec{p}_{\mathrm{xd}_i}$ refer to the same vertex $\vec{p}$ in the reference frames of *patient* and *xducer*$_i$, respectively. So we would like to know how to determine $G_{\mathrm{pt} \to \mathrm{xd}_i}$ and $G_{\mathrm{xd}_i \to \mathrm{pt}}$, such that:

$$\vec{p}_{\mathrm{xd}_i} = \vec{p}_{\mathrm{pt}} \, G_{\mathrm{pt} \to \mathrm{xd}_i} \qquad \text{and} \qquad \vec{p}_{\mathrm{pt}} = \vec{p}_{\mathrm{xd}_i} \, G_{\mathrm{xd}_i \to \mathrm{pt}} \tag{2.9}$$

To calculate $G_{\mathrm{pt} \to \mathrm{xd}_i}$, it is necessary to travel along the branches of the tree that connect *patient* with *xducer*$_i$:

$$G_{\mathrm{pt} \to \mathrm{xd}_i} = G_{\mathrm{pt} \to \mathrm{gr}} \, G_{\mathrm{gr} \to \mathrm{ap}} \, G_{\mathrm{ap} \to \mathrm{xd}_i} \tag{2.10}$$

where the subscripts gr and ap refer to *graph* and *applicator*, respectively. Now $G_{\mathrm{pt} \to \mathrm{gr}}$ is the transformation from a child (*patient*) to its parent (*graph*)—this is, by definition, the transformation of the child. So $G_{\mathrm{pt} \to \mathrm{gr}} = G_{\mathrm{pt}}$. Conversely, $G_{\mathrm{gr} \to \mathrm{ap}}$ is the transformation for a parent (*graph*) to its child (*applicator*), which is the inverse of the transformation of a child to its parent. So $G_{\mathrm{gr} \to \mathrm{ap}} = G_{\mathrm{ap}}^{-1}$. Similarly, $G_{\mathrm{ap} \to \mathrm{xd}_i} = G_{\mathrm{xd}_i}^{-1}$. So Equation 2.10 becomes:

$$G_{\mathrm{pt} \to \mathrm{xd}_i} = G_{\mathrm{pt}} \, G_{\mathrm{ap}}^{-1} \, G_{\mathrm{xd}_i}^{-1} \tag{2.11}$$

A similar analysis can yield $G_{\mathrm{xd}_i \to \mathrm{pt}}$. Alternatively, if $G_{\mathrm{pt} \to \mathrm{xd}_i}$ is already known, $G_{\mathrm{xd}_i \to \mathrm{pt}}$ can be determined by recognizing these two transformations are inverses of each other:

$$G_{\mathrm{xd}_i \to \mathrm{pt}} = G_{\mathrm{pt} \to \mathrm{xd}_i}^{-1} = G_{\mathrm{xd}_i} \, G_{\mathrm{ap}} \, G_{\mathrm{pt}}^{-1} \tag{2.12}$$

2.1.1 Computational Short Cuts

Computational savings can be achieved when performing several types of matrix operations in this computer graphics matrix paradigm. Specifically, G matrix inversion, $G_A G_B$ matrix multiplication, and $\vec{p}\,G$ vector-matrix multiplication can be performed with half to three-quarters the computational effort (and time) as that necessary to perform the same operations on general 4-vectors (*i.e.* 4-component vectors) and 4×4 matrices.

The canonical form of the G transformation matrix lends itself more easily to matrix inversion than the general 4×4 matrix. It is a trivial exercise to demonstrate that:

$$G^{-1} = \left| \begin{array}{cc} \Re_3 & \vec{0}^T \\ \vec{t} & 1 \end{array} \right|^{-1} = \left| \begin{array}{cc} \Re_3^{-1} & \vec{0}^T \\ -\vec{t}\,\Re_3^{-1} & 1 \end{array} \right| \tag{2.13}$$

Thus only a 3×3 matrix need be inverted, instead of a 4×4 matrix. Since dense matrix inversion is typically $\mathcal{O}(n^3)$ operations (where $n \times n$ is the size of the matrix being inverted), a computational savings of around 40% is achieved.

In the general case of matrix multiplication of two 4×4 matrices, 64 **floating point** multiplications and 48 floating point additions are used. In the current paradigm, however, the fourth column of G_A and G_B is always $|0\ 0\ 0\ 1|^T$, so only 48 multiplications and 36 additions need be performed, for a computational savings of 25%.

In truth, the computational savings in these matrix inversion and matrix multiplication operations, though satisfying, do not result in measurably faster program performance. To see why, we take the case of planning a patient treatment with the FSUM, and its 56 transducers. In the worst (most computationally involved) scenario, we would like to know the 56 $G_{\mathrm{pt}\to\mathrm{xd}_i}$ and 56 $G_{\mathrm{xd}_i\to\mathrm{pt}}$ transformation matrices, for a total of 112. Equation 2.12 shows that to obtain all the $G_{\mathrm{xd}_i\to\mathrm{pt}}$, we need to perform a single matrix inversion (G_{pt}^{-1}), a matrix multiplication to calculate $G_{\mathrm{ap}}\,G_{\mathrm{pt}}^{-1}$, and another matrix multiplication to calculate $G_{\mathrm{xd}_i}\,G_{\mathrm{ap}}\,G_{\mathrm{pt}}^{-1}$ for each transducer; this is a total of one matrix inversion and 57 matrix multiplications. Then to obtain each the $G_{\mathrm{pt}\to\mathrm{xd}_i}$ we need to perform a matrix inversion on each $G_{\mathrm{xd}_i\to\mathrm{pt}}$, resulting in 56 matrix inversions. So all 112 transformation matrices were obtained at the computational price of 57 matrix inversions and 57 matrix multiplications. The user sitting in front of the computer terminal cannot register the short time it would take a computer (operating at millions of **FLOPs**—floating point operations per second) to perform these few calculations, whether or not the matrix operation algorithms it used were computationally efficient.

But computational savings in vector-matrix multiplication can indeed be valuable, because so many more of this type of matrix operation are performed. To give a quick example, when performing SAR field predictions it is necessary to determine the coordinates of each point in the patient lattice in the reference frame of each transducer. The number of points in a typical patient lattice is $\mathcal{O}(10^4\text{–}10^5)$, which, when multiplied by 56 transducers, results in $\mathcal{O}(10^5\text{–}10^7)$ vector-matrix multiplications.

In the general case of multiplication of a 4-vector by a 4×4 matrix, 16 multiplication and 12 addition operations are necessary. But in the transformation paradigm, because the fourth column of $\vec{p}$ is always 1 and the fourth column of G is always $|0\ 0\ 0\ 1|^T$, only 9 multiplication and 9 addition operations are necessary. This produces a computational savings of about 40% (because multiplication is a much more computationally costly operation than addition).

2.2 AVS: For Scientific Data Visualization

AVS is both a software product, Application Visualization System, and the company that makes it, Advanced Visual Systems Inc. (In this thesis, AVS will refer exclusively to the software.) AVS is described as a data visualization environment, and its oldest part, the **Geometry Viewer**, is a 3-D **surface renderer**, and is central to the graphical requirements of this thesis.

The Geometry Viewer is built on PHIGS (Programmer's Hierarchical Interactive Graphics System), which is used for displaying graphical **primitives**—simple graphical objects such as lines, triangles, and text. Complex objects are constructed from many primitives. The Geometry Viewer also uses geometric primitives, although they are not quite as primitive as those used by PHIGS. In general, graphical limitations of PHIGS are also limitations of the Geometry Viewer. Furthermore, these limitations are usually low-level, and difficult to overcome. For example, a triangle is defined in PHIGS by the (x, y) coordinates and RGB (red, green, and blue) color values for each of its three vertices. To color the triangle, RGB values are interpolated (using barycentric weighting of the vertex colors) to blend colors smoothly between vertices. But if the color is meant to represent a value above (*e.g.* red) or below (*e.g.* blue) a certain threshold value, then we would like to see a triangle with one red vertex and two blue vertices colored in two distinct, uniformly colored regions, instead of by a smooth blend.

Since its first incarnation, AVS has expanded to include a number of data manipulation and visualization capabilities. Isolated functions are put in **modules**, and modules are connected to make **flow networks**. This modular structure promotes clear thinking and organization, and also provides a framework for custom development of new modules to perform custom functions. There are limitations in AVS customization as well. For example, while custom data structures can be created in AVS and passed between modules, these data structures cannot be sized dynamically, but must instead be of a fixed size.

HYPER/Plan is a custom module under development at the JCRT—initially by Mark Dopheide, and more recently by Jørgen L. Hansen and James M. Pelagatti. It was conceived as a **geometric** patient treatment planning system. This means it was designed to provide graphical representations of the patient and the treatment applicator, and allow the user to manipulate them to plan the geometry of the treatment. The representations of the patient and applicator need to be able to move *together*, to change the point of view of the user; and *separately*, to change their relative positions and orientations. HYPER/Plan has another graphical capability related to power deposition: it gives the user an idea of where power will be deposited by projecting square tubes from transducers that are powered on. This simple display of the qualitative power deposition field is only a very rough approximation of the true field, but it gives a "quick and dirty" indication of where heating is likely to occur for a given geometric arrangement of the patient and applicator. Figure 2-2 shows the key features of HYPER/Plan: the 3-D Geometry Viewer (upper right), containing the representations of the patient organ surfaces and the FSUM power applicator; the geometric control panel (left), with widgets to control the position and orientation of *patient*, *applicator*, or *graph* (*i.e.* both the patient and applicator together); the applicator power control panel (lower right), allowing power on or off for each transducer.

AVS geometric objects are called **geoms**, and they come in several flavors. The anatomic surface representations generated in HYPER/Plan are made out of the **polytriangle** type of geom, which consists of polytriangles (strips of connected triangles), polylines (connected line segments), and disjoint lines (unconnected line segments). The objects can be rendered as shaded surfaces, by showing the polytriangles, as wire frameworks, by showing the polylines and disjoint lines, or as a combination of both.

2.3 IMEX and Mosaic: For Generation of Anatomic Geoms

The patient anatomy displayed in HYPER/Plan is custom generated for each patient, and often for each treatment. This process begins with a 3-D patient image obtained from some medical imaging technology. Typically CT (computed tomography) is used, but MRI (magnetic resonance imaging), PET (positron emission tomography), or any alternative imaging modality

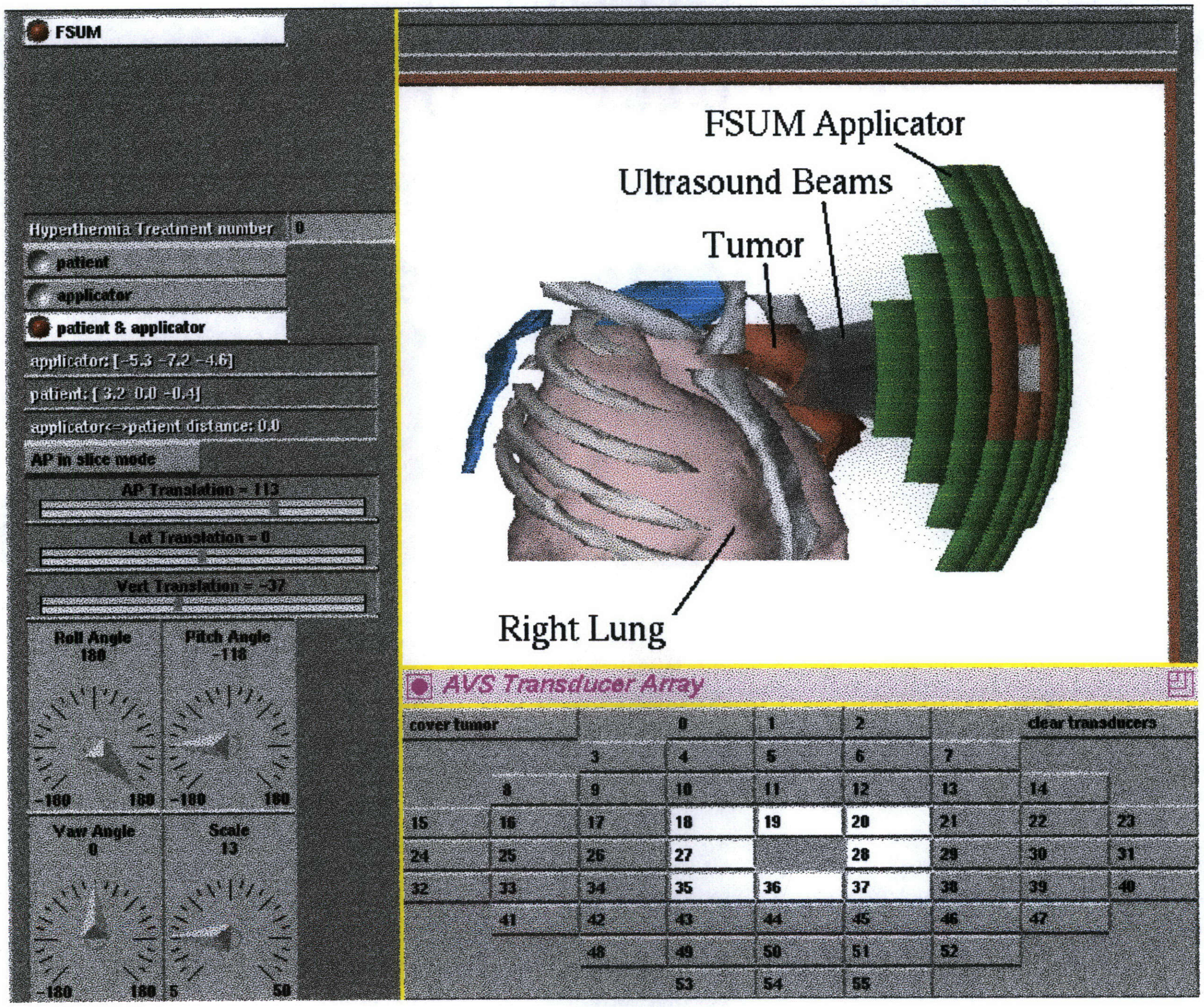

Hyperthermia Treatment number 0

applicator: [-5.3 -7.2 -4.6]

patient: [3.2 0.0 -0.4]

applicator<=>patient distance: 0.0

AP Translation = 113

Lat Translation = 0

Vert Translation = -37

Roll Angle 180

Pitch Angle -118

Yaw Angle 0

Scale 13

Figure 2-2: Typical image from HYPER/Plan, in color.

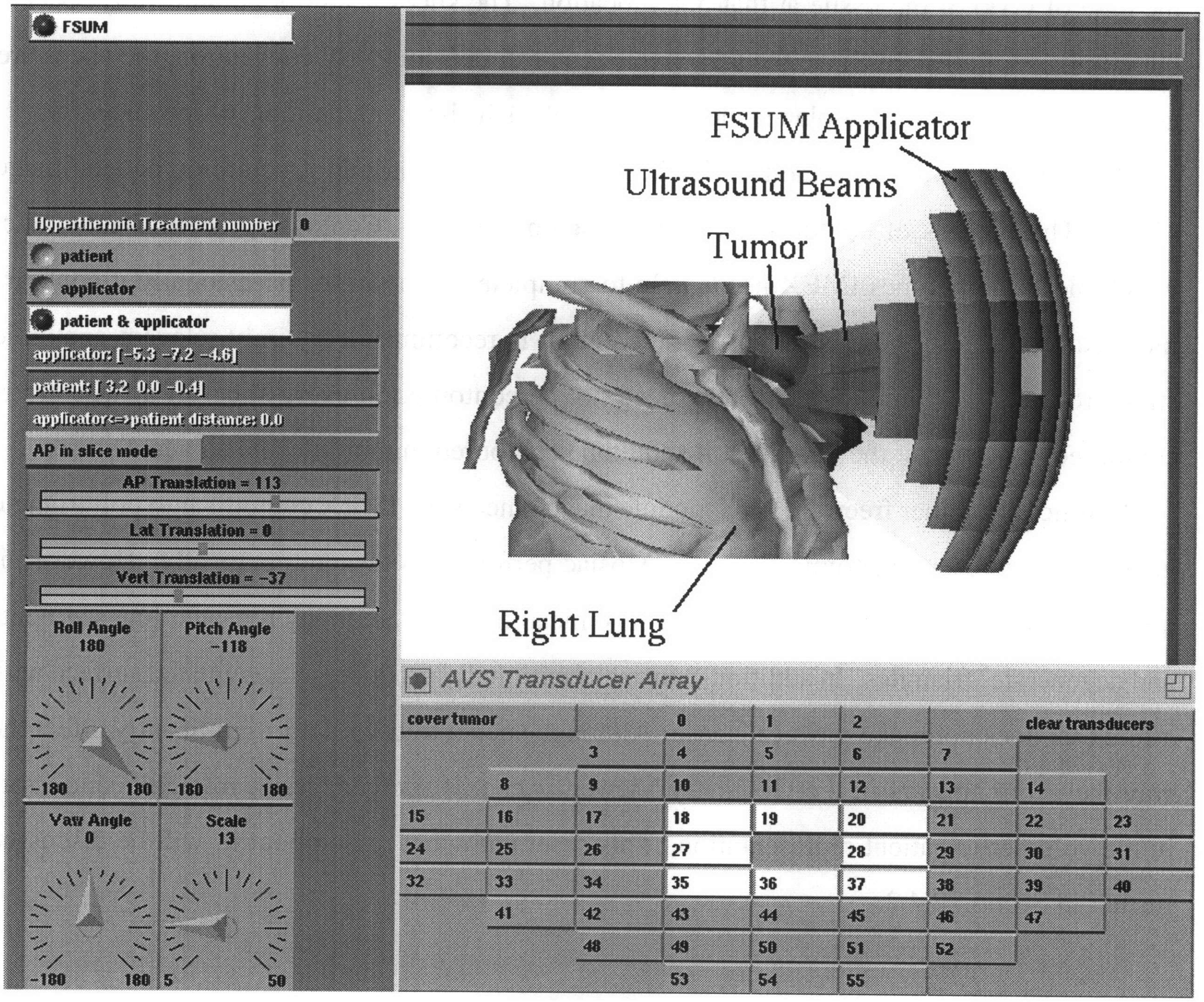

Hyperthermia Treatment number 0

○ patient

○ applicator

● patient & applicator

applicator: [-5.3 -7.2 -4.6]

patient: [3.2 0.0 -0.4]

applicator<=>patient distance: 0.0

AP in slice mode

AP Translation = 113

Lat Translation = 0

Vert Translation = -37

Roll Angle 180

Pitch Angle -118

Yaw Angle 0

Scale 13

Figure 2-2: Typical image from HYPER/Plan.

that can produce an `<.ima>` image file can be used to create the patient image as well. `<.ima>` is the standard patient image file format developed and used at the JCRT, and its format reflects how patient images are actually acquired. The 3-D image is a collection of parallel 2-D slices through the patient. Each 2-D image is a collection of rectangular (typically square) **pixels**, and the color or intensity of the pixel reflects the value of some property (*e.g.* radiodensity, in the case of CTs) of the tissue at that pixel location. The slices need not be uniformly spaced, but all pixels of all slices have the same rectangular dimensions. By convention, the slices are generally parallel to the xy-plane, and the origin of each slice is the middle of the slice.

IMEX is a freeware AVS module that is used to contour anatomic structures in patient image slices. The process of contouring is termed **segmentation**. Contouring is semi-automatic, which means sometimes IMEX needs help to complete a contour, or occasionally it contours incorrectly. In both these cases, user intervention is recommended. Only relevant anatomic structures need be contoured, and they need not be contoured in every slice. If a structure is contoured, however, at the very least it should be contoured in multiple and adjacent slices.

Mosaic[4] is another freeware AVS module that connects the IMEX contours into polytriangle geoms that represent anatomic surfaces. Mosiac performs its task automatically. However, it does not generate particularly efficient geoms, meaning there are many repeated line segments and degenerate[5] triangles. In addition, Mosiac occasionally produces a triangulated surface with a fold that does not make physical sense. Although such a fold does not significantly affect the way the geom appears in the Geometry Viewer, it can, if ignored, result in significant errors in the volumetric patient representation. This case, and what to do about it, will be discussed further in Section 2.4.2.

2.4 Volumizer: For Surface to Volumetric Representation Conversion

Volumizer[6] is the AVS module that automatically generates the volumetric patient representa-

---

[4] This Mosaic module is not to be confused with the NCSA Mosaic World Wide Web browser.

[5] A **degenerate** triangle has three colinear vertices and no area. The degenerate triangles generated by Mosaic are invariably composed of only one or two distinct vertices.

[6] Thanks to Dr. Gregory T. Martin, who conceived the name "Volumizer."

tion, a.k.a. the patient **mesh** and the patient **lattice**. Because the patient geometry is irregular, this volumetric representation is critical for 3-D power deposition and thermal analysis, whether the calculation method be finite difference, finite element, or some other numerical technique. In the context of HYPER/Plan, the initial patient model is a surface model (obtained from a volumetric patient image first contoured by IMEX, then triangulated by Mosaic), so conversion of this surface patient model to a volumetric patient model is necessary before power deposition and heat transfer modeling can be performed.

Volumizer takes as input all the patient anatomic geoms, and generates a field that completely encloses the imaged portion of the patient. Each point of the field is identified by 3-D coordinates, and a scalar field value or data value. The field value is a code number that corresponds to an anatomic structure. Tumor, *e.g.*, is identified by the number 11, so every point of the patient mesh that resides within the tumor volume has data value 11.

Volumizer automatically generates a regular lattice, although there is no reason (short of the necessary effort) it could not be customized to generate an irregular lattice that conforms better to the patient anatomy. Once the coordinates of each lattice point are known, Volumizer determines which anatomic structure (if any) each point resides within.

Now the 2-D version of Volumizer's objective, *i.e.* the determination of whether a point is inside a polygon is an extensively studied problem, and there are several well-known solution methods. Haines [36] gives a good review article on the subject. The most popular family of solutions is probably the crossings test, but other solution methods certainly exist, such as the angle summation and triangle fan methods). All of these methods mentioned can be naturally extended to 3-D (see Carvalho and Cavalcanti [16] for a 3-D analog of the angle summation method), but the one that will be developed in Volumizer is based on the crossings test. What is original in the Volumizer algorithm is that it is optimized for determining whether a point is inside a polyhedron of the type generated by Mosaic—constructed of triangles arranged in parallel layers.

Conceptually, the way Volumizer determines whether a point lies within a given geom is to shoot a ray from the point to infinity (in any direction), and determine how many times the ray intersects the enclosed surface of the geom. If the number of intersections is odd, the point is inside the geom, and if the number is even, the point is outside. This strategy is illustrated in

2-D in Figure 2-3. The general inside point, P_1, emanates two sample rays which intersect the perimeter L an odd number of times; similarly, the rays coming from the general outside point, P_2, intersect L an even number of times.

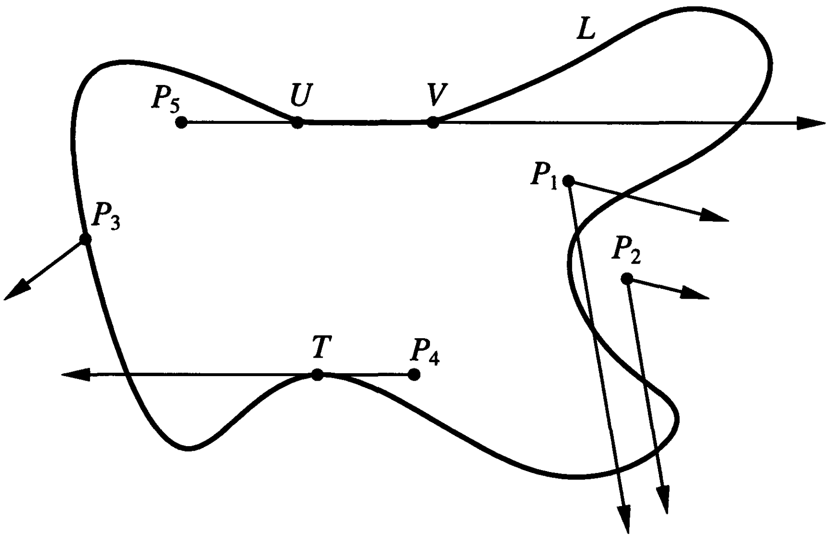

Figure 2-3: Central concept of Volumizer.

As is often the case with simple concepts, implementation is fairly involved. Reasons for difficulty of implementation fall into two categories: special cases and optimizations. Some of the special cases are illustrated in Figure 2-4, and they will be addressed later, after discussing the specifics of the implementation of Volumizer.

Before proceeding to implementation, however, a sample tissue type field generated by Volumizer is shown in Figure 2-4. The grid indicates different organ types by different color, with blue signifying tissue within the patient volume but not within a specific organ structure. A gray plane indicates the tranverse plane through the patient corresponding to the displayed slice of the tissue type field.

2.4.1 Computational Implementation

The anatomic polytriangle geom surfaces are composed of triangles, and a sample (albeit simple) surface is shown in Figure 2-5A. $PQRS$ is a tetrahedron, and we would like to know if the point V lies within it. A ray x' parallel to the x-axis is drawn from V, and it is easy to see the ray intersects the surface of $PQRS$ in two places: $\triangle PQR$ at T and $\triangle QRS$ at U. It takes a little

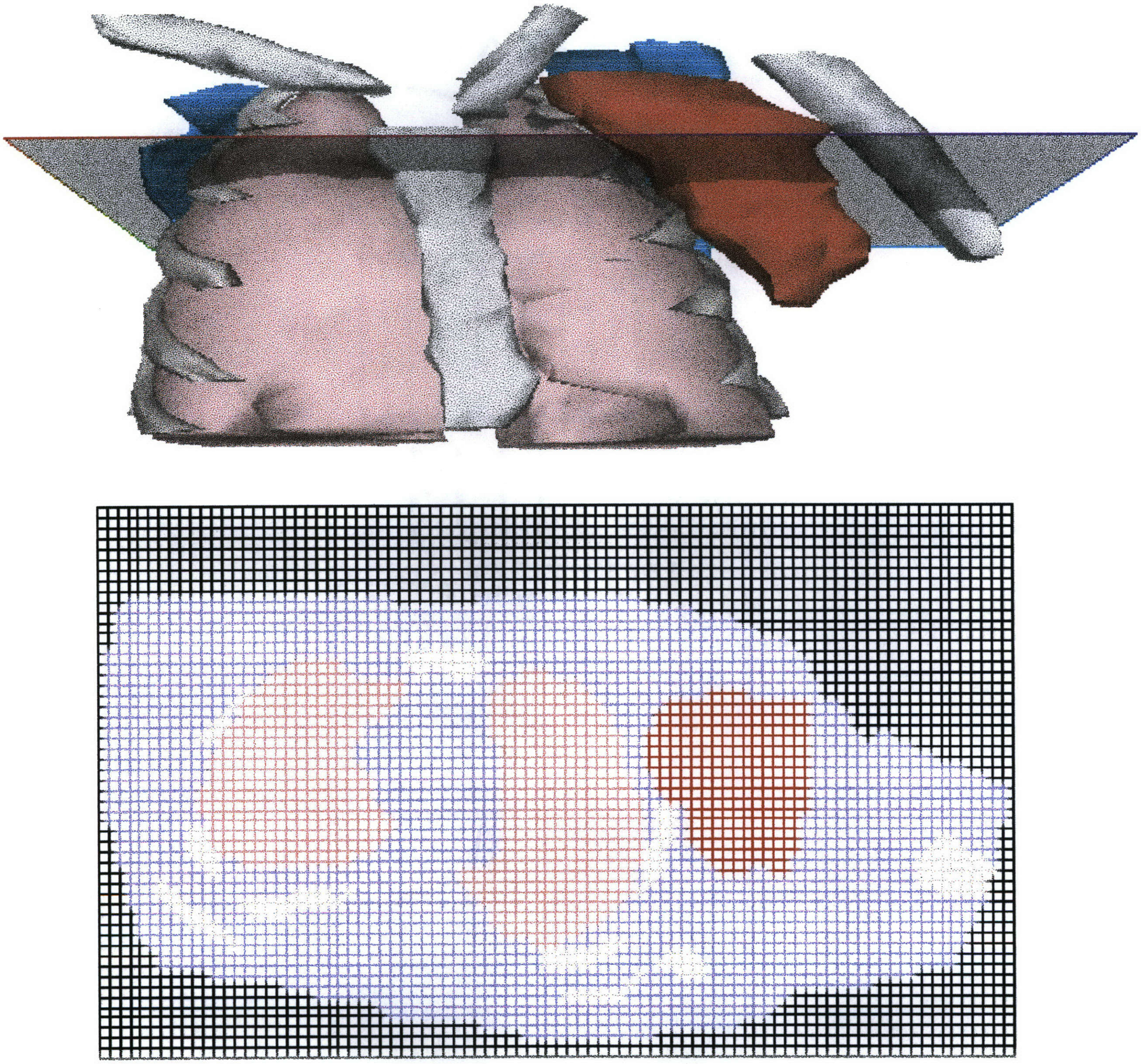

Figure 2-4: Cross-section through a typical tissue type field generated by Volumzer, in color.

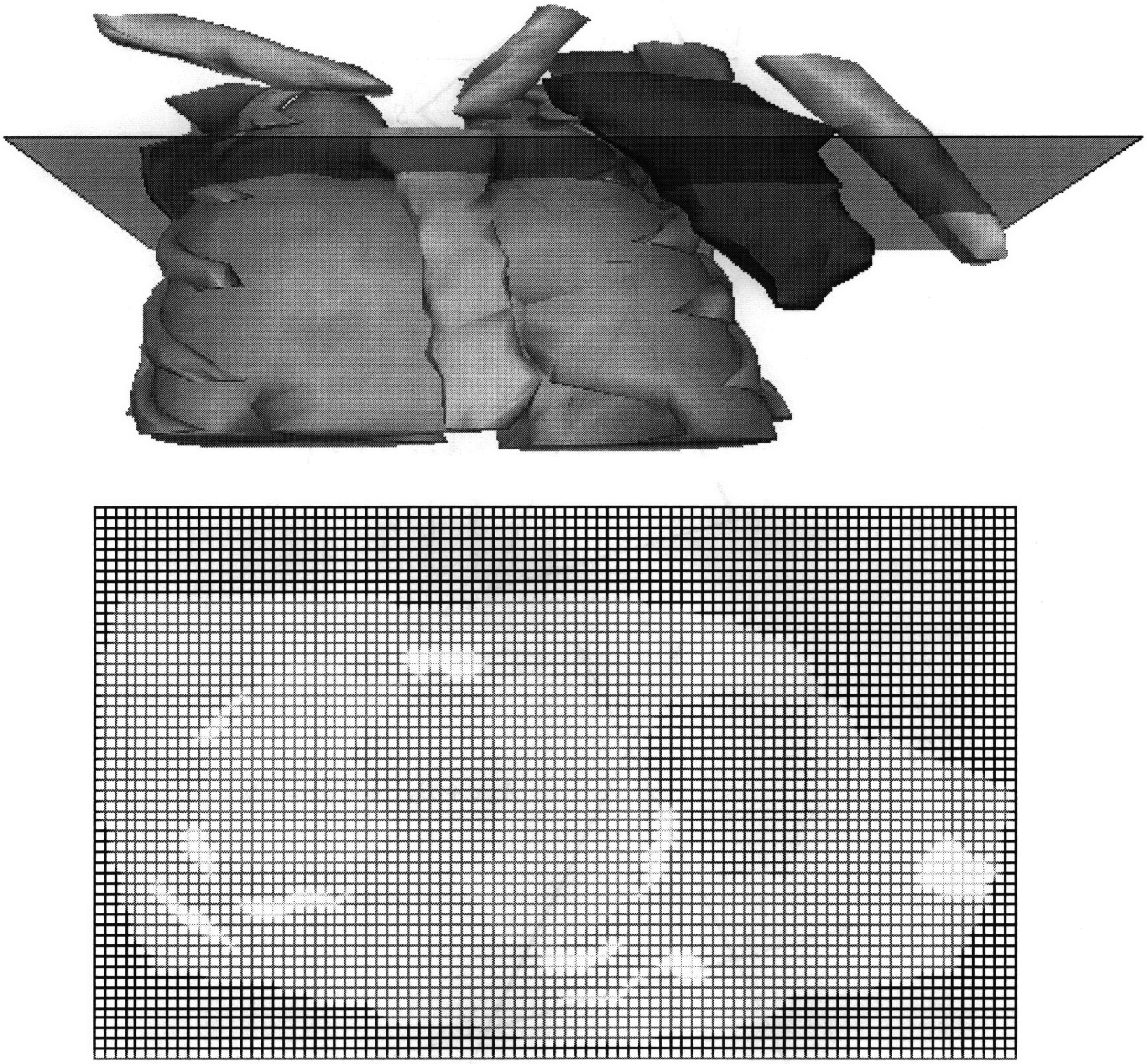

Figure 2-4: Cross-section through a typical tissue type field generated by Volumzer.

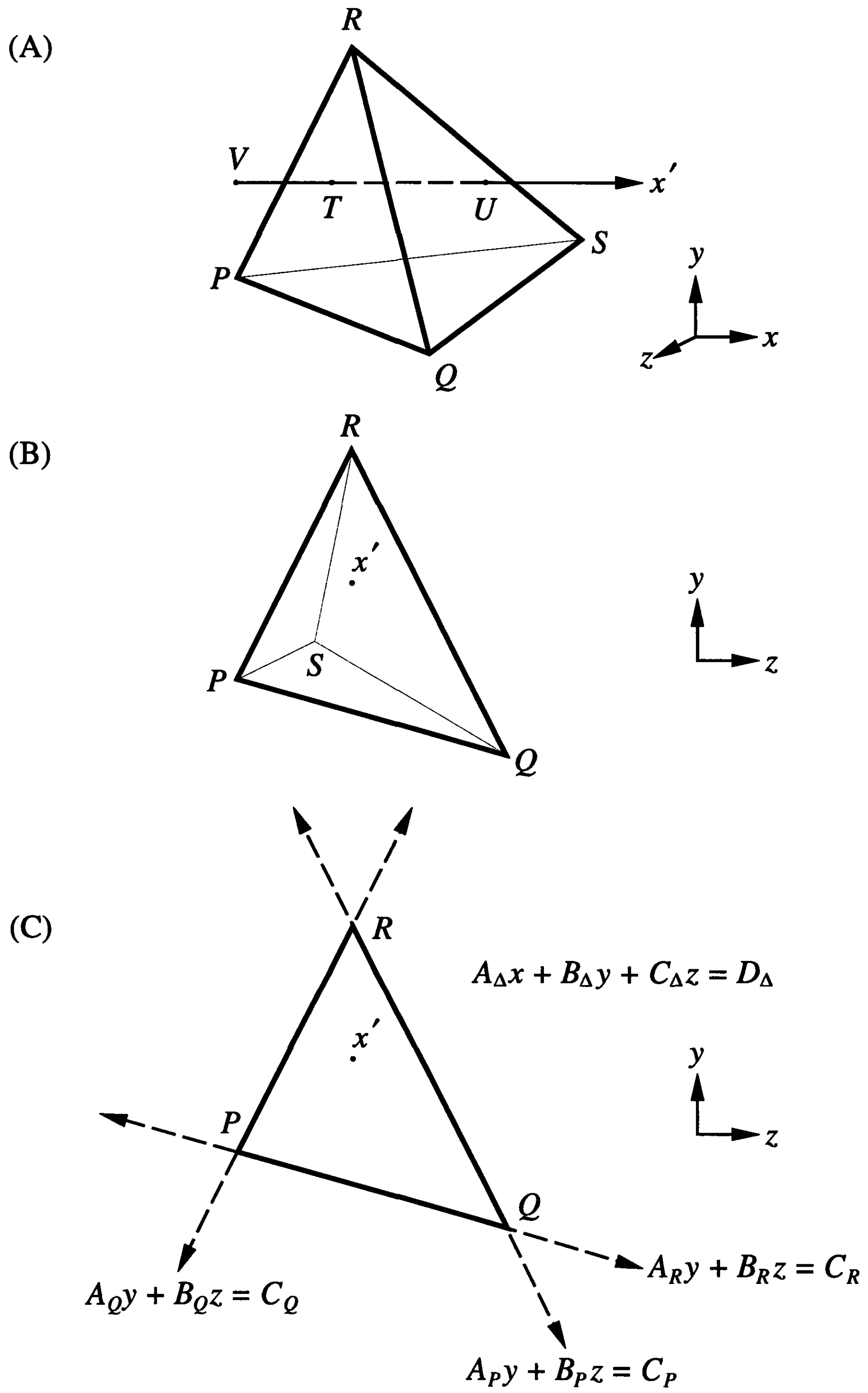

Figure 2-5: How to determine if a point is inside a triangulated surface.

more work for the computer to "see" this, however. First, the computer looks at the projections of the tetrahedron's four constituent triangles on the yz-plane, as shown in Figure 2-5B. Second, the computer determines whether the line (not just the ray) x' intersects the projections of the triangles. (If the line intersects the projection of a triangle, then it will also intersect the triangle itself. This is only true because the projection is parallel to the line.) This determination of intersections is performed for all triangles composing the surface (*i.e.* $\triangle PQR$, $\triangle PQS$, $\triangle PRS$, and $\triangle QRS$, in the present example). Third and last, the computer determines for all triangles that intersect the line x' (*i.e.* the ray x' extended infinitely in both directions) the x coordinate of the intersection, and counts the number of intersections that occur between V, (v_x, v_y, v_z), and the end of the ray x', $(+\infty, v_y, v_z)$.

Figure 2-5C illustrates how to determine if the line x' intersects $\triangle PQR$, and if so, how to determine the x coordinate of the intersection. (See Section B.1 for more details.) In general, a line in the yz-plane is defined by the equation $Ay + Bz = C$. (A or B, but not both, can equal 0, and C can equal 0.) For example, the line $\overline{PQ}$ is defined by $A_R\, y + B_R\, z = C_R$. The line divides the yz-plane into two semi-infinite regions, and all (y, z) pairs in one region (not including the boundary, *i.e.* the line itself) can be defined by the inequality $A_R\, y + B_R\, z > C_R$; similarly, all the pairs in the other region can be defined by $A_R\, y + B_R\, z < C_R$. By my convention, the constants A_R, B_R, and C_R are such that for all points within $\triangle PQR$ the first inequality holds. Define the corresponding lines for the other two sides of the triangle ($\overline{PR}$ and $\overline{QR}$). Then:

$$\text{If}\quad \left.\begin{aligned} A_P\, v_y + B_P\, v_z &> C_P \\ A_Q\, v_y + B_Q\, v_z &> C_Q \\ A_R\, v_y + B_R\, v_z &> C_R \end{aligned}\right\} \implies (v_y, v_z) \text{ lies within the } yz \text{ projection of } \triangle PQR. \tag{2.14}$$

If Equation 2.14 holds true, the next matter is to determine the x coordinate of the intersection of the line x' with the *un*projected triangle $\triangle PQR$. That triangle lies in a plane defined by $A_\triangle\, x + B_\triangle\, y + C_\triangle\, z = D_\triangle$. Given v_y and v_z, it is now a trivial matter to determine the x coordinate of the point of intersection of $\triangle PQR$ and line x'.

This procedure must be repeated for each of the constituent triangles of the geom surface. The x coordinates of all intersection points between the triangles of the geom surface and the line x' are determined, and those that fall between v_x and $+\infty$ (*i.e.* on the ray x') can be counted. If the count is odd, the point V lies inside the geom, and if the count is even it lies outside.

There is a slightly easier, less direct way to count the number of intersections between V and the end of ray x'. Unfortunately, reasons alluded to in Section 2.3 and discussed in Section 2.4.2 preclude this alternative technique, but it is worth mentioning anyway because it parallels the result of Equation 2.14. Just as a line divides a plane into two semi-infinite planar regions, a plane divides a 3-D space into two semi-infinite 3-D regions. All the points in one of the semi-infinite regions are defined by $A_\triangle x + B_\triangle y + C_\triangle z > D_\triangle$, and all those in the other by $A_\triangle x + B_\triangle y + C_\triangle z < D_\triangle$. By my convention, points that lie in the region that contains the $+\infty$ end of the ray x' are defined by the second inequality. Then:

$$\text{If } A_\triangle v_x + B_\triangle v_y + C_\triangle v_z > D_\triangle \implies V \text{ lies between } T \text{ and the end of ray } x', \qquad (2.15)$$

i.e. V is in the $+x$ direction of the unprojected triangle $\triangle PQR$.

Another point worth mentioning is why a line x' parallel to the x-axis is favored over other directions. At first glance, lines parallel to any of the three orthogonal directions (x-, y-, or z-axis) are equivalent, and any of them are preferable to oblique directions because projections are easier to perform (*i.e.* less computationally involved) in the three orthogonal directions. But for reasons related to anatomy, lines parallel to the y-axis are poor choices.

In the coordinate system of the anatomic geoms generated by Mosaic the y-axis extends from head to toe (or toe to head).[7] Within each scanned slice of the patient the organ contours generated in IMEX are closed curves, and these curves are connected into a surface representation by Mosaic. If an organ is not completely contained in the region of the patient that was imaged, it does not make sense to close the surface representation of the organ where it intersects the boundary of the imaged region. A similar situation arises if an organ is not contoured in every image slice in which it appears. Sometimes Mosaic closes the organ surface anyway, and sometimes it does not. Figure 2-6 shows an image from HYPER/Plan in which the contoured skin surface is open on the top and bottom, but the lungs are both closed on the bottom, where they intersect the boundary of the imaged region. If an anatomic geom is open on its top or bottom, the algorithmic concept of Volumizer will not work if rays or lines parallel to the y-axis are used. But even if a geom is open on its top or bottom, it will still appear closed on its sides, so using rays or lines parallel to the x- or z-axis will both work, and work equally well. By my convention, lines parallel to the x-axis are used.

---

[7] *N.B.*: This is not the same coordinate system as the one typically used in medical imaging systems, such as CT, where it is the z-axis that extends from head to toe (or toe to head).

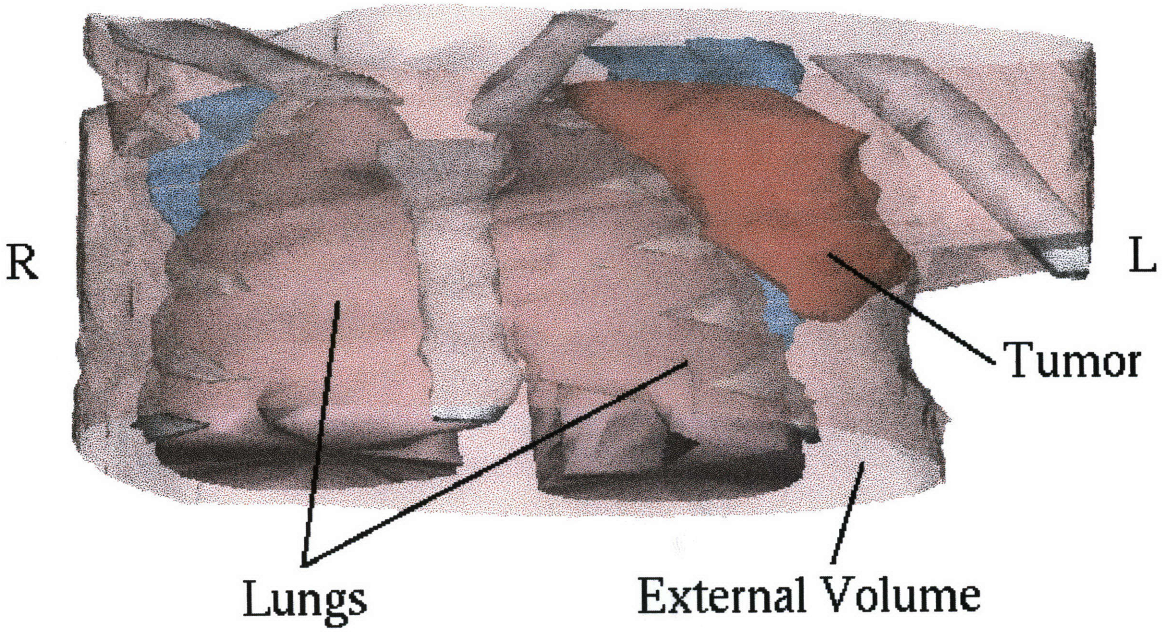

Figure 2-6: 2-D organ surfaces in HYPER/Plan, in color. The external volume is open on top and bottom, but other organs, *e.g.* the lungs, are closed.

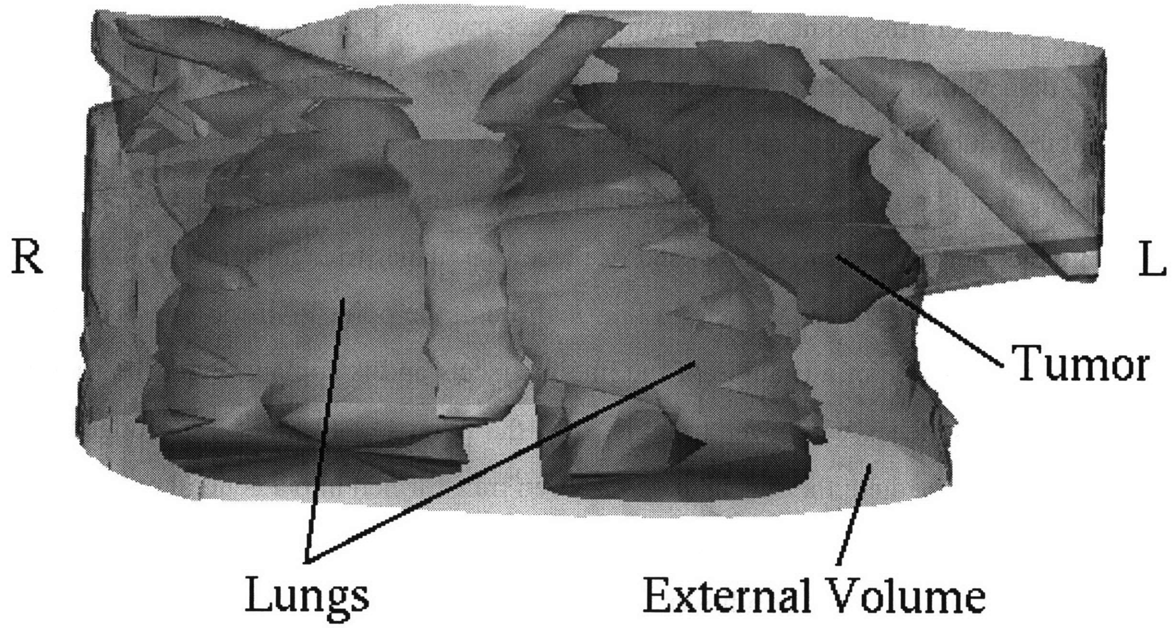

Figure 2-6: 2-D organ surfaces in HYPER/Plan. The external volume is open on top and bottom, but other organs, *e.g.* the lungs, are closed.

2.4.2 Geometric Special Cases

The points P_3, P_4, and P_5 in Figure 2-3 on page 42 illustrate three special cases. P_3 is a point that lies on the perimeter itself, so whether it is inside or outside is ambiguous. The ray shown coming out of point P_4 is tangent to the perimeter at T, so it intersects L an even number of times even though P_4 is inside the perimeter. Finally, P_5 intersects L throughout the entire length of the line segment $\overline{UV}$—an infinite number of intersections, neither odd nor even. In practice, all three of these special cases can be handled when they occur by "fudging" the point, *i.e.* slightly perturbing the coordinates of the point. This is a legitimate procedure because even if the coordinates of the point were known to an accuracy of 1 μm (which they most certainly are not), then within experimental error they could be fudged by 0.1 μm, and that would be sufficient to reduce the special case to the general case.

Fudging would probably be difficult to implement if the enclosed surface were everywhere differentiable, but because it is composed of piecewise planar triangular pieces it is relatively straightforward. Using the example of a line x' through the point V, if the line is observed to intersect exactly a side of a triangle, if the line intersects and is coplanar with the triangle, or if the point V itself lies within the triangle, then the point V and line x' are fudged and the transgression is remedied; the special case has been transformed into a general case.

There is one other special case, alluded to in Section 2.3, that should not exist at all, but does exist because of a Mosaic idiosyncrasy. Consider two coplanar triangles, $\triangle JKM$ and $\triangle JLM$ in Figure 2-7A, that make up part of a triangulated surface of a geom. This geometry also contains a third implied and somewhat redundant triangle, $\triangle JKL$, which covers the same territory as the other two combined. A line that intersected $\triangle JKM$ would also intersect $\triangle JKL$, registering two intersections where only one should exist. Figure 2-7B illustrates a variation on this idea. $\triangle QRS$ and $\triangle QST$ are two non-coplanar triangles that make up part of a geom surface. But the four triangles $\triangle PQR$, $\triangle PRS$, $\triangle PST$, and $\triangle PTQ$ give an alternate, slightly different representation of the same patch of surface represented by the geom.[8] A line that intersects $\triangle PQR$, for example, will (probably) also intersect $\triangle QRS$. In this case there are technically two distinct surfaces covering the same surface region $QRST$, but there should

---

[8] Technically, of course, the hexahedron (six-sided solid) $PQRST$ is a legitimate triangulated surface in its own right. But this example is meant to show two different but close representations of the same patch of surface, like two pieces of paper, one on top of the other.

only be one.

Part of Mosaic's personality is that it occasionally generates duplicate sets of triangles that correspond to the same patch of surface, and the sets can be equivalent, as in Figure 2-7A, or slightly different, as in Figure 2-7B. These funny patches, or **folds** (my terminology), are not generated frequently, but the fact that they occur at all demands they be addressed. A general line (meaning a line that does not fall into one of the special case categories illustrated in Figure 2-3, page 42) intersects an enclosed surface an even number of times; but if the line passes through a fold, then it may intersect the surface an odd number of times. Thus an odd number of intersections between a general *line* and an enclosed surface indicates the presence of a fold. In contrast, a general *ray* can intersect a surface an odd or even number of times, so it cannot be used to indicate the presence of a fold. This is why the specific algorithm used in Volumizer intersects a line with a geom, and not a ray. In the case of an odd number of intersections between a general line and an enclosed surface, the two points of intersection which are closest to each other (and they may be identical) are combined into a single point in the middle.

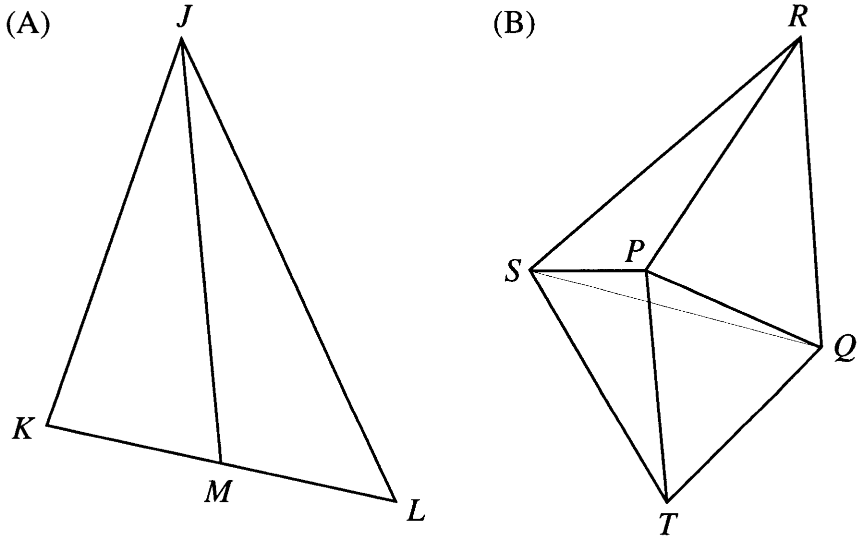

Figure 2-7: Idiosyncratic cases in Mosaic.

2.4.3 Computational Optimization

Volumizer basically performs three tasks:

1. Organizes information about the constituent triangles that make up the triangulated geoms.

2. Generates automatically the 3-D coordinates of the patient lattice, the boundaries of which surround the volume of the patient image.

3. Determines which anatomic structure, if any, each lattice point resides within.

2.4.3.1 Pre-Processing

The first task falls under the general computational technique of **pre-processing**. The idea behind this technique is that by investing a little time and effort up front, great savings in time and effort can be had later on. In the case at hand, information about the triangles of each geom is calculated and organized so that it can be easily accessed later on.

First, the extreme x, y, and z coordinates of each geom are determined, forming a **bounding box** on the geom. This is important because if the lattice point lies outside the bounded region of the geom then it is outside the geom itself, and no more work need be done.

Second, the constants of the equations defining the three lines of the sides of each triangle (see Equation 2.14), and the equation defining the plane in which the triangle lies (see Equation 2.15) are calculated and stored for each triangle. By calculating these constants once and storing them, rather than calculating them for every point in the lattice, an enormous amount of time is saved.

Finally, the triangles of each geom are ordered and numbered. The purpose of this ordering is to limit the number of triangles that have to be tested for intersection with a line. To give an analogy, if I am trying to find room 1997 in an unfamiliar building, I will start (and end!) my search on the 19th floor, and I need not worry about trying doors on any of the other floors of the building. Triangles are ordered according to the minimum y coordinate of the triangle ($\min_y(\triangle)$).[9] In cases where two triangles have the same $\min_y(\triangle)$, they are ordered according to $\max_y(\triangle)$. When the y extents of two triangles are both equal, they are sorted according to $\min_z(\triangle)$; and if they are still equal, by $\max_z(\triangle)$. Figure 2-8 and Table 2.1 illustrate how some sample triangles would be sorted (using only information about the y extents). The triangles are sorted using the ANSI standard `qsort()` function, which resides in the C library associated with `<stdlib.h>`. This routine uses the quick sort algorithm [88], and sorts in $\mathcal{O}(n \log n)$

---

[9] Here are two examples to elucidate notation: $\min_y(\triangle)$ is the minimum y coordinate of a triangle; $\max_z(\triangle_3)$ is the maximum z coordinate of triangle #3.

time.

Triangles are numbered in five ways: sorted, y ascending, y descending, z ascending, and z descending order. The first three numbering schemes are illustrated in Figure 2-8. The sorted order numbers, s_i, are indicated inside the triangles in Figure 2-8. (There are $n = 9$ triangles, and i is the index number of a given triangle, with $1 \leq i \leq n$.) The sorted ordering may be considered an identity ordering, with $s_i = i$, and the sorted ordering numbering scheme is the principal way of identifying the triangles (*i.e.* $\triangle_{s_i} = \triangle_i$).

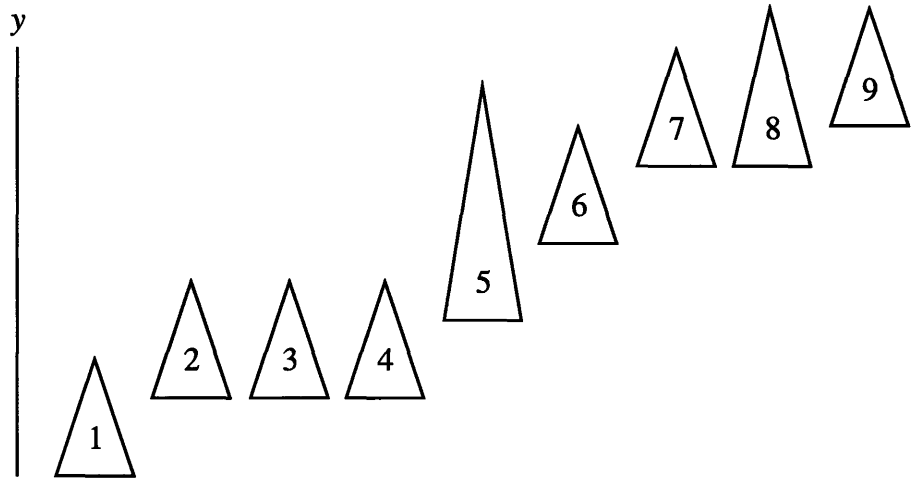

Figure 2-8: Ordering triangles in Volumizer—Example #1.

Table 2.1: Ordering triangles in Volumizer—Example #1. Sorted, y ascending, and y descending order numbering of triangles.

s_i	1	2	3	4	5	6	7	8	9
a_{y_i}	1	2	2	2	5	5	7	8	8
d_{y_i}	1	4	4	4	5	6	7	9	9

The second number associated with each triangle is the y ascending order number, a_{y_i}. In this numbering scheme, a_{y_i} corresponds to the highest s_i such that $\min_y(\triangle_{a_{y_i}}) > \min_y(\triangle_j)$ for any $j < a_{y_i}$. This numbering scheme is important because if a point V satisfies the inequality $v_y > \min_y(\triangle_{a_{y_i}})$, then there is no need to test if a line going through V intersects any triangles j with $s_j < a_{y_i}$. In the building analogy, if I know room 1997 is at least as high as the 19th floor, I need not search any room below the 19th floor.

The third number associated with each triangle is the y descending order number, d_{y_i}. In this numbering scheme, d_{y_i} corresponds to the lowest s_i such that $\max_y(\triangle_{d_{y_i}}) < \max_y(\triangle_j)$ for any $j > d_{y_i}$. This numbering scheme complements the ascending order numbering scheme, and it is important because if a point V satisfies the inequality $v_y < \max_y(\triangle_{d_{y_i}})$, then there is no need to test if a line going through V intersects any triangles j with $s_j > d_{y_i}$. Continuing the building analogy, if I know room 1997 is at least as low as the 19th floor I need not search any room above the 19th floor. Table 2.1 gives s_i, a_{y_i}, and d_{y_i} for the triangles shown in Figure 2-8.

The triangles that comprise the anatomic surface representations in HYPER/Plan can easily accommodate a further level of optimization. With few exceptions, the vertices of each (non-degenerate) triangle in these geoms connect parts of contours from two adjacent slices from the patient image. Thus when the y ascending and y descending order numberings are determined, many triangles will share the same $\min_y(\triangle)$ and $\max_y(\triangle)$. In this case, these triangles with the same extents in the y-axis can be further numbered in z ascending and z descending order, and a_{z_i} and d_{z_i} are analogous to a_{y_i} and d_{y_i}, respectively, and determined in analogous fashion. In other words, when triangles i in the range $n_1 \leq n_2$ share the same $a_{y_i} = n_1$ and $d_{y_i} = n_2$, then (and only then) a_{z_i} and d_{z_i} are determined, with $n_1 \leq a_{z_i} \leq d_{z_i} \leq n_2$. Each triangle has an associated rectangle in the yz-plane defined by the y and z extents of the triangle, and (for the most part) only those triangles whose y and z extents contain the point (v_y, v_z) need to be checked for intersection with the line x' through the point V. An example of all five numbering schemes is given in Figure 2-9 and Table 2.2. The question of how to exploit these numbering schemes for computational speed will be explicitly examined in Section 2.4.3.3.

2.4.3.2 Grid Generation

The grid, in the present context of grid generation, refers to the 3-D coordinates of the patient anatomic mesh. As Volumizer is currently implemented, grid generation is performed fully automatically and very simply. The bounding box around the volume of the patient image is determined by taking the minimum and maximum extents in the x, y, and z directions. A grid **resolution**, or **spacing**, is defined by the user, and has a default value of 1 cm. The grid is then generated as a cubic lattice with a lattice spacing equal to the grid resolution, and the grid volume coincides with the patient image volume.

2.4.3.3 Anatomic Mesh Generation

Once the coordinates of the lattice points of the grid have been determined, it is necessary to determine for each grid point which (if any) anatomic structure it lies within. Optimization in performing this task takes place in two ways, one taking advantage of the pre-processing discussed in Section 2.4.3.1, and one taking advantage of the grid coordinates.

The first level of optimization involves the various order numberings of the triangles that make up the geoms. The lowest (s_{low}) and highest (s_{high}) sorted order numberings of triangles that may intersect the line x' going through the point V are determined. Then only the triangles with $s_{\text{low}} \ll s_{\text{high}}$ need be checked for intersection. s_{low} and s_{high} are determined by a binary search algorithm [88], which operates in $\mathcal{O}(\log n)$ time. It is these order numberings that optimize Volumizer for the anatomic geoms generated by Mosaic; the order numberings allow Volumizer to take advantage of the geom geometric characteristics, *i.e.* that the geom polyhedra comprise faces that are only triangular (and not some other kind of polygon), and that the triangles are arranged in parallel layers (which correspond to the planes of the CT slices).

The second level of optimization in anatomic mesh generation requires the coordinates of the grid to be organized in a specific way. When multiple points lie on the same line x' parallel to the x-axis, there is no need to determine, for every point, the intersections between x' and the triangles that make up the geoms. The intersections need be determined just once, and then they can be used to evaluate which points on the line x' reside within which geoms. As the grid generation routine is currently implemented (see Section 2.4.3.2), multiple grid points on the same x' is the rule, and allows for substantial savings in computational time. This optimization method provides another reason to identify intersections between *lines* and triangles, instead of intersections between *rays* and triangles. Were intersections between rays and triangles determined instead, this optimization could not be used.

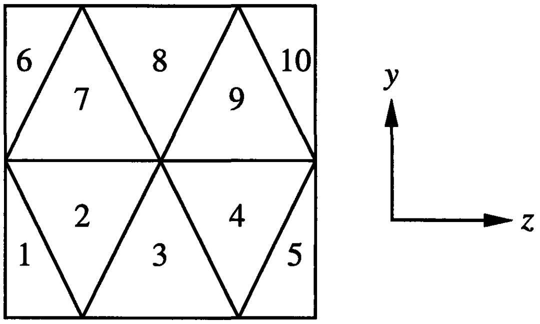

Figure 2-9: Ordering triangles in Volumizer—Example #2.

Table 2.2: Ordering triangles in Volumizer—Example #2. Sorted, y ascending, y descending, z ascending, and z descending order numbering of triangles.

s_i	1	2	3	4	5	6	7	8	9	10
a_{y_i}	1	1	1	1	1	6	6	6	6	6
d_{y_i}	5	5	5	5	5	10	10	10	10	10
a_{z_i}	1	1	3	4	4	6	7	8	9	9
d_{z_i}	1	2	3	4	5	7	7	8	9	10

Chapter 3

Ultrasound Power Deposition: Background

Power tends to corrupt, and absolute power corrupts absolutely.
— Lord John Acton, in a letter to Mandell Creighton, 1887

In hyperthermia, thermal energy is deposited in tissue to elevate the tissue temperature. The volumetric power deposition, or specific absorption rate **SAR**, refers to the rate of this thermal energy deposition. In the context of this thesis, SAR is administered by ultrasound radiation (although there are other ways SAR can be administered—most notably by microwave radiation). There are many ways that SAR can be administered clinically, experimentally, and theoretically, but in this thesis we will largely restrict ourselves to SAR by ultrasound radiation. This chapter provides a background in acoustic physics and discusses methods other investigators have used to compute the Rayleigh-Sommerfeld diffraction integral, which is used to calculate the acoustic pressure field from a planar acoustic source. The next chapter, Chapter 4, discusses computational advances in ultrasound modeling made in the course of this thesis.

3.1 Acoustic Physics Primer

The reader will be served well by a brief discussion of basic acoustic physics. This will elucidate where the important Rayleigh-Sommerfeld diffraction integral (Equation 3.23) comes from, and what some of its limitations are. (For greater rigor or more explanation, please refer to Fahy [28], Hynynen [47], Morse and Ingard [71], or Wells [101].)

Notation can be confusing, in large part because the same letter is used to indicate different aspects of the same quantity, and frequently the differences are subtle. Nevertheless, this time-honored tradition will be perpetuated here. To elucidate the notation, and to minimize the reader's frustration in dealing with the notation, an example will be presented. Vectors in general will be indicated with an arrow, as in $\vec{u}$, the instantaneous velocity of a medium at a specific location in space. In the 1-D case, velocity is simply the scalar u. The **magnitude** of u is given by $|u|$, and of $\vec{u}$ by $\|\vec{u}\| = \sqrt{\vec{u}\cdot\vec{u}}$. For the case of quantities that vary sinusoidally in time, the **amplitude** u_a of the quantity u is indicated by a subscripted a, such as $u = u_\mathrm{a}\cos\omega t = u_\mathrm{a}e^{j\omega t}$.[1] Finally, the time-averaged value of a quantity is signified by angle brackets ($\langle\ \rangle$), as in the time-averaged velocity squared $\langle u^2\rangle = u_\mathrm{a}^2/2$ for sinusoidally varying u.

For non-attenuating plane wave motion in 1-D (along the x-axis), the conservation of mass (continuity) equation can be expressed as:

$$\kappa\frac{\partial p}{\partial t} = -\frac{\partial u}{\partial x} \tag{3.1}$$

where p is the **acoustic pressure** (the deviation of the pressure from the baseline pressure P), u is the local **particle velocity** of the medium, and $\kappa \equiv \rho^{-1}(\partial\rho/\partial P)_s$, the isentropic compressibility, more commonly known as the **adiabatic compressibility**.[2] The conservation of momentum is given by control volume analysis:

$$\frac{\partial p}{\partial x} = -\rho\frac{\partial u}{\partial t} \tag{3.2}$$

In fact, these continuity equations have already been simplified by eliminating higher-order terms, based on the assumptions that particle velocity and pressure are both "small."[3] (These

---

[1] Strictly speaking, $u = \mathrm{Re}(u_\mathrm{a}e^{j\omega t})$, *i.e.* just the real part of the complex quantity $u_\mathrm{a}e^{j\omega t}$. By convention, however, in this representation of u, $u_\mathrm{a}e^{j\omega t}$ is left as a complex quantity. Note that $|u| = |u_\mathrm{a}e^{j\omega t}| = u_\mathrm{a}|\cos\omega t|$, not $|u| = u_\mathrm{a}$; in other words, there is a distinction between the magnitude of u, $|u|$, and the amplitude of u, u_a. In some conventions u_a can be a complex quantity, which allows the expression $u_\mathrm{a}e^{j\omega t}$ to convey phase information distinct from time; in this thesis, however, amplitude will denote the magnitude of this complex quantity, *i.e.* no phase information will be conveyed by the amplitude. Another variation in convention allows the amplitude to be a vector, $\vec{u}_\mathrm{a}$, describing oblique vibration in 2-D or 3-D. For clarity and simplicity in this thesis, again, amplitude will be restricted to a scalar quantity.

[2] The subscript s indicates constant entropy. Equation 3.1 assumes the sound waves compress and rarefy isentropically, an assumption taken by Hueter and Bolt [43, page 31]. Morse and Ingard indicate that in cases of high frequency (about 1 GHz in gases, *e.g.*) or very high thermal conductivity, however, compression and rarefaction may be considered isothermal, and the **isothermal compressibility** $\kappa_T \equiv \rho^{-1}(\partial\rho/\partial P)_T$ (the subscript T indicates constant temperature) should be used instead of κ [71, page 230].

[3] To give an example of how Equations 3.1 and 3.2 are affected when particle velocity and pressure are not

higher-order terms arise because ρ does not vary strictly linearly with p, and κ is not strictly constant with varying p.) Equations 3.1 and 3.2 can be combined to eliminate u and produce the well-known **wave equation**:

$$\frac{\partial^2 p}{\partial t^2} = c^2 \frac{\partial^2 p}{\partial x^2} \tag{3.3}$$

where $c = 1/\sqrt{\kappa \rho}$ is the wave speed, also known as the speed of sound.

In 3-D, the continuity and conservation of momentum equations take on the forms:

$$\kappa \frac{\partial p}{\partial t} = -\nabla \cdot \vec{u} \tag{3.4}$$

and:

$$\nabla p = -\rho \frac{\partial \vec{u}}{\partial t} \tag{3.5}$$

Particle velocity and pressure can be related to each other through a **velocity potential** Ψ, which is defined implicitly by:

$$\vec{u} = -\nabla \Psi \tag{3.6}$$

Combining Equations 3.5 and 3.6 produces the relationship between pressure and velocity potential:

$$p = \rho \frac{\partial \Psi}{\partial t} \tag{3.7}$$

Substituting expressions for particle velocity and pressure in terms of velocity potential into Equation 3.4 results in a wave equation for velocity potential:

$$\frac{\partial^2 \Psi}{\partial t^2} = c^2 \nabla^2 \Psi \tag{3.8}$$

The pressure wave equation can be obtained very simply by differentiating Eq.3.8 with respect to time, and multiplying by density:

$$\frac{\partial^2 p}{\partial t^2} = c^2 \nabla^2 p \tag{3.9}$$

---

small, Morse and Ingard provided the more precise versions [71, pages 243 and 247]:

$$\kappa \frac{\partial p}{\partial t} = -(1 + \kappa p)\frac{\partial u}{\partial x} - \rho u \frac{\partial p}{\partial x} \quad \text{and} \quad \frac{\partial p}{\partial x} = -\rho \frac{\partial u}{\partial t} - \rho u \frac{\partial u}{\partial x}$$

Clearly these equations are rather complex and unwieldy, and as such they are eschewed in favor of their first-order counterparts whenever possible. (Furthermore, even the more precise equations have limitations, *e.g.* they are not valid beyond second order.)

The pressure and particle velocity were already seen to be related to each other through the velocity potential. In addition, their ratio defines the **acoustic impedance** Z:

$$Z_n = \frac{p}{u_n} \tag{3.10}$$

where $u_n = \vec{u} \cdot \hat{n}$, the velocity component normal to the plane of interest, $\hat{n}$, is the unit vector in the same direction, and Z_n is the acoustic impedance in the $\hat{n}$ direction. The acoustic impedance is indirectly a function of wave frequency, since frequency affects both pressure and normal particle velocity, although for plane waves acoustic impedance is independent of frequency. The acoustic impedance is seen to be a property not only of the medium, but also of the pattern of wave propagation. In its most rigorous sense acoustic impedance is used to relate the pressure to the velocity component normal to a surface, in which case the concept of acoustic impedance is meaningful only at surfaces.

The wave **energy density** E is the volumetric energy associated with a wave as it propagates, and comprises terms for kinetic energy and potential energy associated with the compression and rarefaction of the medium:

$$E = \frac{\rho \|\vec{u}\|^2}{2} + \frac{\kappa p^2}{2} \tag{3.11}$$

Conservation of energy for the case of no energy absorption or creation gives the **acoustic intensity** $\vec{I}$, which measures power flux associated with wave transmission:

$$-\nabla \cdot \vec{I} = \frac{\partial E}{\partial t} \tag{3.12}$$

Alternatively, the acoustic intensity can be seen to be the power flux associated with pressure-volume work:

$$\vec{I} = p\vec{u} \tag{3.13}$$

Equation 3.13 is often preferable to Equation 3.12 because it gives an explicit expression for the acoustic intensity.

For the intensity in the normal direction $\hat{n}$, I_n, in the case where pressure and normal particle velocity vary sinusoidally with the same frequency (although not necessarily in phase), the time-averaged normal intensity is:[4]

$$\langle I_n \rangle = \langle p u_n \rangle = \frac{1}{2} p_{\mathrm{a}}^2 \operatorname{Re}(Z_n^{-1}) = \frac{1}{2} u_{n_{\mathrm{a}}}^2 \operatorname{Re}(Z_n) \tag{3.14}$$

---

[4] Contrary to what was suggested by Fahy [28, page 167], $[\operatorname{Re}(Z)]^{-1} \neq \operatorname{Re}(Z^{-1})$ (unless Z is real).

A continuous wave acoustic source vibrating with velocity component normal to the suface $u_n\{\vec{v}_\mathrm{b}\} = u_{n_\mathrm{a}} e^{j(\omega t+\varphi_{u_n}\{\vec{v}_\mathrm{b}\})}$, where $\vec{v}_\mathrm{b}$ is an arbitrary point on the source surface and φ is the phase, produces surface acoustic pressure $p\{\vec{v}_\mathrm{b}\} = p_\mathrm{a} e^{j(\omega t+\varphi_p\{\vec{v}_\mathrm{b}\})}$. The mean power $\langle \dot{q} \rangle$ emitted from the source with surface A is given using Equation 3.14:

$$\langle \dot{q} \rangle = \int_A \langle I_n \rangle \, dA = \int_A \langle p u_n \rangle \, dA = \int_A p_\mathrm{a} u_{n_\mathrm{a}} \frac{\cos(\varphi_p - \varphi_{u_n})}{2} \, dA \tag{3.15}$$

As indicated in Equation 3.13, the acoustic intensity is the product of a pressure and a velocity. An alternative way of viewing this product is to equate the acoustic intensity with the product of the "static" pressure of a propagating acoustic wave and the speed at which the wave propagates:

$$\vec{I} = \vec{\Pi} c \tag{3.16}$$

where $\vec{\Pi}$ is the **radiation pressure**. Note that radiation pressure is a vector quantity, unlike the acoustic pressure.

3.1.1 Plane Wave Solution

Plane waves correspond to the solution of the 1-D wave equation given in Equation 3.3. For a sinusoidal wave propagating in the $+x$ direction in a non-attenuating medium, with $\Psi\{0,t\} = \Psi_\mathrm{a} e^{j\omega t}$, the solution to the wave equation is:

$$\begin{aligned} \Psi\{x,t\} &= \Psi_\mathrm{a} e^{j(\omega t - kx)} \\ p\{x,t\} &= j\omega\rho\Psi\{x,t\} \quad , \quad p_\mathrm{a} = \omega\rho\Psi_\mathrm{a} \\ u_x\{x,t\} &= jk\Psi\{x,t\} \quad , \quad u_\mathrm{a} = k\Psi_\mathrm{a} \end{aligned} \tag{3.17}$$

u_x indicates the particle velocity consists only of the component in the x direction. In this case, the acoustic impedance, in general a complex quantity, is everywhere the real product $Z_x = p/u_x = \rho c$.

Substitution of Equation 3.17 into Equation 3.11 gives the energy density, which on the average is:

$$\langle E \rangle = \frac{1}{2}\left(\frac{\rho u_\mathrm{a}^2}{2} + \frac{\kappa p_\mathrm{a}^2}{2}\right) = \frac{\rho u_\mathrm{a}^2}{2} = \frac{p_\mathrm{a}^2}{2\rho c^2} \tag{3.18}$$

From Equation 3.13, the acoustic intensity (which is a scalar for the 1-D case, and is associated with the x direction), on the average, is:

$$\langle I_x \rangle = \frac{u_{\mathrm{a}} p_{\mathrm{a}}}{2} = \frac{\rho c u_{\mathrm{a}}^2}{2} = \frac{p_{\mathrm{a}}^2}{2\rho c} \tag{3.19}$$

For this wave motion, then, $\langle I_x \rangle = \langle E \rangle c$; and, in fact, $I_x = Ec$.

There are clear similarities between Equations 3.14 and 3.19, and the similarities form the basis of some simplifications that are usually assumed in acoustic physics exegeses (often without justification). Specifically, the quantity ρc in Equation 3.19 takes the place of the acoustic impedance in Equation 3.14, which leads to the casual observations that $Z = \rho c$, and that the acoustic impedance is a scalar, real (*i.e.* not complex) quantity. These observations are true for plane wave vibration, but they are *not* true in general. Nevertheless, they are often applied to acoustic physics problems.

3.1.2 Spherical Wave Solution

Spherically symmetric waves radiating outward from a spherical source of radius R, with the velocity potential at the source surface $\Psi\{R,t\} = \Psi_{\mathrm{a}}\{R\}e^{j(\omega t - kR)}$, have the wave function solution:

$$\begin{aligned}
\Psi\{r,t\} &= \frac{R}{r}\Psi_{\mathrm{a}}\{R\}e^{j(\omega t-kr)} \quad , & \Psi_{\mathrm{a}}\{r\} &= \frac{R}{r}\Psi_{\mathrm{a}}\{R\} \\
p\{r,t\} &= j\omega\rho\Psi\{r,t\} \quad , & p_{\mathrm{a}}\{r\} &= \omega\rho\Psi_{\mathrm{a}}\{r\} \\
u_r\{r,t\} &= jk(1-j/kr)\Psi\{r,t\} \quad , & u_{\mathrm{a}}\{r\} &= \sqrt{1+(kr)^{-2}}\,k\Psi_{\mathrm{a}}\{r\}
\end{aligned} \tag{3.20}$$

u_r is the velocity in the radial direction, the only non-zero velocity component for this geometry. The pressure amplitude $p_{\mathrm{a}}\{r\} = p_{\mathrm{a}}\{R\}R/r$ varies with radial position, as does the radial particle velocity amplitude $u_{\mathrm{a}}\{r\} = u_{\mathrm{a}}\{R\}(R/r)[1+(kr)^{-2}]/[1+(kR)^{-2}]$. Furthermore, $u_{\mathrm{a}} = p_{\mathrm{a}}\sqrt{1+(kr)^{-2}}/\rho c$. If $R \ll \lambda$ the spherical source is called a **simple source**, and in the limit as $R \to 0$ the source becomes a **point source**.

The solution in Equation 3.20 indicates pressure and particle velocity are not entirely in phase. In the near field of the spherical source, when $r < \lambda$, they are significantly (up to 90° for a point source) out of phase, but in the far field, when $r \gg \lambda$, they are essentially in phase. The acoustic impedance (in the radial direction) is $Z_r = \rho c/(1 - j/kr)$.

The average energy density is:

$$\langle E\rangle = \frac{p_{\mathrm{a}}^2}{2\rho c^2}\left[1 + (kr)^{-2}/2\right] \tag{3.21}$$

The average acoustic intensity (which is again 1-D but associated now with the radial direction) is:

$$\langle I_r\rangle = \frac{p_{\mathrm{a}}^2}{2\rho c} \tag{3.22}$$

So in the spherical wave case, $I_r \neq Ec$, although the relationship approaches equality as $r \rightarrow \infty$.

3.1.3 Rayleigh-Sommerfeld Diffraction Integral

The solution of the wave equation for a planar source embedded in an infinitely rigid baffle is an important case because many real ultrasound transducers are modeled in this way. The source can be any shape, and it can comprise unconnected regions in the plane, but it must lie in the plane of the baffle. Typically the motion of the source surface in the direction normal to the surface, u_n, is constrained by $u_n = u_{n_{\mathrm{a}}} e^{j(\omega t-\varphi)}$, where $u_{n_{\mathrm{a}}}$ and phase φ need not be uniform over the source. The rest of the plane is constrained by no vibration, *i.e.* $u_n = 0$; and no pressure gradient normal to the boundary, *i.e.* $\partial p\{\vec{v}_{\mathrm{b}}\}/\partial n = 0$. ($\vec{v}_{\mathrm{b}}$ refers to an arbitrary point on the boundary, *i.e.* the plane, and n refers to the direction normal to the plane, $\hat{n}$.) These two constraints—no velocity or pressure gradient normal to the boundary—are actually equivalent conditions, as can be seen from Equation 3.2 (page 60) or Equation 3.5 (page 61). This is because a pressure gradient induces an acceleration in the direction opposite the gradient; but on the surface of the rigid plane baffle, normal velocity is zero, and normal acceleration is zero, so normal pressure gradient must be zero, too. (*N.B.*: velocity and pressure gradient components *parallel* to the plane baffle need not be zero.)

The solution for the velocity potential for this embedded planar source, called the **Rayleigh-Sommerfeld diffraction integral** or simply the diffraction integral, is based on the spherical source solution. An explicit derivation is given in Section B.2, and the result, *i.e.* the diffraction integral itself, is repeated here:

$$\Psi\{\vec{v},t\} = \int_A \frac{u_n}{2\pi d} e^{-jkd}\, dA \tag{3.23}$$

where $\vec{v}$ is the field point of interest, A is the source surface, dA is a differential part of A, and d is the distance between $\vec{v}$ and dA. On a pedagogical note, the form of Equation 3.23, *i.e.* the integral part of the right-hand side of the equation, can be seen to come relatively directly from Huygen's principle.

For the case in which angular velocity ω is constant over the radiating surface, and using the relation $p = \rho\partial\Psi/\partial t$ (see Equation 3.7), the diffraction integral can be converted into:

$$p\{\vec{v}, t\} = j\omega\rho \int_A \frac{u_n}{2\pi d} e^{-jkd}\, dA = \frac{j\rho c}{\lambda} \int_A \frac{u_n}{d} e^{-jkd}\, dA \tag{3.24}$$

This equation is valid even if normal particle velocity amplitude and phase are not spatially constant over the radiating surface.

3.1.4 Planar Reflection

Specular reflections of sound off boundaries can often be modeled by an rigid, infinite planar boundary bordering a semi-infinite medium. The sound field that results from a spherical source placed in a semi-infinite medium bounded by an infinitely rigid planar boundary is discussed now (although the method can be extended to accommodate an arbitrary source). The boundary conditions are again no vibration ($u_n = 0$) and no normal pressure gradient ($\partial p\{\vec{v}_\text{b}\}/\partial n = 0$). The solution can be achieved using the method of images, in which two identical sources are placed symmetrically on opposite sides of the boundary. The symmetry of this arrangement, shown in Figure 3-1A, produces the desired boundary conditions using a real source, located at P, and an identical virtual or imaginary source, located at P'. R is the location of an arbitrary point in the sound field. So $p\{\vec{r}\}$, the acoustic pressure at R resulting from direct sound transmission from P, and also reflected sound transmission, which looks like direct transmission from P', is given by:

$$p\{\vec{r}, t\} = p_\text{sph}\{\overline{PR}, t\} + p_\text{sph}\{\overline{P'R}, t\} \tag{3.25}$$

where p_sph is the pressure from a spherical source, given in Equation 3.20. In the limit as the real source moves closer to the boundary (Figure 3-1B), the two sources coalesce into a single source on the boundary with twice the power of the original real source:

$$\lim_{P \to P'} p\{\vec{r}, t\} = p_\text{sph}\{\overline{PR}, t\} + p_\text{sph}\{\overline{P'R}, t\} = 2p_\text{sph}\{\overline{PR}, t\} \tag{3.26}$$

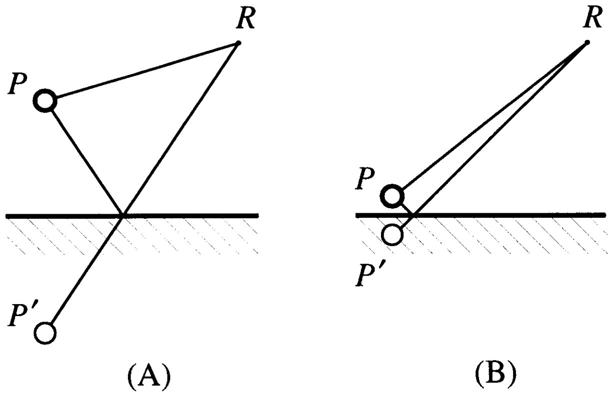

Figure 3-1: Determination of acoustic pressure field from a spherical source in a semi-infinite medium bounded by an infinitely rigid plane.

3.1.5 Planar Reflection and Refraction

The physics of ultrasound reflection and refraction is analogous to that of light. When the length scales involved are large compared to the wavelength, the physics is governed by the familiar **Snell's law**, illustrated in Figure 3-2. An incident wave traveling through medium 1 encounters a locally planar interface at an incident angle θ_i from the normal. Part of the wave is reflected from the interface at reflection angle $\theta_\mathrm{r} = \theta_\mathrm{i}$, and the rest is transmitted through medium 2 at an transmission angle θ_t. Snell's law states:

$$\frac{\sin \theta_\mathrm{i}}{\sin \theta_\mathrm{t}} = \frac{c_1}{c_2} \tag{3.27}$$

where c_1 and c_2 are the wave speeds in medium 1 and 2, respectively. If $c_2 < c_1$, there is a critical value of the incident angle θ_i, θ_i^*, such that when $\theta_\mathrm{i} > \theta_\mathrm{i}^*$ all of the incident wave is reflected, and none is transmitted; this phenomenon is called **total internal reflection**. The critical angle θ_i^* is given by Equation 3.27 when transmission angle $\theta_\mathrm{t} = \pi/2$:

$$\sin \theta_\mathrm{i}^* = \frac{c_1}{c_2} \tag{3.28}$$

In the specific case of ultrasound, the local pressure and particle velocity must be continuous at the interface. Using these two constraints, it is possible to determine how the incident pressure wave is divided into the transmitted and reflected pressure waves. A derivation is given in Wells [101, pages 16–17], but the results will be summarized here. Let p_i, p_t, and p_r be the acoustic pressures at the interface of the incident, transmitted, and reflected waves, respectively.

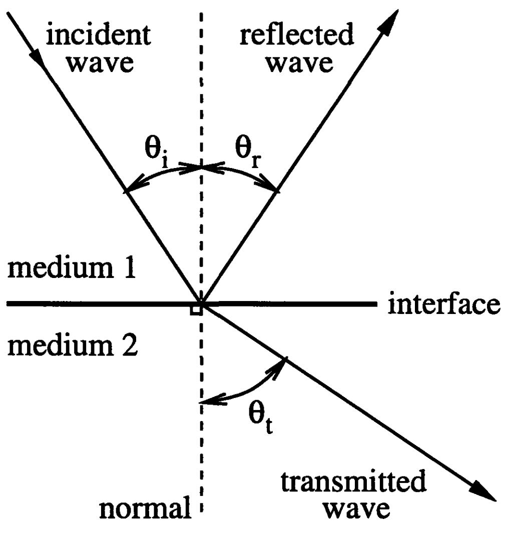

Figure 3-2: Snell's law and wave transmission and reflection (adapted from Wells [101, page 16]).

The ratio p_t/p_i is called the **pressure transmittivity** of the surface, and the ratio p_r/p_i is the **pressure reflectivity**, and they are given by:

$$\frac{p_t}{p_i} = \frac{2Z_2 \cos\theta_i}{Z_2 \cos\theta_i + Z_1 \cos\theta_t} \qquad \text{(or 0 if } \theta_i \geq \theta_i^*\text{)} \tag{3.29}$$

and:

$$\frac{p_r}{p_i} = \frac{Z_2 \cos\theta_i - Z_1 \cos\theta_t}{Z_2 \cos\theta_i + Z_1 \cos\theta_t} \qquad \text{(or 1 if } \theta_i \geq \theta_i^*\text{)} \tag{3.30}$$

where Z_1 and Z_2 are the acoustic impedances of medium 1 and 2, respectively. Since the incident, transmitted, and reflected waves are all plane waves in this example, $Z_1 = \rho_1 c_1$ and $Z_2 = \rho_2 c_2$.

Similarly, let I_i, I_t, and I_r be the acoustic intensities at the interface of the incident, transmitted, and reflected waves, respectively. Using Equation 3.19 to determine the intensity of a plane wave, the **intensity transmittivity** and **intensity reflectivity** are given by:

$$\frac{I_t}{I_i} = \left(\frac{4Z_2 Z_1 \cos\theta_i \cos\theta_t}{Z_2 \cos\theta_i + Z_1 \cos\theta_t}\right)^2 \qquad \text{(or 0 if } \theta_i \geq \theta_i^*\text{)} \tag{3.31}$$

and:

$$\frac{I_r}{I_i} = \left(\frac{Z_2 \cos\theta_i - Z_1 \cos\theta_t}{Z_2 \cos\theta_i + Z_1 \cos\theta_t}\right)^2 \qquad \text{(or 1 if } \theta_i \geq \theta_i^*\text{)} \tag{3.32}$$

3.1.6 Acoustic Absorption

Thus far discussion of acoustic physics has assumed lossless wave propagation, *i.e.* there is no **attenuation** of energy, either through **absorption** or **scattering**, in the wave as it propagates through the medium. The conversion of wave mechanical energy into thermal energy via absorption is (on a very simple level) the mechanism of heating in ultrasound hyperthermia, and without absorption there is no ultrasound hyperthermia. Thus ultrasound hyperthermia requires the tissue in the target volume not be lossless.

The so-called **classical mechanism** of absorption credits viscous losses as the source of absorption. This mode of absorption is important in fluids, but in biological tissues **relaxation** processes dominate. Relaxation processes occur in systems with coupled compartments, meaning energy can by moved from one compartment to another. (To give an example of two compartments in a biological tissue, consider water inside a cell, and protein dissolved in the water. Protein transfer between these two compartments has been suggested as a molecular mechanism of ultrasound absorption in tissues [101, pages 132–134].) An ultrasound wave can impart some of its energy into a compartment (*e.g.* by transiently increasing temperature during the compressional phase of the wave), and before the wave recovers that energy (*i.e.* during the rarefactional phase) some of it has already moved to a different compartment from which the wave cannot extract all of the energy it gave. The discrepancy in imparted and recovered energy is the absorbed energy. Theoretical arguments suggest that biological tissues typically have multiple different relaxation processes which together account for the majority of the ultrasound absorption.

Ultrasound attenuation refers to overall loss of energy (or equivalently loss of acoustic pressure amplitude) of an ultrasound wave as it travels through a medium. Absorption accounts for much of the attenuation, but scattering is another mechanism of attenuation.[5] Scattering is divided into three qualitatively different behaviors: **specular reflection**, when the characteristic length L of the obstacle is much greater than the ultrasound wavelength λ (*i.e.* $L \gg \lambda$); **diffuse reflection**, when $L \ll \lambda$; and a combination of the two in the transitional region, where $L \sim \lambda$. The wave field that results from attenuation in a purely absorbing medium (*i.e.* no scattering) is

---

[5] As remarked by Goss *et al.* [35, page 181], "Attenuation ... [is] often measured, with ultrasonic absorption in biological tissues receiving little attention. Thus the distinction between attenuation and absorption is not often appreciated."

termed the **primary** field [8]. The field that results when scattering and absorption take place is typically called the **diffracted** field, and the difference between the diffracted and primary fields is called the **scattered** field [90].[6] In a sound field in which scattering takes place, wave mechanical energy continuously scatters from some areas to others, and it is possible to have a wave geometry in which scattering causes an *increase* in acoustic pressure at some points in the scattered field, compared to the primary field. In such cases, attenuation (by scattering) is said to take place, even though the scattering increases the acoustic pressure.

In general in biological systems, scattering contributes much less to attenuation than does absorption; so scattering is ignored, and attenuation is taken to be equal to absorption [29, 30, 46, 93, 101].[7] Important exceptions to this rule occur at tissue-air and soft tissue-bone interfaces, where the acoustic impedance of the media on opposite sides of the interface is poorly matched. In such cases, significant wave **reflection** and **refraction** occurs. Wave patterns can in practice be determined using **Huygen's principle** of summing the wave contributions of Huygen's sources. Using Huygen's principle, scattering can be seen to encompass the wave phenomena of reflection and refraction.

In media that attenuate sound through absorption, energy is taken from the wave motion and converted into thermal energy in the medium. This absorbed energy, of course, is (on a very simple level) the mechanism of heating in ultrasound hyperthermia. The volumetric power absorbed is proportional to the wave energy flux, which is the magnitude of the intensity:

$$\dot{Q} = 2\alpha \left\| \vec{I} \right\| \tag{3.33}$$

where α is the **absorption coefficient**, and 2α is simply the constant of proportionality between acoustic intensity magnitude $\left\| \vec{I} \right\|$ and volumetric power absorption $\dot{Q}$. Of greater practical interest is the time-averaged volumetric power, which is proportional to the average magnitude of the intensity:

$$\langle \dot{Q} \rangle = 2\alpha \left\langle \left\| \vec{I} \right\| \right\rangle \tag{3.34}$$

For planar waves (traveling in the $+x$ direction) which undergo attenuation due to absorption,

---

[6] Given this meaning of "diffraction," the Rayleigh-Sommerfeld diffraction integral (see Equation 3.23, page 65), which gives the velocity potential in a uniformly non-absorbing, non-scattering medium, is perhaps something of a misnomer. But this rather academic issue may best be left to science historians. . . .

[7] In cases where very tight focuses are generated and required, it may not be possible to ignore scattering.

but without scattering, energy conservation leads to the intensity solution:

$$\langle I_x\{x\}\rangle = \langle I_x\{0\}\rangle e^{-2\alpha x} \tag{3.35}$$

or, with Equation 3.19:

$$\frac{p_a\{x\}^2}{2} = \frac{p_a\{0\}^2}{2} e^{-2\alpha x} \tag{3.36}$$

Equations 3.36 and 3.17 can easily be transformed into the pressure solution:

$$\begin{aligned} p_a\{x\} &= p_a\{0\}e^{-\alpha x} \\ p\{x,t\} &= p_a\{0\}e^{j(\omega t - kx) - \alpha x} = p_a\{0\}e^{j(t - k'x)} \end{aligned} \tag{3.37}$$

where $k' = k - j\alpha$ is the **complex wave number**. Equation 3.37 illustrates that the absorption coefficient really indicates how pressure amplitude decays, and only secondarily how acoustic intensity magnitude decays (since $\left\langle \left\| \vec{I} \right\| \right\rangle \propto p_a^2$). Another way of looking at this is that α^{-1} is seen to be the length constant[8] for attenuation of pressure, whereas $(2\alpha)^{-1}$ is the length constant for attenuation of intensity.

When attenuation is achieved through scattering as well as absorption, a **scattering coefficient** σ and **attenuation coefficient** μ are often used in Equation 3.37 in analogous fashion to α. Whereas absorption coefficient α indicates the differential fractional decrease in pressure amplitude per differential distance of wave propagation that is due to absorption, scattering coefficient σ indicates the same for decreases due to scattering, and attenuation coefficient μ for decreases due to the combination of absorption and scattering. These quantities are related through $\mu = \alpha + \sigma$. When the effects of scattering are considered unimportant, $\mu \approx \alpha$.

For spherical waves (traveling outward in the positive r direction) undergoing absorption, energy conservation gives essentially the same intensity solution as that of the planar case:

$$\langle I_r\{r\}\rangle = \langle I_r\{R\}\rangle e^{-2\alpha(r-R)} \tag{3.38}$$

With Equations 3.22 and 3.20, this leads to the pressure solution:

$$\begin{aligned} p_a\{r\} &= p_a\{R\}e^{-\alpha(r-R)} \\ p\{r,t\} &= \frac{R}{r}p_a\{R\}e^{j(\omega t - kr) - \alpha(r-R)} = \frac{R}{r}p_a\{R\}e^{j[\omega t - kR - k'(r-R)]} \end{aligned} \tag{3.39}$$

---

[8] Here the length constant denotes the distance the planar wave must propagate to decrease the relevant parameter, pressure amplitude p_a or acoustic intensity magnitude $\left\| \vec{I} \right\|$ in this case, to $e^{-1} \approx 37\%$ of its initial value. The absorption coefficient α is measured in Np/cm, where Np indicates **nepers**, and Np/cm is "length constants per cm." $1\,\text{Np} = 20\log_{10} e \approx 8.686\,\text{dB}$.

3.1.7 Non-Linear Absorption

The Rayleigh diffraction integral assumes the amplitude of the acoustic pressure is infinitesimal. This approximation is necessary for absolute rigor because if the pressure amplitude were finite the pressure would not oscillate quite symmetrically; *i.e.* rarefaction would not exactly mirror compression. Intuitively this can be seen because rarefaction cannot produce absolute pressures smaller than that of a vacuum (*i.e.* 0 Pa), but compression can proceed without practical limit (certainly multiple times atmospheric pressure). This asymmetry results in more time spent in rarefaction than compression, and the asymmetry is increasingly apparent as the acoustic pressure amplitude increases. If this non-linear effect ceases to be negligible, then pressure p can no longer be accurately represented by $p\{t\} = p_0 e^{j\omega t}$, but is instead represented by the Fourier series $p\{t\} = \lim_{i=1}^{\infty} p_i \, e^{j\, i\omega t}$. In addition, as pressure increases the wave speed itself varies with the phase of vibration of the medium, due to non-linearities in the medium compressibility; furthermore, this varying wave speed distorts the wave front, increasing non-linear effects and introducing higher harmonics. Barring attenuation of non-linearities (from absorption, *e.g.*), the compounding distortion eventually leads to discontinuities in the wave front, a phenomenon called shock which limits energy propagation by the wave [47]. This introduction of harmonic frequencies in non-linear wave propagation can have important consequences for energy deposition because the absorption coefficient α (which is related to SAR as shown in Equation 3.34) is empirically a function of ultrasound frequency f [93, 101]:

$$\alpha(f) \approx a_1 f^{a_2} \tag{3.40}$$

where a_1 and a_2 are tissue-dependent constants, and a_2 is slightly larger than 1 (*e.g.* $a_2 = 1.2$). The theoretical possibility of using non-linear absorption in hyperthermia has been suggested [48], but will not be pursued further here. Thus acoustic pressure amplitudes will be assumed to be small enough in subsequent analyses that non-linear absorption is negligible.

3.1.8 Gaussian Source Solution

Expanding on the work of Aanonsen *et al.* [1], Du and Breazeale [25] and Breazeale and Huang [15] derived an analytic solution for the acoustic pressure field from an infinite planar Gaussian source. (Interestingly, Du and Breazeale used different approximations in their derivation than did Breazeale and Huang, but the final analytic results were the same. However, only the earlier derivation, [25], included a term related to absorption.) The source vibrates with the profile $u_n\{r,t\} = u_{n_{\max}}\,\mathrm{Gauss}(r,\sigma_{\mathrm{s}})e^{j\omega t}$, where $\mathrm{Gauss}(r,\sigma) \equiv \exp(-r^2/2\sigma^2)$, and σ_{s} is the **Gaussian source width**. ($\mathrm{Gauss_o}(\xi,\sigma) \equiv \mathrm{Gauss}(\xi,\sigma)/\sigma\sqrt{2\pi}$ is the Gaussian normalized such that the area under the Gaussian $\int_{-\infty}^{\infty} \mathrm{Gauss_o}(\xi,\sigma)\,d\xi = 1$. See Figure 3-3.) The pressure field of this Gaussian source is given by:

$$p\{r,z,t\} = p_{\max}\exp\left(\frac{-r^2}{2\sigma_{\mathrm{b}}'^{\,2}}\right)\frac{\sigma_{\mathrm{s}}}{\sigma_{\mathrm{b}}'}e^{-\alpha z}e^{j(\omega t-kz+\varphi)} \tag{3.41}$$

where $p_{\max} = \rho c u_{n_{\max}}$, $\sigma_{\mathrm{b}}'\{z\} \equiv \sigma_{\mathrm{s}}\sqrt{1+z'^{\,2}}$, $z'\{z\} \equiv z/k\sigma_{\mathrm{s}}^2$, and $\varphi = z'r^2/2\sigma_{\mathrm{b}}'^{\,2} - \tan^{-1} z'$ is the phase. z' is a dimensionless version of the the beam depth z, σ_{b} is the **Gaussian beam width**, and $\sigma_{\mathrm{b}}'\{z\}$ is the analytical solution for the Gaussian beam width. *N.B.*: The Gaussian source described above is infinite in spatial extent, although for practical purposes it only vibrates within a circle of nominal radius $2\sigma_{\mathrm{s}}$ to $4\sigma_{\mathrm{s}}$ (depending on the desired degree of accuracy) centered at the maximum vibration, with the rest of the plane effectively being a rigid baffle. Furthermore, the terms Gaussian source width (*i.e.* σ_{s}) and Gaussian beam width (*i.e.* σ_{b}) do not give the respective widths of the source and beam, at least not in the conventional sense of the term width; instead, they give the respective length constants associated with the Gaussian profiles of the source vibration and the acoustic beam from the source.

Du and Breazeale observed that Equation 3.41 described a field whose tranverse cross-section is always Gaussian, with decreasing axial pressure and increasing Gaussian length constant as depth z increases. In addition, they remarked the pressure field lacked the extrema present in near fields of uniformly vibrating (circular) sources, and it also lacked the side lobes seen in the far field of such sources.[9] Equation 3.41 was derived based on the Rayleigh-Sommerfeld diffraction integral. Although it is not a rigorously valid solution (as approximations were

---

[9] In general, the **near field** (also called the **Frésnel zone**) and the **far field** (also called the **Fraunhofer zone**) are characterized by qualitatively different interference patterns; the acoustic pressure amplitude field is usually observed to have peaks and troughs in the near field (except for simple and point sources), but to decrease inversely with distance in the far field. If an acoustic source is divided into simple spherical or point sources, the acoustic wave contributions from these sources travel along essentially parallel paths in the far field, but oblique paths in the near field. The nominal transition between near and far field is the distance a^2/λ, where a is the radius or half-width of the source, and λ is the acoustic wavelength. For a uniformly vibrating planar source, there is a main region, or **main lobe**, of constructive interference in the far field in which the entire source is essentially equidistant from any given point in the main lobe. To the sides of the main lobe—but still in the far field—are smaller **side lobes**, which are regions where constructive interference is locally maximal. **Directivity functions** characterize the locations and relative magnitudes of the lobes.

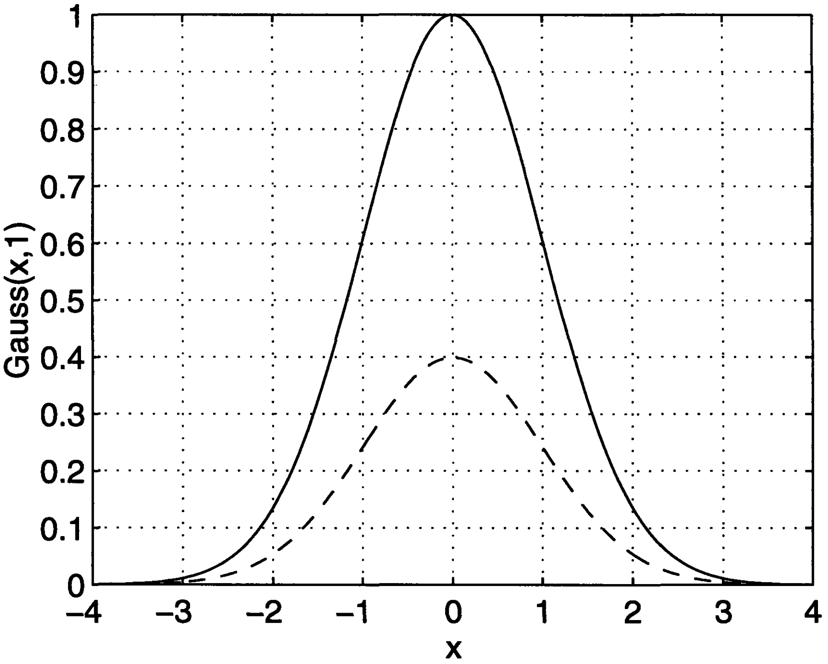

Figure 3-3: The Gaussian function, with $\sigma_s = 1$. Solid line (—) indicates $\text{Gauss}(x, 1)$; dotted line (· · ·) indicates $\text{Gauss}_o(x, 1)$.

used in the derivation), it is a closed-form solution. This fact is very valuable in acoustic beam parameterization, and it will be exploited to parameterize FSUM acoustic beams in Section 4.2.2. Figure 3-4 depicts contours of the pressure amplitude (p_a) field in the rz-plane, of Gaussian sources of Gaussian source width $\sigma_s = 0.6$, 0.8, 1.0, and 1.2 cm, with absorption coefficient $\alpha = 0\,\text{Np/cm}$ (the absorption of water) and wavenumber $k = 42\,\text{cm}^{-1}$ (the wavenumber in water of the ultrasound waves emanating from the FSUM transducers, *i.e.* 1 MHz vibration in water).

3.2 Practical Acoustic Physics

The acoustic physics thus far presented has been developed in a reasonably rigorous fashion here, with the exception of Section 3.1.6 on attenuation. The main assumptions used were that acoustic perturbations, *i.e.* p and u, were small. In general acoustic waves were taken to be purely sinusoidal, and continuous wave (as opposed to pulsed wave). In cases where attenuation was considered, absorption was taken to be equal to attenuation, *i.e.* scattering was insignificant.

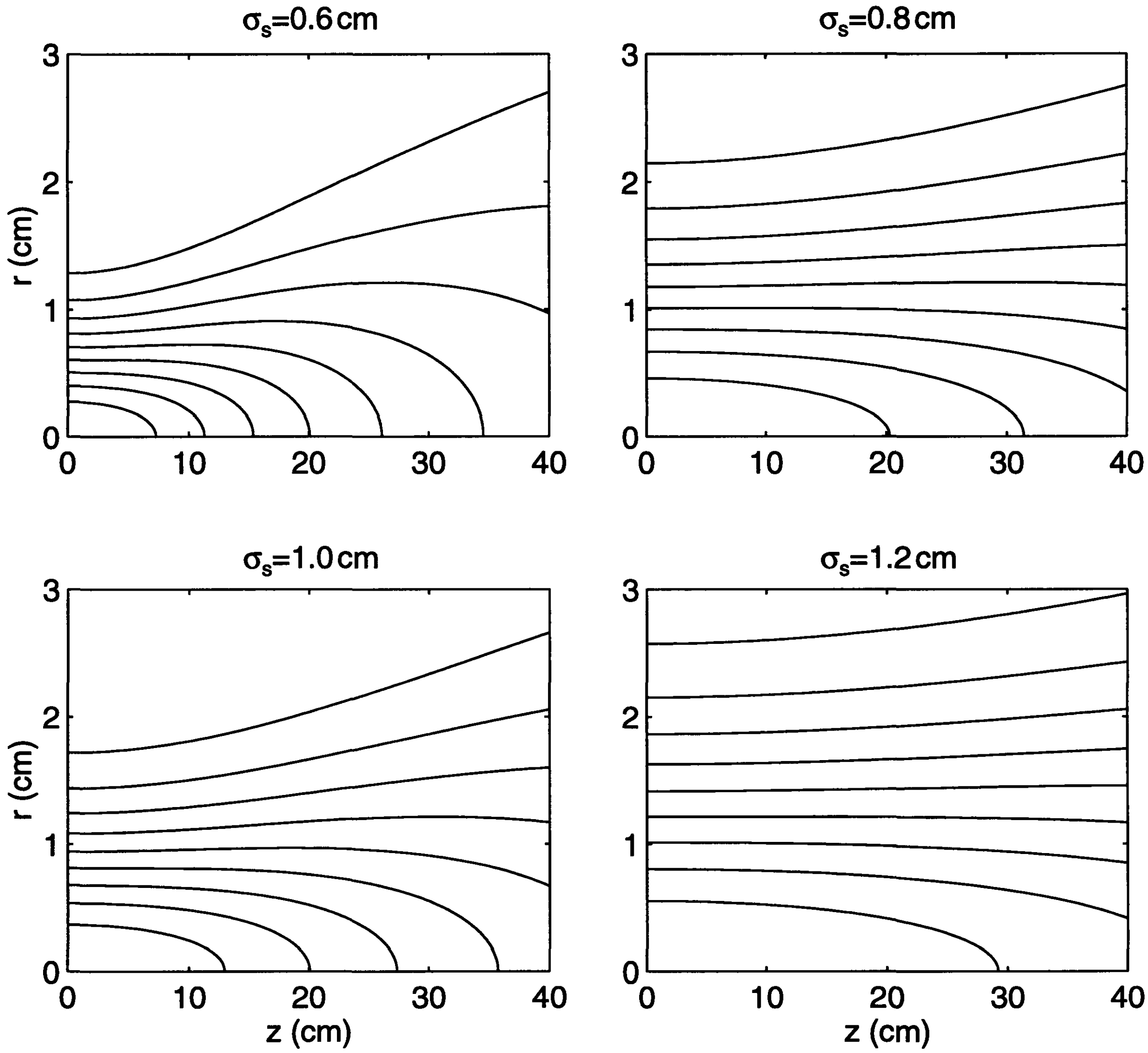

Figure 3-4: Contours in the rz-plane of the pressure amplitude (p_a) field of Gaussian sources with Gaussian source widths $\sigma_s = 0.6$, 0.8, 1.0, and 1.2 cm and wavenumber $k = 42\,\text{cm}^{-1}$. (r, z) are cylindrical coordinates, with $z = 0$ corresponding to the plane containing the source, and $r = 0$ to the center of the source. Contour lines are at multiples of 10% of $p_{\text{max}} = p_a\{0, 0\}$.

In real systems it is not necessarily advantageous to solve problems with this level of rigor, for several reasons. Real media are not ideal or perfectly homogeneous in their wave transmission, absorption, reflection, or scattering, and it would be impractical to model every detail of geometry, boundary condition, and medium property in a real system. But even if it were practical to set up the equations that model a very complex system, actually solving the equations would be a computationally monumental task. Absorption coefficients are not accurate to better than 10% or 20% [35], and may be even worse, so simple models that reduce computation to tolerable levels are preferred.

In practice, a number of further simplifying assumptions are made to model ultrasound transmission and absorption. These relate to three main areas: the technique of modeling a sound source as the superposition of simple sources; the modification of this technique to accommodate acoustic attenuation by absorption; and the evaluation of the volumetric power deposition field given the acoustic pressure field. The first two areas will be discussed in subsequent sections, and the third area will be discussed now.

The purpose of ultrasound modeling in hyperthermia is to determine the SAR field $\dot{Q}$. Equation 3.34 shows how to obtain $\langle\dot{Q}\rangle$ from $\left\langle\left\|\vec{I}\right\|\right\rangle$, and Equation 3.12 shows how to obtain $\left\langle\left\|\vec{I}\right\|\right\rangle$ from p and $\vec{u}$. In practice, however, acoustic impedance is taken to be the real quantity $Z = \rho c$ and time-averaged intensity is taken to be $\left\langle\left\|\vec{I}\right\|\right\rangle = p_{\mathrm{a}}^2/2\rho c$, as in the plane wave case. Thus once the p_{a} field is determined:

$$\langle\dot{Q}\rangle = \frac{\alpha p_{\mathrm{a}}^2}{2\rho c} \tag{3.42}$$

This equation is felt to be reasonably accurate (except very near simple sources).

3.2.1 Superposition of Simple Source Solutions

Frequently investigators model acoustic sources as a large number of simple or point sources that are closely spaced (a fraction of a wavelength apart) on the surface of the modeled source [27, 47, 80, 103]. This technique is valid to arbitrary accuracy as the simple sources approach point sources, but only if the simple source solutions themselves are perfectly accurate. For certain simple geometries, the simple source is known, such as the hemispherical source embedded in an infinite rigid plane (which is the same as the solution for the simple source in an infinite medium,

Ψ_{sph}). For most geometries, however, the simple source solution is not known; in these cases, investigators usually make the assumption that the simple source solution Ψ_{sph} is still valid. For example, Ellis and O'Brien [27] used the Ψ_{sph} solution to calculate the pressure field from a concave cylindrical slice geometry; Diederich and Hynynen [24] for convex cylindrical slices; Kossoff [56], Madsen *et al.* [64], O'Neil [80], Penttinen and Luukkala [83] for concave spherical radiators. Most investigators acknowledge the use of the Rayleigh-Sommerfeld diffraction integral in non-planar geometries is not rigorously correct, although it approaches perfect rigor as the radius of curvature of the modeled source approaches infinity (assuming the rest of the plane is an infinite rigid baffle). O'Neil suggested that when the width of the transducer is large compared to the wavelength, the diffraction integral will be close to correct for modeling curved transducers, at least in the main part of the acoustic beam.

The solutions for acoustic pressure in the cases of planar or spherical wave propagation with absorption (Equations 3.37 and 3.39, respectively) do not satisfy the wave equation derived earlier (Equation 3.9). This makes sense because the wave equation assumed all wave mechanical energy stayed in the wave without energy or momentum loss from attenuation. This author did not unearth a derivation of the wave equation with absorption, nor even a statement of the equation, but Ellis and O'Brien [27] submitted the lossy Helmholtz equation to describe acoustic pressure attenuation through absorption:

$$\nabla^2 p + {k'}^2 p = 0 \tag{3.43}$$

where the complex wavenumber $k' = k - j\alpha$. Equations 3.37 and 3.39 are seen to satisfy Equation 3.43.

The solution for a spherical source in an absorbing medium (Equation 3.39) can be substituted for the solution in a non-attenuating medium (Equation 3.20) in the derivation of the pressure solution for a planar source (Equation 3.24) to yield:

$$p\{\vec{v}, t\} = \frac{j\rho c}{\lambda} \int_A \frac{u_n}{d} e^{-jk'd}\, dA \tag{3.44}$$

This equation is exact when the complex wavenumber k' is uniform throughout medium (assuming the conditions necessary for the validity of Equation 3.24 still hold).

For the case in which absorption coefficient α varies in space, the spherical source solution is modified to be:

$$p\{r,t\} = \frac{R}{r}p_{\mathrm{a}}\{R\}e^{j\left[\omega t - kR - \int_R^r k'\{\xi\}\xi d\xi\right]} = \frac{R}{r}p_{\mathrm{a}}\{R\}e^{j(\omega t - kr) - \int_R^r \alpha\{\xi\}d\xi} \tag{3.45}$$

Strictly speaking, this solution assumes the absorption coefficient is a function only of the radial position r (or the dummy variable ξ), and not of the other two spherical coordinates ϕ and θ. Nevertheless it is used in practice to provide the spherical source solution in inhomogeneous media [47, 62]. Using Equation 3.45 to accommodate the general planar source in an infinite rigid plane, Equation 3.44 becomes:

$$p\{\vec{v},t\} = \frac{j\rho c}{\lambda}\int_A \frac{u_n}{d}e^{-jkd - \int_\ell \alpha d\ell}\, dA \tag{3.46}$$

where ℓ refers to the straight line from the differential source element dA to the field point $\vec{v}$.

3.3 Numerical Solution of Rayleigh-Sommerfeld Diffraction Integral

The Rayleigh-Sommerfeld diffraction integral yields an analytic solution only in a very few cases, such as along the central axis of a planar circular uniformly radiating source [53]. In general, however, the solution is not analytic, and calculation of the solution is notoriously computationally intensive. Historically, most efforts at numerical solution have concentrated on specific transducer geometries, or specific regions in the insonated field. In chronological order, important elucidations of the diffraction integral include O'Neil [80] (concave spherical radiator solution along the central axis and in the focal plane), Freedman [33] (rectangular radiator solution along the central axis), Zemanek [103] (circular radiator near field solution), Lockwood and Willette [61] (general planar radiator near field solution), Penttinen and Luukkala [83] (concave spherical radiator near field solution), Archer-Hall and Gee [5] (diffraction integral reduction from double to single integral for an axisymmetric source solution using, and Madsen *et al.* [64] (concave spherical radiator entire insonated field solution).

A common and general numerical technique to solve the diffraction integral is to approximate the radiating surface as a collection of small hemispherical sources [47], sometimes called monopole sources [27]. The source size must be small compared with the sound wavelength, and in the limit they approach point sources.

Other techniques have focused on converting the 2-D diffraction integral into an equivalent 1-D integral. Madsen *et al.* [64] and Swindell *et al.* [94] observed the pressure field contributions from all the points on the radiator equidistant from a field point are in phase. The contribution from an arc of equidistant points is therefore proportional to the length of the arc, so the diffraction integral is reduced to a 1-D integral over different arcs. Lockwood and Willette [61] and Penttinen and Luukkala [83] developed an impulse-response technique which, given the impulse-response of the radiator, provided the continuous wave pressure field in a 1-D integration over time.

3.3.1 Acoustic Pressure Field of Rectangular Source

Ocheltree and Frizzell [79] reported a numerical method to solve Equation 3.24 relatively quickly and accurately. Figure 3-5 illustrates the geometry of this so-called rectangular radiator method, which will be described now. The acoustic source surface A is divided into N small rectangular regions of areas A_i, heights h_i, and widths w_i, where $1 \leq i \leq N$. (In general the source surface may comprise multiple transducers; Figure 3-5 shows four transducers.) The N rectangles need not share the same dimensions, but constraints on the rectangle widths and heights must be met (see Equation 3.49). Each rectangle has its own local coordinate system (x_i, y_i, z_i), and each can be related to a global coordinate system (x, y, z). The contribution to the complex acoustic pressure at a field point $\vec{v}$ from the i^{th} subelement is given by:

$$p_i\{\vec{v}_i, t\} \approx \frac{j\rho c}{\lambda} u_{n_i} \frac{e^{-(\alpha+jk)\,d_i}}{d_i} \operatorname{sinc} \frac{k v_{x_i} w_i}{2d_i} \operatorname{sinc} \frac{k v_{y_i} h_i}{2d_i} A_i \tag{3.47}$$

where d is the distance from an arbitrary point on the subelement surface to the field point, d_i is the distance from the center of the subelement surface to the field point, $\operatorname{sinc}\theta \equiv (\sin\theta)/\theta$, and $\vec{v}_i = (v_{x_i}, v_{y_i}, v_{z_i})$ is the field point in the local coordinate system. The total pressure at $\vec{v}$ from the entire emitting surface is given by:

$$p\{\vec{v}, t\} \approx \sum_{i=1}^{N} p_i\{\vec{v}_i, t\} \tag{3.48}$$

"Small" is a relative term, when deciding how small to make the rectangular subelements A_i, and it depends on two things: The normal velocity of the source surface must be essentially constant over the entire rectangular subelement A_i, and the distance d between the field point

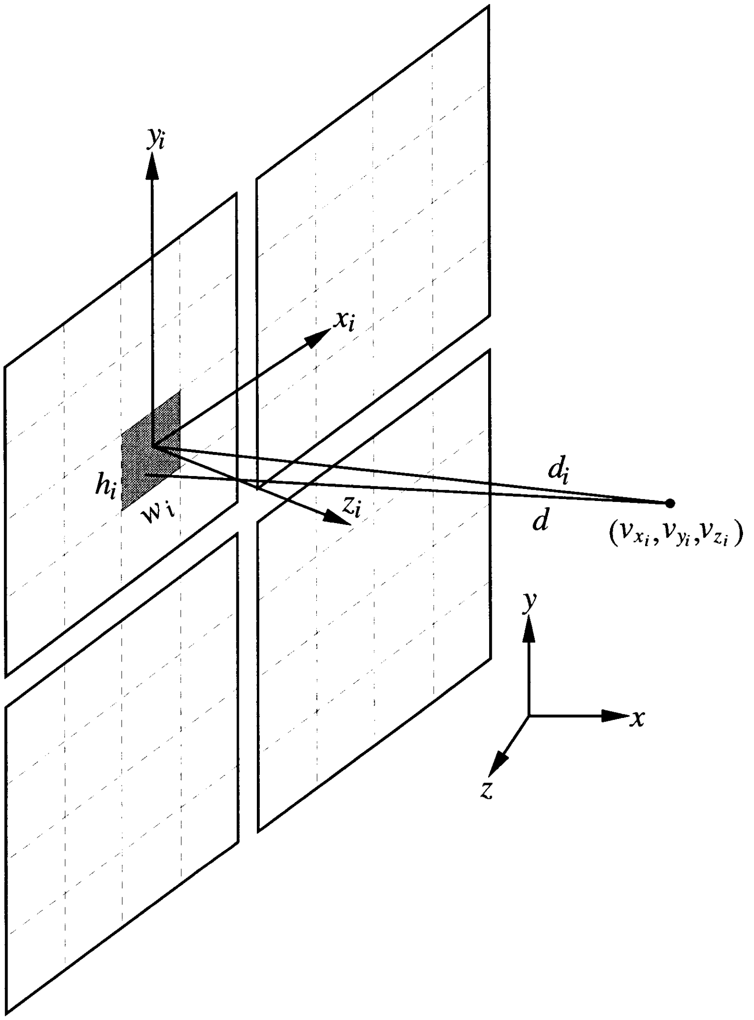

Figure 3-5: Determination of acoustic pressure field by summing contributions from rectangular subelements. Here four coplanar rectangular transducers are shown, with dotted lines indicating rectangular subelements.

$\vec{v}_i$ and a differential area dA_i on the subelement must be essentially constant as well. For calculations such as those pursued by Ocheltree and Frizzell, transducers were assumed to vibrate uniformly, so the former condition is trivially met. When the latter condition is met, the field point is in the far field of the rectangular subelement; the sinc terms in Equation 3.47 are seen to be directivity functions (see Footnote 9 on page 73). The constraint on d is met when:

$$h_i, w_i \leq \sqrt{\frac{4\lambda v_{z_i}}{F_{\text{O\&F}}}} \tag{3.49}$$

(See Equation 11 in [79].) Here $F_{\text{O\&F}}$ is a fudge factor that stipulates a tougher constraint as it increases. In the acoustic simulations of Ocheltree and Frizzell, $F_{\text{O\&F}} = 10$ was empirically determined to give accurate approximations for pressure. (The constraint in Equation 3.49 is the limiting constraint only when normal surface velocity u_n is essentially constant over the subelement A_i. Were this not the case, a second constraint on subelement height h_i and subelement width w_i based on normal surface velocity would need to be determined, and the more stringent of the two constraints would be the limiting and relevant constraint.)

According to the derivation of Ocheltree and Frizzell, the above constraint on d (Equation 3.49) in fact should have been:

$$h_i, w_i \leq \sqrt{\frac{4\lambda d_i}{F_{\text{O\&F}}}} \tag{3.50}$$

(note that v_{z_i} was replaced by d_i). However, when repeating the simulations of Ocheltree and Frizzell, the constraint in Equation 3.50 was found to be insufficiently strict. The more stringent constraint in Equation 3.49, which Ocheltree and Frizzell used without explanation, proved adequate. (This shift from d_i to v_{z_i} in the constraint equation is discussed further in Section 4.1.5 on page 106).

Equation 3.47 is not valid for a non-uniformly absorbing medium, but the medium of interest, namely the patient, is non-uniformly absorbing. Inhomogeneities affect this equation both directly and indirectly—indirectly because discontinuous inhomogeneities, *i.e.* boundaries, are sites of reflection and refraction of sound waves. The amount of reflection that occurs at a boundary is largely determined by the ratio of the acoustic impedances of the media on both sides of the boundary. For this reason the most clinically important reflections to consider occur at soft tissue-bone and tissue-air interfaces. Ultrasound refraction is significant only at very curved surfaces or surfaces nearly parallel to the direction of sound wave propagation, so refraction is usually ignored [29, 30]. For the current analysis, all scattering effects will continue to be ignored.

Lu *et al.* [62] modified Equation 3.47 for breast model simulations based on one central assumption: density ρ and wave speed c were essentially identical between breast tissue (br) and water (w), so ultrasound reflections did not occur in their model. (According to their model, the breast was immersed in degassed water, a common ultrasound coupling medium between the ultrasound transducers and the patient. Involvement of the chest wall was assumed to be negligible in their analysis, and was ignored.) Equation 3.47 was modified because α was now a function of position instead of a constant (although wavenumber k, like wave speed, remained a constant). The result of their assumption yielded:

$$p\{\vec{v}_i, t\} \approx \frac{j\rho c}{\lambda} \sum_{i=1}^{N} u_{n_i} \frac{e^{-(\alpha_{\mathrm{w}} d_{\mathrm{w}_i} + \alpha_{\mathrm{br}} d_{\mathrm{br}_i} + jkd_i)}}{d_i} \operatorname{sinc} \frac{k v_{x_i} w_i}{2d_i} \operatorname{sinc} \frac{k v_{y_i} h_i}{2d_i} A_i \tag{3.51}$$

where d_{w_i} is the part of d_i over which sound waves propagate through water, and d_{br_i} is the same for breast tissue. This equation differs from Equation 3.47 only in the exponential term. Assuming soft tissues in general and water share the same density and wave speed, Equation 3.51 can be generalized to:

$$p\{\vec{v}_i, t\} \approx \frac{j\rho c}{\lambda} \sum_{i=1}^{N} u_{n_i} \frac{e^{-\left[\int_{\ell_i} \alpha \, d\ell_i + jkd_i\right]}}{d_i} \operatorname{sinc} \frac{k v_{x_i} w_i}{2d_i} \operatorname{sinc} \frac{k v_{y_i} h_i}{2d_i} A_i \tag{3.52}$$

Chapter 4

Ultrasound Power Deposition: Advances

> *Nearly all men can stand adversity, but if you want to test a man's character, give him power.*
>
> — Abraham Lincoln

Advances in ultrasound modeling that took place in the course of this thesis are detailed in this chapter. These advances fall into three principal categories: accurate and rapid acoustic modeling of rectangular and cylindrical wedge acoustic sources (Section 4.1), acoustic modeling of individual (Section 4.2) and multiple (Section 4.3) FSUM transducers based on acoustic measurements and computer simulations, and the development of the Fanned Absorption Method (FAM), a technique for modifying the acoustic pressure field in a non-absorbing medium to obtain the acoustic pressure field in an absorbing medium (Section 4.4). The chapter ends with a summary of the modeling results obtained here, and some of their implications (Section 4.5).

The work developed in this chapter is important for thermal modeling of hyperthermia induced by ultrasound power applicators because the SAR field is a critical input parameter in thermal models. The numerical method developed in Section 4.1 greatly accelerates acoustic simulations of non-uniformly vibrating rectangular sources. These simulations are important for modeling individual FSUM transducers, and they are crucial for providing theoretical justification of the FAM.

4.1 Acoustic Pressure Field of Rectangular or Cylindrical Wedge Source

Ultrasound transducers shaped like rectangles or subsections of cylinders are commonly used to heat tumor tissue in hyperthermia cancer therapy. Intracavitary devices, used to treat prostate, rectal, and vaginal tumors, for example, use cylindrical transducers in a convex geometry, with sound radiating outward from the transducers. In contrast, external devices, for treatment of deep tumors, surround the patient and use a concave geometry, with sound radiating toward the center of the cylinder.

The rectangular radiator method of Ocheltree and Frizzell [79] (see Section 3.3.1) was developed to rapidly calculate the acoustic pressure field from a rectangular source. This method can be easily modified to accommodate transducers in the shape of a "rectangular" subsection of a right circular cylinder (as shown in Figure 4-2 on page 87). Whereas the original technique subdivided a rectangle into smaller rectangles, the modified technique subdivides a cylinder subsection into like parts. The modified technique is herein expanded to allow calculation of the sound pressure field from a cylinder subsection. The derivation given here parallels that given by Ocheltree and Frizzell, but aspects of the implementation are specific to sources in the shape of a cylindrical subsection.

As usual, the Rayleigh-Sommerfeld diffraction integral serves as the starting point of the acoustic pressure field calculation (see Equation 3.44 on page 77). As mentioned before, this integral is rigorously correct for a planar source embedded in an infinite rigid baffle, but not for the cylindrical geometry. Nevertheless, it is often used for a variety of non-planar sources, including cylinder subsections [24, 27].

4.1.1 Abstract

The rectangular radiator method, a technique for rapid calculation of acoustic pressure fields from acoustic sources that are planar, rectangular, and vibrate in a spatially uniform pattern, is extended to accommodate cylindrical sources and spatially heterogeneous vibration. Pressure fields were calculated for uniform and rectangular paraboloid vibration patterns for square sources with sides from 0.5 to 100 wavelengths. For planar sources acoustic beam contours

showed remarkable similarity between these two vibration modes. On the axis of symmetry (longitudinal axis), rectangular paraboloid vibration was observed to elevate both peaks and troughs in pressure amplitude in the near field, but decrease pressure amplitude in the far field.

4.1.2 Introduction

Ultrasound power transducers are commonly used to heat tissue in hyperthermia cancer treatment. Treatment systems often use transducers that are rectangular or cylindrical in shape [24, 26, 62, 95], and the acoustic pressure fields are modeled to help design power applicators and to predict power deposition fields. Ocheltree and Frizzell [79] developed a technique capable of rapid pressure field calculation for rectangular acoustic sources, the rectangular radiator method. This method was based on the summation of complex pressure field contributions from rectangular subelements of the source to calculate the pressure field from the entire source. A common way of performing pressure field calculations is by approximating the source by a large number of point or simple sources, and summing the pressure field contributions [27, 47]; the algorithm by Ocheltree and Frizzell achieves its computational efficiency by significantly reducing the number of subelements for which the pressure field contribution must be calculated and then summed.

The algorithm will be expanded here in two ways. First, the method will be modified to allow pressure field calculations from sources that do not vibrate uniformly, such as Gaussian transducers [25] and clamped transducers [72]. Second, the method will be modified to allow pressure field calculations from sources that are shaped like a "rectangular" subsection of a circular cylinder—henceforth referred to as a cylindrical wedge—as depicted in Figure 4-2.

The derivation performed by Ocheltree and Frizzell was a partial second-order analysis, meaning not all first- and second-order terms were considered. Here a complete second-order analysis will be presented, with benefits over the original algorithm that are three-fold. First, the new constraint equations (used to determine the degree to which sources must be subdivided for accurate pressure field calculation) from the current analysis give more accurate constraint equations. Second, a potential consequence of including first-order terms in the present analysis is that the number of subdivisions necessary to achieve a given level of accuracy in pressure field calculation may be reduced (although this is not always possible). And third, sources which do not vibrate uniformly can be more easily accommodated by the complete second-order analysis, with constraint equations that consider non-uniformities in vibration. The derivation presented here proceeds in essentially the same fashion as that of Ocheltree and Frizzell, but all first- and second-order terms are considered.

4.1.3 Methods

For a continuous wave planar acoustic source embedded in an infinite plane rigid baffle, and radiating into a non-scattering medium of constant sound absorption coefficient, the complex sound pressure p at a point in the field is given by:

$$p\{\vec{v},t\} = \frac{j\rho c}{\lambda}\int_A \frac{u_n}{d} e^{-(\alpha+jk)d}\, dA \tag{4.1}$$

where $j = \sqrt{-1}$, ρ is density of the medium, c is speed of sound in the medium, λ is acoustic wavelength, A is source surface area, u_n is the normal component of the velocity of the differential source area dA, d is the distance from the field point to the differential source area dA, α is the absorption coefficient, and k is the acoustic wavenumber ($k \equiv 2\pi/\lambda$). The surface A can be broken up into N subsurfaces A_i, with $1 \leq i \leq N$, and the total sound pressure field is then given by the sum of the pressure contributions from each subsurface p_i (*i.e.* $p = \sum_{i=1}^{N} p_i$), where:

$$p_i\{\vec{v},t\} = \frac{j\rho c}{\lambda}\int_{A_i} \frac{u_n}{d} e^{-(\alpha+jk)d}\, dA_i \tag{4.2}$$

4.1.3.1 Rectangular Acoustic Source Solution

A rectangular source is broken up into rectangular subelements. Figure 4-1 illustrates the local canonical coordinate system used for a rectangular subelement A_i centered at its local origin. (This local coordinate system (x_i, y_i, z_i) can be related to a global coordinate system (x, y, z), as shown earlier in Figure 3-5 on page 80.) The field point $\vec{v}_i$ is located at $(v_{x_i}, v_{y_i}, v_{z_i})$ in the local reference frame, the width and height of the subelement are w_i and h_i, and its corners are located at $(\pm w_i/2, \pm h_i/2, 0)$. Equation 4.2 then becomes:

$$p_i\{\vec{v}_i,t\} = \frac{j\rho c}{\lambda}\int_{-h_i/2}^{h_i/2}\int_{-w_i/2}^{w_i/2} \frac{u_n}{d} e^{-(\alpha+jk)d}\, dx_i\, dy_i \tag{4.3}$$

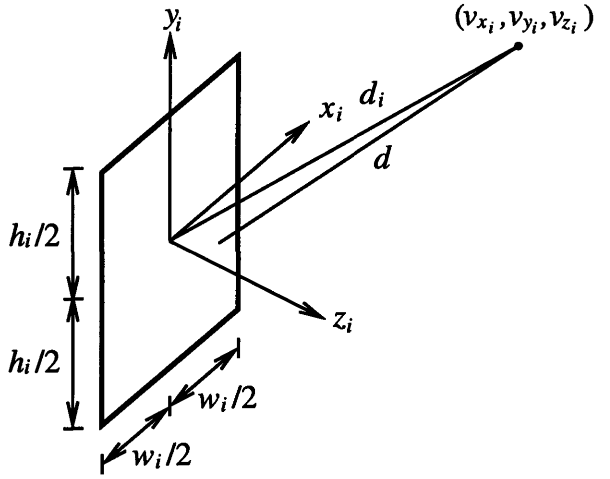

Figure 4-1: Canonical Cartesian coordinate system for a rectangular source.

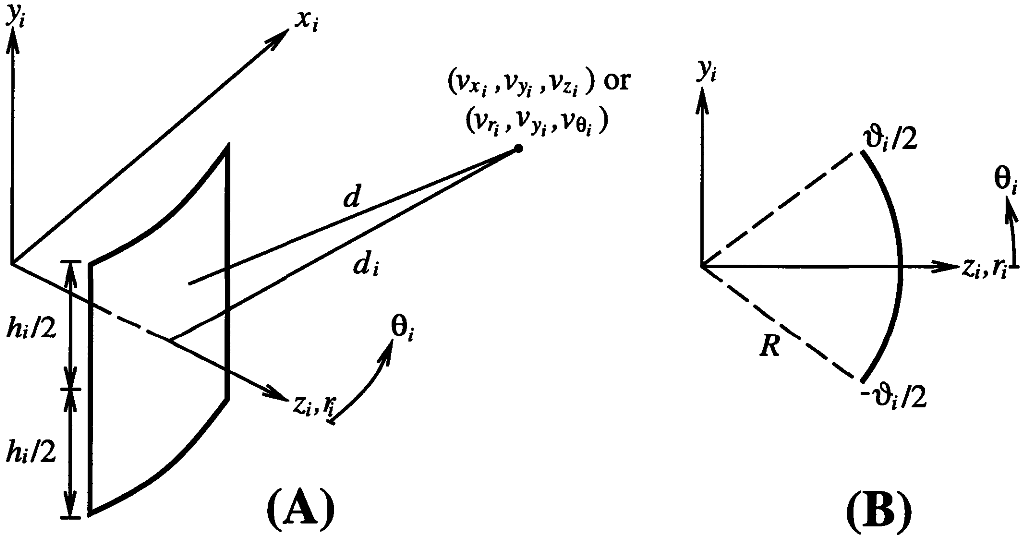

Figure 4-2: Canonical Cartesian and cylindrical coordinate systems for a cylindrical wedge source. (A) shows the three-dimensional perspective view, and (B) the cross-sectional view through the x_iy_i- and $r_i\theta_i$-plane.

The distance d_i from the field point $\vec{v}_i$ to the center of subelement A_i (the origin) is given implicitly by $d_i^2 = v_{x_i}^2 + v_{y_i}^2 + v_{z_i}^2$. The distance d from the field point $\vec{v}_i$ to an arbitrary point on the subelement surface $(x_i, y_i, 0)$ is given by:

$$d^2 = (v_{x_i} - x_i)^2 + (v_{y_i} - y_i)^2 + v_{z_i}^2 = d_i^2 \left(1 - \frac{2v_{x_i}x_i}{d_i^2} - \frac{2v_{y_i}y_i}{d_i^2} + \frac{x_i^2}{d_i^2} + \frac{y_i^2}{d_i^2}\right) \tag{4.4}$$

Equation 4.3 requires expressions for d and d^{-1}, which are given approximately by second-order Taylor series:

$$d \approx d_i \left[1 - \frac{v_{x_i}x_i}{d_i^2} - \frac{v_{y_i}y_i}{d_i^2} + \frac{x_i^2}{2d_i^2}\left(1 - \frac{v_{x_i}^2}{d_i^2}\right) + \frac{y_i^2}{2d_i^2}\left(1 - \frac{v_{y_i}^2}{d_i^2}\right) - \frac{v_{x_i}v_{y_i}x_iy_i}{d_i^4}\right] \tag{4.5}$$

$$\frac{1}{d} \approx \frac{1}{d_i}\left[1 + \frac{v_{x_i}x_i}{d_i^2} + \frac{v_{y_i}y_i}{d_i^2} - \frac{x_i^2}{2d_i^2}\left(1 - \frac{3v_{x_i}^2}{d_i^2}\right) - \frac{y_i^2}{2d_i^2}\left(1 - \frac{3v_{y_i}^2}{d_i^2}\right) + \frac{3v_{x_i}v_{y_i}x_iy_i}{d_i^4}\right] \tag{4.6}$$

Equation 4.5 is substituted into Equation 4.3 to yield:

$$\begin{aligned}
p_i &\approx \frac{j\rho c}{\lambda}\int_{-h_i/2}^{h_i/2}\int_{-w_i/2}^{w_i/2}\frac{u_n}{d}\exp\Bigg\{-(\alpha + jk)d_i\left[1 - \frac{v_{x_i}x_i}{d_i^2} - \frac{v_{y_i}y_i}{d_i^2}\right.\\
&\qquad \left. + \frac{x_i^2}{2d_i^2}\left(1 - \frac{v_{x_i}^2}{d_i^2}\right) + \frac{y_i^2}{2d_i^2}\left(1 - \frac{v_{y_i}^2}{d_i^2}\right) - \frac{v_{x_i}v_{y_i}x_iy_i}{d_i^4}\right]\Bigg\}\, dx_i\, dy_i\\
&= \frac{j\rho c}{\lambda}\int_{-h_i/2}^{h_i/2}\int_{-w_i/2}^{w_i/2}\frac{u_n}{d}e^{-(\alpha+jk)d_i}\exp\left[\alpha\left(\frac{v_{x_i}x_i}{d_i} + \frac{v_{y_i}y_i}{d_i}\right)\right]\exp\left[jk\left(\frac{v_{x_i}x_i}{d_i} + \frac{v_{y_i}y_i}{d_i}\right)\right] \qquad (4.7)\\
&\qquad \times \exp\Bigg\{-(\alpha + jk)\left[\frac{x_i^2}{2d_i}\left(1 - \frac{v_{x_i}^2}{d_i^2}\right) + \frac{y_i^2}{2d_i}\left(1 - \frac{v_{y_i}^2}{d_i^2}\right) - \frac{v_{x_i}v_{y_i}x_iy_i}{d_i^3}\right]\Bigg\}\, dx_i\, dy_i
\end{aligned}$$

Substituting $u_n\{x_i, y_i\} \approx u_{n_0} + u_{n_x}x_i + u_{n_y}y_i + \frac{1}{2}u_{n_{xx}}x_i^2 + \frac{1}{2}u_{n_{yy}}y_i^2 + u_{n_{xy}}x_iy_i$, Equation 4.6, and the Taylor series for the exponential function into Equation 4.7 yields (up to second-order terms):

$$\begin{aligned}
p_i &\approx \frac{j\rho c}{\lambda d_i}e^{-(\alpha+jk)d_i}\int_{-h_i/2}^{h_i/2}\int_{-w_i/2}^{w_i/2}\left(u_{n_0} + A_x x_i + A_y y_i + A_{xx}x_i^2 + A_{yy}y_i^2 + A_{xy}x_iy_i\right)\\
&\qquad \times \exp\left[jk\left(\frac{v_{x_i}x_i}{d_i} + \frac{v_{y_i}y_i}{d_i}\right)\right]\, dx_i\, dy_i
\end{aligned} \tag{4.8}$$

where u_{n_0} is a constant; $u_{n_x} = \partial u_n/\partial x_i$, $u_{n_y} = \partial u_n/\partial y_i$, $u_{n_{xx}} = \partial^2 u_n/\partial x_i^2$, $u_{n_{yy}} = \partial^2 u_n/\partial y_i^2$, and $u_{n_{xy}} = \partial^2 u_n/\partial x_i\, \partial y_i$ are evaluated at the local origin; and:

$$
\begin{aligned}
A_x &= u_{n_x} + \frac{u_{n_0} v_{x_i}}{d_i}\left(\frac{1}{d_i} + \alpha\right) \\
A_y &= u_{n_y} + \frac{u_{n_0} v_{y_i}}{d_i}\left(\frac{1}{d_i} + \alpha\right) \\
A_{xx} &= \frac{u_{n_{xx}}}{2} + \frac{u_{n_x} v_{x_i}}{d_i}\left(\frac{1}{d_i} + \alpha\right) - \frac{u_{n_0}}{2d_i^2}\left(1 - \frac{3v_{x_i}^2}{d_i^2}\right) - \frac{u_{n_0}}{2d_i}(\alpha + \boxed{jk)\Bigl(1} - \frac{v_{x_i}^2}{d_i^2}\Bigr) \\
&\quad + \frac{u_{n_0}\alpha v_{x_i}^2}{d_i^2}\left(\frac{1}{d_i} + \frac{\alpha}{2}\right) \\
A_{yy} &= \frac{u_{n_{yy}}}{2} + \frac{u_{n_y} v_{y_i}}{d_i}\left(\frac{1}{d_i} + \alpha\right) - \frac{u_{n_0}}{2d_i^2}\left(1 - \frac{3v_{y_i}^2}{d_i^2}\right) - \frac{u_{n_0}}{2d_i}(\alpha + \boxed{jk)\Bigl(1} - \frac{v_{y_i}^2}{d_i^2}\Bigr) \\
&\quad + \frac{u_{n_0}\alpha v_{y_i}^2}{d_i^2}\left(\frac{1}{d_i} + \frac{\alpha}{2}\right) \\
A_{xy} &= u_{n_{xy}} + \left(\frac{u_{n_x} v_{y_i}}{d_i} + \frac{u_y v_{x_i}}{d_i}\right)\left(\frac{1}{d_i} + \alpha\right) + \frac{u_{n_0} v_{x_i} v_{y_i}}{d_i^2}\left(\frac{3}{d_i^2} + \frac{3\alpha + jk}{d_i} + \alpha^2\right)
\end{aligned}
$$

The boxed terms in the expressions for A_{xx} and A_{yy}, namely the $ju_{n_0}k/2d_i$ terms, are the only terms in A_x, A_y, A_{xx}, A_{yy}, and A_{xy} considered by Ocheltree and Frizzell [79] in their derivation. This significance of this observation is that by considering *all* the terms that comprise A_x, A_y, A_{xx}, A_{yy}, and A_{xy}, a new solution equation for p_i and new constraint equations can produce faster pressure field computations (to the same level of accuracy) than can be achieved by the original rectangular radiator method of Ocheltree and Frizzell.

Equation 4.8 is exact to second order; if the second-order terms in Equation 4.8 are sufficiently small to ignore, then:

$$
\begin{aligned}
p_i \approx{}& \frac{j\rho c w_i h_i}{\lambda d_i} e^{-(\alpha + jk)d_i}\Biggl[u_{n_0}\,\mathrm{sinc}\,\frac{kv_{x_i} w_i}{2d_i}\,\mathrm{sinc}\,\frac{ky_{z_i} h_i}{2d_i} \\
&+ \frac{j}{2}\left(A_x w_i\,\mathrm{ginc}\,\frac{kv_{x_i} w_i}{2d_i}\,\mathrm{sinc}\,\frac{kv_{y_i} h_i}{2d_i} + A_y h_i\,\mathrm{sinc}\,\frac{kv_{x_i} w_i}{2d_i}\,\mathrm{ginc}\,\frac{kv_{y_i} h_i}{2d_i}\right)\Biggr]
\end{aligned}
\tag{4.9}
$$

where $\mathrm{sinc}\,\xi \equiv (\sin\xi)/\xi$ and $\mathrm{ginc}\,\xi \equiv (\mathrm{sinc}\,\xi - \cos\xi)/\xi$.[1] (*Cf.* Equation 4.9 to Equation 10 in [79].)

---

[1] The sinc function is seen in the literature; the ginc function is not. To 99.9% accuracy, $\mathrm{sinc}\,\xi \approx 1 - \xi^2/6 + \xi^4/120$ for $|\xi| \leq 1.25$, and $\mathrm{ginc}\,\xi \approx \xi/3 - \xi^3/30 + \xi^5/840$ for $|\xi| \leq 1.5$.

Equation 4.9 is accurate when the second-order terms are small compared to the maximum source surface normal velocity $u_{n_{\max}}$, the maximum normal speed amplitude of the entire acoustic source (not just the rectangular subelement). Specifically, the constraints are $|A_{xx}|(w_i/2)^2$, $|A_{yy}|(h_i/2)^2$, $|A_{xy}|(w_i/2)(h_i/2) < u_{n_{\max}}/F$, where F is a constraint factor that increases as desired accuracy increases. Assuming that $\alpha \ll k$ (as Ocheltree and Frizzell [79] did), and that $u_{n_0} \sim u_{n_{\max}}$, $u_{n_x} \sim 2u_{n_{\max}}/s_x$, $u_{n_y} \sim 2u_{n_{\max}}/s_y$, $u_{n_{xx}} \sim 4u_{n_{\max}}/s_x^2$, $u_{n_{yy}} \sim 4u_{n_{\max}}/s_y^2$, and $u_{n_{xy}} \sim 4u_{n_{\max}}/s_x s_y$, where s_y and s_z are the y and z dimensions of the entire acoustic source, the constraints from the second-order terms become (approximately):

$$\begin{aligned}
w_i &< \frac{2}{\sqrt{F}}\left[\frac{2}{s_x}\left(\frac{1}{s_x}+\frac{1}{d_i}+\alpha\right)+\frac{1}{d_i}\left(\frac{1}{d_i}+\frac{k}{2}\right)+\frac{\alpha^2}{2}\right]^{-\frac{1}{2}} \\
h_i &< \frac{2}{\sqrt{F}}\left[\frac{2}{s_y}\left(\frac{1}{s_y}+\frac{1}{d_i}+\alpha\right)+\frac{1}{d_i}\left(\frac{1}{d_i}+\frac{k}{2}\right)+\frac{\alpha^2}{2}\right]^{-\frac{1}{2}} \qquad (4.10) \\
w_i h_i &< \frac{4}{F}\left[\frac{4}{s_x s_y}+2\left(\frac{1}{s_x}+\frac{1}{s_y}\right)\left(\frac{1}{d_i}+\alpha\right)+\frac{1}{d_i}\left(\frac{3}{d_i}+k\right)+\alpha^2\right]^{-1}
\end{aligned}$$

For the case of a uniformly vibrating source ($u_n = u_{n_0}$), the constraints can be simplified to:

$$\begin{aligned}
w_i, h_i &< \frac{2}{\sqrt{F}}\left[\frac{1}{d_i}\left(\frac{1}{d_i}+\frac{k}{2}\right)+\frac{\alpha^2}{2}\right]^{-\frac{1}{2}} \qquad (4.11) \\
w_i h_i &< \frac{4}{F}\left[\frac{1}{d_i}\left(\frac{3}{d_i}+k\right)+\alpha^2\right]^{-1}
\end{aligned}$$

(*Cf.* Equation 4.11 to Equation 11 in [79].)

4.1.3.2 Cylindrical Wedge Acoustic Source Solution

A cylindrical wedge source is broken up into cylindrical wedge subelements. Figure 4-2 (page 87) illustrates the local canonical coordinate system used for a cylindrical wedge subelement A_i centered at its local origin, and with radius of curvature R. The field point is located at $(v_{x_i}, v_{y_i}, v_{z_i})$ and $(v_{r_i}, v_{y_i}, v_{\theta_i})$ in Cartesian and cylindrical[2] coordinate systems, respectively, the sides of the subelement are $R\vartheta_i$ and h_i, and its corners are located at at

---

[2] The usual cylindrical coordinate system is (r, θ, z), but this system is abandoned here in favor of (r, y, θ) because in acoustic field calculations the z direction usually corresponds to the nominal direction of sound radiating from the acoustic source. Furthermore, the use of the (r, y, θ) system facilitates comparison of corresponding results throughout Section 4.1 between rectangular and cylindrical wedge sources.

$(R\sin(\vartheta_i/2), \pm h_i/2, \pm R\cos(\vartheta_i/2))$ and $(R, \pm h_i, 2, \pm\theta_i/2,)$ in the two coordinate systems. Equation 4.2 then becomes:

$$p_i\{\vec{v}_i, t\} \approx \frac{j\rho c}{\lambda} \int_{-h_i/2}^{h_i/2} \int_{-\vartheta_i/2}^{\vartheta_i/2} \frac{u_n}{d} e^{-(\alpha+jk)d} R d\theta_i \, dy_i \tag{4.12}$$

The distance d_i from the field point $\vec{v}_i$ to the center of subelement A_i ($(R, 0, 0)$ in cylindrical coordinates, $(0, 0, R)$ in Cartesian coordinates) is given implicitly by $d_i^2 = v_{x_i}^2 + v_{y_i}^2 + (v_{z_i} - R)^2$. The distance d from $\vec{v}_i$ to an arbitrary point on the subelement surface (R, y_i, θ_i) is given by:

$$\begin{aligned} d^2 &= (v_{x_i} - R\sin\theta_i)^2 + v_{y_i}^2 + (v_{z_i} - R\cos\theta_i)^2 \\ &= d_i^2 \left[1 + \frac{2v_{x_i}R\sin\theta_i}{d_i^2} - \frac{2v_{y_i}y_i}{d_i^2} + \frac{y_i^2}{d_i^2} + \frac{2v_{z_i}R(1-\cos\theta_i)}{d_i^2}\right] \\ &\approx d_i^2 \left(1 - \frac{2v_{x_i}R\theta_i}{d_i^2} - \frac{2v_{y_i}y_i}{d_i^2} + \frac{y_i^2}{d_i^2} + \frac{v_{z_i}R\theta_i^2}{d_i^2}\right) \end{aligned} \tag{4.13}$$

Continuing the derivation in the same fashion as for the rectangular subelement case leads to the result:

$$\begin{aligned} p_i \approx{} & \frac{j\rho c}{\lambda d_i} e^{-(\alpha+jk)d_i} \int_{-h_i/2}^{h_i/2} \int_{-\vartheta_i/2}^{\vartheta_i/2} \left[u_{n_0} + A_\theta R\theta + A_y y_i + A_{\theta\theta}(R\theta_i)^2 + A_{yy}y_i^2 + A_{\theta y}R\theta_i y_i\right] \\ & \times \exp\left[jk\left(\frac{v_{x_i}R\theta_i}{d_i} + \frac{v_{y_i}y_i}{d_i}\right)\right] R d\theta_i \, dy_i \end{aligned} \tag{4.14}$$

where u_{n_0} is a constant; $u_{n_\theta} = \partial u_n/\partial\theta_i$, $u_{n_y} = \partial u_n/\partial y_i$, $u_{n_{\theta\theta}} = \partial^2 u_n/\partial\theta_i^2$, $u_{n_{yy}} = \partial^2 u_n/\partial y_i^2$, and $u_{n_{\theta y}} = \partial^2 u_n/\partial\theta_i\,\partial y_i$ are evaluated at the local center of the subelement (*i.e.* $(R, 0, 0)$ in local cylindrical coordinates, and $(0, 0, R)$ in local Cartesian coordinates); and:

$$\begin{aligned} A_\theta &= \frac{u_{n_\theta}}{R} + \frac{u_{n_0}v_{x_i}}{d_i}\left(\frac{1}{d_i} + \alpha\right) \\ A_y &= u_{n_y} + \frac{u_{n_0}v_{y_i}}{d_i}\left(\frac{1}{d_i} + \alpha\right) \\ A_{\theta\theta} &= \frac{u_{n_{\theta\theta}}}{2R^2} + \frac{u_{n_\theta}v_{x_i}}{Rd_i}\left(\frac{1}{d_i} + \alpha\right) - \frac{u_{n0}}{2d_i^2}\left(\frac{v_{z_i}}{R} - \frac{3v_{x_i}^2}{d_i^2}\right) - \frac{u_{n0}}{2d_i}(\alpha + jk)\left(\frac{v_{z_i}}{R} - \frac{v_{x_i}^2}{d_i^2}\right) \\ &\quad + \frac{u_{n_0}\alpha v_{x_i}^2}{d_i^2}\left(\frac{1}{d_i} + \frac{\alpha}{2}\right) \\ A_{yy} &= \frac{u_{n_{yy}}}{2} + \frac{u_{n_y}v_{y_i}}{d_i}\left(\frac{1}{d_i} + \alpha\right) - \frac{u_{n0}}{2d_i^2}\left(1 - \frac{3v_{y_i}^2}{d_i^2}\right) - \frac{u_{n0}}{2d_i}(\alpha + jk)\left(1 - \frac{v_{y_i}^2}{d_i^2}\right) \end{aligned}$$

$$+\frac{u_{n_0}\alpha v_{y_i}^2}{d_i^2}\left(\frac{1}{d_i}+\frac{\alpha}{2}\right)$$

$$A_{\theta y} = \frac{u_{n_{\theta y}}}{R} + \left(\frac{u_{n_\theta} v_{y_i}}{Rd_i} + \frac{u_{n_y} v_{x_i}}{d_i}\right)\left(\frac{1}{d_i}+\alpha\right) + \frac{u_{n_0} v_{x_i} v_{y_i}}{d_i^2}\left(\frac{3}{d_i^2} + \frac{3\alpha + jk}{d_i} + \alpha^2\right)$$

(Again, Equation 4.14 is exact to second order.) Ignoring the second-order terms in Equation 4.14:

$$\begin{aligned} p_i \approx{}& \frac{j\rho c R\vartheta_i h_i}{\lambda d_i} e^{-(\alpha+jk)d_i}\left[u_{n_0}\operatorname{sinc}\frac{kv_{x_i}R\vartheta_i}{2d_i}\operatorname{sinc}\frac{kv_{y_i}h_i}{2d_i}\right. \\ &\left.+\frac{j}{2}\left(A_\theta R\theta_i \operatorname{ginc}\frac{kv_{x_i}R\vartheta_i}{2d_i}\operatorname{sinc}\frac{kv_{y_i}h_i}{2d_i} + A_z h_i \operatorname{sinc}\frac{kv_{x_i}R\vartheta_i}{2d_i}\operatorname{ginc}\frac{kv_{y_i}h_i}{2d_i}\right)\right] \end{aligned} \tag{4.15}$$

The constraints from the second-order terms are $|A_{\theta\theta}|(R\vartheta_i/2)^2, |A_{yy}|(h_i/2)^2, |A_{\theta y}|(R\vartheta_i/2)(h_i/2) < u_{n_{\max}}/F$. Assuming again that $\alpha \ll k$, and that $u_{n_0} \sim u_{n_{\max}}$, $u_{n_\theta} \sim 2u_{n_{\max}}/\sigma_\theta$, $u_{n_y} \sim 2u_{n_{\max}}/s_y$, $u_{n_{\theta\theta}} \sim 4u_{n_{\max}}/\sigma_\theta^2$, $u_{yy} \sim 4u_{n_{\max}}/s_y^2$, and $u_{n_{\theta y}} \sim 4u_{n_{\max}}/\sigma_\theta s_y$, where σ_θ and s_y are the θ and y dimensions of the entire acoustic source (and $s_\theta = R\sigma_\theta$ is the arc length of the entire source), the constraints become (approximately):

$$\begin{aligned} R\vartheta_i &< \frac{2}{\sqrt{F}}\left\{\frac{2}{s_\theta}\left(\frac{1}{s_\theta}+\frac{1}{d_i}+\alpha\right)+\frac{1}{2d_i}\left[\left(\frac{1}{d_i}+k\right)\frac{|v_{z_i}|}{R}+\frac{3}{d_i}+k\right]+\frac{\alpha^2}{2}\right\}^{-\frac{1}{2}} \\ h_i &< \frac{2}{\sqrt{F}}\left[\frac{2}{s_y}\left(\frac{1}{s_y}+\frac{1}{d_i}+\alpha\right)+\frac{1}{d_i}\left(\frac{1}{d_i}+\frac{k}{2}\right)+\frac{\alpha^2}{2}\right]^{-\frac{1}{2}} \\ R\vartheta_i h_i &< \frac{4}{F}\left[\frac{4}{s_\theta s_y}+2\left(\frac{1}{s_\theta}+\frac{1}{s_y}\right)\left(\frac{1}{d_i}+\alpha\right)+\frac{1}{d_i}\left(\frac{3}{d_i}+k\right)+\alpha^2\right]^{-1} \end{aligned} \tag{4.16}$$

For the case of a uniformly vibrating source ($u_n = u_{n_0}$), the constraints simplify to:

$$\begin{aligned} R\vartheta_i &< \sqrt{\frac{8}{F}}\left\{\frac{1}{d_i}\left[\left(\frac{1}{d_i}+k\right)\frac{|v_{z_i}|}{R}+\frac{3}{d_i}+k\right]+\alpha^2\right\}^{-\frac{1}{2}} \\ h_i &< \frac{2}{\sqrt{F}}\left[\frac{1}{d_i}\left(\frac{1}{d_i}+\frac{k}{2}\right)+\frac{\alpha^2}{2}\right]^{-\frac{1}{2}} \\ R\vartheta_i h_i &< \frac{4}{F}\left[\frac{1}{d_i}\left(\frac{3}{d_i}+k\right)+\alpha^2\right]^{-1} \end{aligned} \tag{4.17}$$

The field point is not necessarily visible to the entire radiating surface of the cylindrical wedge. The parts of the cylindrical wedge which do not enjoy a direct line of sight to the field point are taken to contribute insignificantly to the sound pressure at the field point, so these parts are ignored. A specific protocol to determine the portion of the radiator visible to a given field point is given in Section B.3.

4.1.4 Results

Field Calculations were made for square planar sources and convex and concave cylindrical sources radiating into a non-absorbing medium, and pressures amplitude were normalized to the maximum calculated axial pressure amplitude. For easy comparison with the calculations performed by Ocheltree and Frizzell [79], the square planar sources were sized 0.5λ, 1λ, 2λ, 5λ, 10λ, 20λ, and 100λ on a side (λ is wavelength), and pressure field calculations were performed on the z-axis and in the xz-plane (see Figures 4-3 – 4-9). In addition, two type of source vibration were considered: uniform and rectangular paraboloid. Rectangular paraboloid vibration was felt to be a reasonable approximation of the vibration achieved in clamped transducers [72], and was defined by source surface normal velocity $u_n\{x,y\} = u_{n_{\max}}[1-(2x/s_x)^2][1-(2y/s_y)^2]$, where the source is centered at the origin, and s_x and s_y are the sides in the x and y directions (so $|x| \leq s_x/2$, and $|y| \leq s_y/2$ for $u_n\{x,y\}$).

In addition to the simulations of square planar sources, simulations were performed for cylindrical wedge sections. Specifically, sources $s_y = 10\lambda$ in height and $s_\theta = 10\lambda$ in arc length, with an aperture of $\sigma_\theta = 60°$ and a corresponding radius of curvature $R = 30\lambda/\pi$. Both concave (Figure 4-10) and convex (Figure 4-11) geometries were considered, as were both uniform and rectangular paraboloid vibration. (Rectangular paraboloid vibration in the cylindrical wedge case is analogous to that in the rectangular planar case: $u_n\{\theta,y\} = u_{n_{\max}}[1-(2\theta/\sigma_\theta)^2][1-(2y/s_y)^2]$, with $|\theta| \leq \sigma_\theta/2$ and $|y| \leq s_y/2$.)

The constraint conditions were implemented by iteratively dividing the source into two halves or four quadrants (depending on which constraint conditions were violated) of congruent shape and equal size. In general the displayed fields were calculated with the constraint factor $F = 5$. For error analysis, all fields were also calculated with $F = 100$ to obtain nominal "exact" fields. In addition, for the purposes of comparison fields were also calculated with $F = 2$ and using the Ocheltree and Frizzell [79] constraint equation (with their constraint $F_{\text{O\&F}} = 10$). (In general field calculations using $F = 2$ and $F_{\text{O\&F}} = 10$ required about the same amount of computational effort.) Figure 4-12 shows the maximum and root mean square (RMS) errors in normalized pressure amplitude along the z-axis (up to normalized $x = 4$) for the seven different sizes of square planar source under uniform and rectangular paraboloid vibration. Errors were also calculated for the concave and convex sources and compared to the errors in the square planar case with $s = 10\lambda$, and they were found to be modestly (13%) but inconsistently greater for the curved sources. Pressures were normalized to the maximum pressure in the calculated field, and errors were determined over the calculated axial field points. (Axial pressure was calculationed at normalized axial depth $z/(s^2/4\lambda)$ from 0.01 to 4.00 in increments of 0.01.)

4.1.5 Discussion

Several observations are readily apparent when comparing uniform and rectangular paraboloid vibration pressure field simulations. First, the normalized field beam contours in the yz-plane are remarkably similar, in both the rectangular planar and cylindrical wedge cases (Figures 4-3 – 4-11). (In the rectangular case, the field in the yz-plane is the same as that in the xz-plane because the rectangular sources investigated were square.) Second, in the cylindrical wedge case (Figures 4-10 and 4-11), the same cannot be said as strongly of the normalized beam contours in the xz-plane, particularly in the convex case. And third, the normalized acoustic pressure amplitude p_{a} on the z-axis exhibits interesting and consistent differences in the case of square planar sources (Figures 4-3 – 4-9). Specifically, peaks and troughs in the acoustic pressure amplitude are at the same axial distances with rectangular paraboloid vibration as with uniform vibration, with the sole exception of the last peak, which is closer to the source under rectangular paraboloid vibration; in addition, near field pressures are in general elevated and far field pressures are depressed under rectangular paraboloid vibration, compared with uniform vibration.

The pressure field is understandably complicated by deviation of the source from planarity. In the concave case (Figure 4-10), the geometric focus of the source in general does not overlap with the diffraction focus (*i.e.* the most distal peak, located in the transitional region between near and far field), and the result is a peak at the geometric focus that dwarfs the peak at the diffraction focus. In addition, the geometric focusing action elevates the pressures in the far field (and, as for the planar case, in the near field) under rectangular paraboloid vibration,

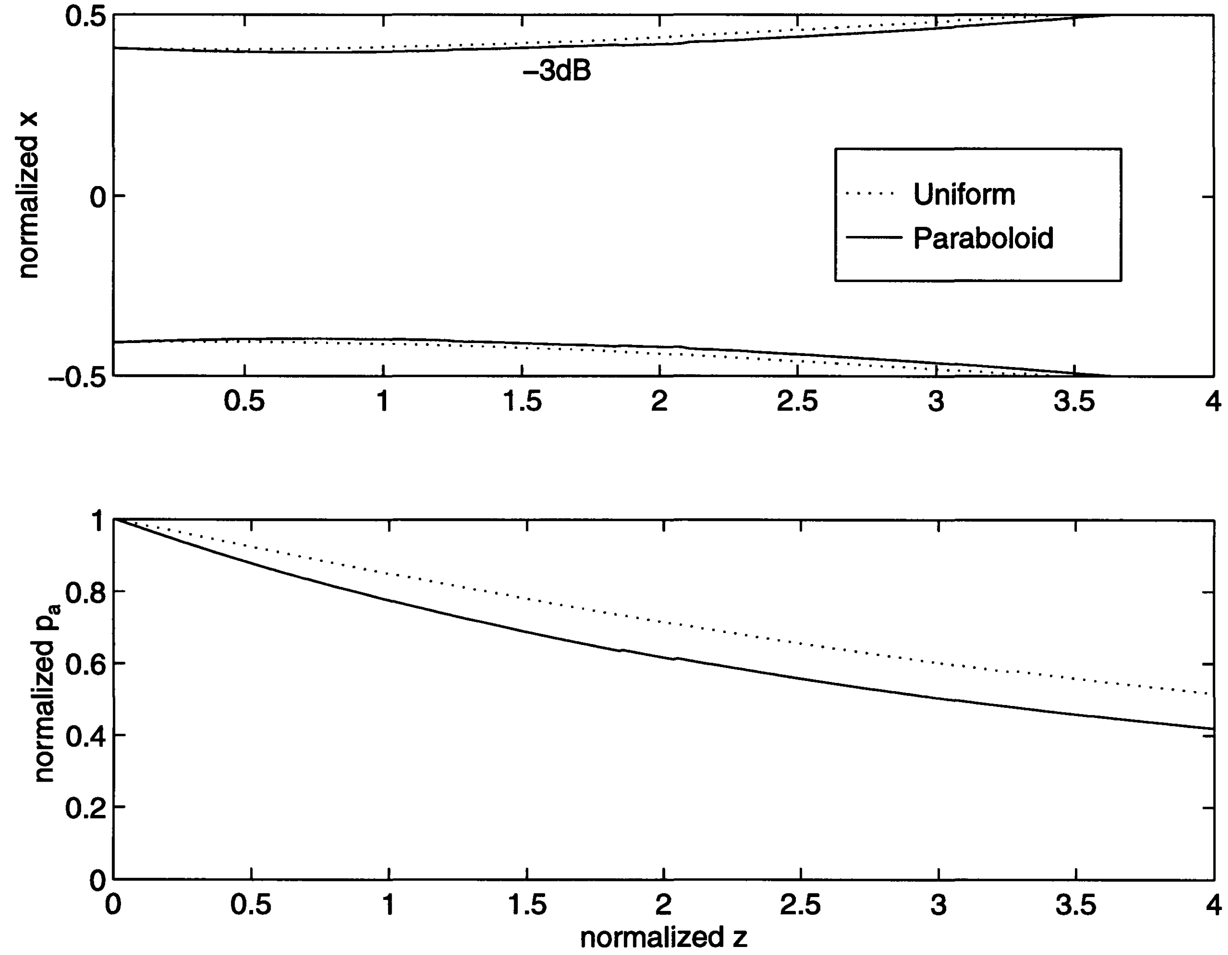

Figure 4-3: Acoustic pressure field of square planar source with side $s = 0.5\lambda$. Top: -3dB contours (and -6dB contours in subsequent figures) of the pressure amplitude of the beam in the xz-plane, normalized at each axial distance. x is normalized by side s, and z by $s^2/4\lambda$, and the source is in canonical coordinates. Bottom: Normalized pressure amplitude p_a on the z-axis. In both subfigures, dotted lines (· · ·) correspond to uniform vibration, and solid lines (—) correspond to rectangular paraboloid vibration.

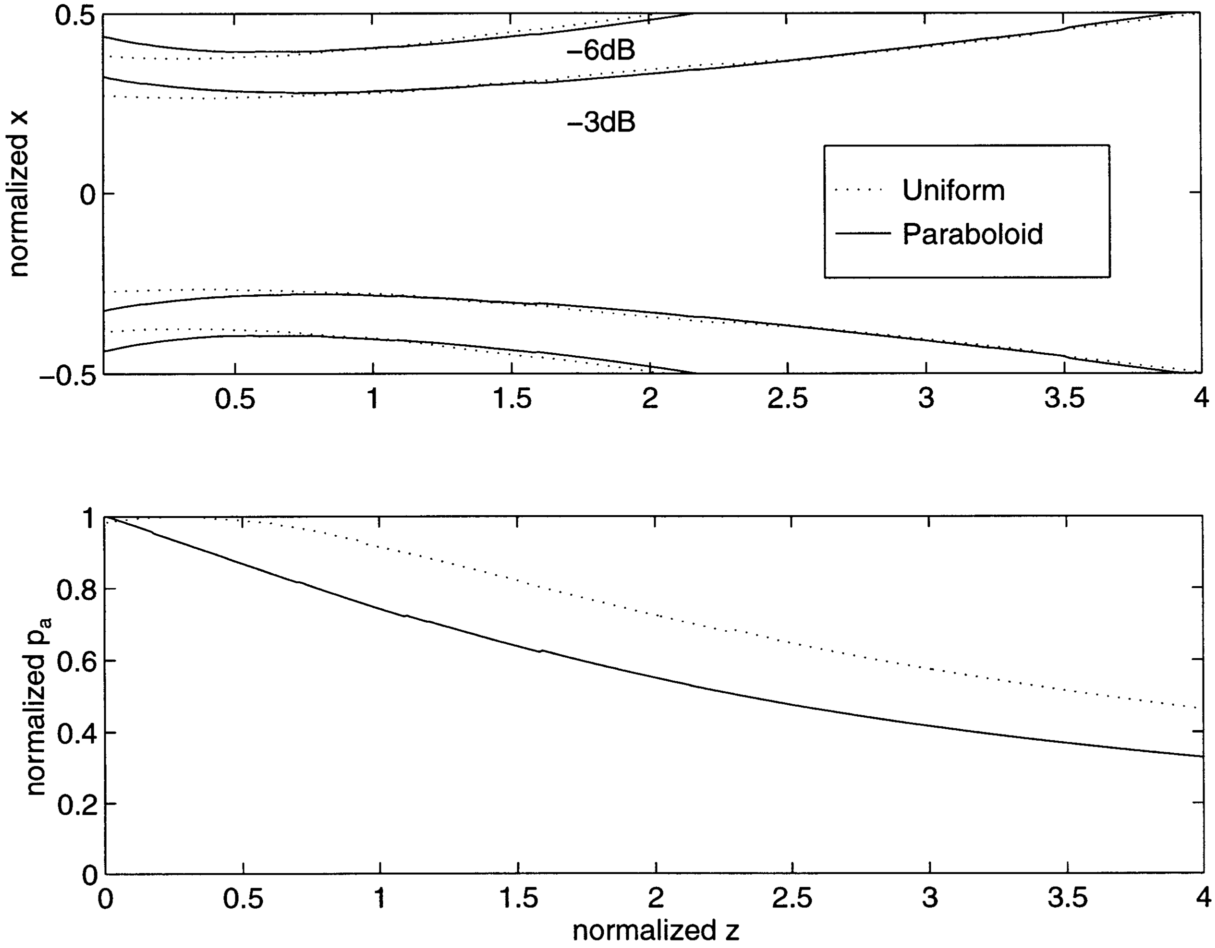

Figure 4-4: Acoustic pressure field of square planar source with side $s = 1\lambda$. (See Figure 4-3 for further explanation.)

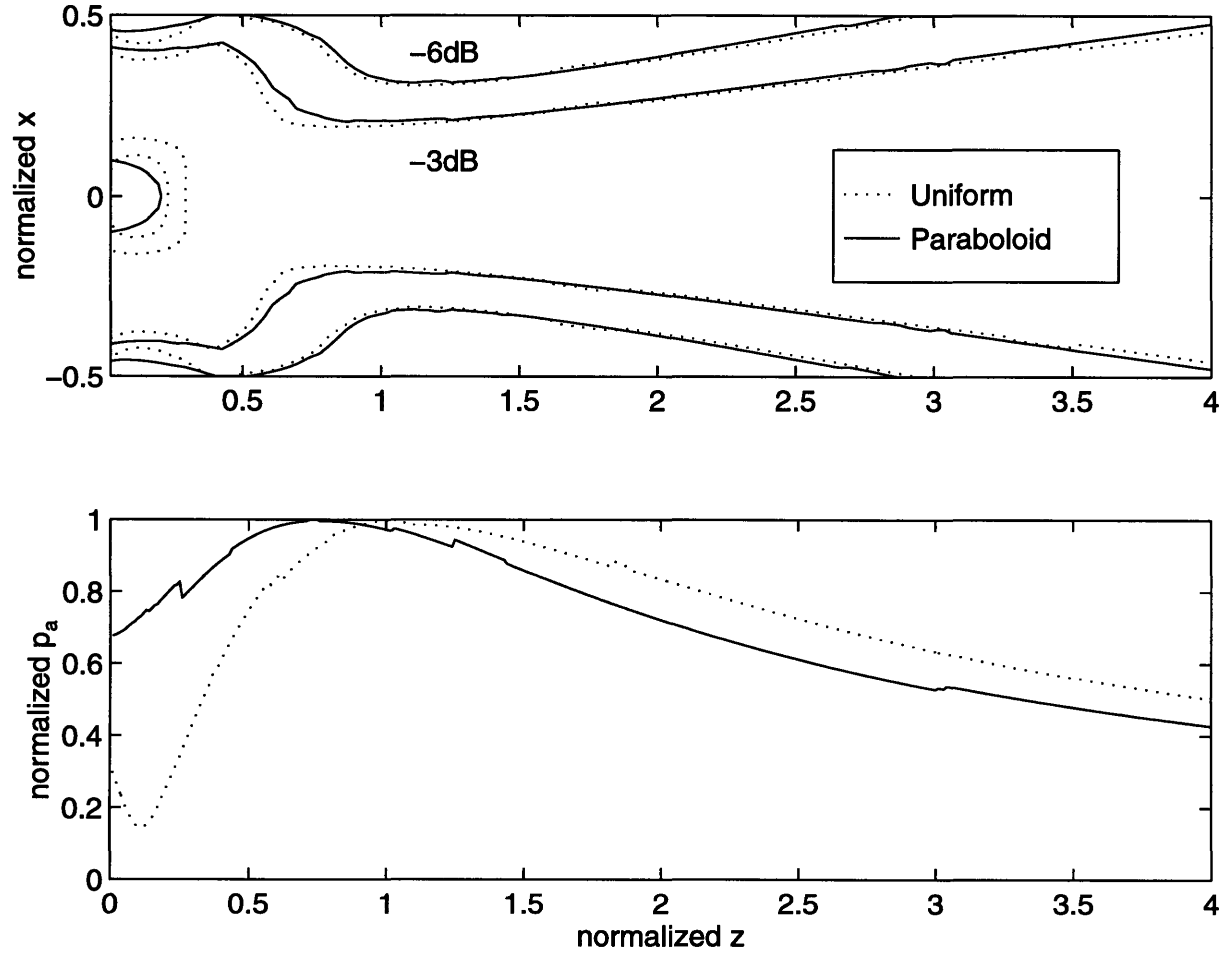

Figure 4-5: Acoustic pressure field of square planar source with side $s = 2\lambda$. (See Figure 4-3 for further explanation.)

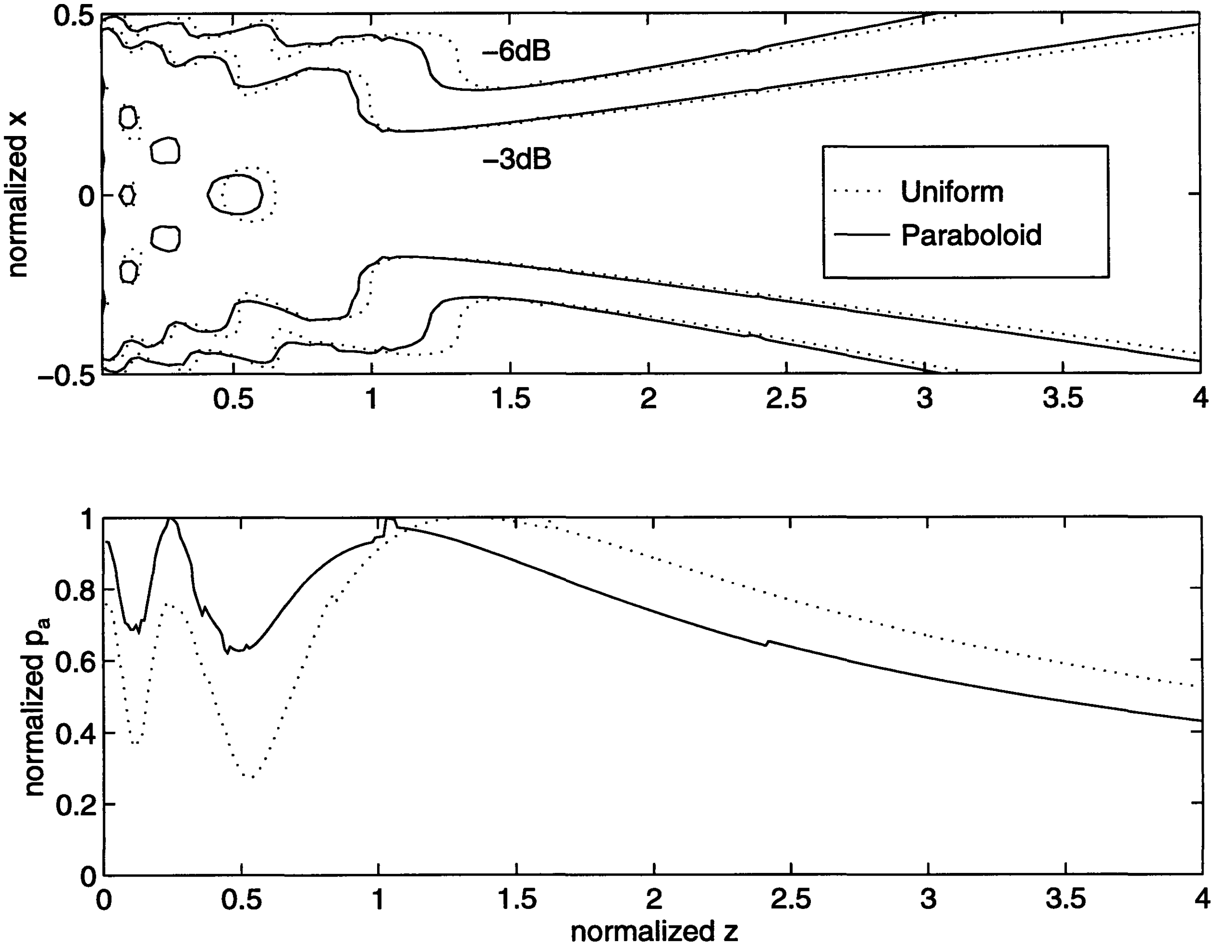

Figure 4-6: Acoustic pressure field of square planar source with side $s = 5\lambda$. (See Figure 4-3 for further explanation.)

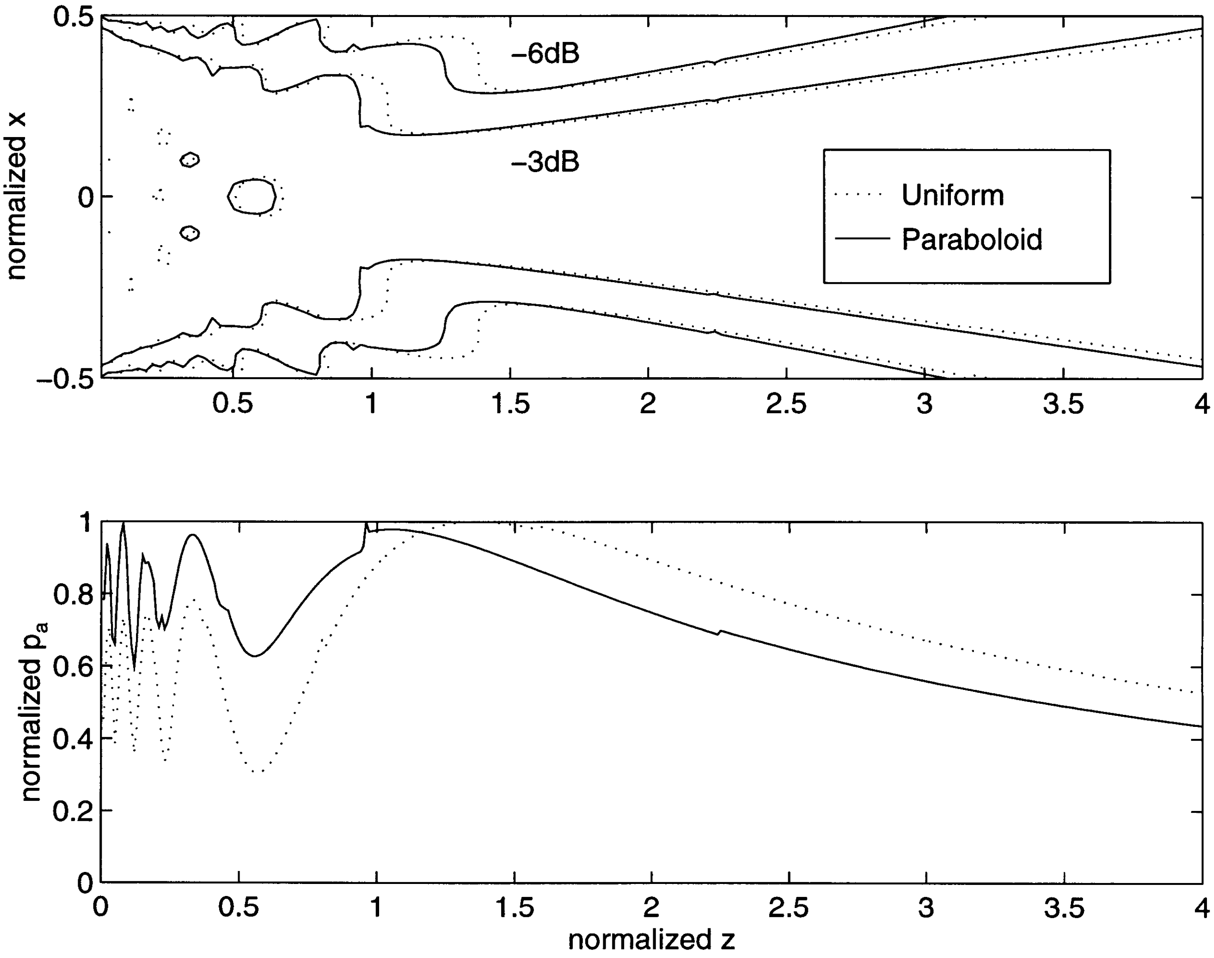

Figure 4-7: Acoustic pressure field of square planar source with side $s = 10\lambda$. (See Figure 4-3 for further explanation.)

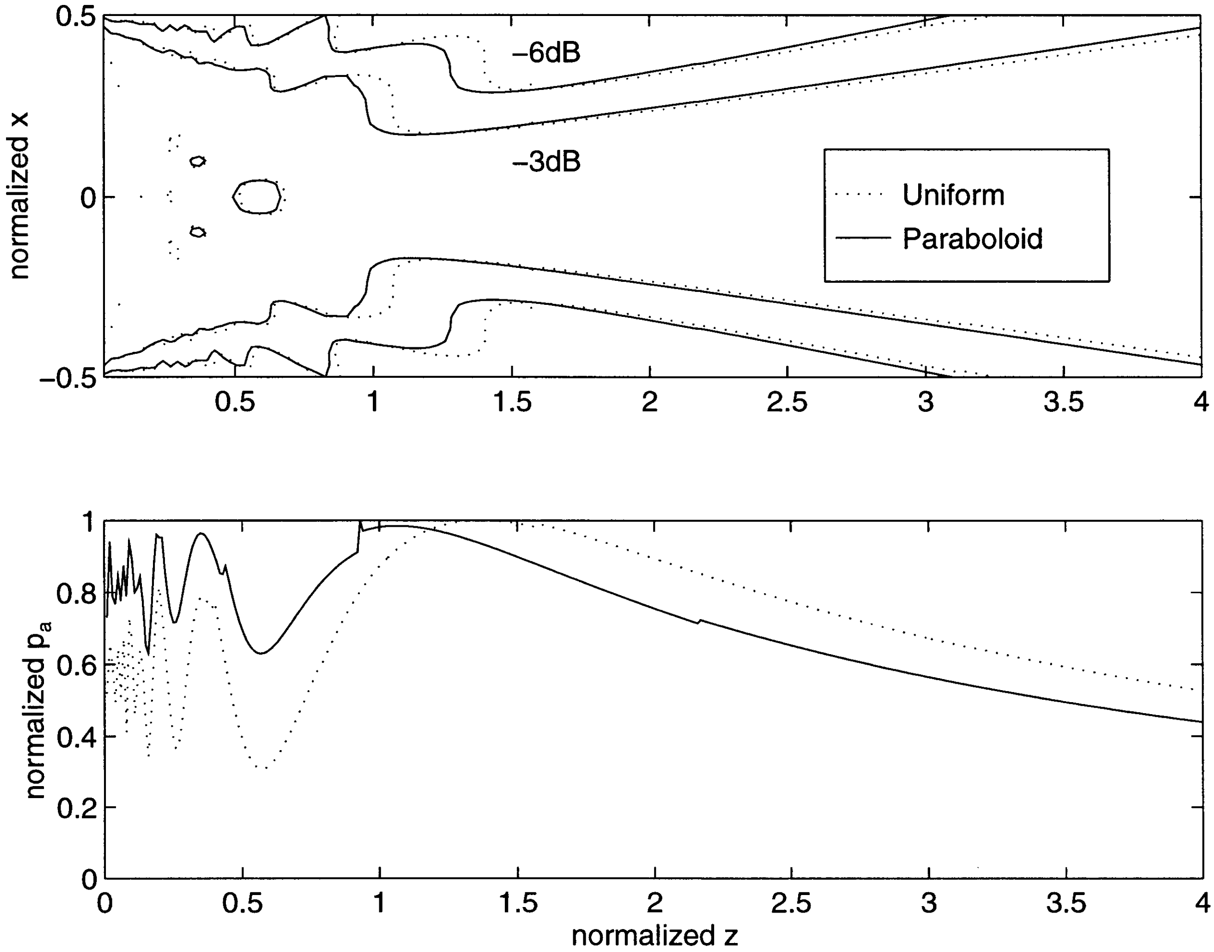

Figure 4-8: Acoustic pressure field of square planar source with side $s = 20\lambda$. (See Figure 4-3 for further explanation.)

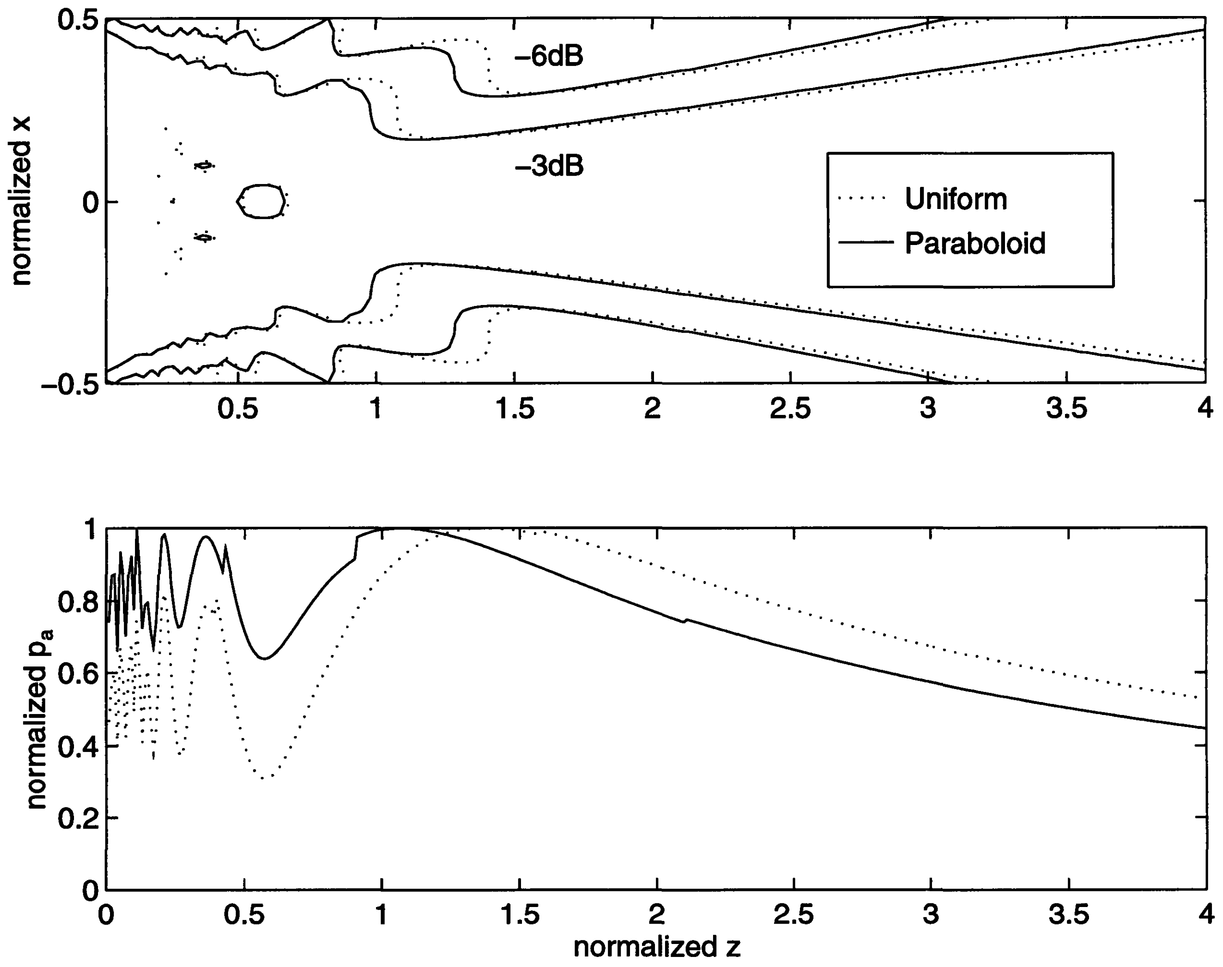

Figure 4-9: Acoustic pressure field of square planar source with side $s = 100\lambda$. (See Figure 4-3 for further explanation.)

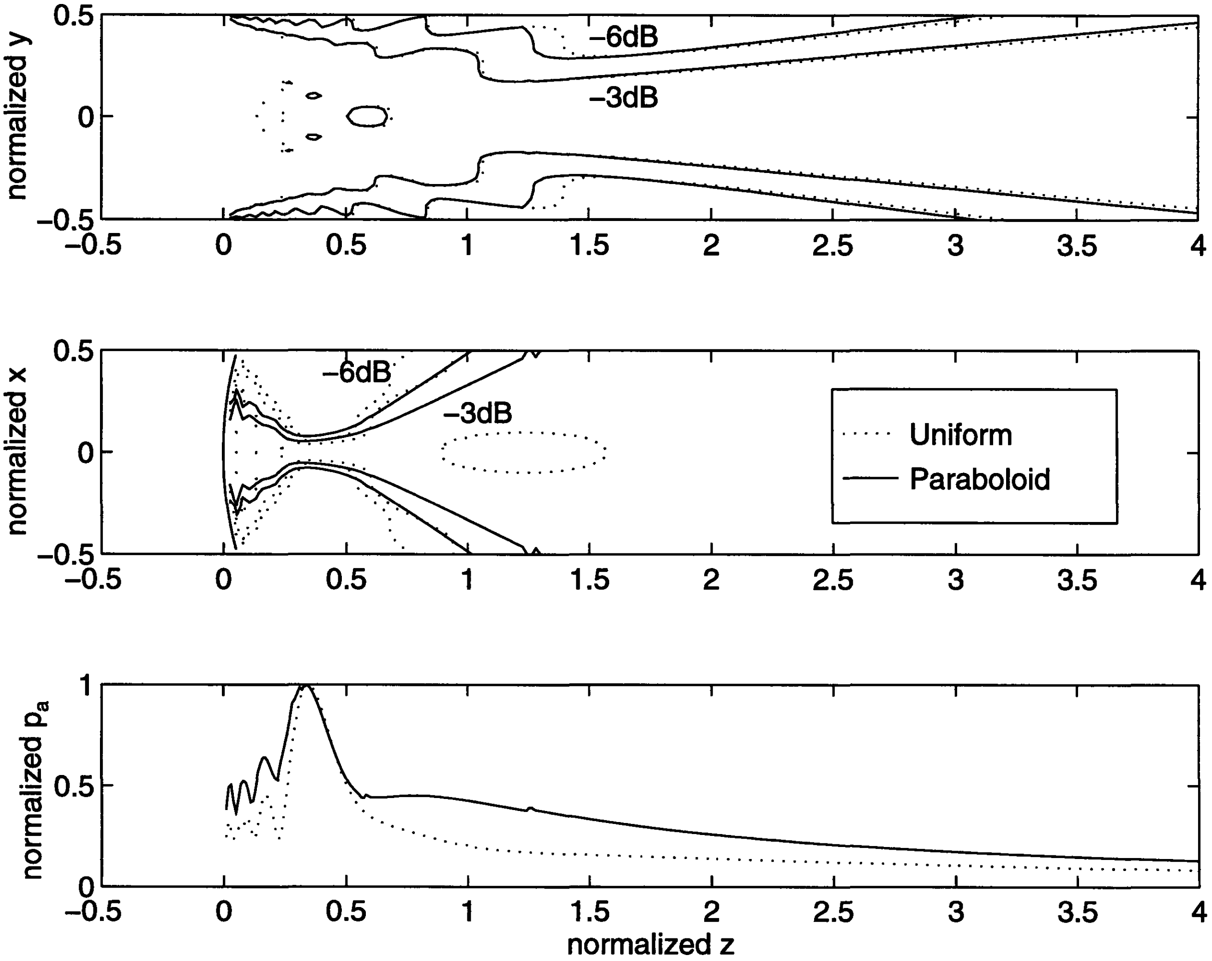

Figure 4-10: Acoustic pressure field of concave cylindrical wedge source with sides $s_y, s_\theta = 10\lambda$, aperture $\sigma_\theta = 60°$, and radius of curvature $R = 30\lambda/\pi$. Top: -3dB and -6dB contours of the pressure amplitude of the beam in the yz-plane, normalized at each axial distance. Middle: -3dB and -6dB contours of the pressure amplitude of the beam in the xz-plane, normalized at each axial distance. x is normalized by side s_θ, y by side s_y, and z by $s^2/4\lambda$. The center of the source (*i.e.* $(0, 0, R)$ in canonical cylindrical coordinates) is taken to be the origin in the subfigures, and the cross-section of the source is shown in the xz-plane. Bottom: Normalized pressure amplitude p_a on the z-axis. In all subfigures, dotted lines $(\cdots)$ correspond to uniform vibration, and solid lines (—) correspond to rectangular paraboloid vibration.

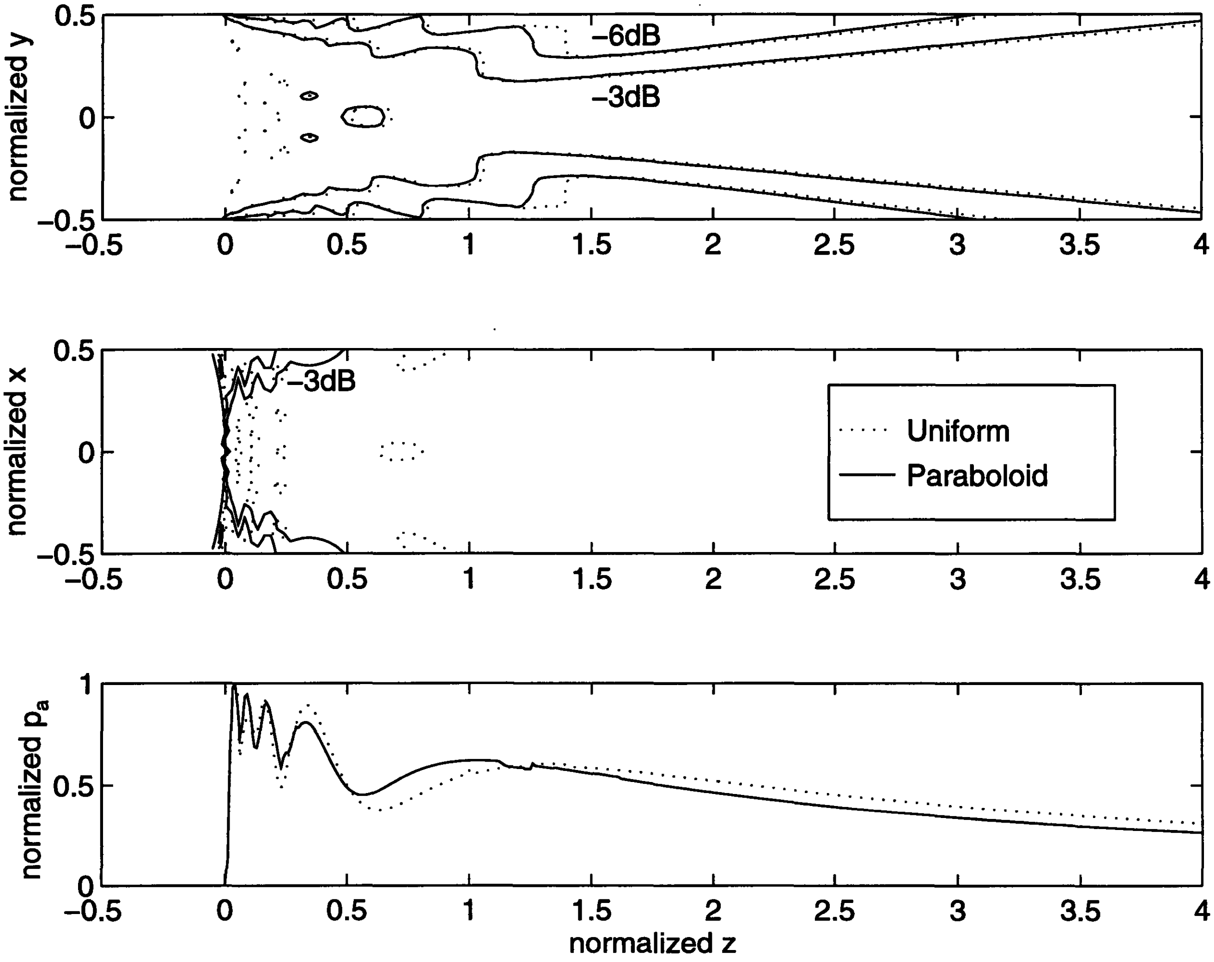

Figure 4-11: Acoustic pressure field of convex cylindrical wedge source with sides $s_y, s_\theta = 10\lambda$, aperture $\sigma_\theta = 60°$, and radius of curvature $R = 30\lambda/\pi$. (See Figure 4-10 for further explanation.)

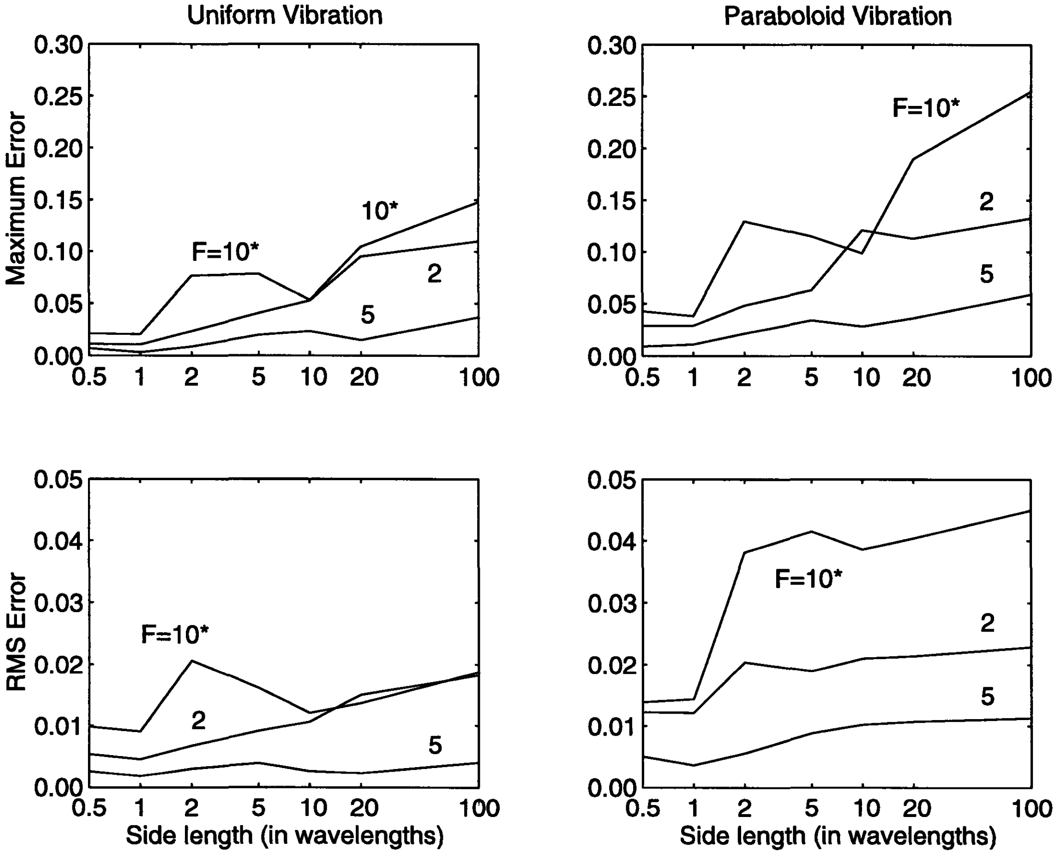

Figure 4-12: Maximum and RMS error in z-axis normalized pressure amplitude for square planar sources of side $s = 0.5\lambda, 1\lambda, 2\lambda, 5\lambda, 10\lambda, 20\lambda$, and 100λ, under uniform and rectangular paraboloid vibration. Curves are labeled according to constraint factor $F = 2$ and 5, and $F = 10^*$ indicates the Ocheltree and Frizzell constraint was used with $F_{\text{O\&F}} = 10$ (see [79]).

compared with uniform vibration. This elevation of pressure amplitude in *both* near and far field under rectangular paraboloid vibration can be viewed from another point of view: Concavity causes more effective geometric focusing for uniform vibration than for rectangular paraboloid vibration, so the *normalized* pressure away from the geometric focus suffers under uniform vibration.

For the convex radiator, these issues associated with the geometric focus disappear, resulting in a simpler picture. Specifically, near field peaks in pressure decrease in magnitude with distance from the source, which makes sense given the geometric divergence of sound from the source. (See Figure 4-11.)

Maximum and RMS error generally increased as the source dimensions increased, by a factor of about four between side $s = 0.5\lambda$ and $s = 100\lambda$. In addition, rectangular paraboloid vibration resulted in a slightly more than doubling of error in general, compared with uniform vibration. Increasing the constraint factor from $F = 2$ to $F = 5$ doubled computational effort but tripled accuracy. $F = 2$ and $F_{\text{O\&F}} = 10$ were comparable in terms of computational effort, and $F = 2$ produced modestly more accurate results in general. (The value $F = 2$ cannot be compared directly to the value $F_{\text{O\&F}} = 10$ used by Ocheltree and Frizzell because their constraint factor is analogous to the one used here, but not identical. Equation 4.11 can be compared to Equation 3.49 to yield the *approximate* relation $F \approx F_{\text{O\&F}}/2\pi$.) As previously mentioned, errors did not seem to be substantially affected by deviations from planarity of the source.

As mentioned in Section 4.1.4 (page 93), the nominal exact pressure field was taken to be the field calculated with $F = 100$. Needless to say, such a constraint factor will provide accuracy superior to that obtained by $F = 2$ or $F = 5$, but it is nevertheless possible that the level of accuracy achieved by using $F = 100$ is not as great as desired. Thus for the case of the square planar source with side $s = 10\lambda$ and rectangular paraboloid vibration, fields were also calculated with $F = 1000$ and $F = 10{,}000$. Maximum and RMS differences between the $F = 100$ and $F = 1000$ fields were 0.2% and 0.03%, respectively, as were the differences between the $F = 100$ and $F = 10{,}000$ fields. (Differences between the $F = 1000$ and $F = 10{,}000$ fields were 0.02% and 0.003%. In general errors were inversely proportional to F, which is expected given the way F was defined.) Thus the fields calculated using $F = 100$ can be expected to have variable levels of accuracy, in general increasing with increasing source size and greater for rectangular paraboloid than uniform vibration, but with a maximum error under 1% and RMS error under 0.1% in any case, at least in the investigated range of source sizes.

An interesting observation is made when comparing the results obtained by Ocheltree and Frizzell [79] and those presented here. The sides of the square acoustic planar sources investigated here were made the same as those investigated by Ocheltree and Frizzell, for the express purpose of comparison. Even though the accuracy of the fields calculated here significantly exceeded that of the fields calculated by Ocheltree and Frizzell (see Figure 4-12), the latter fields appear much "smoother" than the former. Another way of putting this is that there are calculation artifacts that clearly correspond to calculation error, such as on the z-axis at normalized z values near 1.2 in Figures 4-7 – 4-9, that are present here but are absent in the results presented by Ocheltree and Frizzell. This discrepancy in the presence of this particular type of artifact comes about because of differences in the implementation of the constraint equations (Equations 3.49, 4.10, and 4.11). Specifically, here the constraints were implemented by iteratively dividing the subelement into two halves or four quadrants. In contrast, the implementation of Ocheltree and Frizzell was, in one step, to subdivide the entire source into the smallest number of subelements such that the subelements satisfied the constraints (see Equation11 in [79]). (Their constraint used field point component v_{z_i} instead of the distance d_i from the field point to the subelement center; since v_{z_i} is constant over the the entire surface of the planar subelement, their constraint was invariant for every conceivable subelement of a planar source. If they had used d_i, which varies continuously over the planar subelement, then an implementation more akin to the one used here would have been more expedient.) A consequence of iteratively halving or quartering a source is that the ultimate number of subelements into which the source is divided can change drastically (often by a factor of about 2 or 4) between field points near each other; the calculated pressure at the field point associated with fewer subelements usually has greater error, and this phenomenon produces the characteristic artifacts mentioned above. The implementation of Ocheltree and Frizzell results in less radical differences in the number of subelements into which the source is divided, for field points near each other; consequently the calculated pressure has an error that, though present, does not change dramatically between field points near each other. Like many things in life, the artifact has an up side and a down side. The up side is that the reader can quickly get a sense of the magnitude of the maximum error in the field calculation, *i.e.* the size of the artifact. The down side is aesthetic, namely the results produced here, with artifact clearly visible, may induce a certain level of discomfort, particularly when compared with the artifact-free results of Ocheltree and Frizzell; the reader is advised to rest assured, however, that their lack of artifact does not change the reality that significant error is present in their results.

The pressure fields shown here were obtained using the constraint factor $F = 5$. This value may seem too small to generate accurate results, but there are several reasons why this is in fact possible. First, as observed by Ocheltree and Frizzell, in Equation 4.8 (page 88) there is considerable cancellation of each quadratic term as it is integrated over the rectangular or cylindrical wedge subelement (*i.e.* odd components of $A_{xx}x_i^2 \exp(jkv_{x_i}x_i/d_i)$, $A_{xy}x_iy_i \exp[jk(v_{x_i}x_i + v_{y_i}y_i)/d_i]$, *etc.*, cancel out over the subelement). Second, quadratic terms on the average are only one-third their maximum value for a region centered at the origin, but the constraint equations were based on the maximum value. Lastly, the constraints used in Equations 4.10 and 4.16 are considerably more strict than they need be in order to obtain simpler constraint equations. Specifically, the terms making up the quadratic coefficients (*i.e.* A_{xx}, A_{yy}, and A_{xy} for the rectangular source, and $A_{\theta\theta}$, $A_{\theta y}$, and A_{yy} for the cylindrical wedge source) were indiscriminately summed to generate the constraint equations, whereas in the expressions for the quadratic coefficients the terms were variously positive, negative, and imaginary, so in general they would not sum to as great a magnitude as suggested by the constraint equations.

The linear terms (*i.e.* the $\operatorname{sinc}\xi_1 \operatorname{ginc}\xi_2$ terms in Equations 4.9 and 4.15) are often very small compared to the constant terms (*i.e.* the $\operatorname{sinc}\xi_1 \operatorname{sinc}\xi_2$ terms). Ignoring the linear terms typically doubled error, but ignoring them is not recommended because their inclusion does not greatly increase the computational burden, unless the spatial first derivatives of the source surface normal velocity (*i.e.* u_{n_x}, u_{n_y}, and u_{n_θ}) are computationally expensive to evaluate).

A brief discussion about the validity of the diffraction integral is in order. Strictly speaking, the diffraction integral is rigorously correct only for planar sources (embedded in infinitely rigid plane baffles and radiating into a semi-infinite, homogeneously absorbing medium), and not for curved sources such as cylindrical wedges. Nevertheless there is a rich history of application of the diffraction integral to curved sources, including concave cylindrical wedges [27], convex cylindrical wedges [24], and concave spherical sources [56, 64, 80, 83]. As non-planar sources approach the planar condition, however, the diffraction integral approaches perfect rigor (assuming, again, the infinite rigid plane baffle and semi-infinite, homogeneous medium). O'Neil [80] suggested that when the width of the transducer is large compared to the wavelength, the diffraction integral will be close to correct for modeling curved transducers, at least in the main part of the acoustic beam. Even in the case of planar sources, however, the diffraction integral is not rigorously correct in practice because real planar sources lack the infinite rigid planar baffle and semi-infinite homogeneous medium. Thus in the case of rectangular transducers that are connected to form cylindrical arrays [26, 62], or even planar arrays [95], diffraction integral calculations are not perfectly correct. Despite this shortcoming, many investigators see value in solving the diffraction integral because the theoretical solution is generally felt to approximate the empirical solution fairly well, especially in the main part of the acoustic beam.

A result which illustrates where the application of the diffraction integral to field calculation from non-planar sources can break down comes from the case of the concave radiator, shown in the bottom of Figure 4-11. Specifically, the pressure amplitude goes to zero as the z-axis position approaches the source surface. This result is an artifact that arises due to the fact that as a field point approaches a convex radiator, the area of the radiator that is visible at the field point becomes vanishingly small; in the limit as the field point sits on the source surface, none of the radiator will be visible. (See Section B.3 for further explanation.) As evidenced in Figure 4-11, however, this artifact is only relevant at extreme proximity of the field point to the source surface.

Results were presented for square planar sources as small as 0.5λ (half a wavelength), but with small source sizes the calculation method used herein is not necessarily computationally advantageous over the point or simple source method. Ellis and O'Brien [27] used a source spacing of $\lambda/4$, and Diederich and Hynynen [24] used $\lambda/32$. With the former spacing, computational advantage of the rectangular radiator method is achieved when the source side is about $s = 2\lambda$ or larger (with the constraint factor $F = 5$ and for the calculated field cross-sections); with the latter spacing, computational advantage of the rectangular radiator method is achieved for all source sizes considered. In general, the computational advantage of the rectangular radiator method over the simple source method increases dramatically as the size of the source increases. An additional observation worth making is that the evaluation of the acoustic pressure from a source subelement appears fairly involved for rectangular and cylindrical wedge subsources (Equations 4.9 and 4.15), but in general it is not substantially more computationally involved than the corresponding evaluation from a point or simple source. This is because the sinc ξ and ginc ξ terms in general need not be calculated laboriously as transcendental functions, but instead can usually be accurately and rapidly determined from the first three non-zero terms of their respective Taylor series (see Footnote 1 on page 89).

4.2 Acoustic Modeling of Individual FSUM Transducer

The objective of this section is to produce a parameterized model of the acoustic beams of the individual FSUM transducers, which will facilitate rapid SAR field calculations. Observations concerning acoustic measurements and acoustic simulations will be used to develop a parameterized model. Specifically:

1. Pressure amplitude measurements from a single FSUM transducer will be presented. (Section 4.2.1)
2. Acoustic simulations will be performed using the Rayleigh-Sommerfeld diffraction integral to calculate the pressure amplitude field from a simulated FSUM transducer vibrating in uniform, rectangular paraboloid, and Gaussian profiles. These simulations will be compared with the measured pressure field. (Section 4.2.2)
3. The analytic solution for the pressure field from a Gaussian source will be modified to produce a parametric model of the acoustic beam from the FSUM transducer. This model will be compared with the measured pressure amplitude field. (Section 4.2.3)

The geometry of the FSUM as a whole is described later in Section 4.3.1, but in this section only the geometry of *individual* FSUM transducers are of interest. Each transducer is a $3.3 \times 3.3\,\mathrm{cm}$ square, vibrating at 1 MHz—although not necessarily vibrating uniformly over the entire transducer surface (*i.e.* the vibration phase is uniform over the transducer surface, but the vibration amplitude may not be).

4.2.1 Acoustic Pressure Measurements in Water Bath

Acoustic pressure field measurements were taken to characterize FSUM transducers individually and in combination.[3] Transducers radiated into a degassed water bath, and a hydrophone was used to take pressure measurements. The hydrophone signal was proportional to the acoustic pressure amplitude, and contained no information about phase.

Measured fields are presented for transducer #28, xd_{28}, the most thoroughly characterized FSUM transducer by acoustic pressure measurement. (See Section 4.3.1 for the geometric arrangement of the FSUM transducers.) Pressure measurements were taken in seven transverse (*i.e.* xy-) planes at depths of $z = 9.5$, 4.5, 19.5, 24.5, 29.5, 34.5, and 39.5 cm from transducer #28. Within each plane, measurements were taken in 0.25 cm increments in the x direction, and 0.05 cm increments in the y direction. Figure 4-13 shows the pressure amplitude p_a measurements in these planes (with the exception of the $z = 39.5$ cm plane, due to space considerations in the figures), normalized to the deduced maximum pressure amplitude, p_max.[4]

4.2.2 Acoustic Simulation

Computer simulations of pressure fields from individual FSUM transducers were performed for comparison with the measured field. Simulations numerically solved the Rayleigh-Sommerfeld diffraction integral according to the protocol derived in Section 4.1 with $F = 10$, and simulations varied according to source vibration pattern: uniform, rectangular paraboloid (see Section 4.1.4 on page 93); and Gaussian vibration with Gaussian source width $\sigma_\mathrm{s} = 0.5$ and 1.0 cm, shown in that order in Figures 4-14 – 4-17. Simulations were performed in the same seven transverse planes in which hydrophone measurements were taken, although the grid spacing within the planes was 0.2×0.2 cm (as opposed to the 0.05×0.25 cm of the measured field).

Simulated pressures were normalized so that overall beam power was the same as in the measured pressure field. The acoustic power crossing each transverse plane was calculated by summing the square of the pressure field in the plane (see Section 3.2), weighted by the area of the grid pixel (0.04 cm^2 for simulated fields, 0.0125 cm^2 for measured fields).

---

[3] The experiments detailed in this section were performed and/or supervised by Jørgen Hansen.

[4] The actual pressure to which the measured pressure amplitude p_a data were normalized is not especially important. The specific normalization value used here was obtained from the $p_\mathrm{a}\{z\}$ fit depicted in Figure 4-18 on page 123.

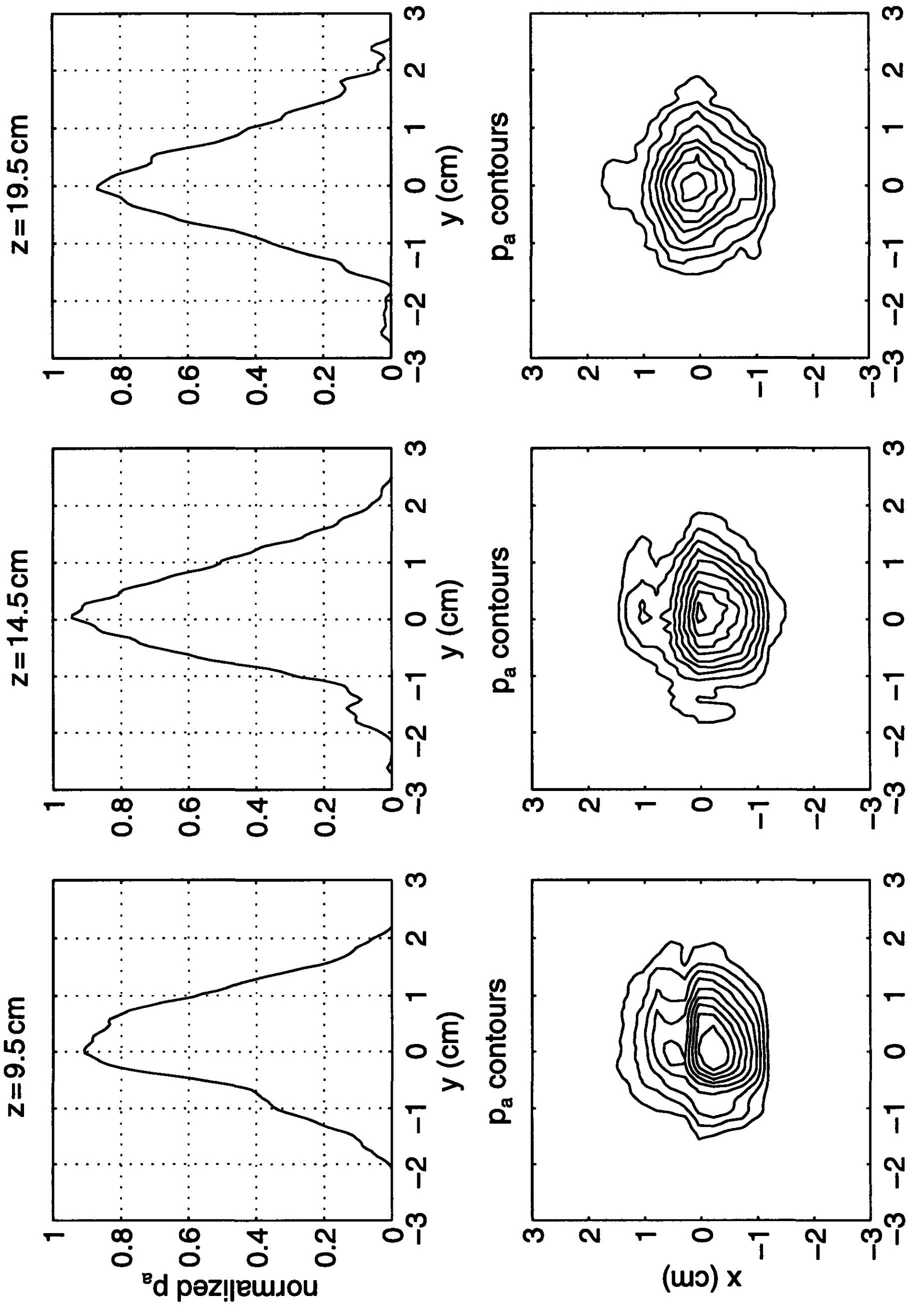

Figure 4-13: Measured pressure amplitude field of FSUM transducer #28, in transverse cross-sections at six depths z. Upper subfigures show normalized pressure amplitude p_a on the y-axis of the cross-sectional plane; lower subfigures show contour plots of p_a at intervals of 10% of the maximum pressure amplitude $p_{\max}$, the maximum pressure amplitude. Part I.

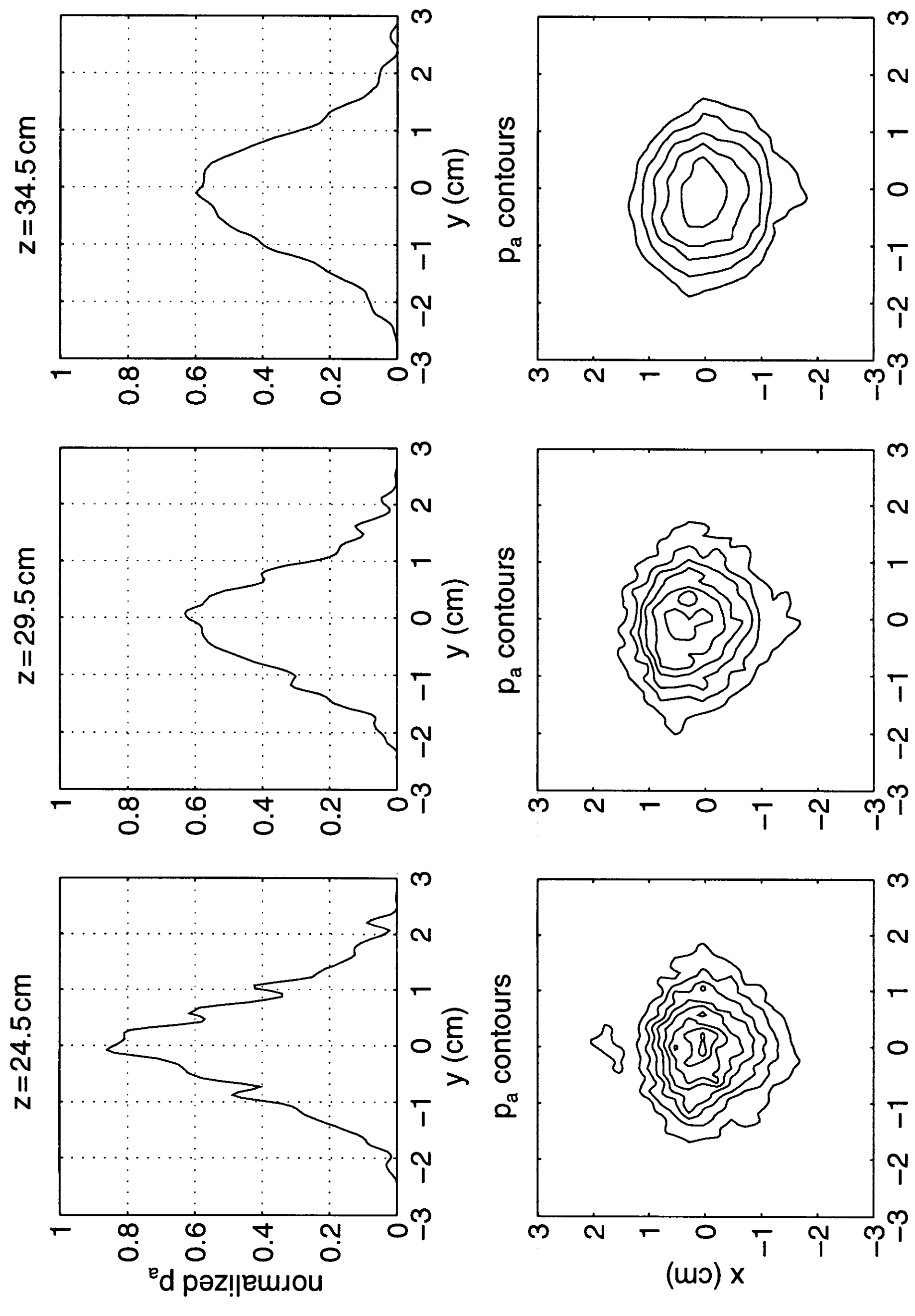

Figure 4-13: Part II.

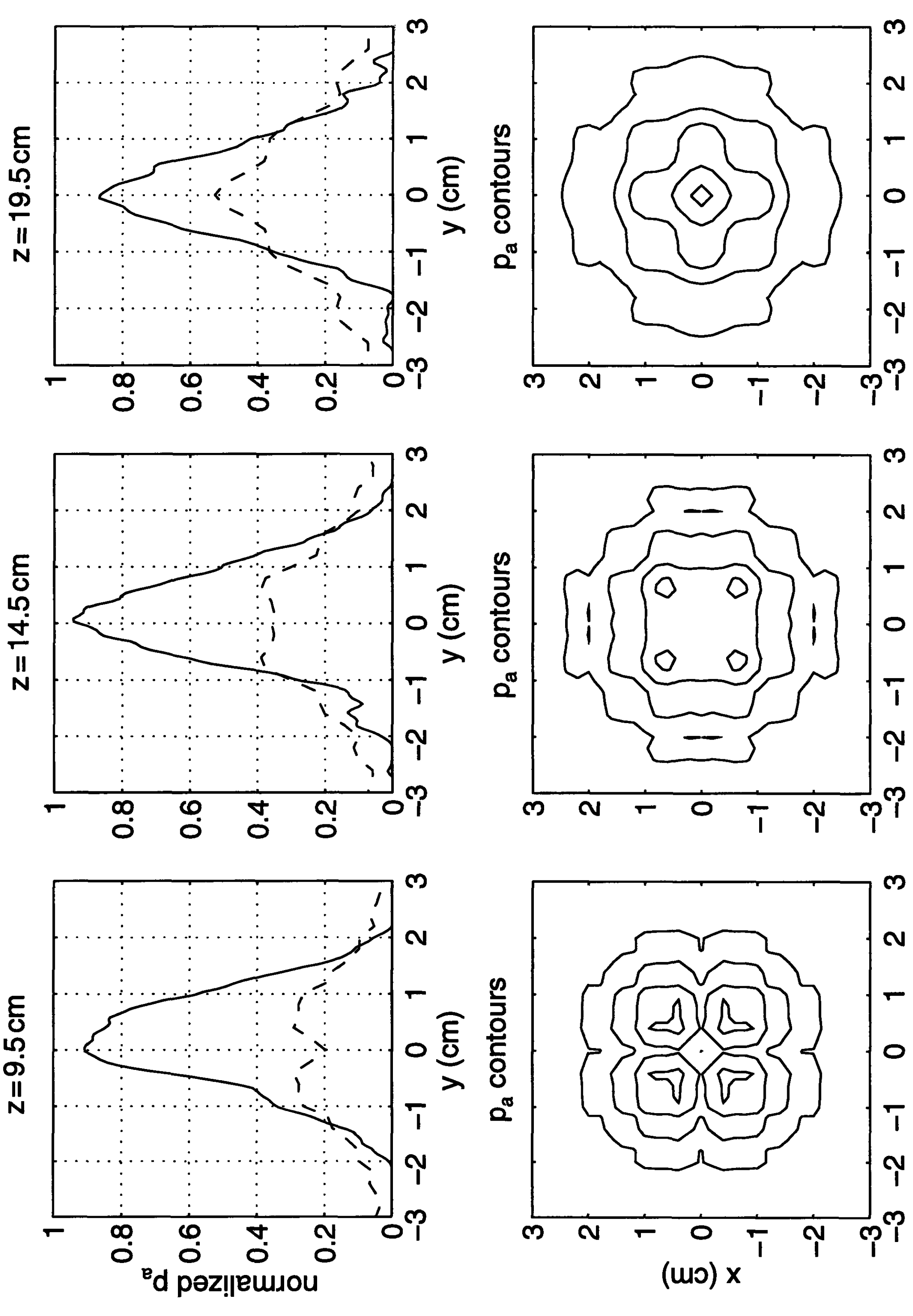

Figure 4-14: Pressure amplitude field of FSUM transducer with *uniform* vibration, simulated by the Rayleigh-Sommerfeld diffraction integral. Field transverse cross-sections are shown at six depths z. Upper subfigures show simulated (dashed lines) and measured (solid lines) normalized pressure amplitude p_a on the y-axis of the cross-sectional plane; lower subfigures show contour plots of simulated p_a at intervals of 10% of p_{max}. Part I.

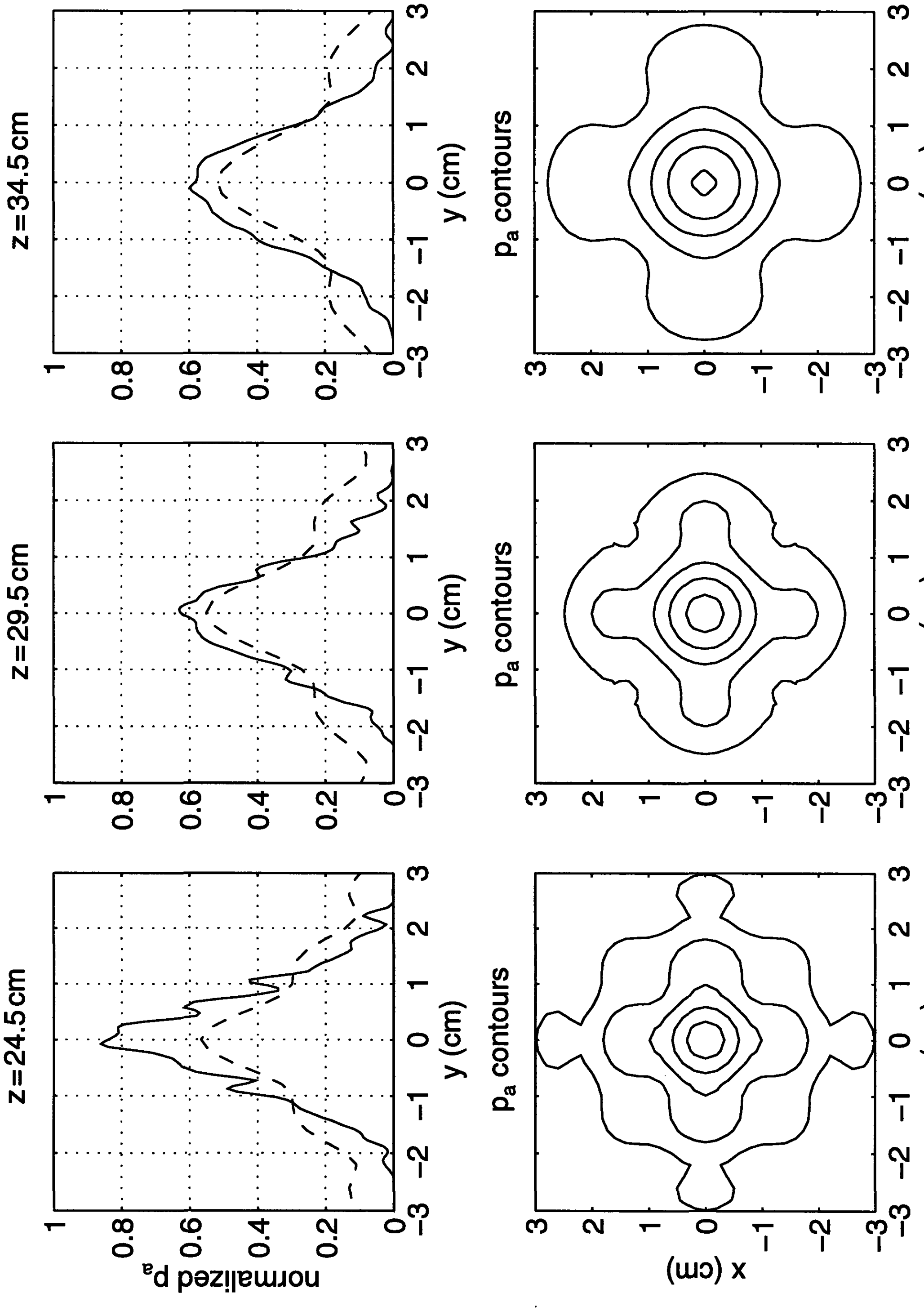

Figure 4-14: Part II.

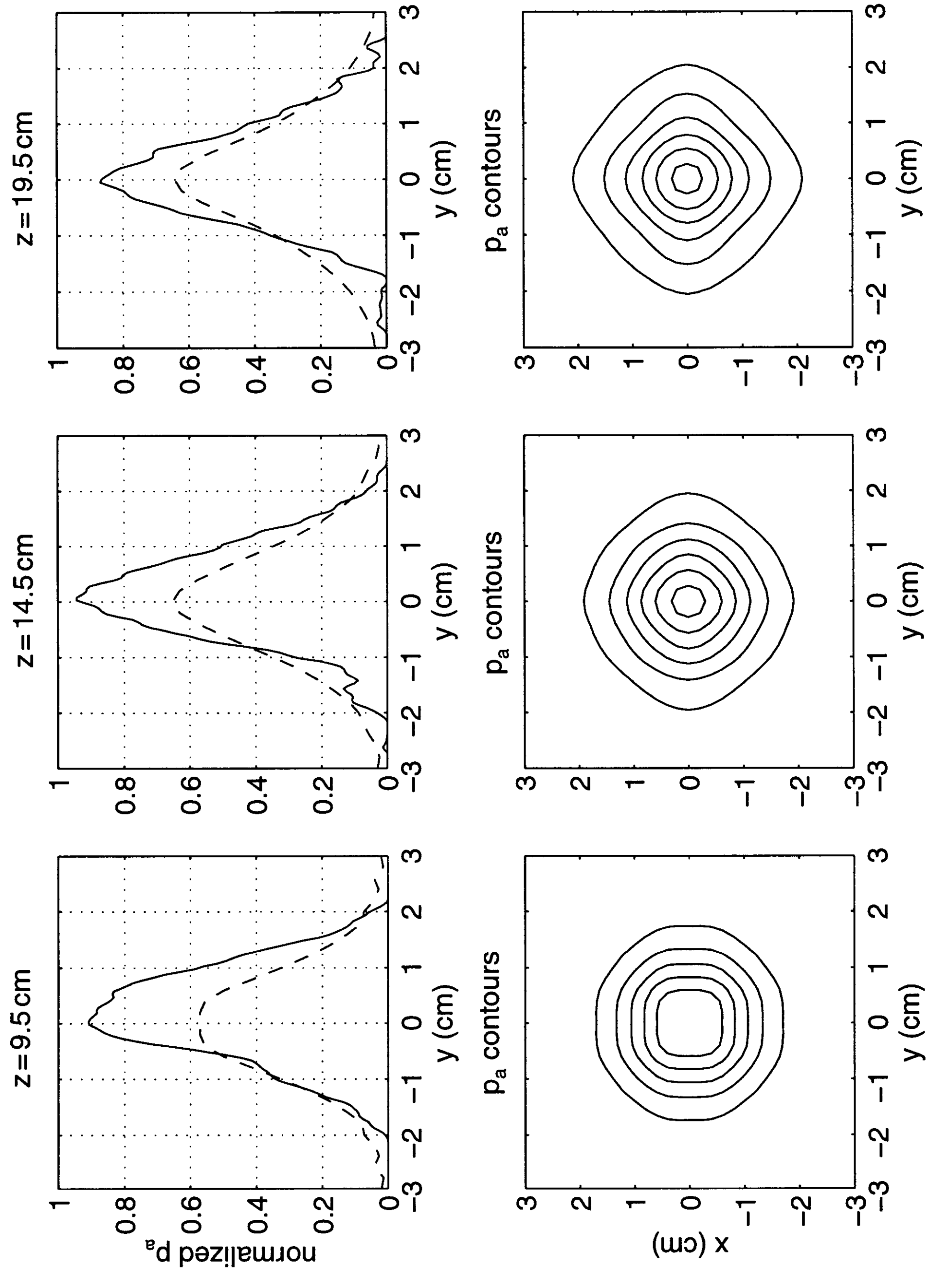

Figure 4-15: Pressure amplitude field of FSUM transducer with *rectangular paraboloid* vibration, simulated by the Rayleigh-Sommerfeld diffraction integral. Field transverse cross-sections are shown at six depths z. Upper subfigures show simulated (dashed lines) and measured (solid lines) normalized pressure amplitude p_a on the y-axis of the cross-sectional plane; lower subfigures show contour plots of simulated p_a at intervals of 10% of $p_{\max}$. Part I.

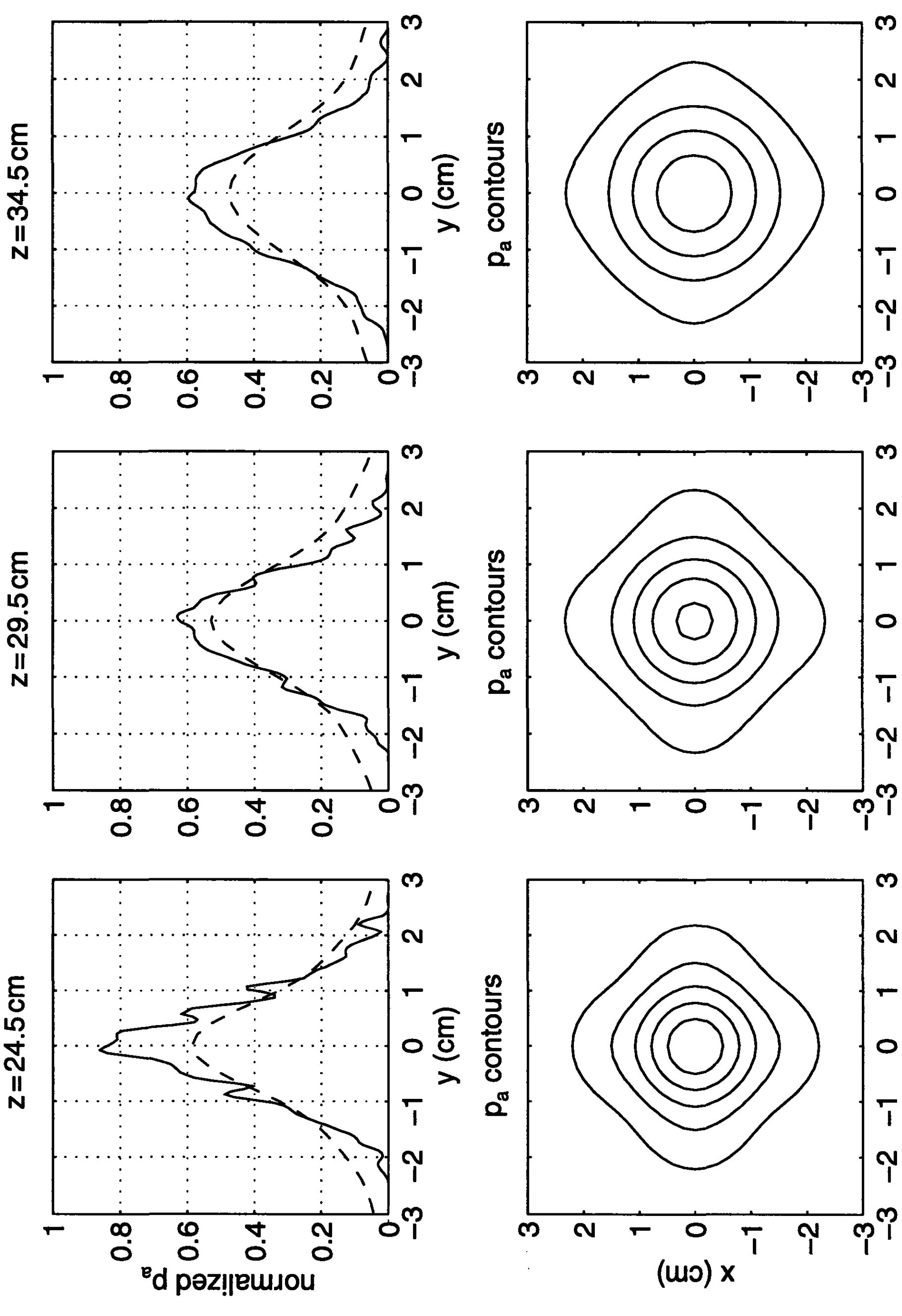

Figure 4-15: Part II.

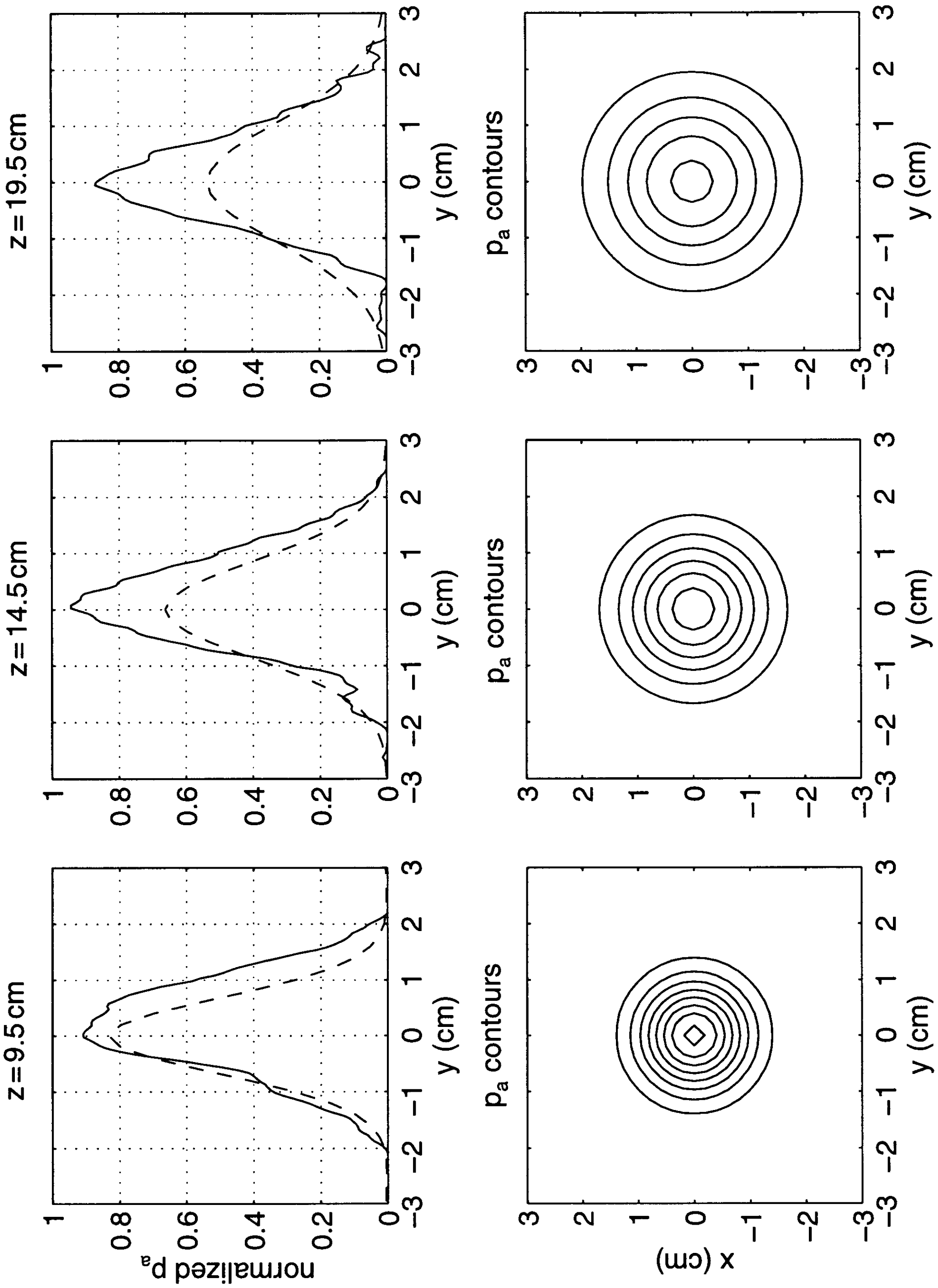

Figure 4-16: Pressure amplitude field of FSUM transducer with *Gaussian* vibration with Gaussian source width $\sigma_s = 0.5\,\mathrm{cm}$, simulated by the Rayleigh-Sommerfeld diffraction integral. Field transverse cross-sections are shown at six depths z. Upper subfigures show simulated (dashed lines) and measured (solid lines) normalized pressure amplitude p_a on the y-axis of the cross-sectional plane; lower subfigures show contour plots of simulated p_a at intervals of 10% of $p_{\max}$. Part I.

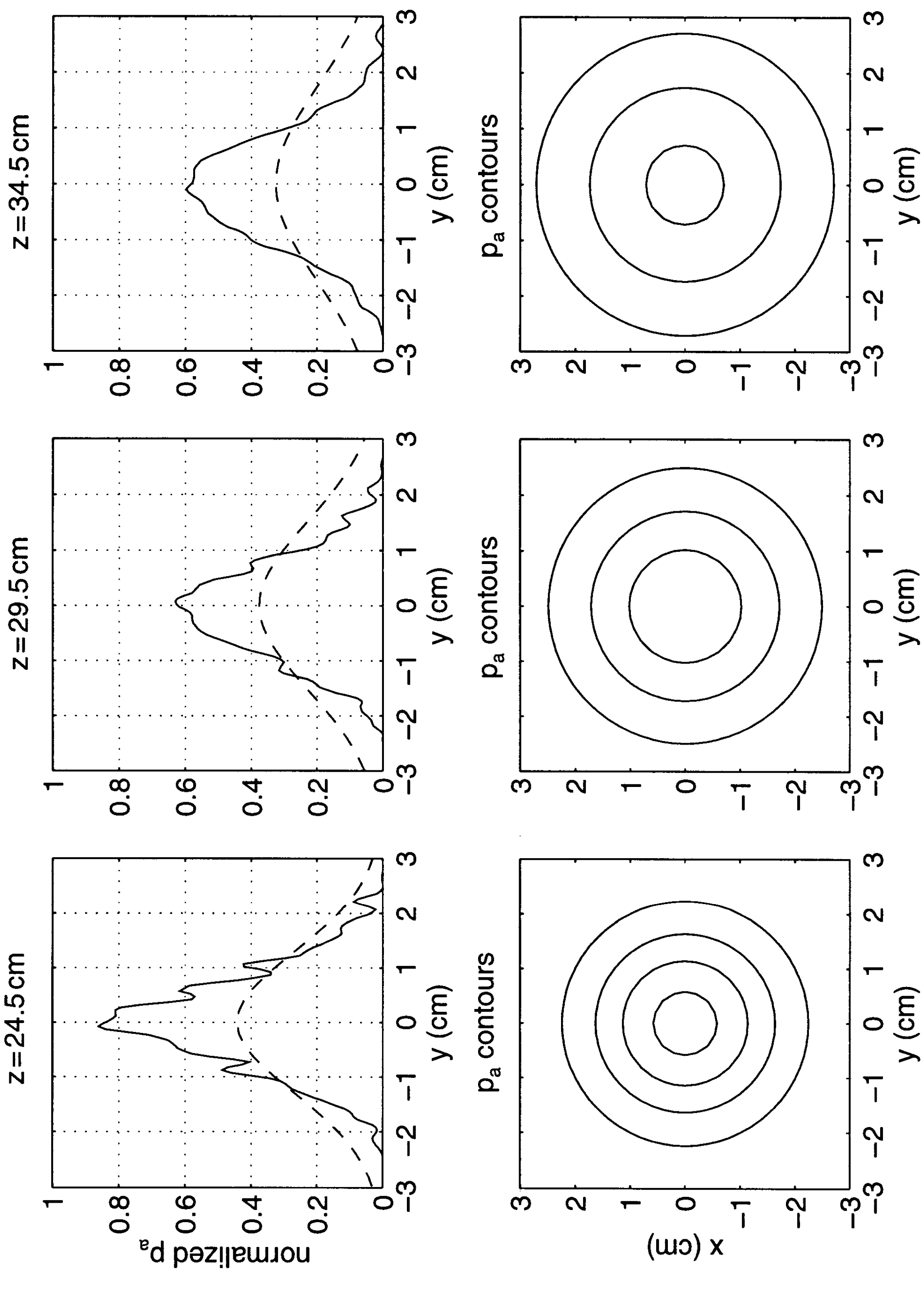

Figure 4-16: Part II.

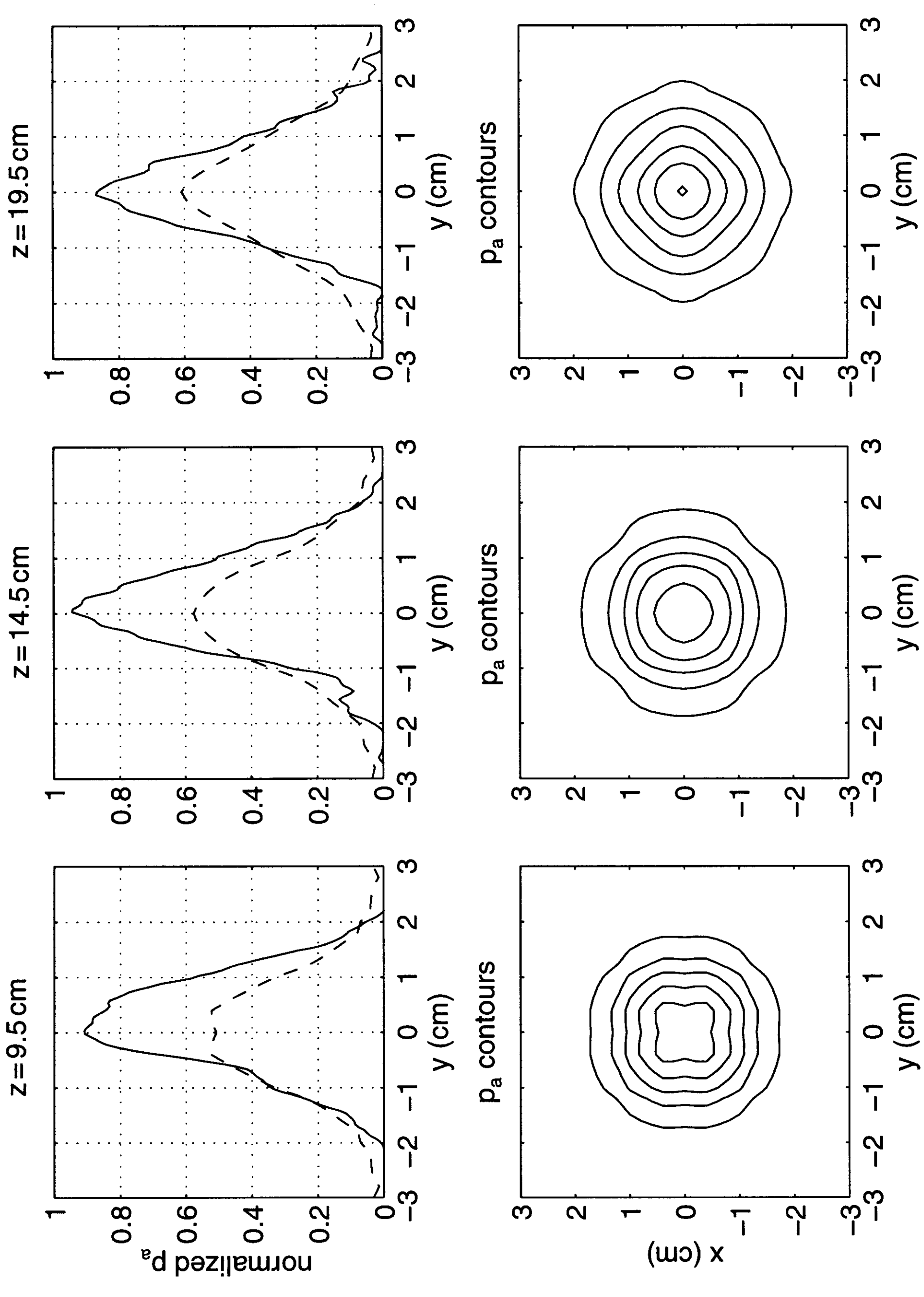

Figure 4-17: Pressure amplitude field of FSUM transducer with *Gaussian* vibration with Gaussian source width $\sigma_{rms} = 1.0\,\text{cm}$, simulated by the Rayleigh-Sommerfeld diffraction integral. Field transverse cross-sections are shown at six depths z. Upper subfigures show simulated (dashed lines) and measured (solid lines) normalized pressure amplitude p_a on the y-axis of the cross-sectional plane; lower subfigures show contour plots of simulated p_a at intervals of 10% of $p_{\max}$. Part I.

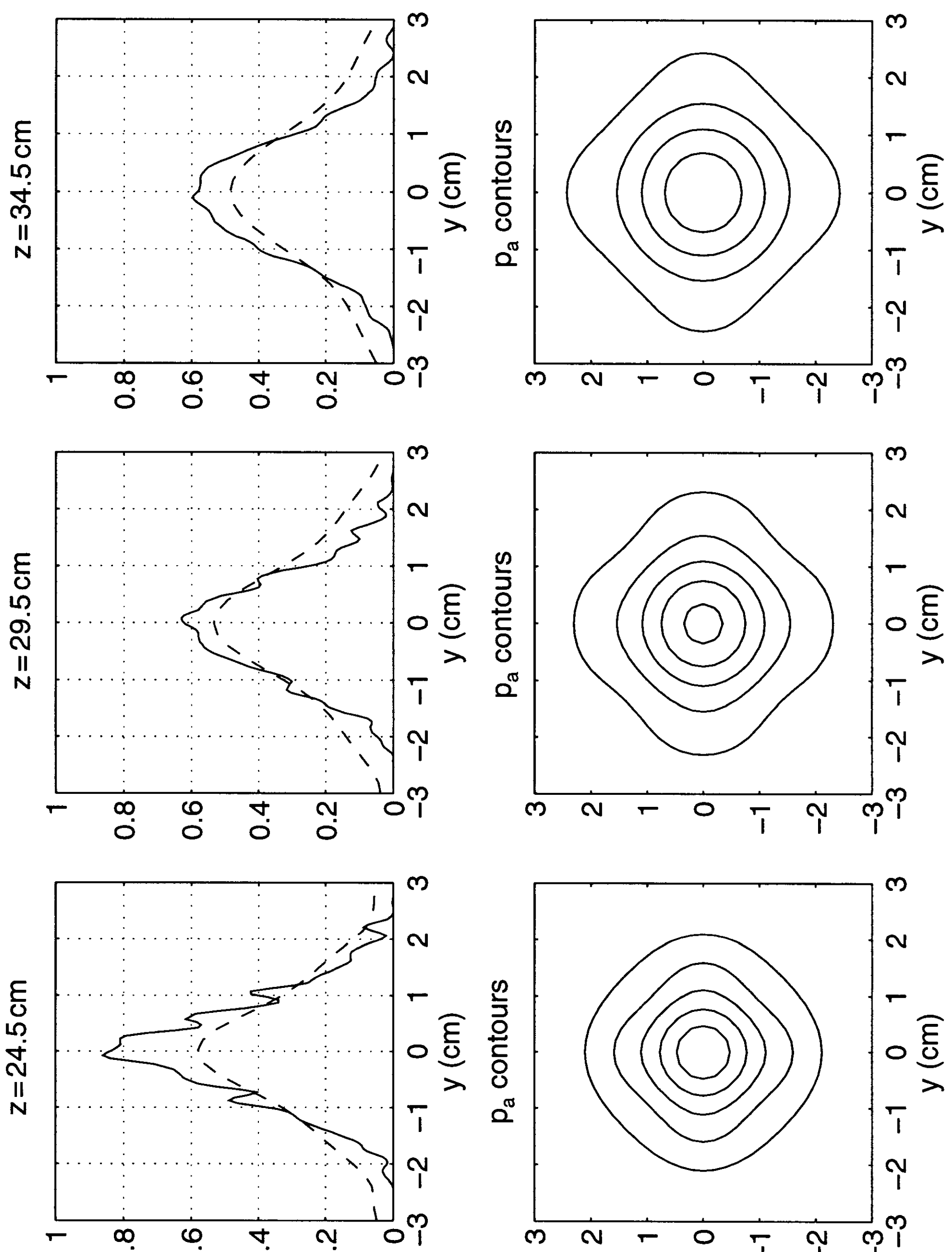

Figure 4-17: Part II.

The simulated field for a uniformly vibrating source (Figure 4-14) is remarkably dissimilar to the measured field (Figure 4-13), particularly in the transverse planes closer to the source. Most obvious are the extreme differences in the peak pressure amplitude p_a within a transverse plane, and the area under the $p_\mathrm{a}\{0, y, z\}$ curves. The reader may question whether the pressure normalization, meant to equate the overall beam power in the simulated and measured cases, was in fact performed correctly. The pressure contour plots show the source of the apparent discrepancy: In the near field the simulated peak pressure and the nominal beam width are rather underrepresented by the pressure curves on the x- and y-axes, $p_\mathrm{a}\{x, 0, z\}$ and $p_\mathrm{a}\{0, y, z\}$. Another important difference between simulated and measured field is that near field extrema are clearly evident in the simulated uniform field, but are essentially absent in the measured field.

The simulated fields for a rectangular paraboloid or Gaussian source vibration pattern enjoy better agreement with the measured field, but there are still shortcomings. The rectangular paraboloid case (Figure 4-15) and the Gaussian case with Gaussian source width $\sigma_\mathrm{s} = 1.0\,\mathrm{cm}$ (Figure 4-17) were remarkably similar. When compared with the measured field, both simulated fields were characterized by beam widths that were slightly too large, and, especially closer to the source, peak pressure amplitudes that were too small. In the case of the Gaussian source with Gaussian source width $\sigma_\mathrm{s} = 0.5\,\mathrm{cm}$ (Figure 4-16), the beam width and peak pressure amplitude matched better to the measured field in transverse planes close to the source, but further from the source the beam width was decidedly too large and the peak pressure amplitude too low. All three of these simulated fields shed the near field extrema present in the uniformly vibrating case.

4.2.3 Parameterization of Acoustic Beam

A parametric model of the acoustic beam from a single FSUM transducer is developed in this section. In this development, it is first observed that the measured transverse cross-sections from the pressure field of a single FSUM transducer presented in Section 4.2.1 have features consistent with the pressure field from a Gaussian acoustic source—although agreement between measured and simulated pressure fields in Section 4.2.2 was not especially good. Then the analytical solution for a Gaussian source (see Section 3.1.8, page 72) is empirically modified to produce a parametric acoustic beam description of an FSUM transducer that agrees well with the pressure measurements. (Parametric acoustic beam models have been consider by others; *e.g.* a parametric acoustic beam model with Gaussian transverse cross-sections in the focal region was investigated by Davis and Lele [21].)

The measured field patterns shown in Figure 4-13 are particularly suggestive of a Gaussian transducer in several ways. Most telling is the apparent lack of near field extrema in the axial pressure field, and in addition the transverse (xy-plane) field cross-sections indicated beam cross-sections with a fair degree of circular symmetry. Nevertheless, simulations of Gaussian transducer vibration performed in Section 4.2.2 did not show exceptionally good agreement with acoustic field measurements. The purpose of this section, then, is to produce a parametric beam model of FSUM transducers which more accurately reflects field measurements.

Within each cross-sectional plane, the measured pressure field from an individual transducer was fit to a Gaussian. Specifically, the parameters p_0, x_0, y_0, and the Gaussian beam width σ_b were fit by least squares (LS) to approximate the measurements by $p_\mathrm{meas}\{x, y, z\} \approx p_0 \,\mathrm{Gauss}\left(\sqrt{(x - x_0)^2 + (y - y_0)^2}, \sigma_\mathrm{b}\right)$, where p_0 and σ_b are the peak pressure and Gaussian beam width of the fitted Gaussian in the cross-sectional plane, and x_0 and y_0 are spatial offsets. Numerical fits were obtained using the fmins function in Matlab 4.1 (The Mathworks, Inc., Natick, MA), which is based on a Simplex search method.

The resulting fit values for p_0 and σ_b were then each fit to the analytical expression for the pressure field for a Gaussian source (see Equation 3.41 on page 73). First, the fitted p_0 values at various depths z were fit for the maximum pressure amplitude p_max and Gaussian source width σ_s by LS to the analytical Gaussian beam equation:

$$p_\mathrm{a}\{0, z\} = p_\mathrm{max}\frac{\sigma_\mathrm{s}}{\sigma_\mathrm{b}'} = \frac{p_\mathrm{max}}{\sqrt{1 + (z/k\sigma_s^2)^2}} \tag{4.18}$$

where $\sigma_\mathrm{b}' \equiv \sigma_\mathrm{s}\sqrt{1 + (z/k\sigma_s^2)^2}$ is the analytical solution for the Gaussian beam width. The result is shown in Figure 4-18. The solid curve indicates with an x the fitted normalized p_0 values at each depth z, and the dashed line is the normalized pressure amplitude curve for the Gaussian beam with the best fit to the x's, given by Gaussian source width $\sigma_\mathrm{s} = 0.81$ cm.

Next, the fitted p_0 values at various depths z were fit for Gaussian source width σ_s by LS to the analytical solution for the Gaussian beam width $\sigma_\mathrm{b}'\{z\} = \sigma_\mathrm{s}\sqrt{1 + (z/k\sigma_s^2)^2}$ (see Equation 3.41).

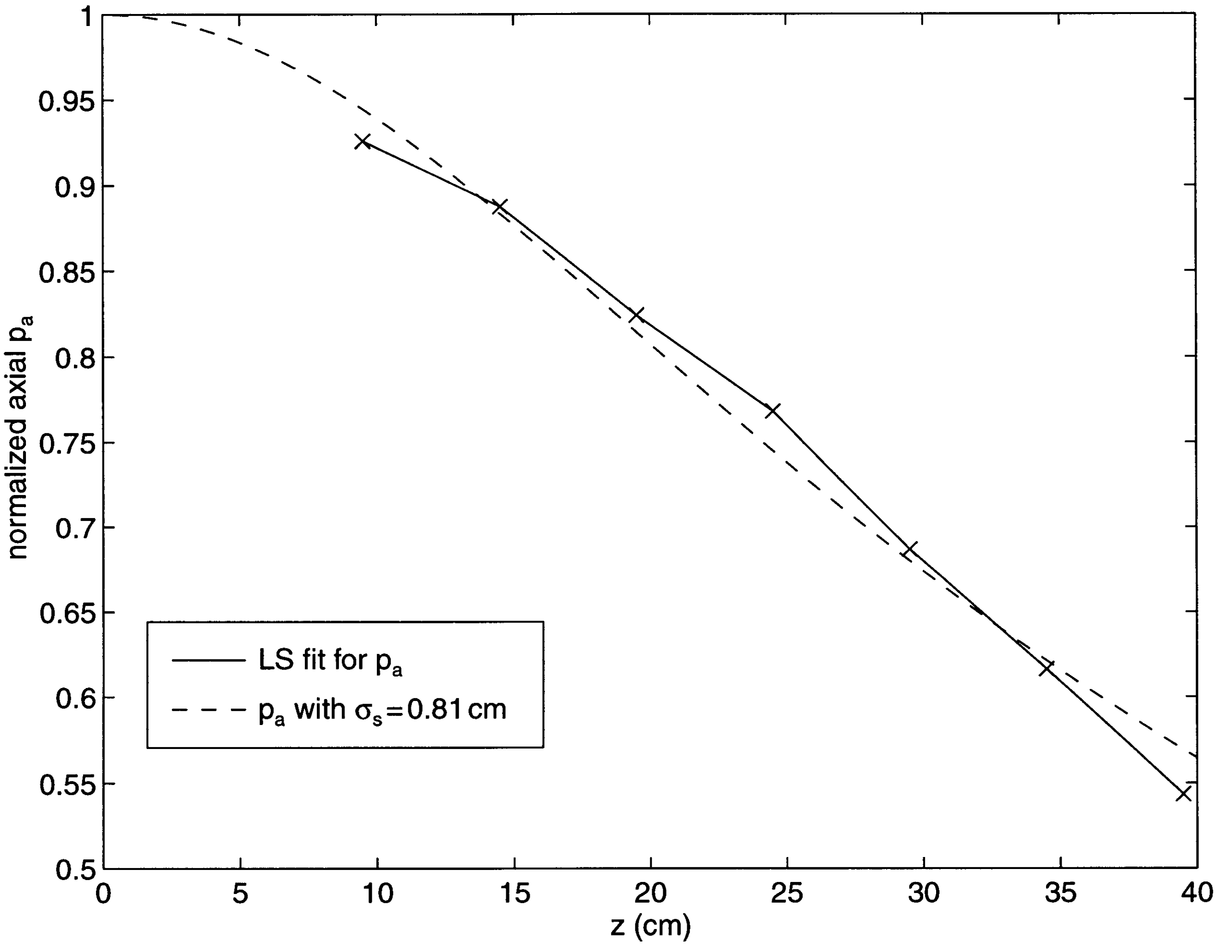

Figure 4-18: Axial pressure amplitude p_a vs. depth z for FSUM transducer #28 measurements and the analytic Gaussian source solution. The solid line with X's indicates the p_a values at the given depths z fitted to measurement. The dashed line corresponds to the analytical Gaussian beam axial pressure solution, $p_\mathrm{a}\{0, z\}$, with Gaussian source width $\sigma_\mathrm{s} = 0.81\,\mathrm{cm}$.

The best fit for the Gaussian source width in this case was $\sigma_{\text{s}} = 0.82\,\text{cm}$ (which is in excellent agreement with the value found in Figure 4-18), and the results are shown in Figure 4-19. The solid curve indicates with an **x** the fitted normalized Gaussian beam width values at each depth z, and the dashed line is the analytical solution for the Gaussian beam width $\sigma'_{\text{b}}\{z\}$, with Gaussian source width $\sigma_{\text{s}} = 0.81\,\text{cm}$. (*N.B.*: $\sigma_{\text{s}} = \sigma'_{\text{b}}\{0\}$.) At first glance, the dashed curve looks as if it could not possibly be the best fit for Gaussian source width, because it resides entirely above the solid curve connecting the fitted values of the Gaussian beam width. Dotted lines corresponding to the analytic solution for the Gaussian beam width curves for 75% and 125% of the deduced Gaussian source width (0.61 and 1.02 cm) give insight into how this is possible: a smaller Gaussian source width σ_{s} produces smaller σ'_{b} for small values of z, but larger σ'_{b} at large values of z.

There is good agreement between the fit values of p_0 and the axial pressure amplitude $p_{\text{a}}\{0, z\}$ curve based on Gaussian source width $\sigma_{\text{s}} = 0.81$ cm in Figure 4-18, but the same cannot be said of the agreement between the fit values of the Gaussian beam width and the analytical solution for the Gaussian beam width based on based on $\sigma_{\text{s}} = 0.82\,\text{cm}$ in Figure 4-19. The Gaussian source pressure equation (Equation 3.41) can be modified (for *empirical* reasons, not theoretical ones) to:

$$p_{\text{a}}\{r, z\} = p_{\text{max}} \exp\left(\frac{-r^2}{2\sigma''^{2}_{\text{b}}}\right) \frac{\sigma_{\text{s}}}{\sigma'_{\text{b}}} e^{-\alpha z} = p_{\text{max}} \exp\left(\frac{-r^2}{2\sigma''^{2}_{\text{b}}}\right) \frac{e^{-\alpha z}}{\sqrt{1 + (z/k\sigma_{\text{s}}^2)^2}} \tag{4.19}$$

where the *modified* Gaussian beam width $\sigma''_{\text{b}}\{z\} = f_1 \sigma'_{\text{b}}\{f_2 z\} = f_1 \sigma_{\text{s}} \sqrt{1 + (f_2 z/k\sigma_{\text{s}}^2)^2}$, and f_1 and f_2 are fudge factors. LS fitting of the modified Gaussian beam width σ''_{b} to the **x**'s in Figure 4-19, and using Gaussian source width $\sigma_{\text{s}} = 0.81\,\text{cm}$, produced the values $f_1 = 0.82$ and $f_2 = 0.58$; this $\sigma''_{\text{b}}\{z\}$ curve is indicated by the dotted line in Figure 4-20. In addition, the curves for the fitted Gaussian beam widths σ_{b} (**x**'s) and the analytical solution for the Gaussian beam width $\sigma'_{\text{b}}\{z\}$ for $\sigma_{\text{s}} = 0.82\,\text{cm}$ that were shown in Figure 4-20 are shown again.

Figure 4-21 shows how this modified Gaussian pressure amplitude solution compares with the acoustic measurements of transducer #28. Predictably, agreement is excellent—predictably, because obtaining strong agreement was the motivation for modifying the *analytical* Gaussian beam width σ'_{b} to the *modified* Gaussian beam width σ''_{b} in the exponential term of Equation 4.19. This modification was not justified on theoretical grounds, but it was clear from

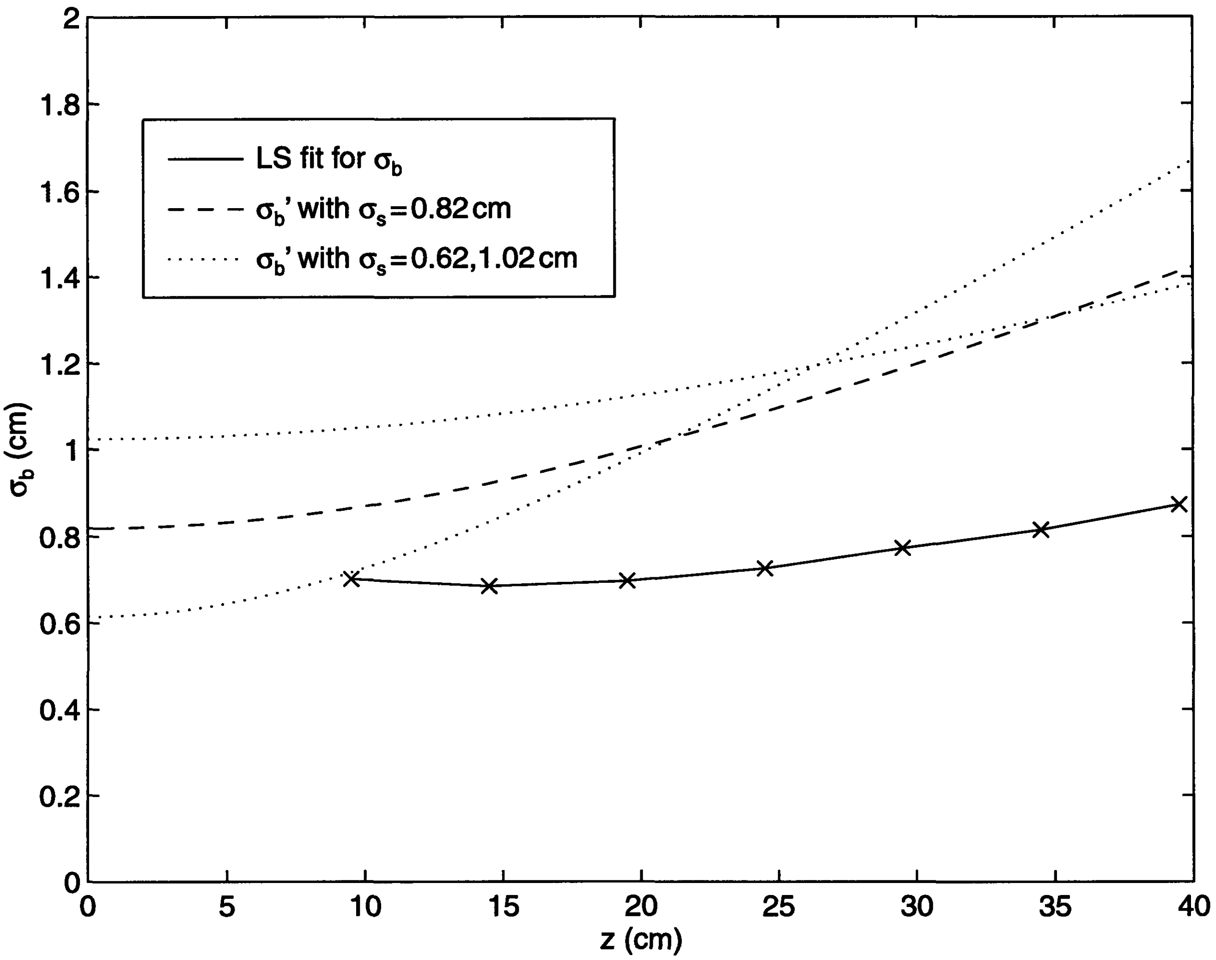

Figure 4-19: Gaussian beam width vs. depth z for FSUM transducer #28 and the *analytic* Gaussian source solution. The solid line with X's indicates the Gaussian beam width σ_b values at the given depths z fitted to measurement. The dashed line corresponds to the analytical solution for the Gaussian beam width $\sigma'_b\{z\}$ for Gaussian source width $\sigma_s = 0.82\,\text{cm}$, and the dotted lines for $\sigma_s = 0.61$ and $1.02\,\text{cm}$.

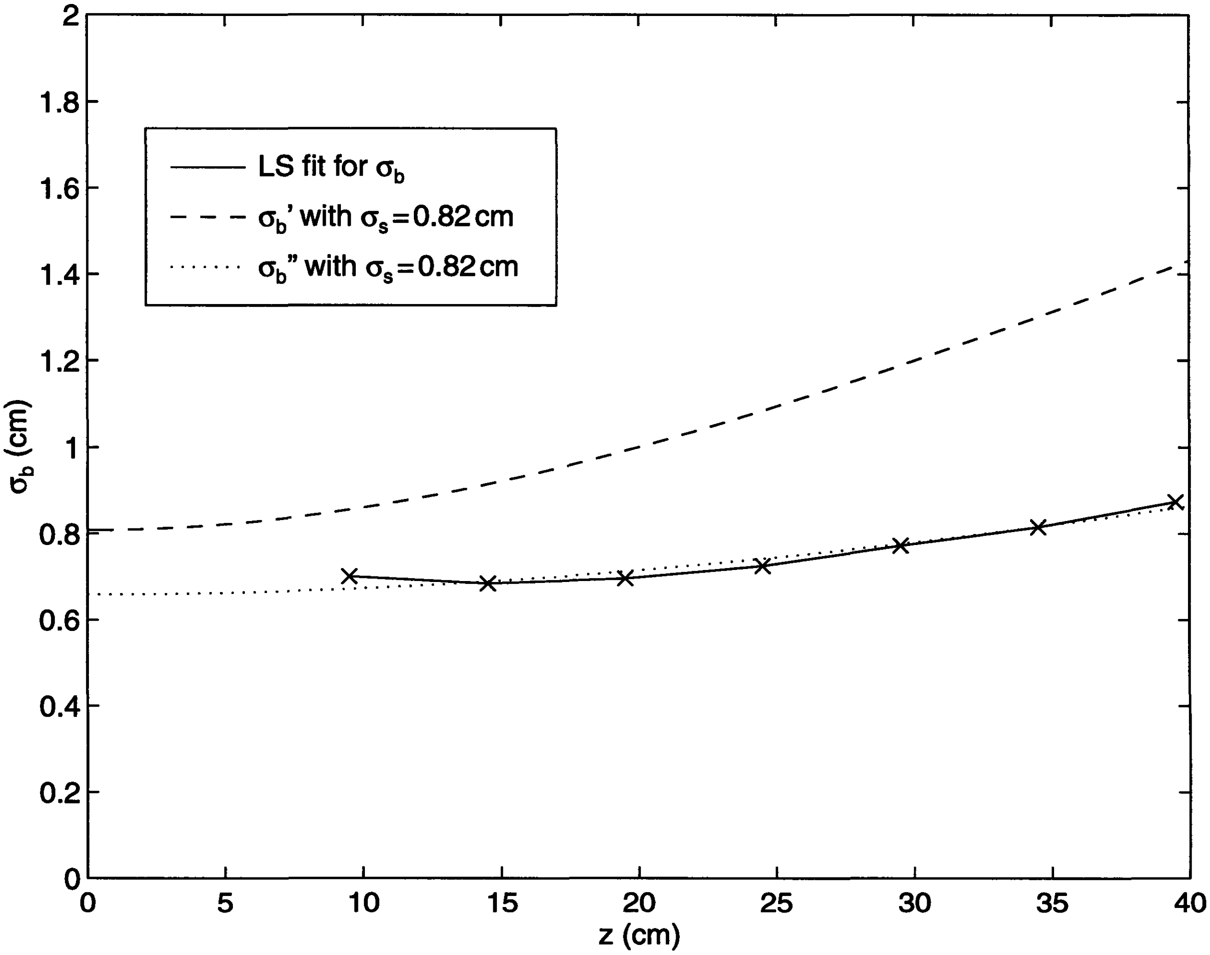

Figure 4-20: Gaussian beam width vs. depth z for FSUM transducer #28 and the *modified* Gaussian source solution. The solid line with x's indicates the Gaussian beam width σ_b values at the given depths z fitted to measurement. The dotted line corresponds to the modified solution for the Gaussian beam width $\sigma_b''\{z\}$ for Gaussian source width $\sigma_s = 0.82\,\text{cm}$. As in Figure 4-19, the dashed line corresponds to the analytical solution for the Gaussian beam width $\sigma_b'\{z\}$ with $\sigma_s = 0.82\,\text{cm}$.

Figures 4-14 – 4-17 that restricting pressure amplitude field characterization to solution of the Rayleigh-Sommerfeld diffraction integral would not provide especially good agreement with the measured field.

The errors between the analytical Gaussian beam (Equation 3.41) and the measured pressure field were calculated, as were the errors between the modified Gaussian beam (Equation 4.19) and the measured pressure amplitude field. The specific simulation parameters were: a Gaussian source width $\sigma_s = 0.81$ cm for both Gaussian beam models, and $f_1 = 0.82$ and $f_2 = 0.58$ for the modified Gaussian description. Pressure amplitude was normalized to $p_{\max} = 1$, and RMS and maximum error were calculated within each transverse plane, over non-zero measured points; and also for all seven transverse planes together, over non-zero measured points. Figure 4-22 indicates the errors calculated for all seven transverse planes; the respective RMS and maximum error over all non-zero measured points were .08 and .43 for the analytical Gaussian beam, and .05 and .38 for the modified Gaussian beam. These errors are perhaps misleadingly large, however, as illustrated in the upper subfigures (pressure amplitude p_a vs. transverse distance y) of Figure 4-21. In this figure (particularly in the transverse planes corresponding to $z = 9.5$ cm and $z = 14.5$ cm), small positional errors of the beam can produce large errors in pressure amplitude because of the steep radial gradient of the beam pressure.

There are several possible explanations for the discrepancy between pressure amplitude fields simulated using the diffraction integral and the measured pressure amplitude field. The non-planar geometry of the FSUM applicator as a whole, and the concomitant acoustic reflections of waves from one transducer off other transducers or the housing of the applicator head, is a likely contributor to the discrepancy, and could conceivably cause the acoustic beam narrowing (compared with simulations) observed in the measurements. Explaining discrepancies between simulated and measured fields is probably not a terribly useful exercise, however—particularly for a device with such dramatic design and construction idiosyncrasies as the FSUM. As suggested by Diederich and Hynynen [24], the Rayleigh-Sommerfeld diffraction integral is appropriate for theoretical studies concerning ultrasound fields, but of course acoustic measurements show the real behavior of the acoustic source. Thus the modified parametric beam model given in Equation 4.19 is an eminently reasonable description of the acoustic beam from transducer #28.

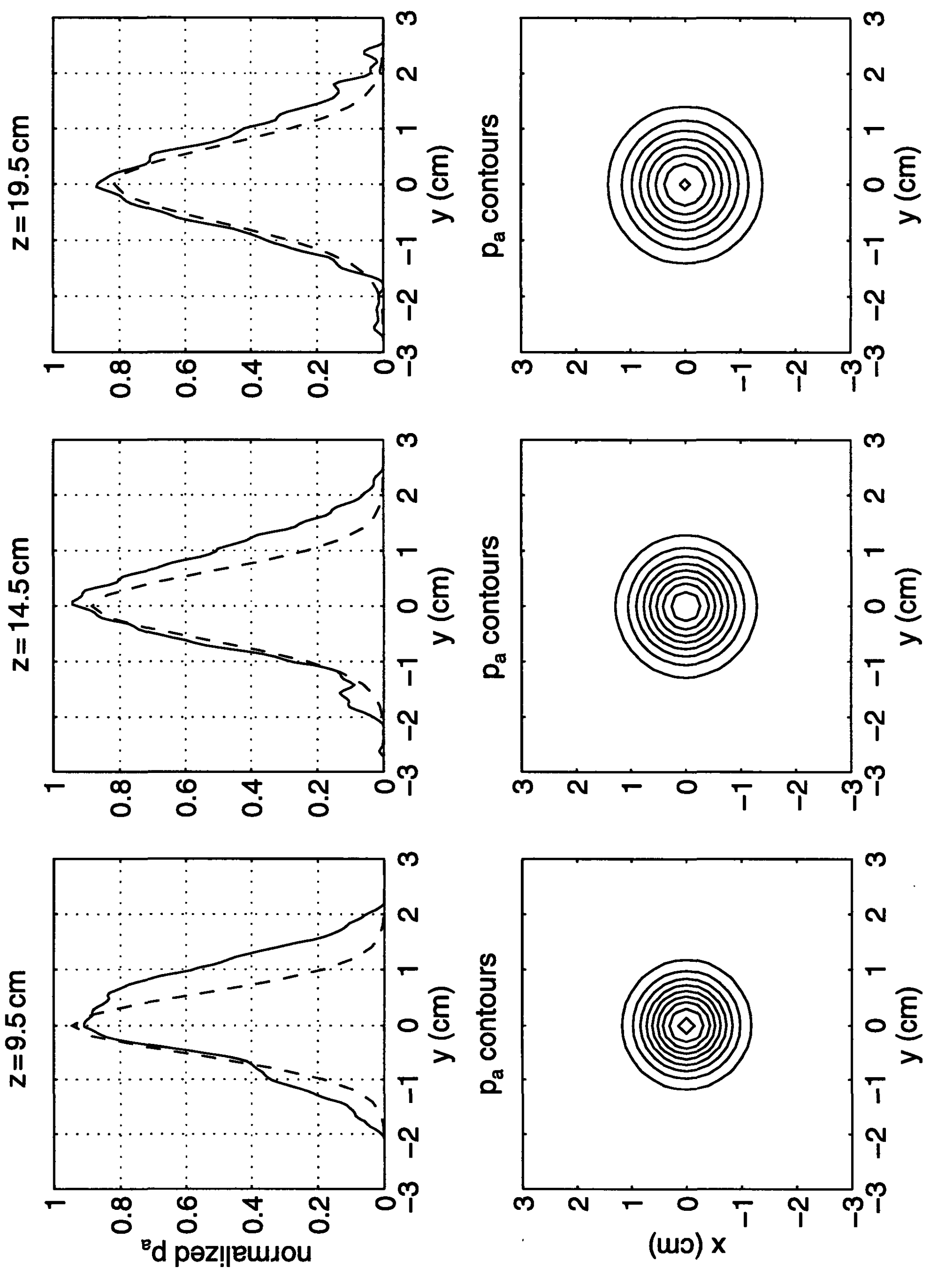

Figure 4-21: Pressure amplitude field of modified Gaussian parametric model. Field transverse cross-sections are shown at six depths z. Upper subfigures show parametric simulated (dashed lines) and measured (solid lines) normalized pressure amplitude p_a on the y-axis of the cross-sectional plane; lower subfigures show contour plots of the parametric model p_a at intervals of 10% of p_{max}. Part I.

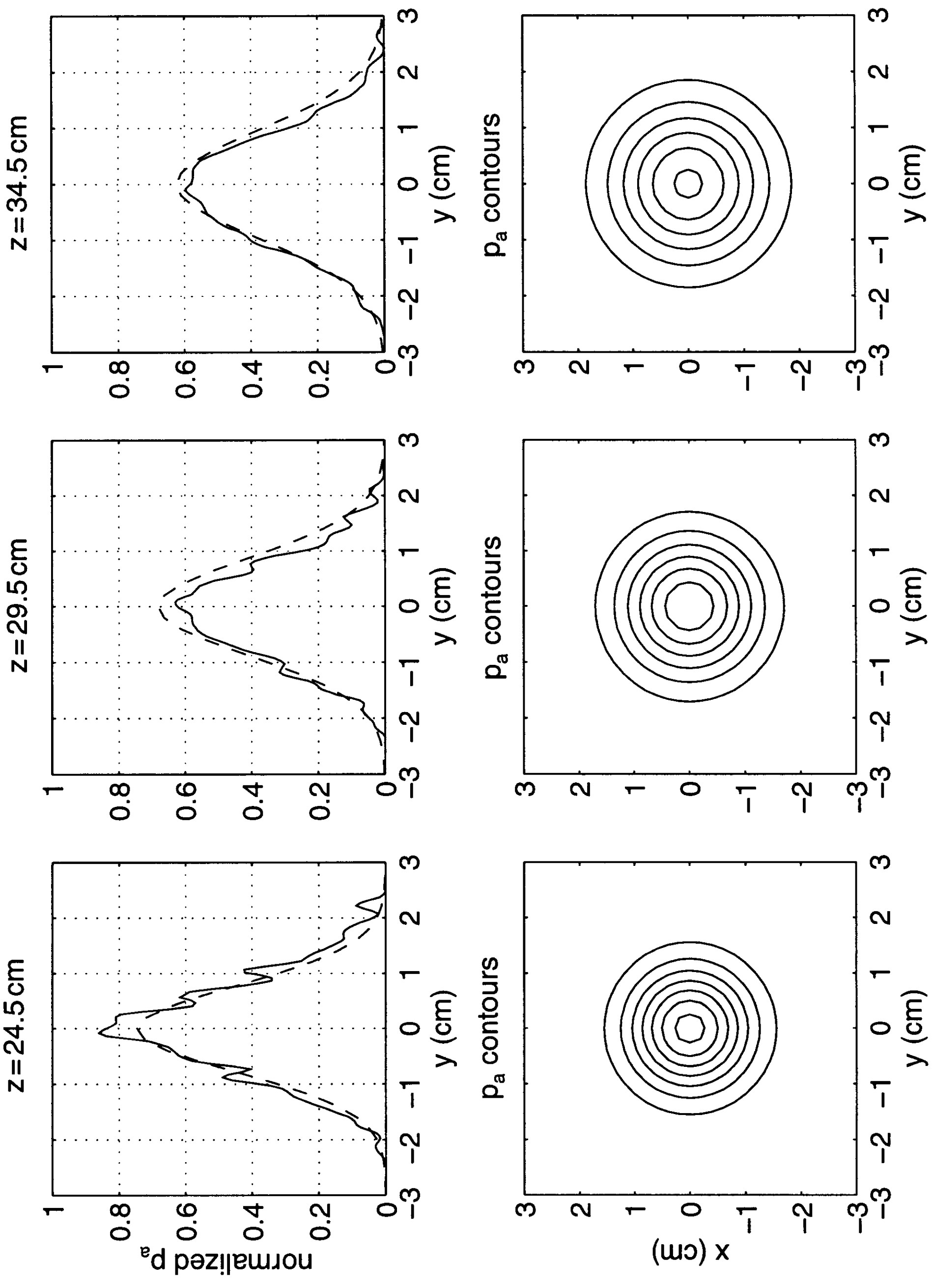

Figure 4-21: Part II.

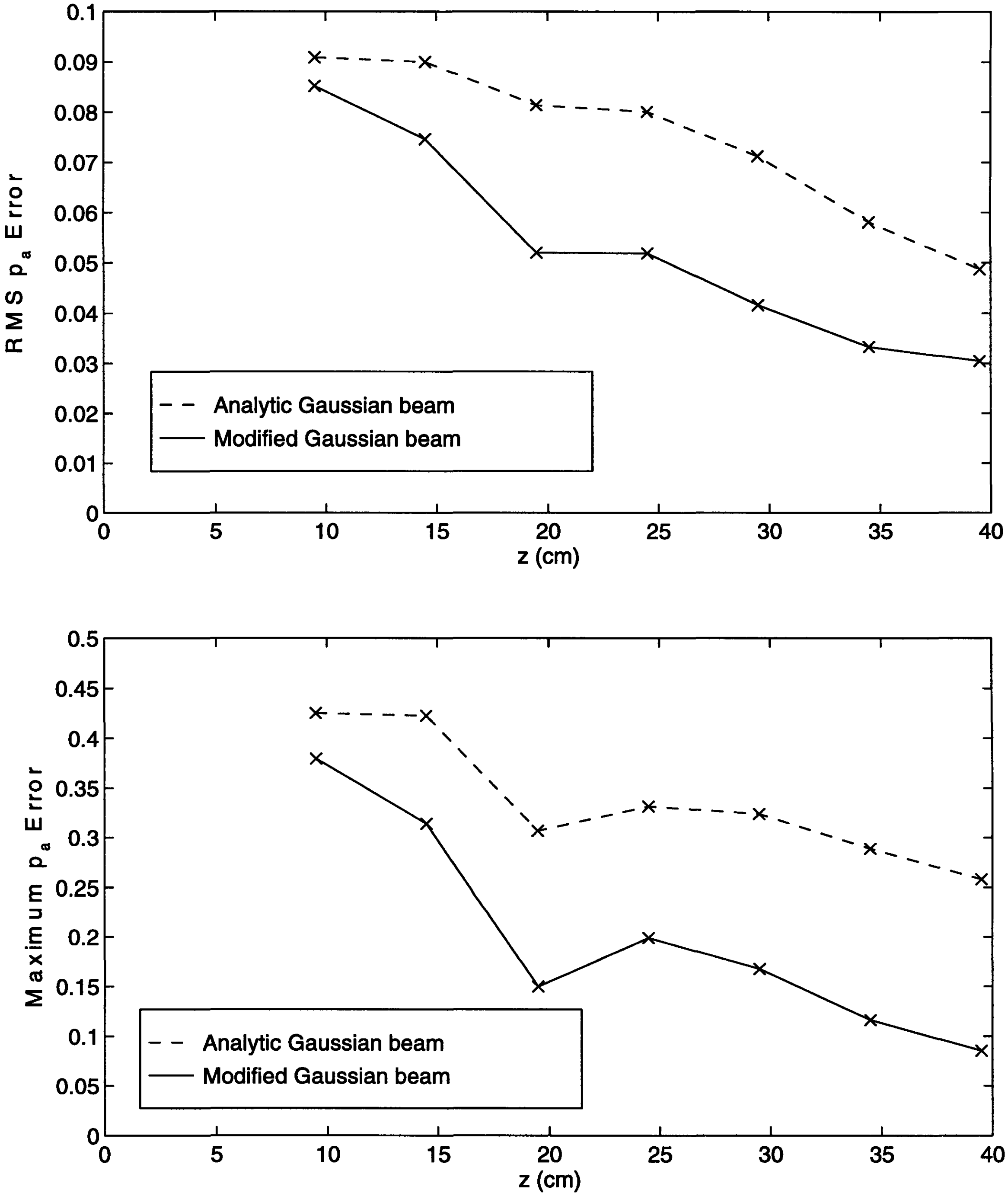

Figure 4-22: RMS and maximum normalized pressure amplitude p_a error for the analytic Gaussian beam model and the modified Gaussian beam model. Errors, marked by x's, were calculated in each of the seven transverse planes at various depths z.

Measurements were also made of beams from other FSUM transducers, and, though the fields were not identical, they exhibited much of the same behavior seen in the beam from transducer #28; in particular, the lack of near field extrema was universally observed. A total of 98 beam cross-sections were measured for 36 different transducers. (Measurements were made on planar grids with 0.15 cm increments in the x direction and 0.05 cm increments in the y direction.) 76 of these beam cross-sections showed clear Gaussian patterns, and 22 exhibited bizarre forms—even when other beam cross-sections of the same transducer were Gaussian. Thus the 76 Gaussian beam cross-sections were fit by LS to $p_{\mathrm{meas}}\{x, y\} = p_0 \, \mathrm{Gauss}(r\{x, y\}, \sigma_{\mathrm{b}})$, where p_0 and the Gaussian beam width σ_{b} are fitting parameters. (The other 22 beam cross-sections were ignored.) The planes of the beam cross-sections contained the nominal focal point of the FSUM, but the cross-sections were in general oblique to the beam. This obliqueness resulted in Gaussian beam cross-sections that were elliptical instead of circular, so the cylindrical coordinate $r\{x, y\}$ was itself a function of five fitting parameters: x_0 and y_0, the x and y offsets; r_{min} and r_{max}, the respective minor and major semiaxes of the ellipse (*N.B.*: $r_{\mathrm{min}} = \sigma_{\mathrm{b}}$); and θ, the angle of rotation of the ellipse in the cross-section. Specifically, $r\{x, y\}^2/r_{\mathrm{min}}^2 = x'^2/r_{\mathrm{min}}^2 + y'^2/r_{\mathrm{max}}^2$, where (x', y') is the 2-D point $(x - x_0, y - y_0)$ rotated through the angle θ. The mean and standard deviation of the fitted Gaussian beam widths for the 76 Gaussian beams was 0.77 ± 0.05 cm, with a range from 0.66 to 0.90 cm. (See Table C.2 in Appendix C for specific transducer Gaussian beam width values.)

Given the available acoustic measurements for the various FSUM transducers, and the relative constancy of the modified Gaussian beam width curve in the region of interest ($z \leq 30$ cm) in Figures 4-20 and 4-21 for transducer #28, it seems expedient to approximate the Gaussian beam width as constant along the axial region of interest (*i.e.* near the focal plane, at a beam depth equal to the radius of curvature of the FSUM device, 23.8 cm). This results in the beam parameterization:

$$p_{\mathrm{a}}\{r, z\} = p_{\mathrm{max}} \exp\left(\frac{-r^2}{2\sigma_{\mathrm{b}}^2}\right) \frac{e^{-\alpha z}}{\sqrt{1 + (z/k\sigma_{\mathrm{s}}^2)^2}} \tag{4.20}$$

where σ_{b} is the fit value of the Gaussian beam width for a specific transducer, or 0.77 cm if no fit exists for the transducer; and the Gaussian source width $\sigma_{\mathrm{s}} = 0.81$ cm, the fit value for transducer #28. Phase issues associated with this parameterization will be discussed in the next section.

4.3 Acoustic Modeling of Multiple FSUM Transducers

In this section the transition is made from modeling the acoustic field of a single transducer excited by itself to modeling multiple transducers excited simultaneously. The transducers of the FSUM are excited coherently, *i.e.* at the same frequency (1 MHz) and in phase with each other. Thus although the device is not a phased array, there are nevertheless constructive and destructive interference patterns that are important to capture in the acoustic model. The approach will be:

1. Pressure amplitude measurements will be presented from a transducer excitation pattern corresponding to multiple, simultaneously excited FSUM transducers. (Section 4.3.3)
2. The modified Gaussian parametric model for pressure amplitude field will be used with several intensity and pressure superposition schemes to determine which scheme most accurately models the observed measurements. (Section 4.3.4)

4.3.1 FSUM Geometry

The FSUM comprises 56 square transducers placed on the inside of a subsection of a spherical shell. The transducers are 3.3 cm on a side, and they subtend a nominal 9° of arc in the directions of their heights and widths. The coordinates of the corners of the transducers were obtained from the CAD description of the FSUM. These design coordinates were given to an accuracy of 10^{-3} cm, in the FSUM reference frame, although the accuracy of the FSUM construction understandably fell considerably short of this.

Figure 4-23 schematizes the FSUM and its canonical coordinate system. (A more detailed schematic of the device can be found in Figure 5-2 on page 176.) The radiating surfaces form a nominal spherical shell of radius 23.8 cm, and dashed lines in the cross-sectional yz-plane in Figure 4-23A indicate the central axes of the ultrasound beams emanating from the transducer surfaces, and how the beams focus at the center of the sphere. The transducers radiate in the $+z$ direction, so Figure 4-23B is facing the *back* (non-radiating) side of the transducers. In addition, the transducers in Figure 4-23B are labeled according to their respective identification numbers, 0–55.

To determine more accurately the real orientations of the individual FSUM transducers, indirect, qualitative pressure measurements were taken in the focal plane ($z = 0$ cm) for all

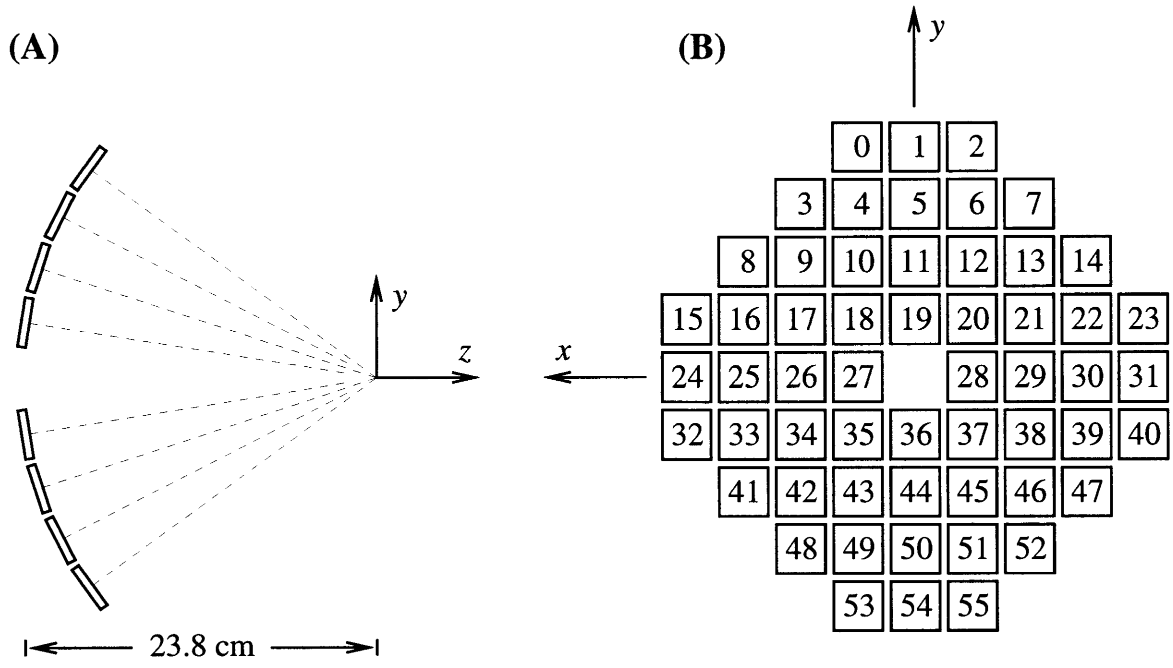

Figure 4-23: Schematic of the FSUM showing the geometric arrangement of its 56 transducers, in the FSUM coordinate system.

56 transducers, one at a time. Specifically, a 1 cm sheet of superflap (an ultrasound absorber) and a thin, temperature-sensitive sheet of liquid crystal were sandwiched between transparent Plexiglas sheets, and placed in a water bath with the liquid crystal sheet in the (designed) focal plane of the FSUM. Transducers were excited individually, causing heating of the superflap and coloration of the liquid crystal. The location of the coloration was determined using a grid drawn on the Plexiglas.

Given perfect device construction, it would be expected that peak pressures in this plane would be observed at $(0, 0, 0)$ cm; however, measurements indicated peak pressures in the focal plane occurred at $(x_i, y_i, 0)$ cm, where i corresponds with the xd_i, $0 \leq i < 56$ (and in general $x_i, y_i \neq 0\,\text{cm}$). To modify the geometric description of the device to account for these offsets, new transducer coordinates were obtained by rotating the original coordinates about the center of (the radiating surface of) the transducers so that the beam would intersect $(x_i, y_i, 0)$ cm instead of $(0, 0, 0)$ cm. Thus the coordinates of the centers of the transducers were unchanged, but the coordinates of the corners were slightly altered. See Section B.4 for details.

4.3.2 FSUM Transducer Power Characteristics

Individual FSUM transducers could receive up to a nominal 35 W of electrical power. Transducer efficiency, the ratio of emitted acoustic power to electric power, ranged from about 0 to 75%, depending on the transducer. Variations in this efficiency were mainly due to differences in transducer natural frequency, differences in coupling between the piezoelectric transducers and their backing, and in some cases poor electrical connection of the transducers. Table C.2 in Appendix C tabulates the relative acoustic pressures of the transducers; the relative maximum power for transducers can be calculated by squaring the relative pressures.

The software that drives the FSUM allowed power to be set from 0 to 100% of maximum power, adjustable within 1%, for each individual transducer. Power settings could be adjusted absolutely or relatively, and any combination of transducers could be adjusted simultaneously as long as the adjustment was the same for each transducer.

4.3.3 Acoustic Pressure Measurements in Water Bath

Acoustic field studies were performed for various combinations of FSUM transducers excited jointly. As in Section 4.2.1, transducers radiated into a degassed water bath, and a hydrophone was used to make pressure amplitude measurements. Figure 4-24 shows which FSUM transducers were excited for one particular set of measurements. For this excitation pattern, measurements were taken in the xz- and yz-planes, in increments of 0.05 cm in the x and y directions and 0.5 cm in the z direction; these measurements are shown in Figure 4-25A and 4-25B, respectively.

Several notable features are exhibited in the p_{a} field shown in Figure 4-25. In particular, there is a substantial degree of high spatial frequency content, and there is a clear concentration of intensity in the focal region (at least in Figure 4-25A). Spatial variations are characteristic of the near field region of acoustic fields, and large variations are indicative of acoustic sources with sides that are considerably larger than the acoustic wavelength. In the case of the excitation pattern under investigation, the side of the combined FSUM source, seven transducers on a side, has a nominal diameter of about 23 cm. A 1 MHz source of this size, with a wavelength of 0.15 cm, produces a near field that spans about 1 m, comfortably containing the entire region in the vicinity of the geometric focus of the device.

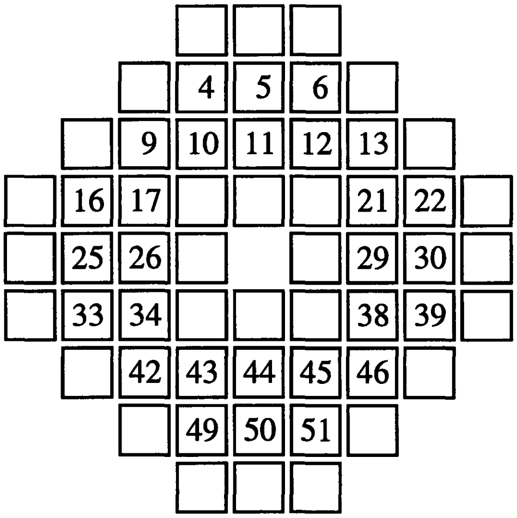

Figure 4-24: FSUM excitation pattern. Numbered transducers were excited, unnumbered were not.

The cross-section of the p_a field shown in Figure 4-25B clearly indicates that the cross-section does not contain the geometric focus of the FSUM; in anatomic terms, it is a para-sagittal plane rather than a mid-sagittal plane. In the case of acoustic radiation into a non-attenuating medium, such as the case here, the geometric focusing action of the FSUM should generate a substantial peak in the pressure field in the vicinity of the focus. (The expected peak is clearly visible in Figure 4-25A.) Since it is not clear how far from mid-sagittal the plane is, comparisons in the next section between measured and modeled fields will be restricted to the xz-plane.

Both planar cross-sections in Figure 4-25 are clearly asymmetric, which, given the symmetric design of the FSUM device, may seem surprising. These asymmetries are caused by several factors, including imperfections in device construction associated with transducer geometry (Section 4.3.1) and power (Section 4.3.2).

4.3.4 Acoustic Simulation

It is unrealistic to expect an acoustic model to capture every peak and valley in the measured field, particularly when the patterns are so complex. Peaks between the modeled and measured fields will frequently fail to match up well, so direct comparison may lead to the mistaken impression of poor modeling. Thus comparison between modeled and measured fields will be made by comparing the fraction of acoustic power in a displayed plane that resides within

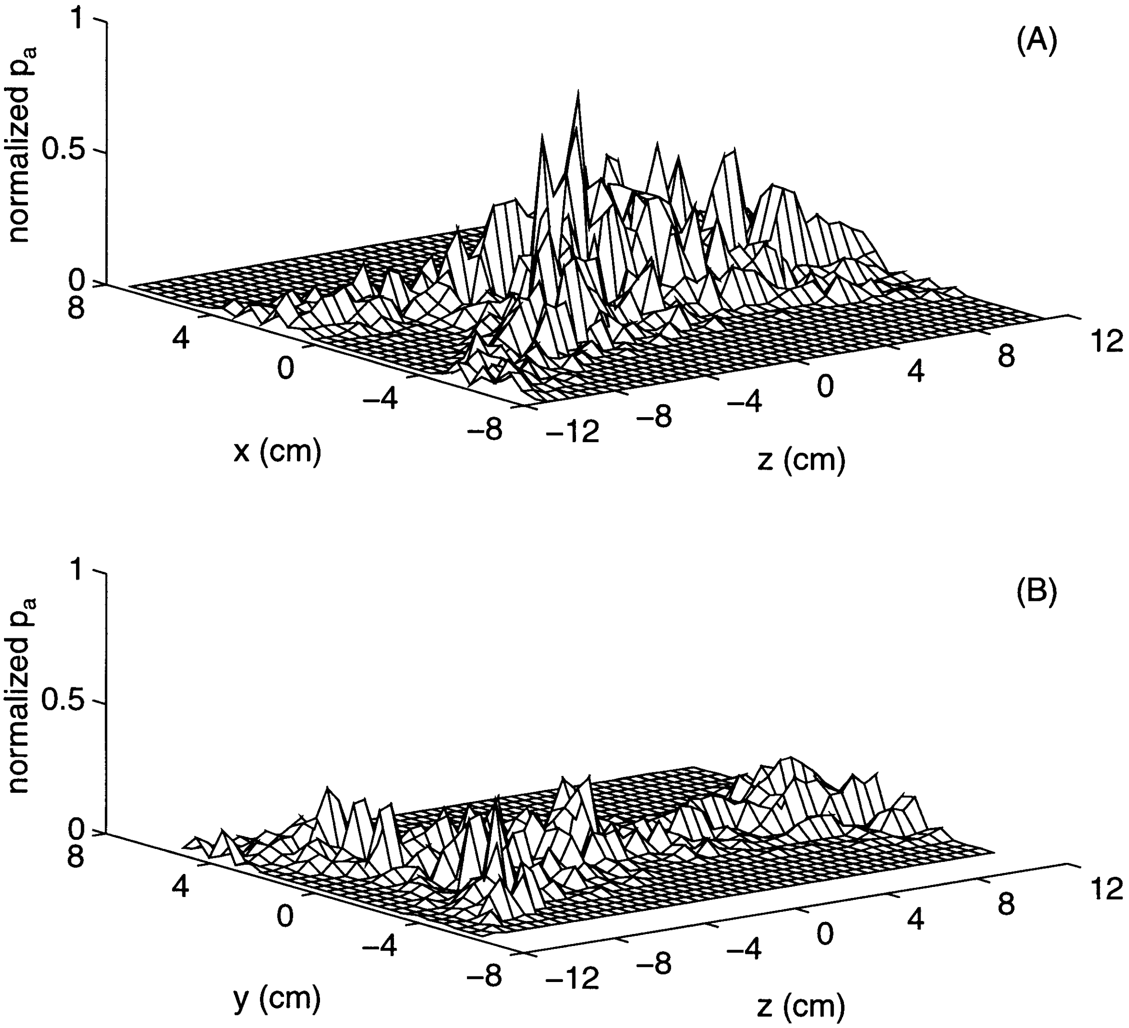

Figure 4-25: Measured pressure amplitude p_a field of FSUM, in the (A) xz- and (B) yz-planes.

squares centered at the device focus. For simplest comparison, modeled p_a field values were calculated on the same grid points in the xz- and yz-planes where measurements were taken. The total acoustic power contained in a plane, $\dot{q}_\mathrm{pl}$, was taken to be proportional to the sum of the squares of the pressures on the grid points; in symbolic terms, $\dot{q}_\mathrm{pl} \propto \sum_{i_\mathrm{pl},j_\mathrm{pl}} p_\mathrm{a}\{i_\mathrm{pl}, j_\mathrm{pl}\}^2$, where $(i_\mathrm{pl}, j_\mathrm{pl})$ spans all grid points in the plane. The power contained in a square in a plane, $\dot{q}_\mathrm{sq}$, was proportional to the sum of the squares of the pressures on the grid points in (and on) the square; or, $\dot{q}_\mathrm{sq} \propto \sum_{i_\mathrm{sq},j_\mathrm{sq}} p_\mathrm{a}\{i_\mathrm{sq}, j_\mathrm{sq}\}^2$, where $(i_\mathrm{sq}, j_\mathrm{sq})$ indicates the grid points contained in the square. The fraction of acoustic power within the square was then given by $\dot{q}_\mathrm{sq}/\dot{q}_\mathrm{pl}$.

Five models were investigated—four based on the parametric model for individual transducers developed in Section 4.2 (see Equation 4.19 on page 124), but differing in the treatment of the phase term (see Equation 3.41 on page 73); and one using the Rayleigh-Sommerfeld diffraction integral (see Equation 3.24 on page 66) for a Gaussian source. Specifically, the five models were:

1. Intensity superposition. In this scheme, the acoustic intensity field contributions from individual transducers are added. This is mathematically equivalent to pressure field contributions that are summed independently: $p_{\mathrm{aFSUM}}\{x, y, z\} = \sqrt{\sum_i p_{\mathrm{a}_i}\{r_i, z_i\}^2}$, where $p_{\mathrm{aFSUM}}\{x, y, z\}$ is the p_a of the entire device at the field point (x, y, z) in device coordinates, and $p_{\mathrm{a}_i}\{r_i, z_i\}$ is the p_a from the i^th transducer (xd$_i$) at the field point (r_i, z_i) in local transducer coordinates. (This scheme is most appropriate for transducers that are excited incoherently.)

2. Pressure superposition with distance-weighted phasing [89]. Here pressure field contributions from individual transducers are obtained using the parametric model, and they are added together as complex pressure fields using a phase term that is proportional to the distance between the center of the transducer and the field point: $p_\mathrm{FSUM}\{x, y, z\} = \sum_i p_{\mathrm{a}_i}\{r_i, z_i\}e^{-jkd_i}$, where $d_i^2 = r_i^2 + z_i^2$.

3. Pressure superposition with depth-weighted phasing. This scheme is similar to distance-weighted phasing, except the depth z_i is used for in phase term: $p_\mathrm{FSUM}\{x, y, z\} = \sum_i p_{\mathrm{a}_i}\{r_i, z_i\}e^{-jkz_i}$.

4. Pressure superposition with Analytic solution phasing. This scheme is similar to the

distance-weighted and depth-weighted phasing, except the phase term comes from the analytic solution of the Gaussian source given in Equation 3.41: $p_{\mathrm{FSUM}}\{x, y, z\} = \sum_i p_{\mathrm{a}_i}\{r_i, z_i\} e^{j(z_i' r_i^2/2\sigma_{\mathrm{b}}'^{\,2} - \tan^{-1} z_i' - k z_i)}$, where $z_i' \equiv z_i/k\sigma_{\mathrm{s}}^2$ and $\sigma_{\mathrm{s}}' \equiv \sigma_{\mathrm{s}}\sqrt{1 + z_i'^{\,2}}$, where σ_{s} for all transducers is taken to be the value determined for transducer #28, namely $\sigma_{\mathrm{s}} = 0.81\,\mathrm{cm}$.

5. Pressure superposition using the Rayleigh-Sommerfeld diffraction integral. This model was based on the solution of the diffraction integral for Gaussian sources, all with Gaussian length constants $\sigma_{\mathrm{s}} = 0.81\,\mathrm{cm}$. Numerical solution was achieved using the method developed in Section 4.1 with $F = 20$.

Figures 4-26 – 4-30 show respectively the respective simulated p_{a} fields in the xz- and yz-planes for the intensity superposition method and the pressure superposition methods using distance-weighted phasing, depth-weighted phasing, analytic solution phasing, and Rayleigh-Sommerfeld diffraction integral. Shown in Table 4.1 is the fraction of acoustic power in squares of 2, 4, and 6 cm on a side and centered at the focus. Data are presented for the measured and five simulated fields.

Table 4.1: $\dot{q}_{\mathrm{sq}}/\dot{q}_{\mathrm{pl}} \times 100\%$, the percentage of acoustic power inside squares of various sides centered at the focus of the FSUM device in the xz- and yz-planes.

	Square Side					
	2 cm		4 cm		6 cm	
Simulation Model	xz	yz	xz	yz	xz	yz
Measured†	23	—	46	—	67	—
Intensity superposition	14	14	31	31	44	45
Pressure superposition						
Distance-weighted	23	22	46	43	59	59
Depth-weighted	24	21	47	42	59	58
Analytic solution	33	31	53	51	65	62
Diffraction integral	21	20	44	43	56	60

†The measured field is clearly not a simulation model, but it is shown here for comparison with the simulated fields. (yz-plane values were not available for the measured field.)

A number of interesting observations can be made concerning Table 4.1 and Figures 4-25 –

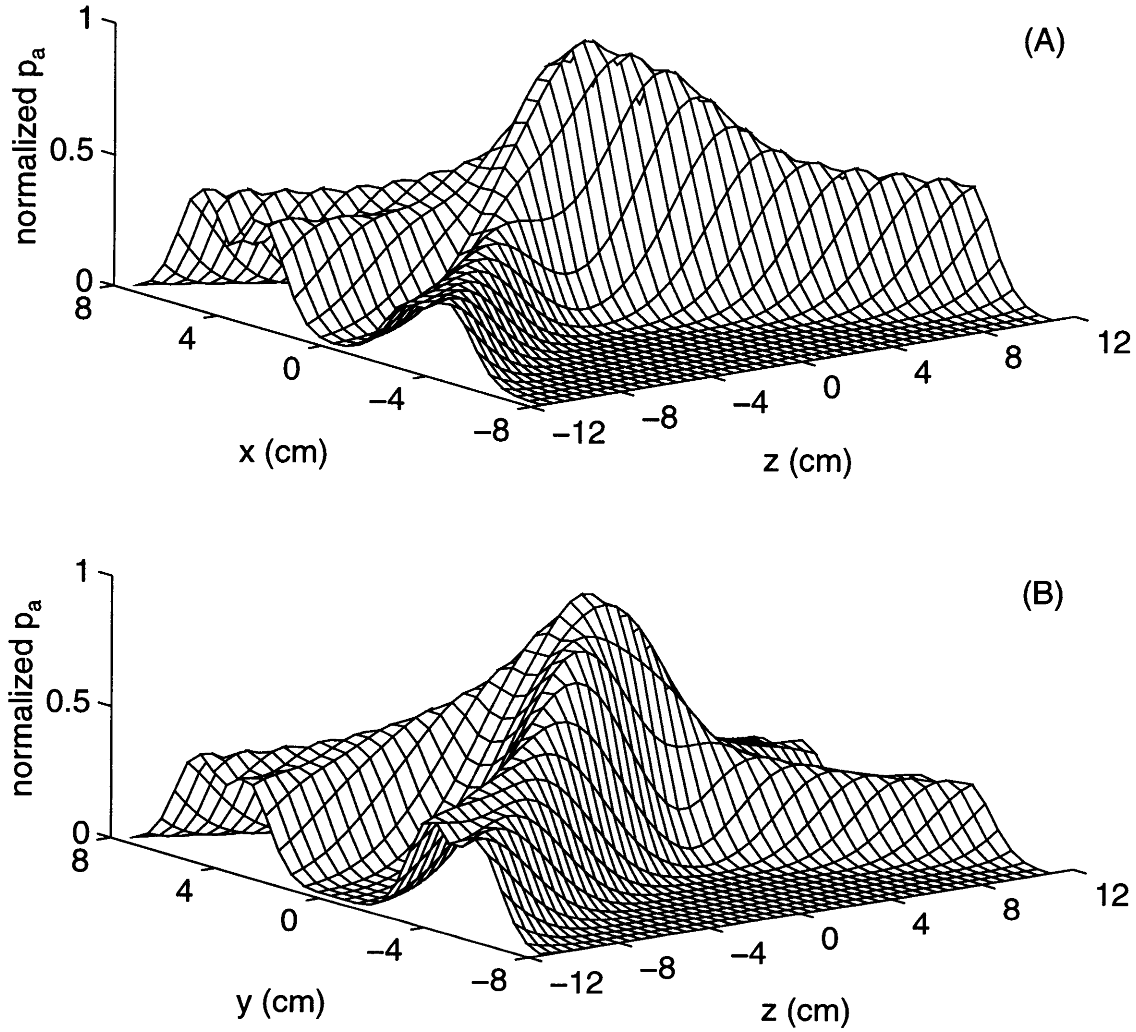

Figure 4-26: Simulated pressure amplitude p_{a} field of FSUM using modified Gaussian parametric model and intensity superposition, in the (A) xz- and (B) yz-planes.

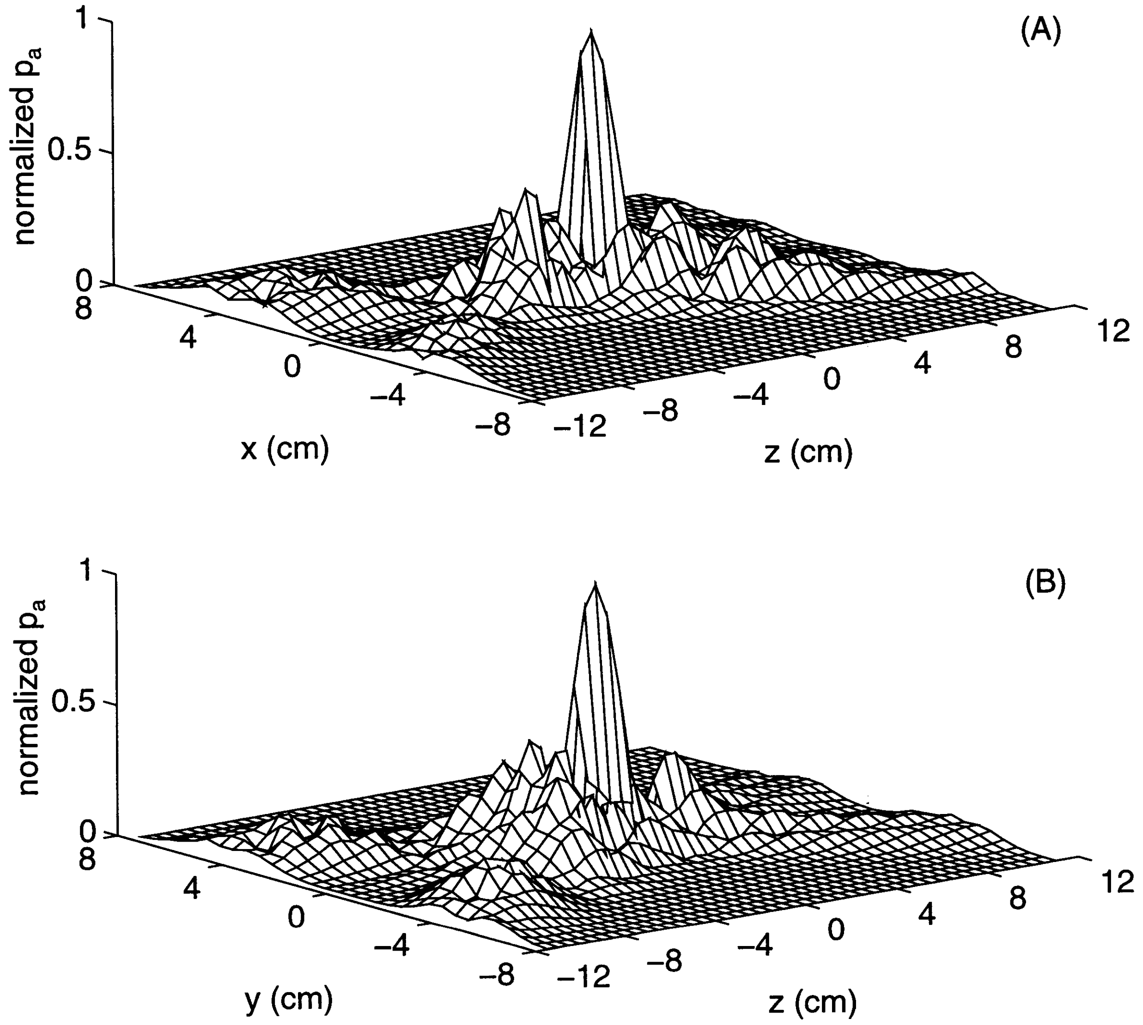

Figure 4-27: Simulated pressure amplitude p_{a} field of FSUM using modified Gaussian parametric model and pressure superposition with distance-weighted phasing, in the (A) xz- and (B) yz-planes.

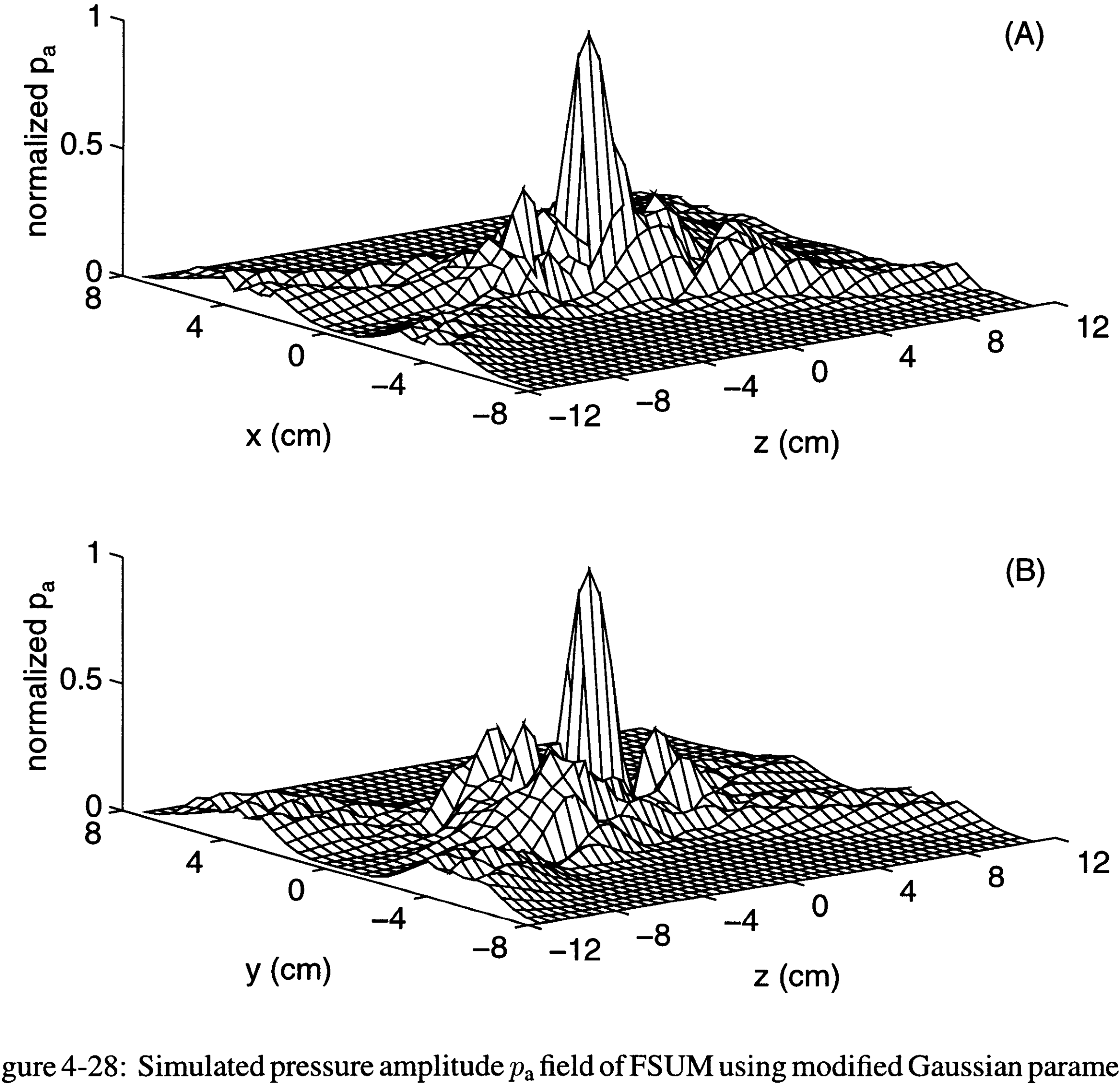

Figure 4-28: Simulated pressure amplitude p_a field of FSUM using modified Gaussian parametric model and pressure superposition with depth-weighted phasing, in the (A) xz- and (B) yz-planes.

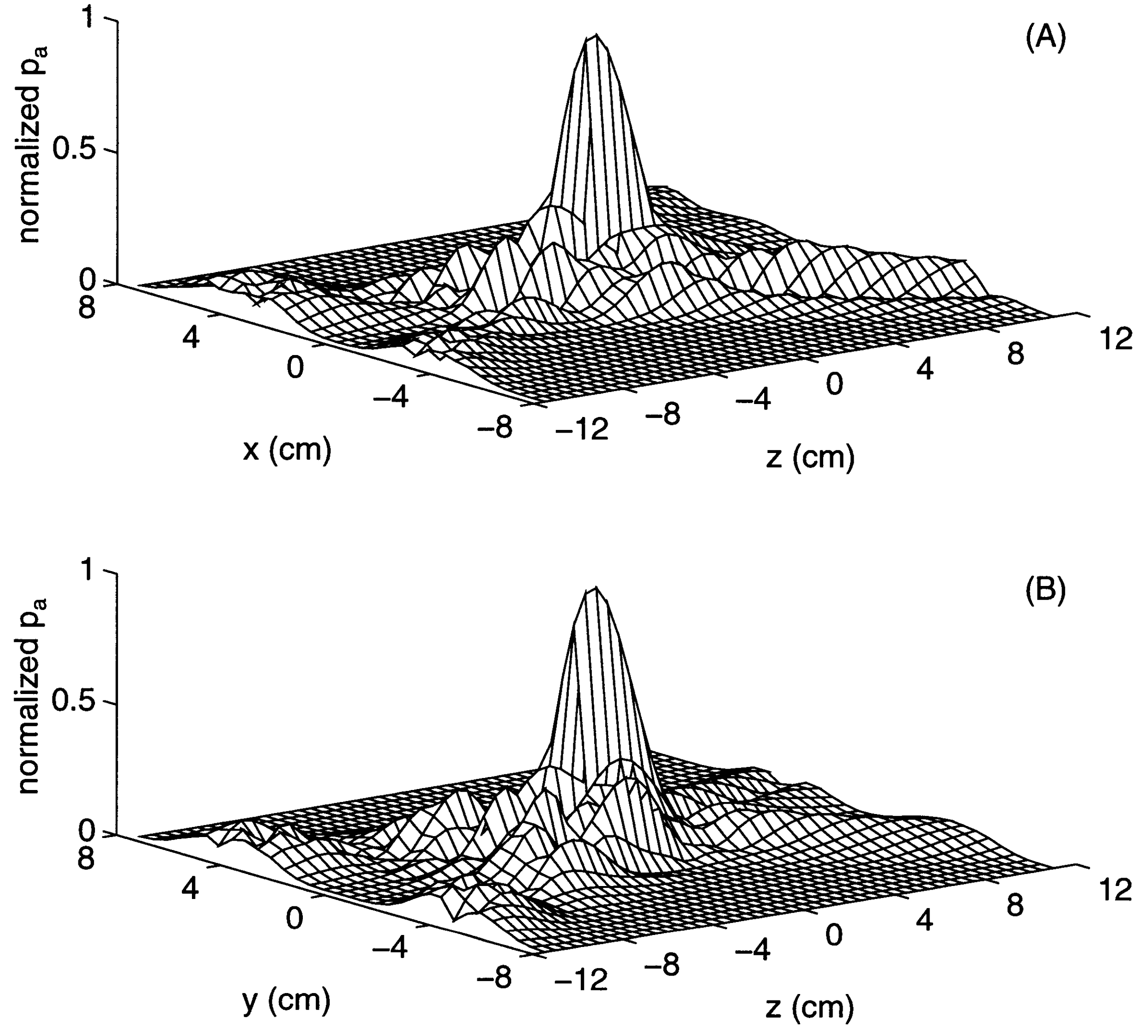

Figure 4-29: Simulated pressure amplitude p_a field of FSUM using modified Gaussian parametric model and pressure superposition with analytic solution phasing, in the (A) xz- and (B) yz-planes.

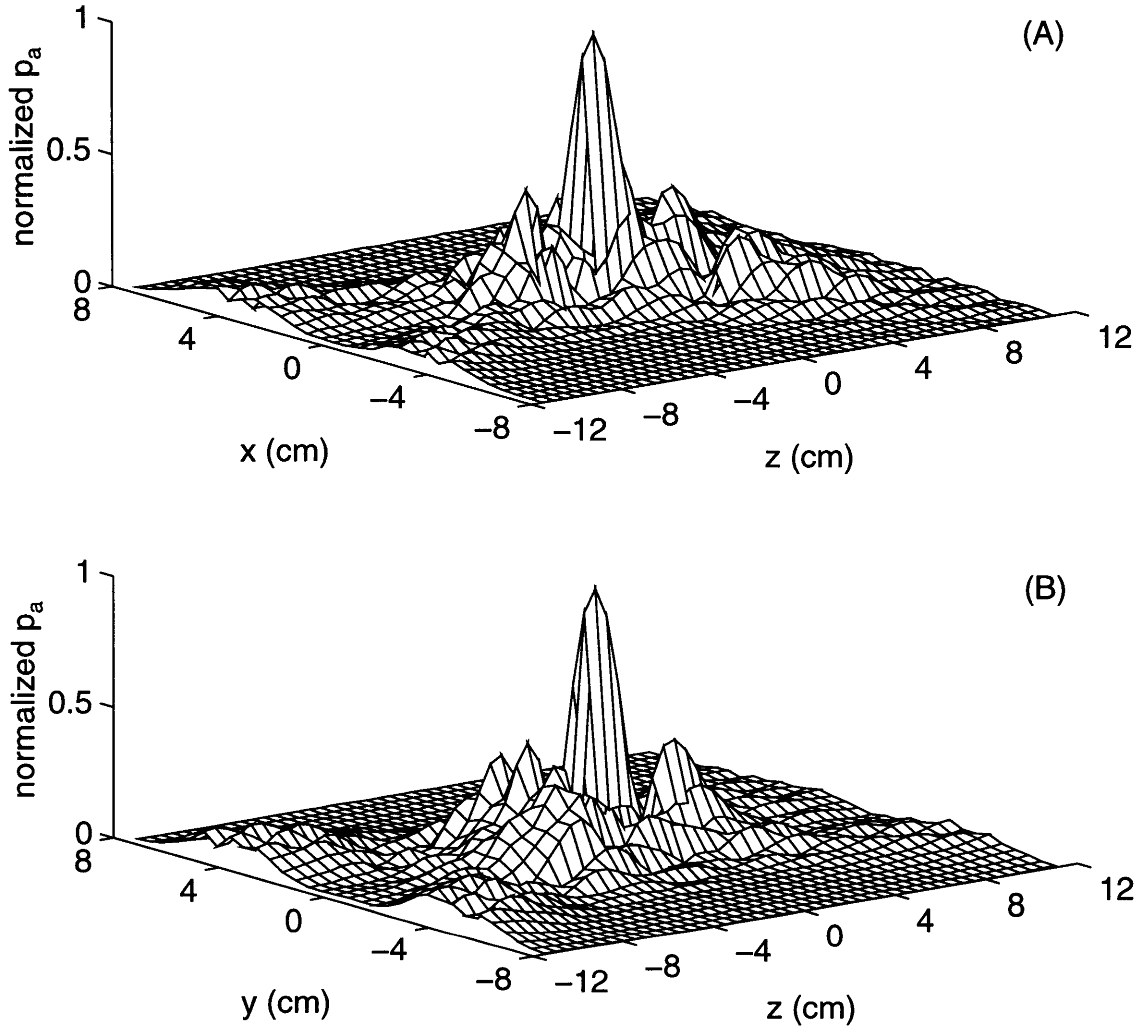

Figure 4-30: Simulated p_a field of FSUM using modified Gaussian parametric model and pressure superposition with the Rayleigh-Sommerfeld diffraction integral, in the (A) xz- and (B) yz-planes.

4-30. The table indicates that the distance- and depth-weighted phasing schemes produce nearly identical fields, in terms of the power calculations performed in the table, and that both agree remarkably well with the measured field, especially in the 2×2 and $4 \times 4\,\mathrm{cm}^2$ squares centered at the focus.

The intensity superposition scheme has the tendency to reduce high peaks in the pressure field, where constructive interference would take place in a different phasing scheme; and conversely to raise valleys and low peaks, where destructive interference would otherwise take place. These effects conspire to diminish the dominance of the focal region in the pressure field, evidenced in Table 4.1 by less power concentration in the squares at the focus.

Given the parametric description of the transducer beams, one might expect the analytic solution phasing scheme would be an attractive choice for phasing, but Table 4.1 suggests otherwise. The original analytic model for a Gaussian beam (Equation 3.41) was of course modified (Equation 4.19) in FSUM acoustic simulations, and perhaps this modification was somehow very incompatible with the original phase term. It is not necessarily surprising that variations in the phasing scheme can result in radically different acoustic fields, however—in fact, phased arrays depend on this phenomenon.

As shown in the table, the analytic solution phasing scheme had superior agreement with measurement in the $6 \times 6\,\mathrm{cm}^2$ square, but overestimated the concentration of power in the smaller squares. Given that the modeling here is motivated by empirical results, a phasing scheme could be conceived that combines features of different phasing schemes. For example, the distance-weighted phasing scheme could be used in a sphere of radius 2 or 3 cm around the focus, and analytic solution phasing outside that sphere. But, in fact, such a phasing strategy would probably not improve agreement between modeled and measured fields. This is because the fraction of the power in the square ring between the 4×4 and $6 \times 6\,\mathrm{cm}^2$ squares was nearly invariant between different modeling schemes: about 13% (compared with 21% for the measured field).

Lastly, the Rayleigh-Sommerfeld diffraction integral model will be discussed. In Table 4.1 this method is seen to exhibit worse agreement with the measured field than the distance- and depth-weighted phased schemes, consistently underestimating the power concentrations in the central squares; nevertheless, this method was not bad. But given that calculation by this method was two or more orders of magnitude slower than any of the phased schemes [89], depending on the constraint factor F, there is no question that the phased schemes are computationally preferred when they provide comparable (or better!) agreement with measurements.

For the FSUM excitation pattern explored here, then, the preferred models are the distance- and depth-weighted phased schemes, which appear nearly equivalent, with the former marginally and insignificantly better. The field cross-sections shown in Figures 4-27 and 4-28 reflect the extreme similarity in these simulations, but they both show significant differences from the measured field cross-sections in Figure 4-25. However, as pointed out by Sidney *et al.* [89]:

> From a clinical point of view, differences in pressure fields are only significant if they result in significantly different calculated temperature fields. In this light, differences in temperature fields are minimized by thermal convection by blood perfusion and thermal conduction in tissue, which attenuate the amplitude of spatial variations in temperature from spatial variations in SAR; furthermore, this thermal attenuation is greater at higher spatial frequency [96, Umemura and Cain].

4.4 Fanned Absorption Method

The FSUM transducer and device modeling of Section 4.2 and Section 4.3 was performed for a non-attenuating medium. Without attenuation from absorption, however, there is no power deposition, and hence no heating. Since hyperthermia is the intended application of the acoustic modeling in this thesis, then, it is clear an adjustment in the model must be made to accommodate ultrasound absorption. It is the objective of this section to develop the Fanned Absorption Method (FAM), a method which takes the acoustic pressure field of a single source radiating into a non-attenuating medium, and modifies it to take into account the affects of absorption. Field contributions from individual transducers can then be combined using distance-weighted phasing (or some other scheme) to obtain the field from the entire device.

Barring scattering, reflection, and refraction effects, ultrasound waves are transmitted radially from their point of origin, propagating along so-called **fan lines**. This spherical geometry for wave transmission is taken quite literally by the class of numerical techniques which subdivide individual acoustic sources into many simple or point sources (Section 3.2.1, page 76). The affects of attenuation from absorption are in practice calculated as the waves propagate along these fan lines (see Equations 3.45 and 3.46).

In radiotherapy, radiation is generally transmitted in the same radial geometry as ultrasound.[5] Milan *et al.* [69] took advantage of this geometry to tabulate radiation dose at 17 different depths along the central axis of the beam, and five different depths along fan lines in a plane containing the central axis. Thus a **fan lattice** comprising fan lines with grid points was established. In this particular case the geometry was triangular, with the triangle apex, the origin of the fan lines, located at the source of radiation. Radiation dose values could be easily interpolated throughout this plane, and various computational protocols were used to calculate off-axis dose and accommodate tissue heterogeneity of radiation absorption and scattering. More sophisticated computational protocols are used now, such as the JCRT Photon Algorithm [54]. (The reader is also referred to Bentel [8] for general discussion of radiation dose calculation.) These algorithms generally operate by tabulating on a fan lattice radiation dose values obtained experimentally using phantoms, interpolating values between tabulated points, and modifying tabulated values according to beam aperture, beam collimator, and tissue heterogeneity.

In the field of computer graphics, **ray-tracing** is used to produce images from scenes that have instances of reflection or refraction. Ironically, then, in computer graphics ray-tracing is used specifically to accommodate wave phenomena which we would like to ignore in ultrasound field prediction. But extended ray-tracing also has the ability to generate images with partially absorbing and scattering media, so it is not surprising that an algorithm similar to ray-tracing can be used for ultrasound field prediction. (We are unaware of a "super-extended" ray-tracer which takes into account wave constructive and destructive interference patterns, but in theory there is no reason why such a ray-tracer could not be made. Ray-tracers are used to generate *visual* images and to illustrate *visual* phenomena—generally for commercial ends, not scientific ones—and the desire to see images which exhibit light diffraction phenomena has not yet arisen.) Ray-tracing is a famously computationally intensive technique, however, and for this reason it is not necessarily desirable to use it to perform acoustic field calculations.

---

[5] Technically ultrasound could be considered a form of radiation, but radiation in the context of radiotherapy generally refers to the specific use of either positive ions (using particle accelerators), gamma rays (gamma knife Co^{60} systems), or x rays (LINAC systems) [63].

4.4.1 Fan Lattice Description

The Fanned Absorption Method (FAM) for rapid acoustic field calculation will now be described. Similar to radiation dose calculation schemes, this method starts with a nominal known pressure field from an acoustic source radiating into a non-attenuating (*i.e.* non-absorbing and non-scattering) medium. The field can be known at discrete spatial locations from measurements or numerical simulations, or it can be known universally through a parametric description of the acoustic beam. A fan lattice is established, and attenuation factors are calculated at each lattice point to calculate the pressure field in the presence of absorption; the attenuation factor is simply the ratio between the pressure amplitude fields with and without absorption.

There are several qualities desired in the fan lattice that comprises the fan lines. First, the shape of the fan lattice should reflect the source geometry in the near field, but the fan lines should radiate spherically in the far field. Second, there should be a simple scheme for interpolating between the lattice points to arbitrary points—much as there is a simple scheme (namely **trilinear interpolation**, Section B.5) for interpolating between Cartesian grid points to fan lattice points. Third, there should be an easy way to handle pressure attenuation calculations as acoustic waves propagate along the fan lines and are absorbed. The reason for wanting these qualities should become clear by the end of this section.

The fan lattice is basically a discretized version of the **fan coordinate system**, and both look like a cross between a sphere and the source geometry. For example, the fan lattice and coordinate system for a square planar source look like a cross between a sphere and a pyramid with a square base, and they are depicted in Figure 4-32A. The source, in the local source coordinate system, is embedded in the xy-plane and centered at the origin O. Acoustic waves are taken to originate at O', a **fan line offset distance** d behind the planar source, and they radiate spherically. Any given fan line is defined by two angles β_x and β_y, termed here **fan angles.**[6] Points along the fan line are given by the r coordinate, which is measured along the fan line *from the surface* of the source, not from O' or O.

A point obviously can be represented in Cartesian coordinates, (x, y, z), or fan coordinates,

---

[6] Fan angles should not be confused with Euler angles, the conventional angles used to describe spherical coordinates.

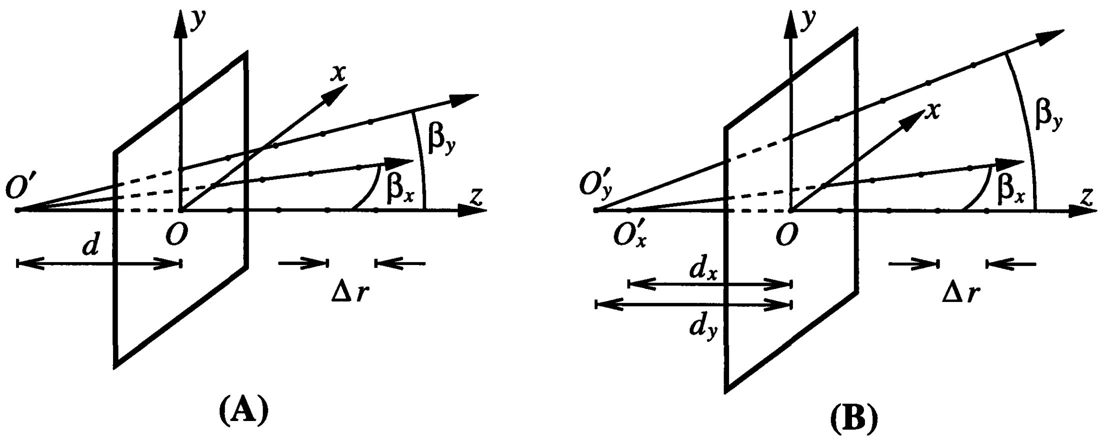

Figure 4-31: Fan lattice schematic. (A) Square source. (B) Rectangular source.

(β_x, β_y, r). Fan coordinates can be converted to Cartesian coordinates:

$$\begin{aligned} z &= \frac{r}{\gamma\{\beta_x, \beta_y\}} \\ x &= (z+d)\tan\beta_x \qquad (4.21) \\ y &= (z+d)\tan\beta_y \end{aligned}$$

where the projection factor[7] $\gamma\{\beta_x, \beta_y\} = \sqrt{\tan^2\beta_x + \tan^2\beta_y + 1}$. Conversely, Cartesian coordinates can be converted to fan coordinates:

$$\begin{aligned} \beta_x &= \tan^{-1}\frac{x}{z+d} \\ \beta_y &= \tan^{-1}\frac{y}{z+d} \qquad (4.22) \\ r &= z\gamma\{\beta_x, \beta_y\} \end{aligned}$$

In the fan lattice, fan lines are placed at discrete angles β_x and β_y with intervals of $\Delta\beta$. Fan lattice points are placed at intervals of Δr along fan lines. Specifically, the (β_x, β_y, r) fan coordinates associated with the fan lattice indices (i, j, k) are given by:

$$\begin{aligned} \beta_x\{i\} &= i\,\Delta\beta \\ \beta_y\{j\} &= j\,\Delta\beta \qquad (4.23) \end{aligned}$$

---

[7] The projection factor is so named because it gives the ratio between the length of an increment along a fan line, and the length of the increment *projected* onto the z-axis.

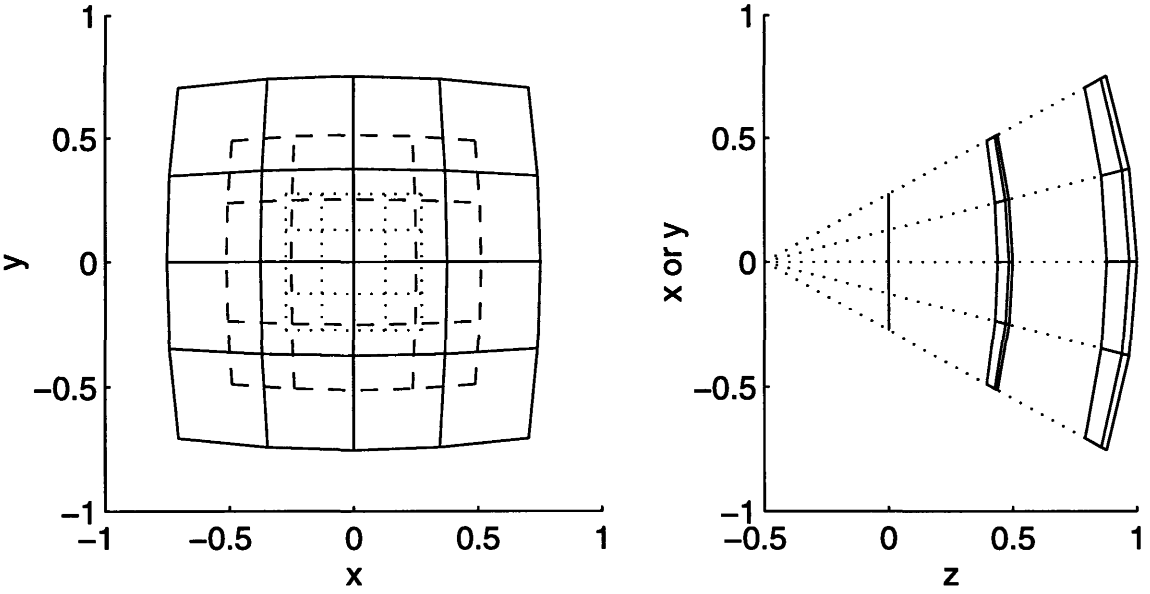

Figure 4-32: Orthogonal views of three layers of the fan lattice for a square planar source.

$$r\{k\} = k\,\Delta r$$

where (i, j, k) are all integers, and $-n \leq i, j \leq n$ and $0 \leq k \leq n_z$. Along a given fan line, the difference in position between adjacent lattice points is $(\Delta x, \Delta y, \Delta z)$, where geometry indicates:

$$\begin{aligned} \Delta z\{i,j\} &= \frac{\Delta r}{\gamma\{i,j\}} \\ \Delta x\{i,j\} &= \Delta z\{i,j\} \tan\beta_x\{i\} \\ \Delta y\{i,j\} &= \Delta z\{i,j\} \tan\beta_y\{j\} \end{aligned} \tag{4.24}$$

The fan lattice looks like a series of quasi-spherical onion layers emanating from the source, with a squarish grid on each layer. Figure 4-32 shows three layers of the fan lattice (including the planar layer coplanar with the source) in orthogonal views, with the fan line offset distance $d = 0.5$ (arbitrary length units). In the xz-plane (and, equivalently, the yz-plane) projection, dotted lines depict the fan lines, and the planar source (not shown) would be in the xy-plane (*i.e.* the $z = 0$ plane).

The matter of how to determine the fan line offset distance d can be an important one, and ultimately comes down to a judicious estimate based on empirical measurements or numerical simulations of the pressure field (as will be illustrated in Section 4.4.2). When the fan line offset distance is determined, however, the desired characteristics of the fan lattice will have been met.

Once the fan lattice is established, the **attenuation factor**[8] f needs to be calculated. This attenuation factor quantifies the attenuation from absorption as acoustic waves propagate down a fan line, and it corresponds to the absorption terms in Equations 3.45 and 3.46 on page 78. Specifically, the pressure field transformed using the FAM so that absorption is taken into account is given by $p_{\text{FAM}} = f p_0$, where p_0 is the pressure field for acoustic radiation into a non-attenuating medium. In the *continuous* description of the fan coordinate system:

$$f\{\beta_x, \beta_y, r\} = \exp\Big(-\int_0^r \alpha\{\beta_x, \beta_y, \xi\} d\xi\Big) \tag{4.25}$$

In the *discrete* description of the fan lattice:

$$f\{i, j, k\} = \exp\left[-\sum_{\xi=1}^{k}(\alpha\{i, j, \xi\}\Delta r)\right] = \exp\left(-\Delta r \sum_{\xi=1}^{k} \alpha\{i, j, \xi\}\right) \tag{4.26}$$

Note that $f\{\beta_x, \beta_y, 0\} = 1$ and $f\{i, j, 0\} = 1$. In practice, $f\{i, j, k\}$ can be calculated iteratively:

$$f\{i, j, k\} = f\{i, j, k-1\} \exp(-\alpha\{i, j, k\}\Delta r) \tag{4.27}$$

which shows that the attenuation factor at a given lattice point depends only on the absorption coefficient at that point and the attenuation factor at the previous (next closest to O') lattice point on the same fan line.

The fan lattice and fan coordinate system describe, in a sense, the geometry of the propagation of acoustic waves from the source. Using them in the FAM to perform acoustic field attenuation calculations can be viewed as a compromise between treating the source *microscopically*, with simple sources radiating acoustic waves spherically; and treating the source *macroscopically*, with the shape of the source reflected in its radiating acoustic waves. Clearly the FAM is not as rigorous an approach as that used in Equation 3.46. But a parametric beam description such as the modified Gaussian in Equation 4.19 (Section 4.2.3) does not accommodate the use of Equation 3.46, so an alternative technique, like the FAM, must be used to deal with attenuation.

4.4.1.1 Rectangular Source

For the general planar rectangular source, with unequal height and width, a modification of the fan coordinate system must be adopted. Figure 4-31B depicts this variation. Now there are two

---

[8] Attenuation factor is not part of the standard nomenclature in ultrasound physics.

fan line offset distances parameters which must be determined, d_x (between O'_x and O) and d_y (between O'_y and O), and Equations 4.21 and 4.22 for coordinate conversion are modified. For conversion from fan to Cartesian coordinates:

$$\begin{aligned} z &= \frac{r}{\gamma\{\beta_x, \beta_y\}} \\ x &= (z + d_x) \tan \beta_x \\ y &= (z + d_y) \tan \beta_y \end{aligned} \tag{4.28}$$

For conversion from Cartesian to fan coordinates:

$$\begin{aligned} \beta_x &= \tan^{-1} \frac{x}{z + d_x} \\ \beta_y &= \tan^{-1} \frac{y}{z + d_y} \\ r &= z\gamma\{\beta_x, \beta_y\} \end{aligned} \tag{4.29}$$

Equations 4.23 is slightly modified to accommodate different increments in angles in the x and y directions:

$$\begin{aligned} \beta_x\{i\} &= i\,\Delta\beta_x \\ \beta_y\{j\} &= j\,\Delta\beta_y \\ r\{k\} &= k\,\Delta r \end{aligned} \tag{4.30}$$

where $-n_x \leq i \leq n_x$, $-n_y \leq j \leq n_y$, and $0 \leq k \leq n_z$.

Figure 4-33 shows, in orthogonal views, three layers of the fan lattice (again including the planar layer coplanar with the source) of a source with $d_x = 0.5$ and $d_y = 1.5$ (arbitrary length units). The xy-plane projection appears rather similar to that in Figure 4-32, but the different curvatures in the x and y directions are clearly evident when comparing the other two projections. Dotted lines show how the *projections* of the fan lines emanate from O'_x in the xz-plane and O'_y in the yz-plane; but as mentioned before, the fan lines themselves do not emanate from a single point. Thus in the case of the general rectangular source, fan lines do not radiate spherically in the fashion of the square planar case.

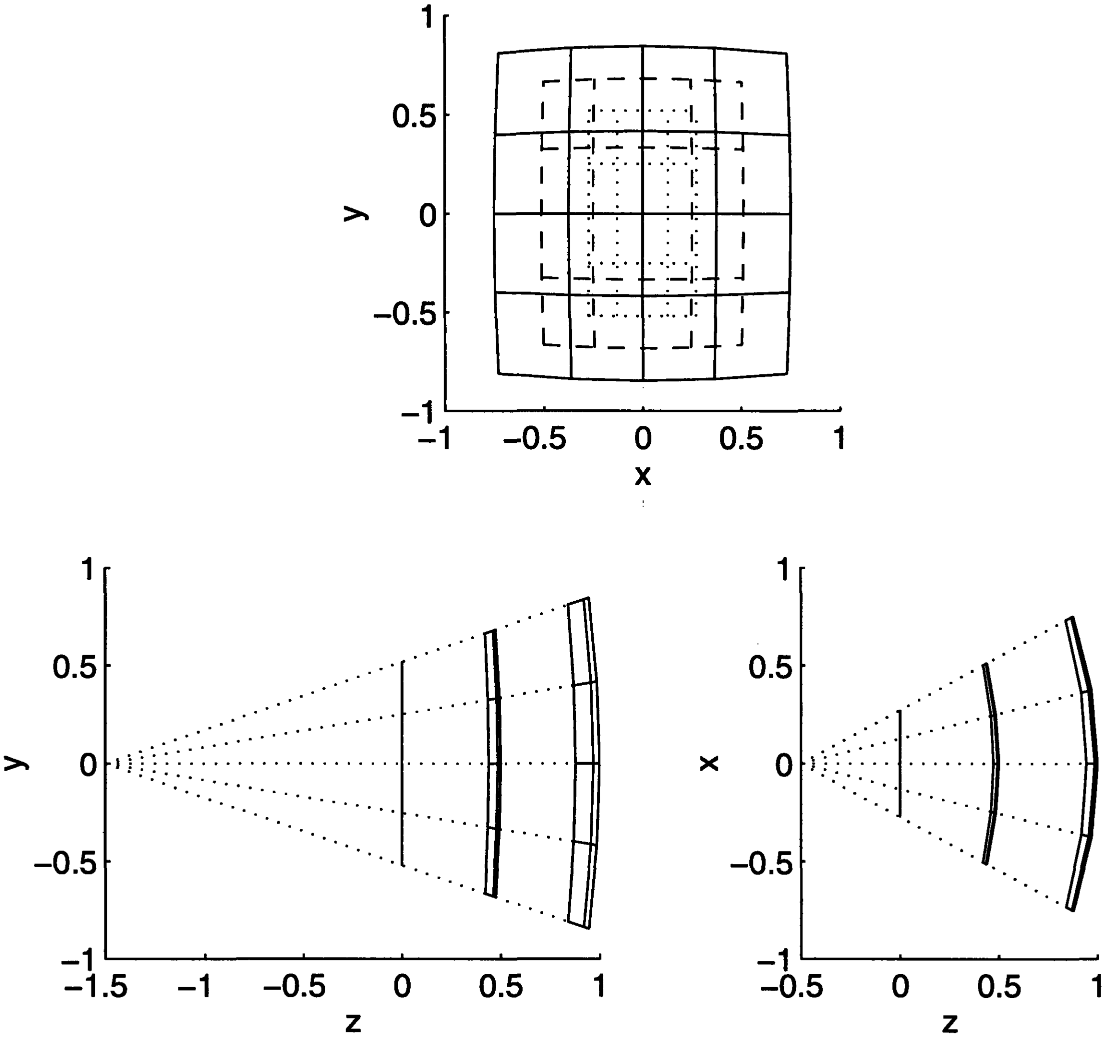

Figure 4-33: Orthogonal views of three layers of the fan lattice for a rectangular planar source.

4.4.1.2 Convex Cylindrical Wedge Source

Another source geometry worth investigating here briefly is that of the convex cylindrical wedge. The fan lattice in this case is similar to that of the rectangular source case, except the fan r coordinate tracks the curved surface of the cylindrical source instead of the planar surface of the rectangular source, making for more rounded lattice layers in the near field.

Figure 4-34 shows the xz-plane cross-section of the convex cylindrical source in its canonical coordinates (refer also to Figure 4-2 on page 87). Once again, it is desired to relate the fan coordinates[9] (β_x, β_y, r) to the Cartesian coordinates (x, y, z), and *vice versa*. The point O and the fan line offset distances d_x ($\overline{O'_xO}$) and d_y ($\overline{O'_yO}$) are analogous to their respective counterparts in Figure 4-33, with the *caveat* that here O, d_x, and d_y vary as a function of fan angle β_x. In principal, when the functional relationships relating d_x and d_y to β_x are determined then conversions between the fan and Cartesian coordinate systems can be performed (using equations similar to Equations 4.28 and 4.29). (Equation 4.30 applies as stated to the fan lattice of a convex cylindrical source.)

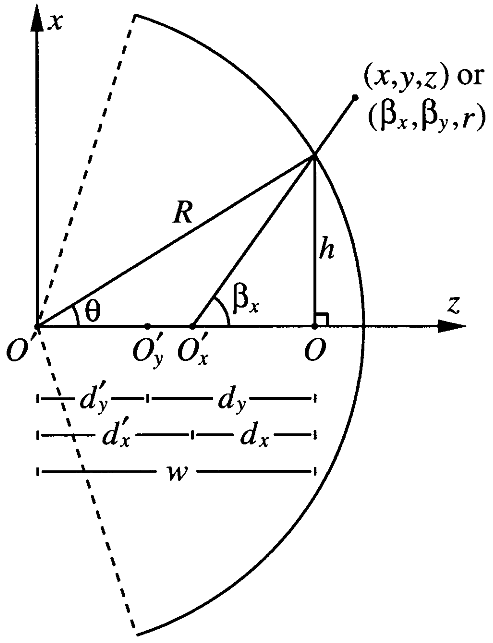

Figure 4-34: Cross-section in xz-plane of convex cylindrical wedge for fan lattice determination.

---

[9] The fan coordinate r should not be confused with the cylindrical coordinate r. In this section only fan coordinates are used.

From Figure 4-34:

$$h = R\sin\theta = d_x \tan\beta_x \tag{4.31}$$

and:

$$\cos\theta = \frac{d'_x + d_x}{R} \tag{4.32}$$

These two equations can be combined to give:

$$(d_x \tan\beta_x)^2 = R^2(1 - \cos^2\theta) = R^2 - (d'_x + d_x)^2 \tag{4.33}$$

Equation 4.33 is a quadratic equation in d_x, with solution:[10]

$$d_x = \cos\beta_x \sqrt{R^2 - {d'_x}^2 \sin^2\!\beta_x} - d'_x \cos^2\!\beta_x \tag{4.34}$$

For the convex cylindrical source, $w = d'_x + d_x = d'_y + d_y$. ($d'_y$ is positive as shown in Figure 4-34, but it would be negative if O'_y were to the left of O'. Furthermore, it is conceivable, for a source with much greater x extent than y extent, that O'_y could lie to the right of O for large β_x, resulting in $d_y < 0$! Unlike O'_y, however, O'_x is constrained to lie between O' and O'_x, so $d'_x, d_x > 0$.) Thus:

$$w\{\beta_x\} = \cos\beta_x \sqrt{R^2 - {d'_x}^2 \sin^2\!\beta_x} + d'_x \sin^2\!\beta_x \tag{4.35}$$

(If O'_x and O' are coincident, then $d'_x = 0$ and Equation 4.35 simplifies considerably to $w\{\beta_x\} = R\cos\beta_x$.) Then Equation 4.28 can be modified for converting fan coordinates into Cartesian coordinates:

$$\begin{aligned} z &= \frac{r}{\gamma\{\beta_x, \beta_y\}} + w\{\beta_x\} \\ x &= (z - d'_x)\tan\beta_x \\ y &= (z - d'_y)\tan\beta_y \end{aligned} \tag{4.36}$$

where w, d'_x, and d'_y are as shown in Figure 4-34. Conversely, Equation 4.29 can be modified for converting Cartesian coordinates into fan coordinates:

$$\beta_x = \tan^{-1}\frac{x}{z - d'_x}$$

---

[10] Of course, the quadratic equation has *two* roots; the given solution corresponds to the positive root. (In the region of interest, $|\beta_x| \leq \pi/2$ and $d_x \geq 0$.)

$$\beta_y = \tan^{-1} \frac{y}{z - d'_y} \tag{4.37}$$

$$r = (z - w\{\beta_x\})\,\gamma\{\beta_x, \beta_y\}$$

The discretized $\beta_x\{i\}$, $\beta_y\{j\}$, and $r\{k\}$ can be obtained from Equation 4.30.

Figure 4-35 shows, in orthogonal views, three layers of the fan lattice (including the cylindrical wedge layer essentially coincident with the source) of a source with radius of curvature $R = 1$, $d'_x = R - 0.5 = 0.5$, and $d'_y = R - 1.5 = -0.5$ (arbitrary length units). Dotted lines show how the *projections* of the fan lines emanate from O'_x in the xz-plane and O'_y in the yz-plane. The views are rather similar to those in Figure 4-33, with the main difference most visible in the xz-plane projection: The $r = 0$ layer is curved (with radius of curvature $R = 1$, the radius of curvature of the source).

4.4.2 Theoretical Validation

The FAM can be viewed as a technique to determine how much an absorbing medium attenuates the acoustic pressure field (compared with acoustic radiation into a non-attenuating medium). For the FAM to perform this task reasonably accurately, two conditions must hold. First, the attenuation achieved by the simple expedient of marching down fan lines and adjusting the attenuation factor at each step must produce a good estimate of the true attenuation. Put another way, the "true" pressure attenuation at a given field point is a combination of all the attenuations experienced by spherical acoustic waves propagating from each differential area of the source, and the attenuation achieved using the FAM must correspond well to this "combined" or "averaged" attenuation.

Second, although the FAM modifies the amplitude of the pressure field, it does not alter its phase. For acoustic fields produced using a single source or multiple incoherent sources, this second condition is not so relevant. This is because it is really the pressure amplitude that is considered important for SAR field calculation. For acoustic fields produced using multiple coherent sources, however, this second condition is critical. This is because the acoustic field for multiple coherent sources is the complex sum of the constituent fields from each source, and this complex addition is very sensitive to phase.

For the task at hand, using the FAM to model the coherently excited FSUM transducers, both

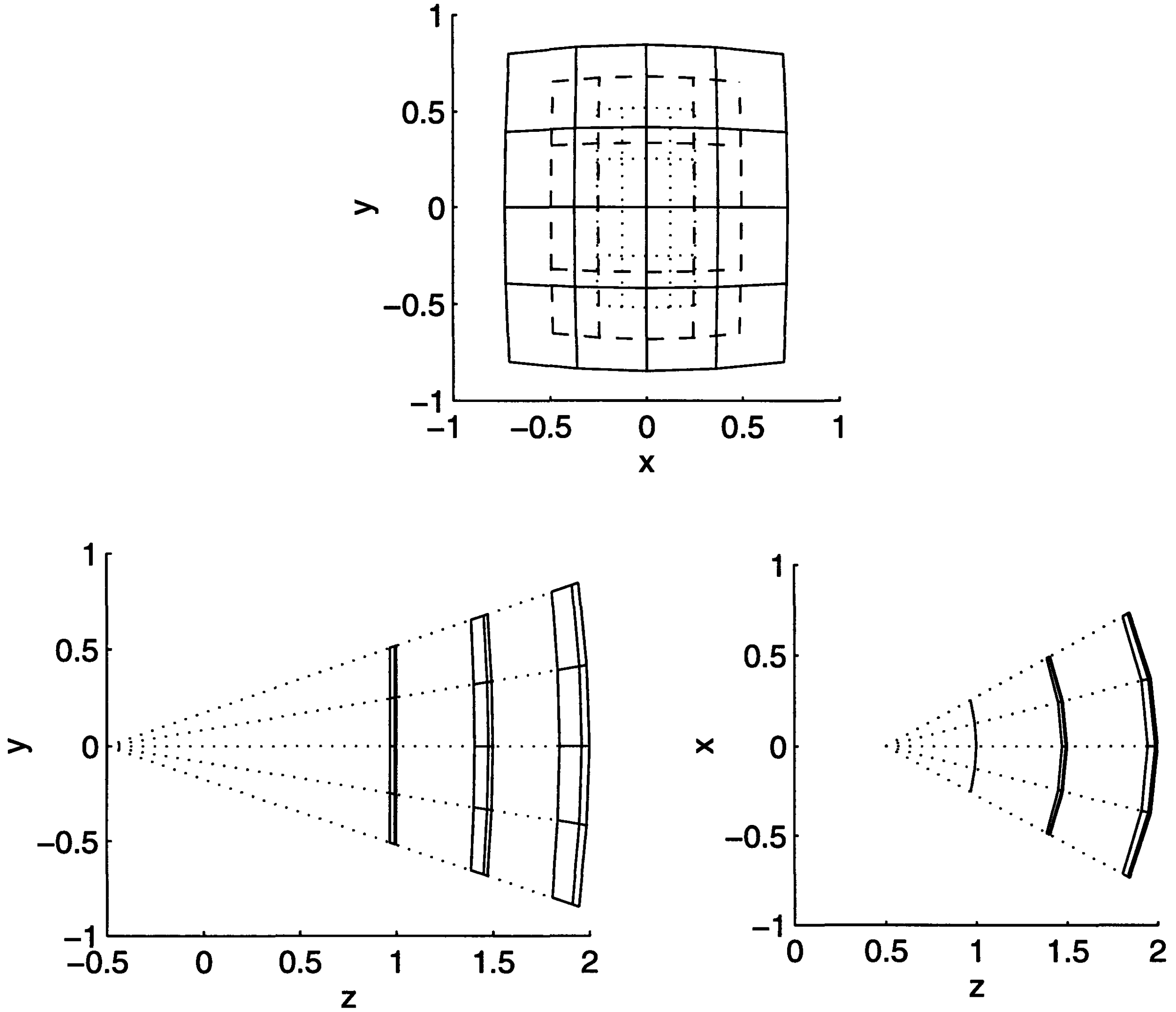

Figure 4-35: Orthogonal views of three layers of the fan lattice for a convex cylindrical wedge source.

conditions (amplitude and phase fidelity) must be validated, and to this end multiple computer simulations were performed of a single FSUM transducer radiating into inhomogeneously absorbing media. Briefly:

1. Using the Rayleigh-Sommerfeld diffraction integral solution method developed in Section 4.1, acoustic simulations are performed to find the pressure field of an FSUM transducer with a Gaussian vibration profile radiation into a non-attenuating medium and eight other medium absorption geometries. These nine fields are taken to be the nominal "exact" pressure field solutions for their respective non-attenuating or absorbing geometries, and they are termed the baseline fields.

2. For pressure *phase* validation, the pressure phase fields for the eight absorbing medium geometries are each compared with the pressure phase field for the non-attenuating medium. These comparisons use only the pressure fields calculated from the acoustic simulations using the diffraction integral, and not any FAM modified pressure fields; thus the FAM pressure phase validation is *in*direct. (Section 4.4.2.1)

3. For pressure *amplitude* validation, FAM modifications of the pressure amplitude field for the non-attenuating medium are performed for all eight absorbing geometries. These FAM-modified pressure amplitude fields are compared with the pressure amplitude fields calculated using the diffraction integral; thus the FAM pressure phase validation is *direct*. (Section 4.4.2.2)

From this description, it is clear that acoustic simulations fell in two broad categories: baseline simulations, which used the Rayleigh-Sommerfeld diffraction integral to solve for the complex pressure field; and FAM simulations, which used the FAM to modify the baseline field calculated for a non-attenuating medium.

In all these simulations, the FSUM transducer was placed in the canonical local source reference frame (see Figure 4-1 on page 87), and complex pressures were calculated on a uniform Cartesian "pressure grid." The FSUM transducer model used in baseline simulations consisted of a $3.3 \times 3.3\,\mathrm{cm}^2$ square transducer vibrating with a Gaussian profile with Gaussian length constant $\sigma_\mathrm{s} = 0.81\,\mathrm{cm}$, and numerical solution was achieved using the method developed in Section 4.1 with constraint factor $F = 20$. To accommodate inhomogeneity in the absorption of the medium, the numerical method was modified in the absorption term in the manner suggested by Equation 3.46 on page 78. Pressure grid points (x_i, y_j, z_k) were in the range $-3.0 \leq x_i, y_j \leq 3.0$ cm and $0.5 \leq z_k \leq 30$ cm, in uniform increments of 0.5 cm in all three directions. Since the Gaussian beam was fairly narrow (the nominal beam width is $2\sigma_\mathrm{b}$ or $4\sigma_\mathrm{b}$), the vast majority of the acoustic energy in the beam from the source surface to somewhat beyond the focal depth of the FSUM device (23.8 cm) was contained in the volume discretized by the grid.

For FAM simulations several values of *d* were investigated. $\Delta\beta$ was chosen so that increments in the fan lattice in the β_x and β_y directions would be 0.5 cm when $r = 30.0$ cm (the furthest part of the pressure grid), and the fan lattice was sufficiently large to completely encompass the pressure grid. Values of *d*, $\Delta\beta$, and Δr are shown in Table 4.2. A final note concerning the implementation of the FAM in these simulations relates to the specific protocol for determining the attenuation factor $f\{\vec{p}\}$ at an arbitrary field point P (*i.e.* a point not necessarily on the pressure grid). As previously suggested, the trilinear interpolation method (Section B.5) can be used; but for simpler computation the **nearest neighbor** method was employed here. In this method $f\{\vec{p}\} = f\{\beta_x\{i\}, \beta_y\{j\}, r\{k\}\}$, where $(\beta_x\{i\}, \beta_y\{j\}, r\{k\})$ is the fan lattice point nearest to the field point P.

Table 4.2: Values for fan line offset distance *d*, fan angle increment $\Delta\beta$, and fan line increment Δr in FAM simulations.

d	$\Delta\beta$	Δr
10 cm	0.72°	0.25 cm
20	0.57	0.25
30	0.48	0.25
40	0.41	0.25
50	0.36	0.25

Four different absorption geometries were considered: uniformly absorbing, absorbing and non-attenuating regions separated by an oblique plane, an on-axis spherical absorbing region, and an off-axis spherical absorbing region. All cases except for the the uniformly absorbing medium geometry are illustrated in Figure 4-36. These cases were chosen because of the relative ease with which the diffraction integral could be solved in the absorbing geometries. (For the second case, on oblique plane was chosen instead of a plane parallel to the source because in the parallel case FAM modified pressure fields differed rather trivially from the baseline pressure fields.) In detail, the geometries were:

1. In this geometry the semi-infinite medium (bounded by the plane of the FSUM transducer) was uniformly absorbing. The specific values of absorption α were:

   A. $\alpha = 0.05\,\mathrm{Np/cm}$ (mild absorption)

   B. $\alpha = 0.10\,\mathrm{Np/cm}$ (severe absorption)

   C. $\alpha = 0\,\mathrm{Np/cm}$ (no absorption)

   (The pressure field in the non-attenuating medium, Geometry 1C, is required before the FAM can be used. *N.B.*: The FAM is not used to approximate this field, since the attenuation factor $f = 0$ everywhere in this field. For an explanation of Np, see Footnote 8 on page 71.)

2. Here the medium was divided by an oblique plane into two regions of different absorption (but with uniform absorption within each region). The equation of the plane in the local transducer reference frame was $-x + z = 15.0\,\mathrm{cm}$, which intersects the beam axis at $(0, 0, 15)\,\mathrm{cm}$. In the region nearer the transducer, $\alpha = 0\,\mathrm{Np/cm}$; in the second region, on the other side of the plane:

   A. $\alpha = 0.05\,\mathrm{Np/cm}$

   B. $\alpha = 0.10\,\mathrm{Np/cm}$

3. Here the medium was divided into an axial spherical region (*i.e.* a sphere centered on the axis of the acoustic beam of the source), and a second region of different absorption comprising the rest of the semi-infinite medium. The sphere had radius $r = 2\,\mathrm{cm}$ and was centered at $(0, 0, 15)\,\mathrm{cm}$. Outside the sphere $\alpha = 0\,\mathrm{Np/cm}$, and inside the sphere:

   A. $\alpha = 0.05\,\mathrm{Np/cm}$

   B. $\alpha = 0.10\,\mathrm{Np/cm}$

4. This case was just like the previous one, except the spherical region was offset from the beam axis. The sphere had radius $r = 2\,\text{cm}$ but was centered at $(2, 0, 15)\,\text{cm}$. Again, outside the sphere $\alpha = 0\,\text{Np/cm}$, and inside the sphere:

   A. $\alpha = 0.05\,\text{Np/cm}$

   B. $\alpha = 0.10\,\text{Np/cm}$

The values of $\alpha = 0.05$ and $0.10\,\text{Np/cm}$ correspond to a range within which lies the nominal ultrasound absorption (at 1 MHz) of most soft tissues [35].

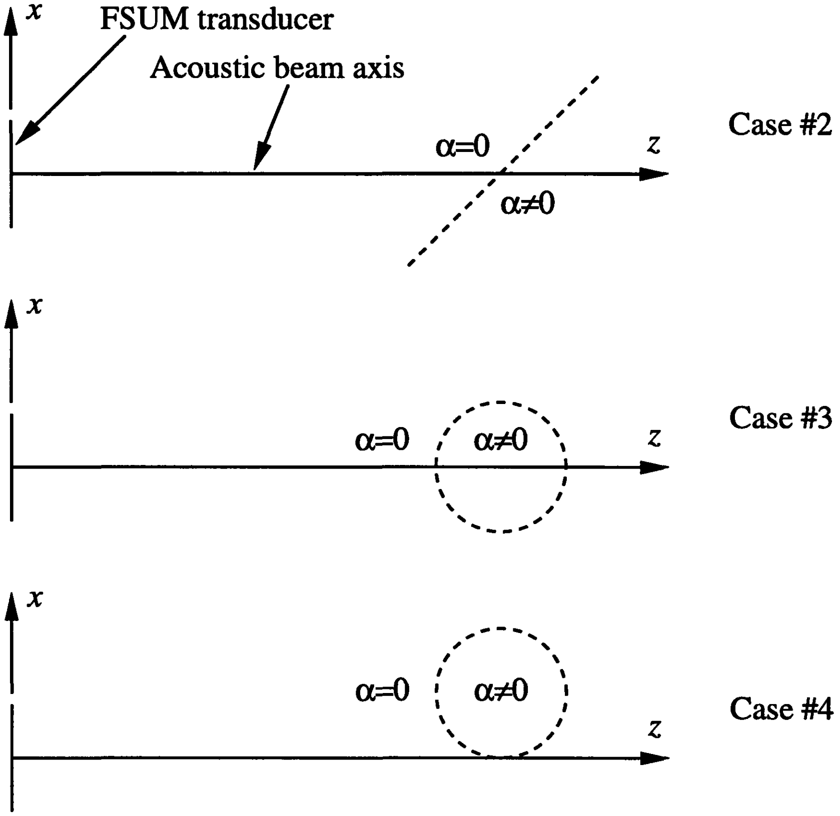

Figure 4-36: FAM validation geometries, drawn to scale. Case #2: An absorbing region and a non-attenuating region divided by an oblique plane; Case #3: An on-axis spherical region of absorption; Case #4: An off-axis spherical region of absorption.

To calculate attenuation from absorption in the baseline simulations, it was necessary to determine path lengths from the source subelements of the source to absorption region boundaries (*i.e.* planar or spherical boundaries), and from absorption region boundaries to field points. It was also necessary to specify absorption region geometries in transformed reference frames, since the source was subdivided into subelements, and the absorption geometry needed to be defined for each subelement. (Details concerning these calculations are given in Section B.6.) To calculate attenuation factors in the FAM simulations it was necessary to determine within which absorption region each fan lattice point resided. This determination was straightforward for planar and spherical geometries. (Refer to Section 2.4.1 for details concerning the planar geometry.)

Theoretical validation of the FAM will proceed in two parts: validation of the pressure phase $\angle p$ field, and validation of the pressure amplitude p_a field.

4.4.2.1 Pressure Phase Validation

All FAM simulations share the same $\angle p$ field with the $\angle p_0$ field (where p_0 is the baseline pressure field in a non-attenuating medium), because the FAM operates by attenuating the amplitude—but not altering the phase—of the p_0 field; *i.e.* $\Delta \angle p = 0$ for all FAM fields. This means that comparing the pressure phase fields of baseline simulations into absorbing media with the $\angle p_0$ field is equivalent to comparing pressure phase fields of corresponding baseline and FAM simulations into absorbing media. This also means that without performing even a single FAM simulation, the applicability of the FAM to a given geometry of *coherently* radiating acoustic sources can be assessed by comparing the presure phase fields of baseline simulations into absorbing media with the $\angle p_0$ field. (If the FAM fails phase validation tests, however, it is still possible that the FAM could pass amplitude validation tests for application to *incoherently* radiating sources.) Thus baseline simulations will be used in lieu of FAM simulations for phase validation.

Four metrics were used to compare the baseline pressure phase fields $\angle p$ in absorbing media (Geometries 1A, 1B, 2A, 2B, 3A, 3B, 4A, and 4B) with the baseline pressure phase field $\angle p_0$ in a non-attenuating medium (Geometry 1C), and all four metrics were based on the phase difference.[11] The first metric, $\overline{|\Delta|} \angle p \equiv \overline{|\angle p - \angle p_0|}$, was the *mean* absolute difference between $\angle p$ and $\angle p_0$ values at corresponding pressure grid points. The second metric,

---

[11] The phase difference $\angle p - \angle p_0$ was constrained between $-180°$ and $180°$, and the absolute value of the phase difference between $0°$ and $180°$.

$|\Delta|_{\max}\angle p \equiv \max\left(\,|\angle p - \angle p_0|\,\right)$, was the ***maximum*** absolute difference between corresponding $\angle p$ and $\angle p_0$ values. The remaining two metrics, $\overline{|\Delta|}\,\angle p_{10\%}$ and $|\Delta|_{\max}\angle p_{10\%}$, were the same as the first two metrics, respectively, except the comparisons were only made over the grid points for which $p > 10\%\,p_{\max}$, where $p_{\max}$ is the maximum amplitude of the p field. Metric calculations were performed over all pressure grid points, and results are summarized in Table 4.3.

Table 4.3: Comparison of the pressure phase fields in baseline simulations, using four metrics.

α	Geometry	$\overline{\lvert\Delta\rvert}\,\angle p$	$\lvert\Delta\rvert_{\max}\angle p$	$\overline{\lvert\Delta\rvert}\,\angle p_{10\%}$	$\lvert\Delta\rvert_{\max}\angle p_{10\%}$
0.05 Np/cm	1A	1°	111°	<1°	<1°
	2A	1	129	<1	2
	3A	2	56	<1	2
	4A	<1	18	<1	3
0.10	1B	1	149	<1	<1
	2B	1	142	<1	4
	3B	4	172	1	4
	4B	1	43	<1	5

In all geometries $\overline{|\Delta|}\,\angle p$ was essentially trivial, but $|\Delta|_{\max}\angle p$ ranged from substantial to huge. However, by confining the comparison to the most significant portion of the acoustic field (*i.e.* where the pressure amplitude field is at least 10% of its maximum value—which corresponds to a nominal acoustic intensity amplitude field that is at least 1% of its maximum value) the metrics improved considerably, with $\overline{|\Delta|}\,\angle p_{10\%}$ and $|\Delta|_{\max}\angle p_{10\%}$ less than or equal to 1° and 5°, respectively. The pressure field associated with Geometry 1B (for example) provides insight into why the pressure field is so small where $|\Delta|\,\angle p$ is large. Figure 4-37 shows a cross-section through the xz-plane of the p_a and $|\Delta|\,\angle p$ fields. This figure clearly demonstrates that regions of large $|\Delta|\,\angle p$ are significantly offset from the beam axis, where the vast majority of the acoustic energy is located. The same point is made from a different perspective in Figure 4-38, in which $|\Delta|\,\angle p$ is plotted against p_a for each grid point in the pressure field calculation. The lack of data points in the upper right-hand corner of the figure indicates that where p_a is large, $|\Delta|\,\angle p$ is not, and *vice versa*. Thus, for practical purposes, the $\angle p$ fields are essentially the same for the absorption geometries that were investigated.

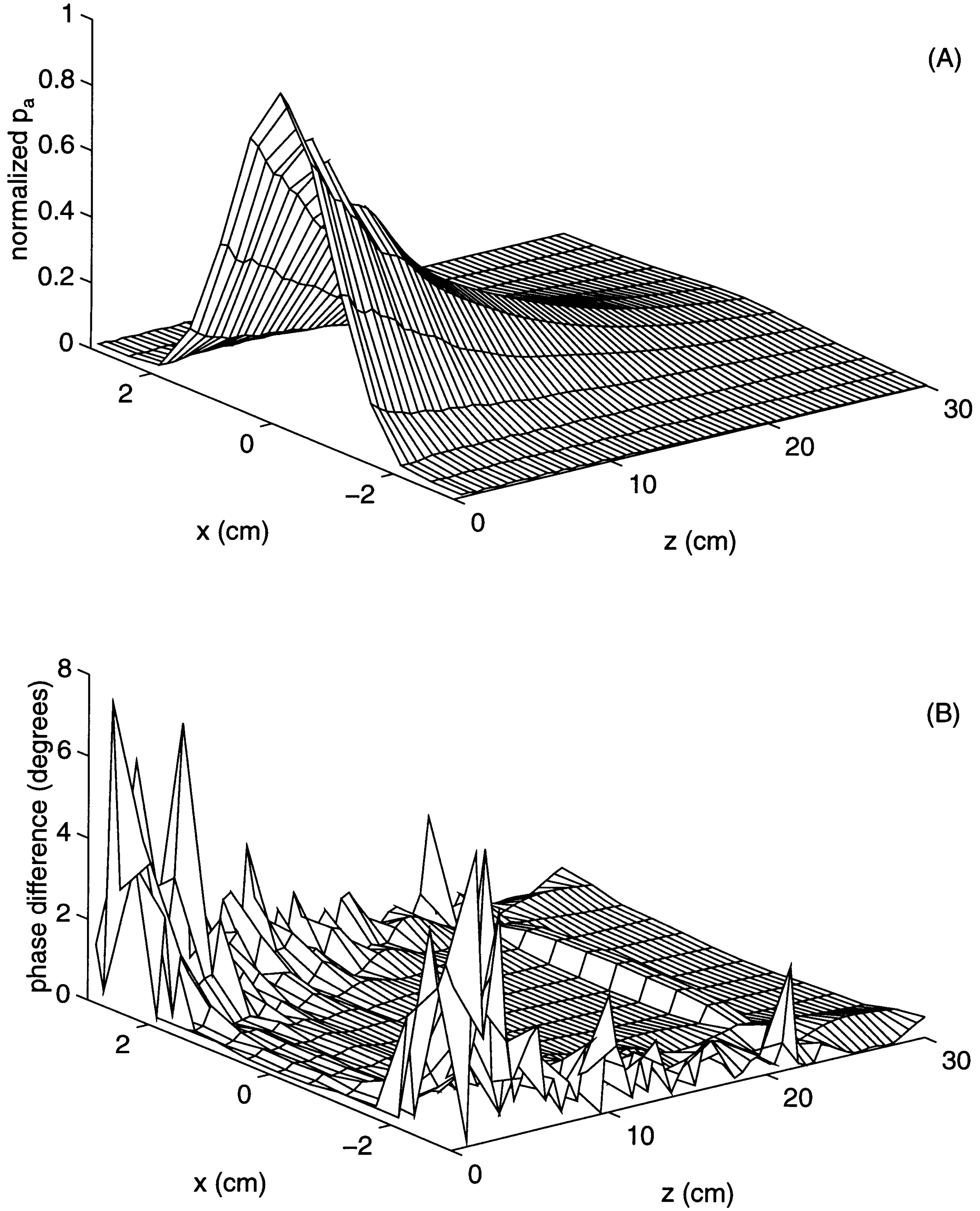

Figure 4-37: Cross-sections, for Geometry 1B, through the xz-plane of (A) the p_a field and (B) the $|\Delta| \angle p$ field.

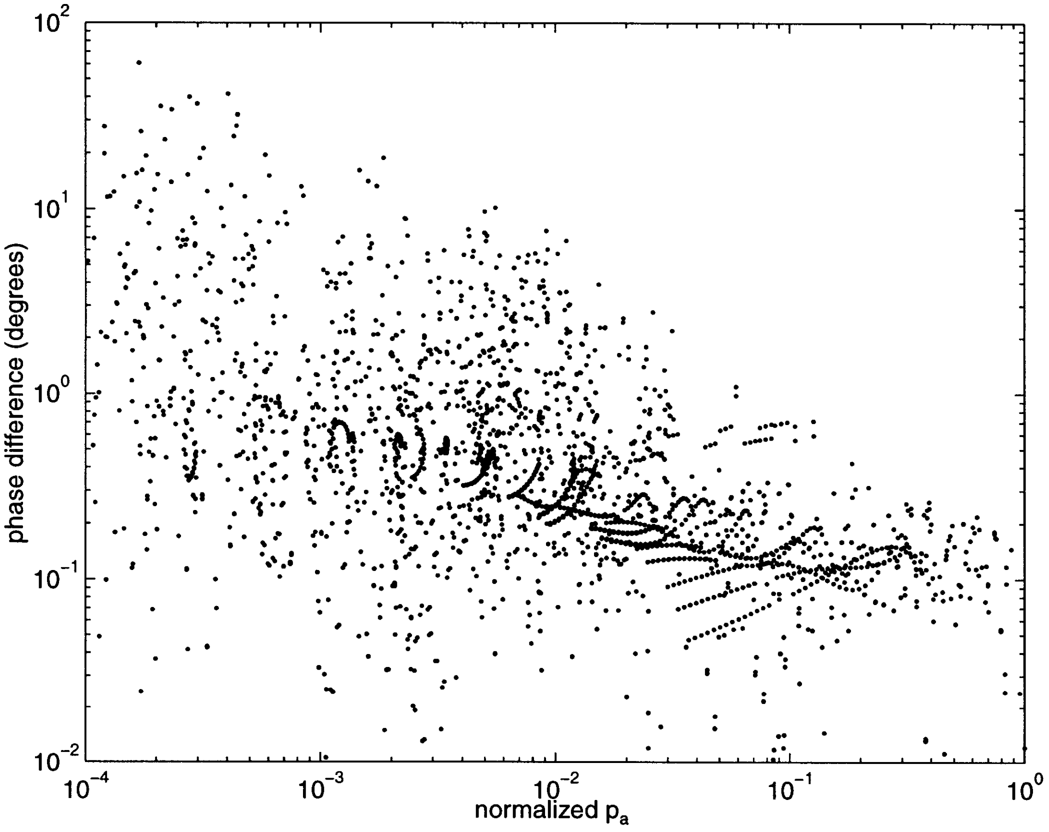

Figure 4-38: p_{a} vs. $|\Delta|\ \angle p$ for Geometry 1B.

4.4.2.2 Pressure Amplitude Validation

Unlike pressure phase validation, pressure amplitude validation actually does require FAM pressure field simulation. In this validation study, pressure amplitude p_a fields from FAM simulations for the absorption geometries were compared with their respective counterparts from the baseline simulations. Two metrics were used: $\overline{|\Delta|}\, p_\mathrm{a}$, the *mean* absolute difference in pressure amplitude, and $|\Delta|_\mathrm{max} p_\mathrm{a}$, the *maximum* absolute difference. As mentioned before, several different values of fan line offset distance d (and fan angle increment $\Delta\beta$) were investigated in the FAM simulation. Table 4.4 summarizes the results for the different absorption geometries and values of fan lines offset distance.

The data for $\overline{|\Delta|}\, p_\mathrm{a}$ indicate agreement that was almost embarrassingly good, and the data for $|\Delta|_\mathrm{max} p_\mathrm{a}$ show very good agreement as well. The results appear very robust with respect to the fan line offset distance d, meaning that variation in d from 10 to 50 cm, a substantial range, makes very little difference. If an "optimal" value for the fan line offset distance were chosen, however, it would probably be $d = 30\,\mathrm{cm}$.

4.4.2.3 Conclusions About Validation

The short version of this section is that the FAM was emphatically validated for the case of the FSUM transducer with Gaussian vibration. There are at least two obvious ways for improving results still further. One, use trilinear interpolation instead of the nearest neighbor method to determine the attenuation factor at an arbitrary field point. And two, in cases where the absorption geometry is defined continuously (as opposed to only at discrete lattice points), implement the FAM as a continuous method (in much the same way the baseline simulations were performed).

How is it possible that the FAM results could be so extraordinary? Gaussian sources are generally well-behaved, and surely this was a significant contributor to the success of the FAM validation. Simulations have been performed with non-Gaussian sources, most notably uniformly vibrating sources. Preliminary analysis suggests that amplitude fidelity of the FAM is not bad for the uniform source, but not nearly as good as for the Gaussian source. (Phase fidelity for the uniform source was not addressed.) It is also possible that for different source shapes or vibration patterns, the FAM could be more sensitive to the choice of fan line offset

Table 4.4: Comparison of normalized pressure amplitude p_{a} and phase $\angle p$ fields between FAM and baseline pressure fields, using two metrics.

Geometry	d	$\overline{\lvert\Delta\rvert}\,p_{\mathrm{a}}$	$\lvert\Delta\rvert_{\mathrm{max}}p_{\mathrm{a}}$
1A	10 cm	0.01%	0.21%
	20	0.01	0.21
	30	0.01	0.21
	40	0.01	0.21
	50	0.01	0.21
2A	10	0.01	0.19
	20	0.01	0.19
	30	0.01	0.19
	40	0.01	0.19
	50	0.01	0.19
3A	10	0.03	1.10
	20	0.03	1.10
	30	0.03	1.10
	40	0.03	1.10
	50	0.03	1.10
4A	10	0.05	2.20
	20	0.05	2.20
	30	0.04	2.20
	40	0.05	2.20
	50	0.05	2.20
1B	10 cm	0.10%	1.10%
	20	0.09	1.10
	30	0.09	1.10
	40	0.10	1.10
	50	0.11	1.10
2B	10	0.19	2.20
	20	0.16	2.20
	30	0.17	2.20
	40	0.19	2.20
	50	0.21	2.20
3B	10	0.05	2.20
	20	0.05	2.20
	30	0.05	2.20
	40	0.05	2.30
	50	0.05	2.20
4B	10	0.10	4.60
	20	0.09	4.60
	30	0.09	4.60
	40	0.09	5.50
	50	0.09	4.60

distance. In any case, preliminary observations suggest that Gaussian transducers are preferable for acoustic modeling by the FAM, and designers of ultrasound devices could simplify acoustic modeling efforts by building devices with Gaussian sources.

In cases in which the FAM achieves reasonable amplitude fidelity but poor phase fidelity, the FAM can still be prudently applied if sources radiate incoherently. And in cases in which the FAM realizes mediocre amplitude fidelity, all is not necessarily lost, at least in the application of ultrasound power to induce biological hyperthermia. For example, the FAM could potentially spatially shift peaks in the pressure field in an absorbing medium, resulting in poor agreement of the peaks between the FAM and actual fields; however, as suggested in the quote on page 145, such variations could be attenuated in the temperature elevation field, producing better agreement where it counts: between the modeled and actual temperature fields.

4.5 Summary of SAR Modeling Results

First, a method was developed to solve rapidly the Rayleigh-Sommerfeld diffraction integral to calculate the pressure field in a uniformly absorbing medium from a non-uniformly vibrating rectangular or cylindrical wedge acoustic source (Section 4.1). Second, a parametric model was developed for the acoustic beam—specifically, the pressure amplitude field—from an individual FSUM transducer radiating into a non-attenuating medium; pressure amplitude field measurements and acoustic simulations of a non-uniformly vibrating FSUM transducer based on the solution of the diffraction integral were both used in this model development (Section 4.2). Third, a model was developed to determine the pressure amplitude field from multiple simultaneously excited FSUM transducers radiating into a non-attenuating medium; this model was based on a scheme of summing pressure field contributions from the parametric beam models of individual FSUM transducers. The most accurate summing scheme was mathematically equivalent to giving the parametric beam models for individual FSUM transducers a phase term proportional to the distance between the field point in the beam and the center of the transducer surface (Section 4.3). Fourth and last, the Fanned Absorption Method (FAM) was developed to take the pressure field from a source radiating into a non-attenuating medium, and modify the field to account for absorption; this method was validated using acoustic simulations based on the solution of the diffraction integral for a Gaussian source of the size of an FSUM transducer (Section 4.4).

The significance of the FAM in modeling the FSUM device is that, according to the FAM pressure phase validation study, the FAM does not significantly alter the pressure phase field from a Gaussian source of the size of an FSUM transducer. This means that the acoustic beam models of individual transducers are expected to have essentially the same pressure phase field, with or without absorption in the medium, so the beam models should superpose according to the same scheme, with or without absorption. Thus to estimate the pressure field from multiple FSUM transducers, the transducer beam models are individually modified by the FAM, and then superposed by the distance-weighted phasing scheme elaborated in Section 4.4.[12]

---

[12] The reader is to be congratulated at this juncture for reaching the end of what may well be the longest dissertation chapter in the history of academics.

Chapter 5

Integration of Models in Treatment System

> *He say "One and one and one is three"*
> *Got to be good-looking 'cause he's so hard to see*
> *Come together right now over me.*
>
> — John Lennon and Paul McCartney, verse in the song "Come Together"
> on the Beatles album *Abbey Road*, 1969

Originally HYPER/Plan was conceived as a *geometric* hyperthermia treatment planner, which means graphical representations of the patient and treatment applicator are interactively positioned and oriented on the monitor until the human planner is satisfied with the visual appearance of the plan. In other words, based only on the relative geometric positions of the patient and applicator, the treatment plan looks like it will heat the target volume effectively.

Such a planning strategy does not use power deposition or thermal modeling. Integrating these kinds of models into a geometric planning system is desirable for at least two reasons. First, treatment planning is improved. In general there is a nominal thermal objective for hyperthermia treatment, *e.g.* to elevate all tumor tissue to at least 43°C for at least 30 min, while keeping other tissues below 41°C. With purely geometric planning, the thermal objective cannot be addressed prior to treatment administration; to generate a treatment plan that considers the thermal objective, power deposition and thermal models must be used.

Second, heat transfer in biological systems is not sufficiently well described that the predicted temperature field (calculated during treatment planning) is considered to be a sufficiently accurate reflection of the temperature field that actually occurred during treatment administration. Even ignoring theoretical issues associated with the validity of diffusive and convective heat transfer equations, there are a number of material power deposition and thermal properties which may not be known more accurately than to 10%, 20%, or even greater error. In practice, therefore, thermal measurements are taken continually during treatment administration. If the spatial density of these measurements is sufficiently great, there is no need to interpolate and extrapolate temperature field values between and around measurement sites. This is the ultimate objective of a number of non-invasive, 3-D temperature field measurement systems, based on MRI [104], electrical impedance tomography (EIT) [9], microwaves [20], etc. In practice in the hyperthermia clinic, however, thermal measurements are taken using invasive sensors on needle probes. Sensors continually measure temperature at a finite number of discrete locations, and these measurements can be used to modify the predicted thermal fields to produce thermal fields that give a more accurate picture of the temperature field that occurred during treatment. This combination of the predicted thermal field with the thermal measurements is called **thermal reconstruction**, and it can be used to quantitatively evaluate the treatment. If the thermal reconstruction can be performed sufficiently quickly, it can be used to monitor treatment in real time or quasi-real time.

Thus for ease and rapidity of treatment 3-D thermal planning and evaluation, *rapid* power deposition and thermal models are necessary. The work developed in Chapter 4, culminating in parametric descriptions of acoustic beams from FSUM transducers and the Fanned Absorption Method (FAM), responded to the need for rapid ultrasound power deposition modeling; and the Finite Basis Element Method (FBEM), conceived by Dr. William H. Newman and jointly developed by Drs. Newman and Gregory T. Martin, responded to the need for rapid thermal modeling. This chapter details the integration within the AVS platform of the geometric planning system with power deposition modeling, thermal modeling, and thermal visualization tools for viewing 3-D SAR and thermal fields. The next chapter, Chapter 6, presents some results of clinical interest that are based on this integration.

5.1 Overview of Integration

The elements necessary to achieve the integration of 3-D geometric, power deposition, and thermal modeling are united in a simplified flow chart in Figure 5-1. The flow chart is divided horizontally into three regions: Geometry, Power Deposition, and Heat Transfer.[1] The first column, Geometry, indicates whence comes the volumetric model of the patient, which is necessary for power deposition and thermal modeling. The patient is imaged (by CT), and the patient image is transformed first into a surface model (using IMEX and Mosaic), and then a volumetric model (using Volumizer). To reiterate, the volumetric model basically consists of a lattice of points, and each point is associated with the type of anatomic organ in which it resides.

The middle column corresponds to Power Deposition. Ignoring for the moment the Thermometry box in Figure 5-1, the SAR model is observed to require the patient volumetric model, tissue power deposition properties, and information about the power applicator. In practice the principal power deposition property considered for ultrasound devices is the ultrasound absorption coefficient α. The nominal 3-D α field is obtained directly from the tissue types given in the patient volumetric model. The Applicator box signifies the geometry of the power applicator (both its own geometry and its position and orientation relative to the patient) and the power excitation pattern.

The third column corresponds to Heat Transfer, and in many ways it is similar to the Power Deposition column. The thermal model also requires the patient volumetric model (which may include thermal boundary conditions), and in addition it requires the SAR field and tissue thermal properties. Tissue thermal properties include mainly thermal conductivity k and blood perfusion w. As in the case of α, nominal 3-D k and w fields are obtained from the patient volumetric model.

The 3-D SAR or temperature field, once calculated, can be displayed on the patient anatomy by a variety of visualization tools, and this visualization is termed here **thermal visualization**. An interactive aspect of the integrated system is illustrated in Figure 5-1 by the arrow with the dotted line from 3-D thermal visualization to Applicator. Specifically, thermal visualization during treatment planning or treatment monitoring may indicate that heating can be improved by changing the position or excitation pattern of the applicator.

Thus far in this discussion Thermometry has not been considered; in other words, only the

---

[1] It is clear from the lyrics at the beginning of this chapter that the Beatles anticipated the advent of an integrated hyperthermia treatment system. Consider: " 'One [geometric] and one [power deposition] and one [heat transfer] is three [types of modeling].' " The next line, "Got to be good-looking 'cause he's so hard to see," surely alludes to visualization, in the oblique fashion typical of the Beatles. And finally, the title and essence of the song, "Come Together," refers to clinical integration of these parts for hyperthermia therapy.

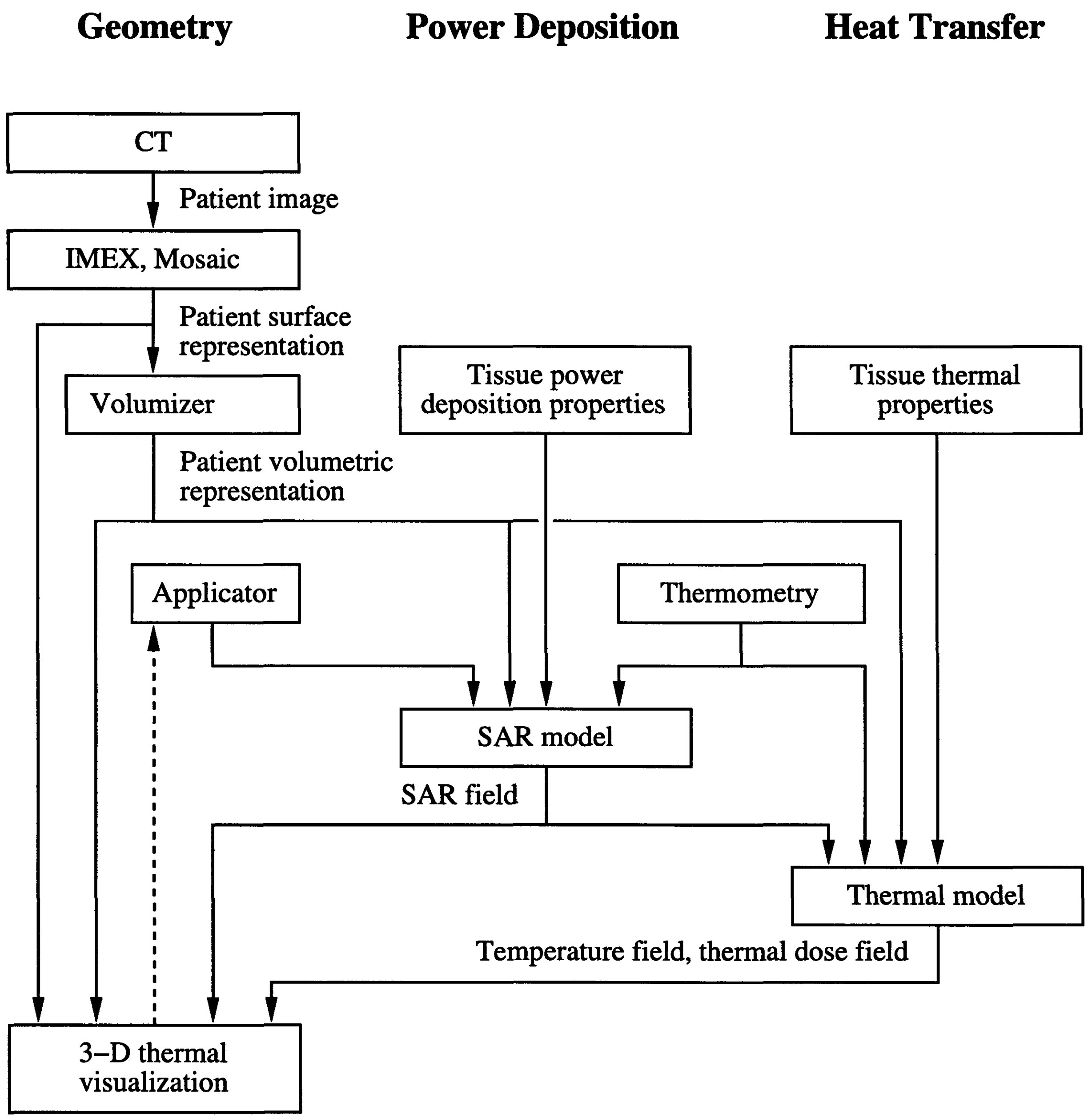

Figure 5-1: 3-D thermal visualization system with integrated geometric, power deposition, and thermal modeling.

treatment planning phase of therapy has been addressed, with predicted SAR and temperature fields. In Figure 5-1 the $\boxed{\text{Thermometry}}$ box is sandwiched between the Power Deposition and Heat Transfer columns, and this position is appropriate because thermometry can be used directly for temperature measurement and indirectly for SAR measurement. With the addition of spatially discrete SAR and temperature measurements, SAR and temperature fields can be reconstructed. As mentioned before, these reconstructed fields can be visualized on the patient anatomy with thermal visualization tools.

Temperature and SAR are not the only quantities that can be measured, and if other power deposition or thermal parameters are measured these measurements can be included into field prediction and reconstruction calculations. Acoustic absorption α cannot be measured by thermometric means alone, although it is certainly possible to measure it, but thermal conductivity k and blood perfusion w can be measured by thermometric means. Spatially discrete measurements of α, k, or w can be incorporated into the relevant parameter field in any one of several ways. First, the field can take on the measured value everywhere within a sphere (or other volume) around the measurement site. Second, the field can take on the measured value everywhere within the anatomic organ containing the sensor site (or the average of measured values if there are multiple measurement sites in the same organ). And third, a more sophisticated model of the parameter, based on a physical and physiological understanding of the parameter, can be used to reconstruct the parameter field in a fashion that is analogous to SAR and temperature field reconstruction.

Thermal dose is a function of temperature integrated in time, *i.e.* $D = \int_{t_1}^{t_2} F\{T\}\, dt$; in a single number thermal dose attempts to quantify thermal history [12]. If the temperature field is continually reconstructed, then the thermal dose field can be continually updated. Needless to say, the thermal dose field can be visualized on the patient anatomy using the thermal visualization tools.

5.2 Elements of Integrated System

Given the overview of the integrated system, we now proceed to descriptions of the individual elements that make up the whole. In cases in which the element has already been described, the reader is referred to the relevant discussion.

5.2.1 Geometry

The first three boxes in the Geometry column of Figure 5-1 concern the patient geometry, and the fourth box relates to the power applicator. The initial patient image, given in `<.ima>` file format, can be considered a volumetric representation of the patient. IMEX is used to contour relevant anatomic organs on the patient image, and Mosaic connects the organ contours to create a patient surface representation. Volumizer creates a patient mesh, a volumetric representation, from the surface representation. There are two important differences between the volumetric representations of the patient given by CT and Volumizer. First, the former is essentially the 3-D radiopacity field of the patient (given in Hounsfield units), whereas the latter is a 3-D tissue type field. And second, the patient mesh produced by Volumizer is the grid on which power deposition and thermal calculations are performed, so it is more directly relevant than the field produced by CT. Brief discussions of the patient image, IMEX, and Mosaic are given in Section 2.3 on page 36, and an extended development of Volumizer is given in Section 2.4 on page 40.

HYPER/Plan, the geometric hyperthermia treatment planning system mentioned briefly in Section 2.2 on page 36, produces in the AVS Geometry Viewer images of the 2-D surfaces of the patient organs and the power applicator (as shown in Figure 2-2 on page 39). Widgets provide interactive control of the position and orientation of the patient and applicator, and also of the transducer excitation pattern. In HYPER/Plan, objects (*viz.* the patient and applicator) are first translated laterally (x-axis in HYPER/Plan), vertically (y-axis), and anteroposteriorly (z-axis), and then rolled (rotated about the x-axis), pitched (y-axis), and yawed (z-axis). Because the order of the translation and three rotation transformations is fixed, the final position and orientation of the objects are well-defined.

5.2.2 Power Deposition

The subject of ultrasound power deposition modeling has been discussed extensively in Chapters 3 and 4. Some of these discussions concerned acoustic sources in general, and some concerned the transducers of the FSUM device specifically. For the remainder of this chapter and all of the next, however, only the FSUM device will be considered. The geometry of this device was given in Section 4.3.1 on page 132, but this description omitted an important mode of operation of the device called **wobulation**, illustrated in Figure 5-2, in which the spherical shell undergoes a quasi-precessional motion within the device housing. The transducers are affixed to a spherical shell, which is connected by an arm to a rigid housing. (The rigid housing and a flexible cover together enclose the spherical shell of transducers and contain a degassed water bath.) In wobulation mode, the arm rotates at angular velocity ω_{wob} about the axis labeled a, and the spherical shell rotates at angular velocity $-\omega_{\text{wob}}$ about the axis labeled a', where a' precesses about a. The speed of wobulation is adjustable, but typically the arm rotates at 0.5 Hz in the clockwise direction, facing the radiating side of the transducers (*i.e.* $\omega_{\text{wob}} = -3\,\text{rad/s}$ in the (nominal) z direction in the FSUM coordinate system—see Figure 4-23, page 133). Although dramatic temporal fluctuations in the SAR field may result from this mode of heating, temporal fluctuations in the resulting temperature field are relatively small. This is because the time constant for thermal equilibration is given roughly by the inverse of perfusion w^{-1} (where w is in the units ml blood/s–ml tissue), and in physiologic systems inverse of perfusion has values considerably longer than the short times associated with the revolution of wobulation, $\mathcal{O}(\omega_{\text{wob}}^{-1})$. (Equation B.39 on page 249 provides further insight.) A reasonable strategy for performing power deposition modeling with wobulation, then, is to divide the continuum of one complete, 360° rotation of the arm into n discrete positions at regular intervals of $(360/n)^\circ$, perform power deposition modeling at each position, and average the n SAR fields. Appendix B.7 addresses the issue of how to transform coordinates between the rigid housing and spherical shell reference frames, given the angular position of wobulation, $\theta_{\text{wob}} = \omega_{\text{wob}} t$.

The implementation of the power deposition model for the FSUM is based on the modified Gaussian beam description developed in Section 4.2, the pressure superposition scheme developed in Section 4.3, and the FAM developed in Section 4.4. To review, the amplitude of the complex pressure field from each FSUM transducer is given by the modified Gaussian beam description multiplied by the local attenuation factor determined by the FAM, and the phase of this complex pressure field is distance-weighted. The complex pressure field contributions from all FSUM transducers are then simply added (as complex fields) to produce the pressure field

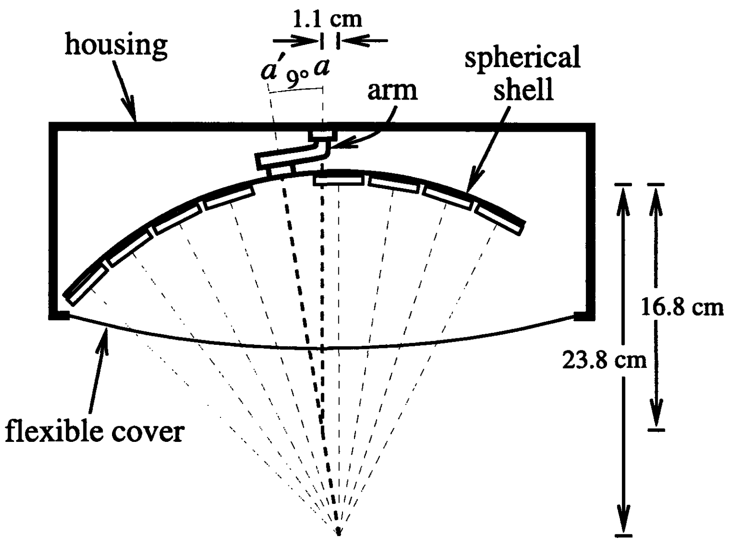

Figure 5-2: Geometry of the wobulation mode of the FSUM.

from the entire FSUM device.

As previously mentioned (see Section 3.1.6, page 70), tissue-air and soft tissue-bone interfaces are problem areas in power deposition modeling because acoustic waves are largely reflected at these boundaries. In particular, soft tissue-bone interfaces can be the site of substantial unwanted heating. When an acoustic wave propagates through soft tissue towards bone, the significant majority of the energy of the wave is reflected at the interface due to the poor acoustic impedance matching between soft tissue and bone; the fraction of wave energy that does cross the boundary into bone, however, is absorbed with such relish that dramatic levels of SAR can occur in the bone. In addition, if the reflected wave passes back through the same soft tissue whence it came (a normal reflection, as opposed to an oblique reflection), then on the soft tissue side of the interface SAR is nearly doubled by the reflection (compared to acoustic wave propagation without reflection). This acoustic phenomenon of a wave propagating and attenuating twice through the same region of tissue—first as an incident wave, then as a reflected wave—can also be observed at soft tissue-air interfaces, where the acoustic impedance mismatch results in practically complete reflection of the acoustic wave.

These interfaces are clearly troublesome, both from the perspective of the acoustic modeler who wants to model accurately the acoustic physics, and that of the clinician who wants to deliver efficacious but safe heating. The way they were addressed in the current FSUM acoustic model was to ignore them; specifically, when FAM fan lines entered air or bone regions the attenuation factor was simply set to zero for the rest of the fan line (in the distal direction). This protocol was not experimentally validated, but some level of justification can nevertheless be achieved. In particular, when pressure field predictions indicate that an acoustic beam has substantial energy in the region at which a FAM fan line crosses a soft tissue-air or soft tissue-bone interface, the user can be notified that substantial heating may occur, and the treatment plan should be adjusted. In the treatment administration phase, thermometry or complaints from the patient would generally indicate that excessive SAR (or temperature) elevation occurred, so prompt action could be taken to change the treatment geometry; the new treatment geometry, which would not suffer from an unacceptable SAR pattern, would then serve as the basis for thermal reconstruction.

5.2.3 Heat Transfer

The thermal model integrated into the treatment system is the Finite Basis Element Method (FBEM), a numerical technique optimized for the solution of the **bioheat transfer equation** (BHTE), or the Pennes BHTE:

$$\frac{1}{\alpha}\frac{\partial T}{\partial t} = \nabla^2 T - \lambda^2 T + \frac{\dot{Q}}{k} \tag{5.1}$$

where α is thermal diffusivity, T is tissue temperature elevation, t is time, λ is **inverse perfusion length,** $\dot{Q}$ is SAR, and k is thermal conductivity. $\lambda^2 \equiv w\rho_{\mathrm{bl}}c_{\mathrm{bl}}/k$, where w is perfusion, ρ_{bl} is blood density, and c_{bl} is blood specific heat capacity. This equation is the normal heat conduction equation with an additional $\lambda^2 T$ term, which models the convective heat transfer of perfusion as a temperature-dependent heat sink. The effects of metabolic heat generation are implicitly taken into account in the BHTE through the use of the tissue temperature elevation T, which is relative to the tissue baseline temperature—*i.e.* the tissue temperature without the power deposition (SAR) of treatment. In this model of tissue heat transfer, blood perfusion attenuates thermal perturbations as they conduct through tissue. This fact is used to computational advantage in FBEM thermal calculations by considering only the portion of the SAR field that is "thermally near" the field point of interest.

The BHTE traces its origins to the landmark paper of Pennes [82]. A number of investigators have looked into the heat transfer mechanisms associated with **thermally significant vessels** [10, 11, 19, 51, 52], modeling heat transfer with various vessel geometries including counter-current arrangements; but in many cases the BHTE models tissue heat transfer sufficiently accurately [17, 18, 86, 102], and it is substantially simpler, both conceptually and computationally, than models that consider vessel geometry.

A brief formulation of the FBEM is now presented to illustrate how it is used to solve the BHTE; the reader is referred to Martin [65], Martin *et al.* [66], Newman [73], and Newman *et al.* [75] for further details, and Newman *et al.* [74] for early related work. The formulation is distilled here to a simple case designed to illustrate the two principal features of the FBEM that allow rapid thermal field computation. The first feature limits the volume of integration over which thermal calculations are performed, and the second precomputes Green's function solutions for finite power sources.

The specific case at hand is the steady-state temperature field solution for a heated volume of infinite spatial extent and uniform thermal properties (*i.e.* uniform k and w). The SAR field can be spatially heterogeneous, but it must be temporally constant. In this case, the temperature elevation $T\{\vec{r}\}$ at a point $\vec{r}$ due to a point power source $\dot{q}\{\vec{p}\}$ at a point $\vec{p}$ is given by:

$$T\{\vec{r}\} = \frac{\dot{q}\{\vec{p}\}\lambda}{k}\, u_{\mathrm{pt}}\{\vec{p},\vec{r}\} \tag{5.2}$$

where $u_{\mathrm{pt}}\{\vec{p},\vec{r}\}$ is the dimensionless **Green's function** solution to the BHTE for a point source.

The temperature elevation field from an entire heated region can be computed as the superposition of the temperature elevation fields from point power sources. Thus, the temperature elevation $T\{\vec{r}\}$ at a point $\vec{r}$ due to heating in a region is given by:

$$T\{\vec{r}\} = \int_V \frac{\dot{Q}\{\vec{p}\}\lambda}{k}\, u_{\mathrm{pt}}\{\vec{p},\vec{r}\}\, dV \tag{5.3}$$

where V is the infinite domain volume, dV is a differential volume located at $\vec{p}$, and $\dot{Q}$ is SAR. ($\dot{Q}\, dV$ in Equation 5.3 corresponds to $\dot{q}$ in Equation 5.2, with $\dot{Q}\, dV$ approaching the point source $\dot{q}$ as dV shrinks to a point.)

For a point power source in a spatially infinite volume of uniform thermal properties, the Green's function solution is:

$$u_{\mathrm{pt}}\{\vec{p},\vec{r}\} = \frac{e^{-\lambda d}}{4\pi\lambda d} \tag{5.4}$$

where $d = ||\vec{r} - \vec{p}\,||$. A critical observation to make here is that $u_{\text{pt}}\{\vec{p}, \vec{r}\}$ attenuates exponentially with distance d, or, equivalently, with the dimensionless parameter λd. This means that an accurate $T\{\vec{r}\}$ calculation can be performed that only considers the contributions of the SAR field in a limited volume V' within a distance n/λ of $\vec{r}$, where $V' \subset V$, and accuracy increases with n, the number of perfusion lengths. Thus the infinite volume V can be divided into the "thermally near" region V' and the "thermally far" region $V_0 = V - V'$; in addition, V' can be divided into N subvolumes V_i, with $V' = \sum_{i=1}^{N} V_i$. Then Equation 5.3 can be transformed into:

$$T\{\vec{r}\} = \sum_{i=0}^{N} \int_{V_i} \frac{\dot{Q}\{\vec{p}\}\lambda}{k} u_{\text{pt}}\{\vec{p}, \vec{r}\}\, dV_i = \sum_{i=0}^{N} \Theta_i\{\vec{r}\} \tag{5.5}$$

where Θ_i is the **Finite Basis Element** (FBE), the temperature elevation field due to the SAR field in the volume V_i. Now although $\Theta_i\{\vec{r}\} \equiv \int_{V_i} (\dot{Q}\{\vec{p}\}\lambda/k) u_{\text{pt}}\{\vec{p}, \vec{r}\}\, dV_i$, when SAR does not vary substantially over the subvolume V_i then Θ_i can be accurately approximated by:

$$\Theta_i\{\vec{r}\} \approx \frac{\dot{Q}\{\vec{p}_i\}\lambda}{k} \int_{V_i} u_{\text{pt}}\{\vec{p}, \vec{r}\}\, dV_i = \frac{\dot{Q}\{\vec{p}_i\} V_i \lambda}{k} u_{V_i}\{\vec{p}_i, \vec{r}\} \tag{5.6}$$

where $\vec{p}_i$ is the center of the subvolume V_i and $u_{V_i}\{\vec{r}\}$ is the Green's function solution for the uniformly heated subvolume V_i at $\vec{r}$. u_{V_i} can be evaluated explicitly; for example, for a spherical subvolume V_i of radius a and centered at $\vec{p}_i$:

$$u_{\text{sph}}\{\vec{p}_i, \vec{r}\} = \begin{cases} \dfrac{3}{(\lambda a)^2} \left[1 - (1 + \lambda a) e^{-\lambda a} \dfrac{\sinh \lambda d}{\lambda d} \right] e^{\lambda d} u_{\text{pt}}\{\vec{p}_i, \vec{r}\}, & 0 \le d \le a \\ \\ \dfrac{3}{(\lambda a)^2} \left(\cosh \lambda a - \dfrac{\sinh \lambda a}{\lambda a} \right) u_{\text{pt}}\{\vec{p}_i, \vec{r}\}, & d > a \end{cases} \tag{5.7}$$

(See Equations 3.15 and 3.16 in [65].) Thus Equation 5.5 is computationally simplified because the FBEs can be calculated explicitly and quickly, and in practice the contributions of only a relatively few (compared with conventional FEM schemes) finite sources need be considered.[2] These are the most important strengths of the FBEM (at least in terms of its computational speed).

The case of a *finite* heated volume with uniform thermal properties is now considered. Each thermal boundary surrounding this region falls into one of three categories: thermal boundary

---

[2] The calculation of Θ_0, the temperature elevation field from heating in the "thermally far" region V_0, is a special case. When it is desired to calculate Θ_0—and this may not be necessary, given V_0 is thermally far from the field point of interest—a nominal $\dot{Q}\{\vec{p}_0\}$ and $\vec{p}_0$ are used.

of the first kind (constant temperature), second kind (constant heat flux), and third kind (forced convection equals heat flux). The thermal contribution from each thermal boundary condition is divided for solution into homogeneous and non-homogeneous components, T_{h} and T_{nh}, respectively. Furthermore, boundaries are approximated by one of two geometries, representing the ends of a spectrum: locally planar, and locally spherical.

Green's function solutions for the homogeneous thermal boundary conditions of all three kinds and both geometries can be computed by the method of images in a manner analogous to the calculation of the acoustic pressure field from an acoustic source in a region bounded by a planar rigid boundary (see Section 3.1.4, page 66). For the planar case, for example, to achieve a homogeneous thermal boundary of:

1. the *first* kind, each power source within the volume is mirrored by an equal (but opposite) virtual power sink mirrored on the opposite side of the thermal boundary;
2. the *second* kind, each source is mirrored by an identical source;
3. the *third* kind, each source is mirrored by an empirically determined source that matches conductive and convective heat flux at the boundary.

A similar though more complicated formulation exists for the spherical boundary geometry (see [65, 66] for details).

Non-homogeneous temperature elevation field contributions T_{nh} for thermal boundary conditions of all three kinds and both geometries can be computed as well. Using the planar case as an example again, for a field point at a distance d from the non-homogeneous thermal boundary, the non-homogeneous temperature elevation field is given for the thermal boundary of:

1. the *first* kind: $T_{\mathrm{nh}_1}\{d\} = T_{\mathrm{b}} e^{\lambda d}$, where T_{b} is the temperature of the boundary;
2. the *second* kind: $T_{\mathrm{nh}_2}\{d\} = \dot{q}''_{\mathrm{b}} e^{\lambda d}/k\lambda$, where $\dot{q}''_{\mathrm{b}}$ is the heat flux at the boundary;
3. the *third* kind: $T_{\mathrm{nh}_3}\{d\} = T_\infty e^{\lambda d}/(1 + \lambda L/\mathrm{Bi}) = T_\infty e^{\lambda d}/(1 + k\lambda/h)$, where T_∞ is the far fluid temperature elevation, L is an arbitrary length scale, $\mathrm{Bi} \equiv hL/k$ is the Biot number, and h is the heat transfer coefficient at the boundary.

Again, a similar but more complicated formulation exists for the spherical geometry (see [65, 66] for details).

The essence of the FBEM formulation has now been presented. There are a number of peripheral issues that could still be addressed, but only two will be considered here. First, if the SAR field is divided into finite spherical subvolumes (as is the preferred custom to date), there will be regions of overlap and/or vacant spaces between adjacent power sources. If the volume contained in overlap does not equal that in vacant spaces, then a **packing factor** f must be introduced to compensate; *viz.*, $\int_V \dot{Q}\{\vec{p}\}\, dV = f \sum_{i=0}^{N} \dot{Q}\{\vec{p}_i\}\, V_i$. For the case of hexagonally close-packed spheres of uniform size,[3] $f = 3\sqrt{2}/\pi \approx 1.35$.

Second, the thermal lattice (comprising points at which temperature is calculated) need not be the same as the power deposition lattice (comprising points at which SAR is given), which affords a certain amount of flexibility. In addition, the SAR field is decoupled from thermal boundary conditions in the FBEM formulation, so interactive changes in one do not require repeated calculations of the other.

5.2.4 Thermal Visualization

Various thermal visualization tools were considered in the course of this project. These tools combine 3-D patient geometry with 3-D thermal fields to convey how the thermal fields spatially relate to the patient. Thermal fields were put into the AVS field structure, a structure which accommodates with equal facility predicted, reconstructed, SAR, temperature, temperature elevation, and thermal dose fields. This field structure, literally a C structure called `AVSfield`, contained thermal data in a 3-D array, with thermal data associated with a 3-D uniform lattice.[4] The tissue type field identified tissue type on the same coordinates as those of the thermal fields.

Thermal visualization tools were investigated in three principal areas:

- Slicing—thermal parameters displayed in pseudocolor on 2-D planar slices through the 3-D thermal field;

---

[3] This calculation of packing factor is considerably simplified by recognizing that hexagonal close-packed (HCP) and face-centered cubic (FCC) crystalline forms share the same density, and then calculating the packing factor for the FCC geometry. See Chapter 2 in Barrett *et al.* [7] for a discussion of crystal structure.

[4] An `AVSfield` structure can actually contain one of three different coordinate descriptions: uniform, rectilinear, or irregular. For simplicity, however, only the uniform type of `AVSfield` was used for thermal fields.

- Surface washing—thermal parameters displayed in pseudocolor on the tumor surface;
- Volumetric plotting—thermal parameters graphed as tumor volume fraction above the indexed thermal parameter.

In the next chapter, Chapter 6, predicted and reconstructed SAR and temperature fields will be presented using the slicing and volumetric plotting tools.

There are a number of possible variations for the slicing tool in particular. For example, slices can be arbitrarily oriented, or they can be restricted to one or more principal planar orientations. The pseudocoloring scheme, to give another example, can use a finite number of discrete colors or an entire continuum of colors. The specific slicing tool presented in Chapter 6 gives 2-D slices in the same planes in which organ contours were made using IMEX. In fact, these contours are superimposed on the 2-D thermal field slice, and to provide additional geometric context a gray plane is displayed through the relevant plane of the patient in the AVS Geometry Viewer.

5.2.5 Thermal Reconstruction

For treatment monitoring and evaluation, 3-D thermal fields can be reconstructed from a combination of the predicted thermal fields and spatially discrete thermal measurements. In thermal reconstruction, predicted fields provide the functional form of the reconstructed field, which is then multiplied by a constant that minimizes error at the discrete measurement sites. There is a certain amount of flexibility in such a reconstructive process. For example, the treatment volume can be divided up into several different regions (*e.g.* by tissue type), with a different multiplication constant in each region; or error minimization can use different weights for the errors associated with different sensors or different regions.

To perform error minimization at the sensor sites it is necessary to know the sensor coordinates (in the patient reference frame) and the predicted field value at sensor sites. Probe location (or more specifically, sensor location) can be determined in several ways. If thermal probes are inserted into the treatment region prior to patient imaging, then the location of the probes can be determined directly from the patient image. Orthogonal (or, with greater difficulty, oblique) x rays or ultrasound images can also be used to locate probes.

Calculation of the predicted thermal field at sensor sites usually involves interpolation between field mesh points, unless sensor sites coincide exactly with field mesh points. Interpolation techniques include trilinear interpolation (see Section B-4), nearest neighbor interpolation (see Section 4.4.2 on page 158), natural neighbor interpolation, and kriging. (See Watson [100] for an overview of interpolation techniques.) Trilinear interpolation was used for the results in Chapter 6 because of its ease of use and the fact that uniform `AVSfields` were used to store and manipulate thermal fields. Given measured and interpolated predicted values at sensor sites, error minimization was achieved using the least squares (LS) or weighted least squares (WLS) method.

5.2.5.1 Discrete Temperature and SAR Measurement

Minimally invasive thermal measurements were taken with needles housing thermistors. These sensors can be used to measure thermal properties, such as tissue thermal conductivity, thermal diffusivity, and perfusion, and thermal parameters, namely temperature and SAR [6, 13, 14, 98] The resistance of the thermistor is a function of temperature, so with calibration temperature measurement by thermistor is straightforward enough. The thermistor probe influences the tissue thermal field, however, and a temperature artifact must be determined to relate the measured temperature to the tissue temperature in the absence of the probe. Evaluation of this artifact will be discussed shortly in the context of SAR measurement.

A thermal probe measures SAR only indirectly; in fact, absolute SAR is not measured at all, but rather instantaneous *change* of SAR [14]. To illustrate this process of SAR measurement, assume thermal equilibrium is achieved under a constant SAR field. At time t_1, the SAR field is instantaneously changed (and then maintained constant). The simulated temperature $T\{t\}$ as a function of time t measured at a single sensor site is shown in Figure 5-3A. For times very close to t_1, before T has changed substantially, the $\nabla^2 T$ and $\lambda^2 T$ terms in the BHTE (Equation 5.1) are not subject to significant changes, so any change in $\partial T/\partial t$ is a direct consequence of the change in $\dot{Q}$, *viz.*:

$$\rho c\left[\left(\frac{\partial T}{\partial t}\right)\{t_1^+\} - \left(\frac{\partial T}{\partial t}\right)\{t_1^-\}\right] = \dot{Q}\{t_1^-\} - \dot{Q}\{t_1^+\} \tag{5.8}$$

where ρ is tissue density and c is tissue specific heat capacity, and t_1^- and t_1^+ are times just before and after t_1, respectively. Figure 5-3A illustrates a step increase in SAR at t_1, and a step decrease at t_2.

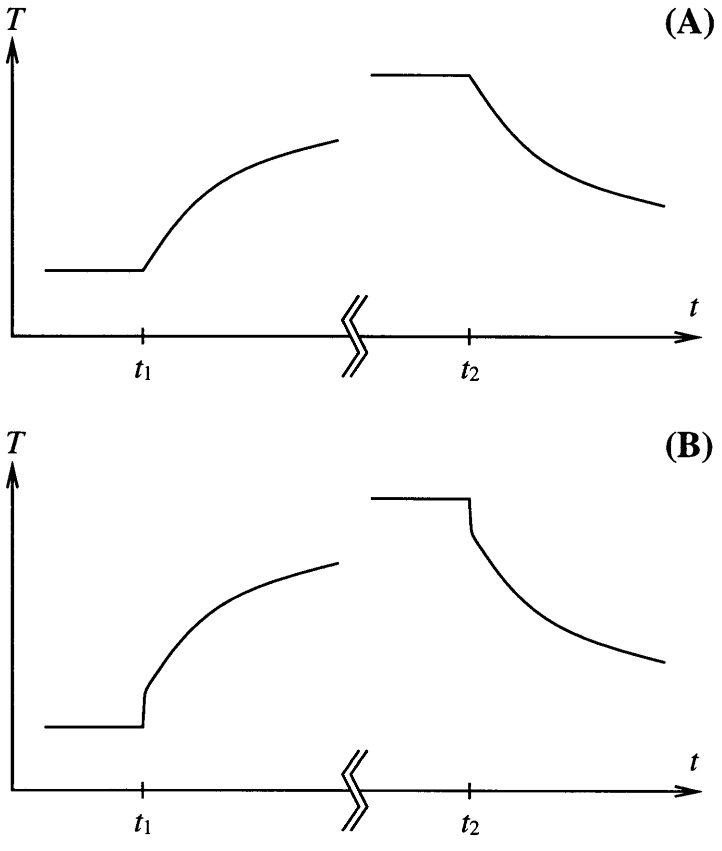

Figure 5-3: Simulated temperature in response to step changes in SAR, measured by thermistor-based thermal sensor, excluding (A) and including (B) temperature artifact.

The simulations in Figure 5-3A ignore temperature artifact from ultrasonic heating of the thermal probe itself. The thermistor and needle of the probe absorb ultrasound energy much more effectively (*i.e.* the ultrasound absorption coefficient is higher) than tissue, and consequently they experience much more rapid changes in temperature (at least initially) than tissue after step changes in SAR. The temperature artifact is illustrated in Figure 5-3B. Immediately after a step up in SAR, T is seen to rise dramatically, but after a short time (about 1 s) a temperature field is achieved around the probe in which the $\nabla^2 T$ term of the BHTE counters the elevated temperature at the probe-tissue interface. After this short time T changes in basically the same way as it did without temperature artifact. Thus Equation 5.8 still holds, with the *caveat* that t_1^+ is far enough after t_1 that the temperature artifact is fully developed. In practice, $(\partial T/\partial t)\{t_1^-\}$ is averaged over a temporal region prior to t_1, and $(\partial T/\partial t)\{t_1^+\}$ is evaluated over a temporal region starting roughly 5 s after t_1. As in Figure 5-3A, Figure 5-3B illustrates a step increase in SAR at t_1, and a step decrease at t_2.

Chapter 6

Results of Clinical Interest

For every problem, there is one solution which is simple, neat and wrong.
— Henry Louis Mencken

The purpose of this chapter is to demonstrate the ability of the integrated system to perform thermal predictions and reconstructions, to showcase visualization tools that can be used to display the thermal fields, to provide a sense of how the user interface works, and to discuss limitations of the system and ways to address them. In the style of an instruction manual, a description of the thermal prediction process is given, with accompanying figures taken from the computer monitor (Section 6.1). This is followed by a discussion of thermal reconstruction, including the presentation of thermal reconstructions based on an actual patient hyperthermia treatment (Section 6.2). This section also lists sources of error in all areas related to thermal prediction and reconstruction, and suggests directions of investigation to reduce these errors.

In the interest of clarity, several font styles are used in this chapter: filenames and C data types and structures are in `typewriter`, AVS module names and control panel labels are in sans serif, and geometric objects are in *italics*. For the special case of HYPER/Plan, HYPER/Plan refers specifically to the module of that name, and HYPER/Plan (regular roman font) refers to hyperthermia geometric planning in general.

6.1 Thermal Prediction

The AVS Network Editor is a user interface in which different AVS modules can be selected and connected interactively. Modules are represented by gray boxes containing the module name, and connections are symbolized by colored lines going from one module port to another. Information flow along connections is unidirectional, from a port on the bottom of one module to one on the top of another. The color of the connection corresponds to the type of information; of those shown, a dark cyan connection indicates a string (*i.e.* an array of characters, `char[]`), red an editlist (which contains geometric information, including geoms), blue an `AVSfield`, and yellow an `AVScolormap` (which gives coloring information). A flow network illustrating the integrated system is given in Figure 6-1, taken from the Network Editor workspace. Inasmuch as it is possible, the architecture of this particular network is meant to reflect the flow chart in Figure 5-1 (page 172). In particular, modules grouped on the left relate to *geometric* modeling, in the middle to *power deposition* modeling, and on the right to *heat transfer* modeling. In addition, all depicted module connections transfer information in the downward direction, and in some cases to the left or right as well. (If the same modules were connected in the same way but their positions were changed, however, it is possible that some connections would transfer information upwards.)

In Figure 6-1, module names that begin with a lower-case letter indicate modules that are part of the standard AVS library of modules, and modules that begin with an upper-case letter indicate custom modules. The uppermost two modules, **Get Patient Name** and **HYPER/Plan**, were not developed in the course of this thesis, but the remaining custom modules were. Modules will be described in turn, starting with modules associated with geometric modeling, then power deposition modeling, heat transfer modeling, and thermal visualization. Last to be considered is a preliminary module associated with thermal reconstruction.

Get Patient Name

The **Get Patient Name** module performs the basic task its name suggests: it lets the user select the patient and treatment. According to the HYPER/Plan convention, the name of the computer directory of the patient treatment is the concatenation of the patient's name and the six-digit treatment date—*e.g.* `sidney060297`. (The different output ports of this module correspond to slightly different versions of the patient treatment name; they all give the absolute pathname of the directory, including the directory name itself, and in addition three of the ports give filenames or parts of filenames.) Figure 6-2 shows the control panel of **Get Patient Name**,

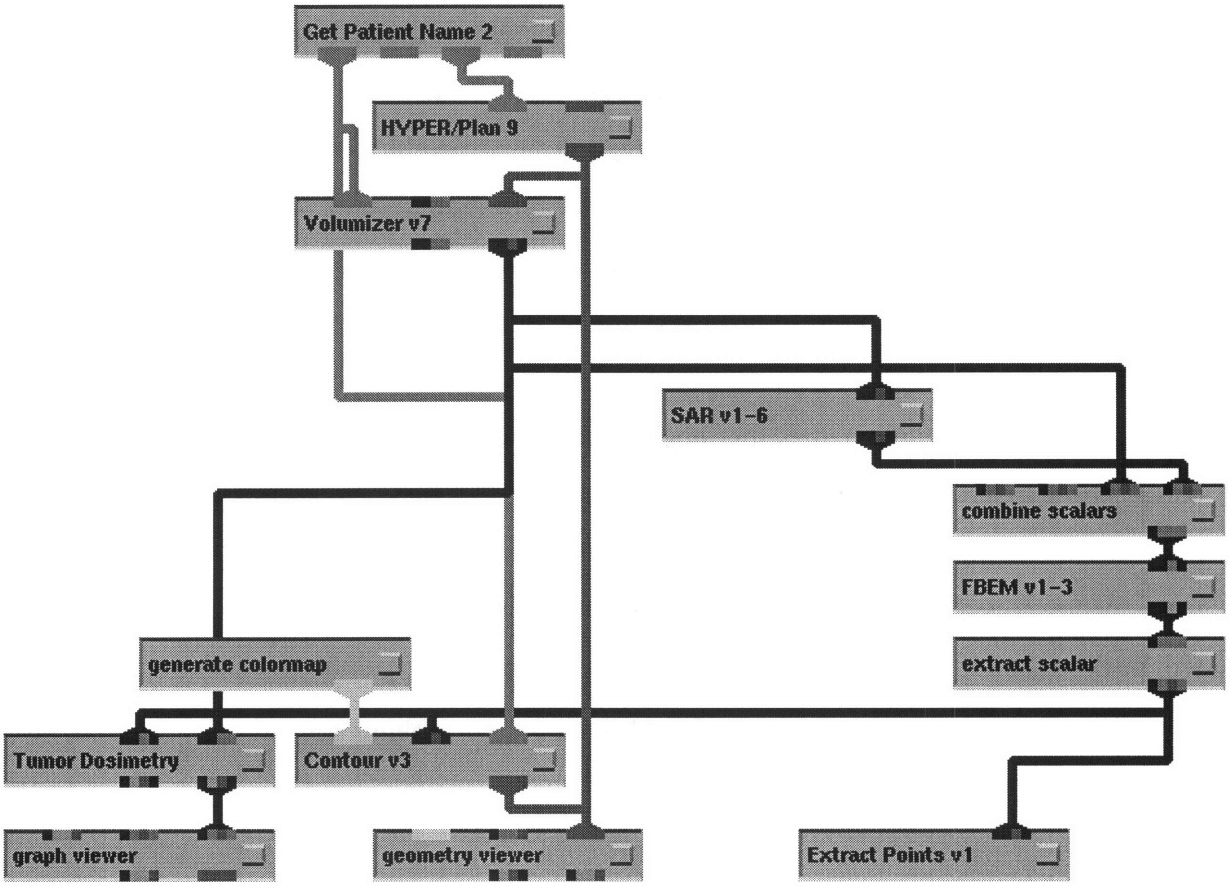

Figure 6-1: AVS network depicting integrated system.

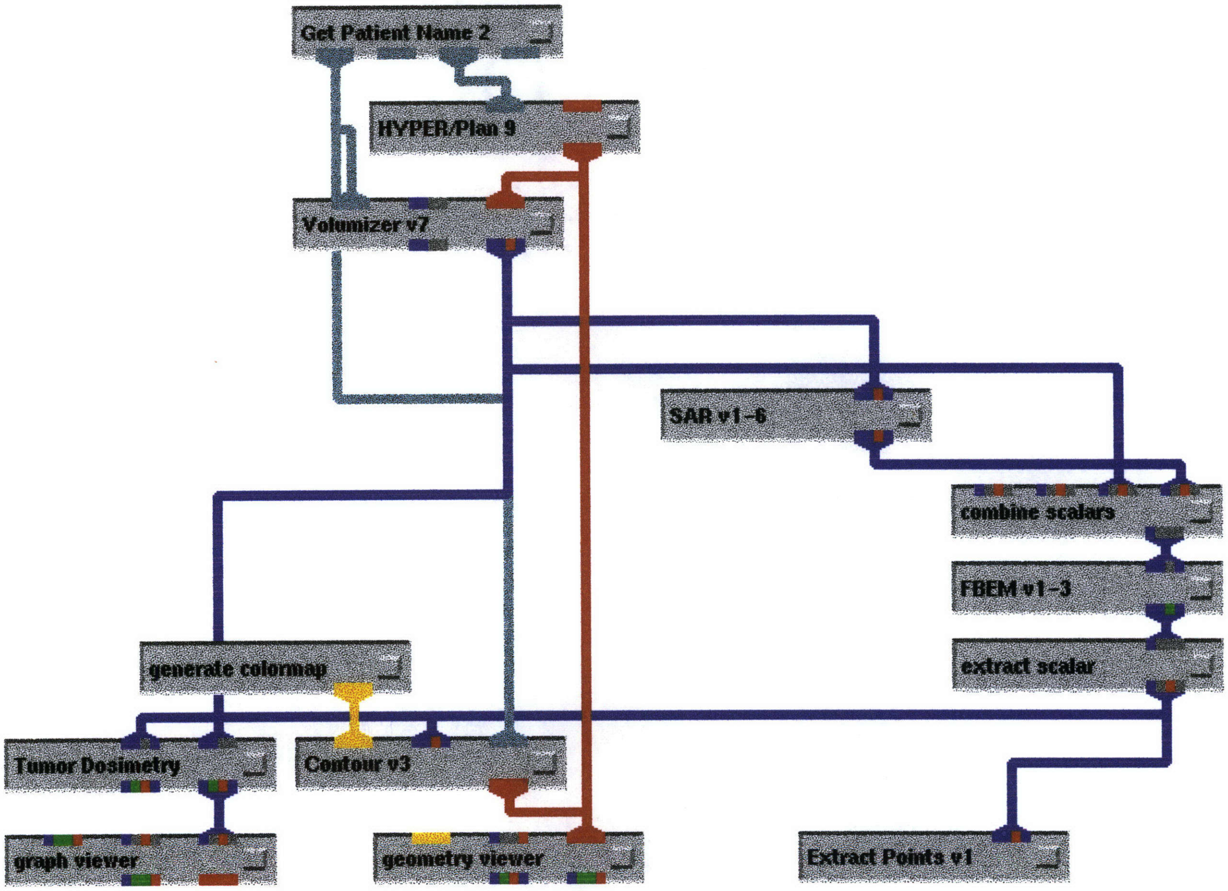

Figure 6-1: AVS network depicting integrated system, in color.

which largely consists of a file browser that lists only directories and `<.ima>` files. To select a patient treatment the user clicks on the `<.ima>` file corresponding to the desired patient treatment.

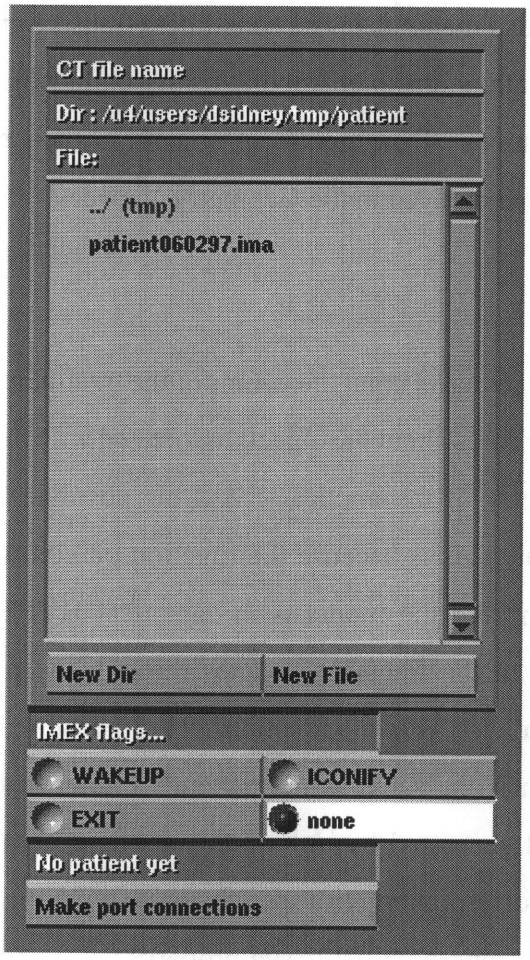

CT file name

Dir : /u4/users/dsidney/tmp/patient

File:

../ (tmp)
patient060297.ima

IMEX flags...

○ WAKEUP ○ ICONIFY
○ EXIT ● none

No patient yet

Figure 6-2: **Get Patient Name** module control panel.

HYPER/Plan

Once the patient treatment is selected, the **HYPER/Plan** module automatically reads the patient anatomic geoms into the Geometry Viewer. This assumes that the tasks of contouring anatomic structures using IMEX and connecting the contours into organ surface representations using Mosaic has already taken place. (These tasks will not be addressed here.) The **HYPER/Plan** control panel is shown in Figure 2-2 on page 39, along with the **HYPER/Plan** geometric output shown in the AVS Geometry Viewer. Widgets—slider bars for translation, and dials for rotation—control the spatial manipulation of one of three selected objects: the patient, the power applicator, or both together. Recall from Section 2.1 (page 29) that manipulating *patient* also manipulates all the child objects of *patient* as well, *i.e.* the organ objects that comprise *patient*; manipulating *applicator* also manipulates its constituent transducers and transducer beams; and manipulating *graph* is tantamount to manipulating its child objects, *patient* and *applicator*. The geometric representations of the treatment objects in their chosen spatial positions and orientations are ultimately displayed in the Geometry Viewer.

Volumizer

The **Volumizer** module takes as its input the geoms of the treatment objects from **HYPER/Plan**. However, **Volumizer** only cares about the objects associated with the patient anatomic structures, and it ignores the geometry of the applicator and the absolute and relative positions of the patient and the applicator. This is because the function of **Volumizer** is to generate a patient volumetric representation, and the model is in canonical HYPER/Plan coordinates (*i.e.* the x and z coordinates are in the transverse planes through the patient, and the y coordinate is in the head-to-toe—or *vice versa*—direction). Furthermore, the reference frame of the volumetric representation is the same as the patient's reference frame in HYPER/Plan. The patient volumetric model generated by **Volumizer** is a tissue type `AVSfield`, with the data value of each field point corresponding to a specific tissue type; for example, tumor is designated by `11`. (Tissue type data—and nominal tissue property values for each tissue type, including acoustic absorption, perfusion, and thermal conductivity—are found in the file designated by the `$HoTPES_tissueProperties` Unix shell variable. Module use of the data in this file is in general transparent to the user.) **Volumizer** has several options for the coordinates of the output tissue type field. The default output field, from the right output port, is a uniform field with coordinates spanning the bounding box of the imaged patient volume, *i.e.* the rectangular parallelepiped volume defined by the maximum x, y, and z extents of the patient surface model; the grid resolution, *i.e.* the distance between adjacent grid points, is adjustable. The alternative output field, which is also from the right output port, has coordinates defined by an optional input template `AVSfield`.

The **Volumizer** control panel is shown in Figure 6-3. Much of the area of the control panel

Dir : /u4/users/dsidney/tmp/patient

File: .../dsidney/avs/hyperplan/data

Grid Resolution 1

Figure 6-3: **Volumizer** module control panel.

concerns actions associated with the `volumized_list` structure which organizes the triangles that make up the patient anatomic surface representations. With a click on the **Kill Vlist** button, the `volumized_list` (if present) can be flushed from the memory of **Volumizer**. **Read Vlist** and **Write Vlist** read and write the `volumize_list` to the file selected in the file browser. Clicking on the **Generate Volumized Field** button creates the tissue type `AVSfield`. Its coordinates comprise a uniform grid of the selected **Grid Resolution** if the **Ignore Template Field** button is depressed or if there is no optional template field present, or the grid of the template `AVSfield` otherwise.

One final capability of **Volumizer** is to crop an optional input `AVSfield` so that its coordinates do not extend beyond the patient bounding box. The `AVSfield` to be cropped is connected to the optional left input port, the **Generate Cropped Field** button is pressed, and the cropped `AVSfield` (with its original data, not necessarily tissue type data) is created at the left output port.

A variation of the **Contour** module (the **Contour** module will be described shortly) can be used to depict the patient volumetric representation generated by **Volumizer**. A sample output can be revisited in Figure 2-4 on page 45.

SAR

The **SAR** module is designed to perform SAR calculations specific to the FSUM heating device, and its control panel is given in Figure 6-4. It takes as input the tissue type `AVSfield` generated by **Volumizer**, and assigns nominal acoustic absorption properties based solely on the tissue type. Clicking on the **Calculate SAR** button predicts the SAR field in an `AVSfield` with the same coordinates as the input tissue type `AVSfield`. SAR calculation uses the acoustic models developed in Chapter 4 and implemented as described in Section 5.2.2. (The file specified by the `$HpApplicatorFSUM3` Unix shell variable gives FSUM transducer coordinates, relative maximum power values, and nominal Gaussian beam widths. Module use of this data is transparent to the user.) If the **Show Beams** button is depressed prior to the initiation of SAR field calculation, then the resulting field simply corresponds to the union of the nominal beam paths of the powered transducers; in this case the output **AVSfield** takes on data values of 1 where field points reside in one or more nominal acoustic beams (*i.e.* within a cylinder of radius 2 cm about the beam axis, and extending up to 30 cm from the transducer surface), and 0 elsewhere. The FSUM transducer power settings are given in one of two ways: if the **Read Power File** is depressed, then the power settings are taken from the selected file; if not, then transducers selected by the **Transducer Array** window of **HYPER/Plan**—see Figure 2-2, page 39—are considered powered at maximal levels, and other transducers are not powered at all. Currently the SAR field is normalized to its maximum value.

Wobulation is taken into account by the **Wobulation Number**. If this integer $n \leq 1$, then the FSUM spherical shell is considered stationary. If $n \geq 2$, then the quasi-precessional wobulation motion of the spherical shell is divided into n equally spaced positions within one cycle of rotation, and the SAR field is averaged over these positions.

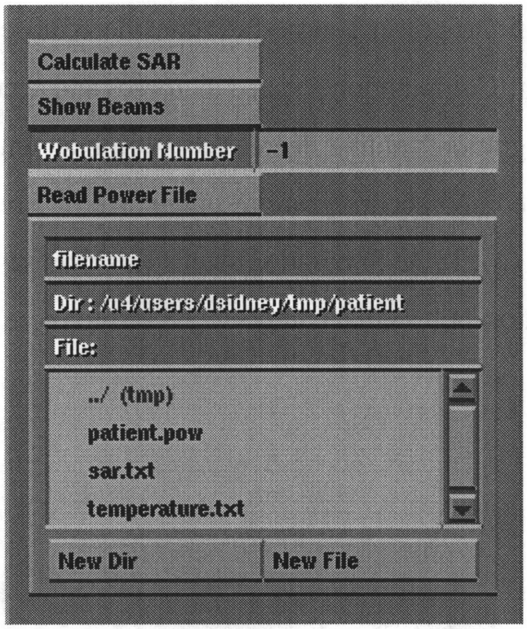

Wobulation Number -1

Dir : /u4/users/dsidney/tmp/patient

Figure 6-4: **SAR** module control panel.

FBEM

The **FBEM** module performs the FBEM thermal model calculations. Its sole input is a vector `AVSfield` that must contain at a minimum tissue type and SAR data, but it can also contain thermal conductivity and perfusion data. If thermal conductivity or perfusion are not supplied, then they take on nominal values according to tissue type. The output of the module is again a vector `AVSfield` containing the temperature and temperature elevation fields at the same coordinates as the input `AVSfield`. The **Compute Temperature Field** button initiates the thermal field calculation.

In the sample AVS network depicted in Figure 6-1, scalar tissue type and SAR input `AVSfields` are joined into a single vector `AVSfield` by the **combine scalars** module, and similarly the vector temperature and temperature elevation output `AVSfield` is trimmed into a scalar `AVSfield` of the chose "channel" (temperature or temperature elevation) by the **extract scalar** module.

FBEM has several settings that govern the speed and accuracy with which thermal calculations are performed, as indicated in Figure 6-5. A slider bar labeled **Source Size** is used to select the radius of the finite power sources used in thermal calculations; likewise, a slider bar labeled **Integration Size** is used to select the radius of the volume around each thermal field point within which finite power sources are considered to contribute to the temperature elevation at that field point. Computational speed increases and accuracy decreases as the source size increases or the integration volume decreases. Nominal settings[1] that give a reasonable compromise between speed and accuracy are a source size of 5 mm and an integration size of three perfusion lengths ($3/\lambda$). If the integration size is less than seven perfusion lengths there is a Perform Error Correction button that can be depressed to increase accuracy as well.[2]

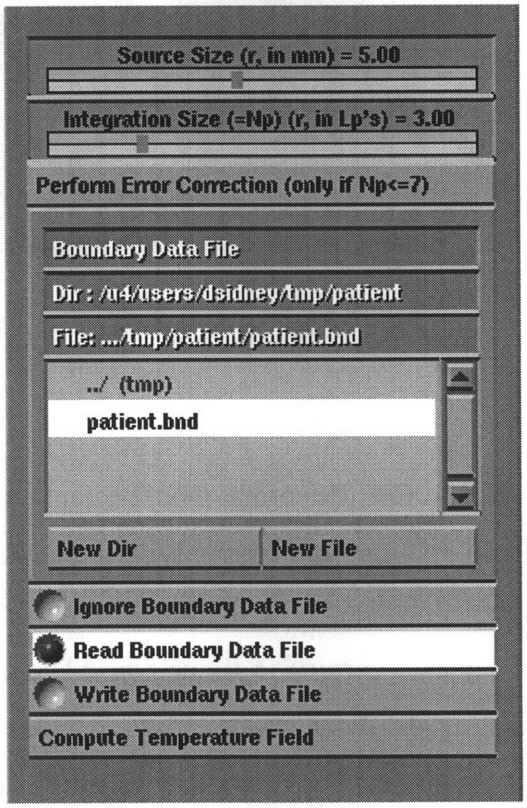

Source Size (r, in mm) = 5.00

Integration Size (=Np) (r, in Lp's) = 3.00

Dir : /u4/users/dsidney/tmp/patient

File: .../tmp/patient/patient.bnd

○ Ignore Boundary Data File

● Read Boundary Data File

○ Write Boundary Data File

Figure 6-5: FBEM module control panel.

The FBEM thermal model requires that the nearest thermal boundary and its geometry (*i.e.* planarity, or concavity and radius of curvature) be known at each thermal field point. FBEM performs these geometric calculations if they have not already been performed. If a file containing the boundary information already exists, it can be ignored by pressing the Ignore Boundary Data File button, in which case FBEM will calculate it anew; or it can be considered by pressing theRead Boundary Data File button. If the user wishes to save newly calculated

---

[1] These settings were suggested by Dr. Gregory T. Martin.

[2] According to Dr. Martin, the use of this button is not generally necessary.

boundary information, the **Write Boundary Data File** button is pressed.

Contour

The **Contour** module is used to display thermal fields in transverse cross-sections. Two elements give anatomic context to the thermal field: first, a gray plane slices the patient anatomy in the selected transverse anatomic plane; and second, the thermal field is actually displayed on a second plane, and organ contours are superimposed over the over the displayed thermal field. Both of these planes appear in the Geometry Viewer, and the latter plane can be spatially manipulated by the mouse or the Geometry Viewer Transformation Editor.

Using the **Contour** visualization tool, Figure 6-6 shows cross-sections through the predicted SAR and temperature fields in a hypothetical treatment plan. The **Contour** control panel is given in Figure 6-7. Trilinear interpolation is performed to determine thermal field values on a regular grid of the selected **Grid Resolution**. A smaller grid resolution value increases the *apparent* smoothness of the displayed thermal field cross-section, but does not actually affect accuracy. The color of the organ contour lines is adjustable to improve contrast between the lines and the colored thermal field; *viz.*, contour lines are colored according to the selected RGB values, each ranging from 0 to 1. The **slice number** is the number in the `<.ima>` file of the chosen transverse cross-section. This number may increase in the head-to-toe direction, or *vice versa*; at this time there is no convenient way for the **Contour** module to know explicitly which of these two patient orientations is correct, so a **Flip Head and Feet** button is available to alter the orientation of the patient if necessary.

Tumor Dosimetry

The purpose of the **Tumor Dosimetry** module is to generate a volumetric thermal field suitable for display as a graph in the AVS Graph Viewer. Specifically, the fraction of the tumor volume over which the thermal field exceeds an index value is plotted as a function of the index value in the Graph Viewer. This can be a powerful visualization tool because in a single glance the user can obtain a general sense of the thermal "coverage" of the tumor by the thermal field. **Tumor Dosimetry** takes as input two `AVSfields`. The left input port is the thermal field, *e.g.* SAR, temperature, or thermal dose field; and the right input port is the tissue type field. The

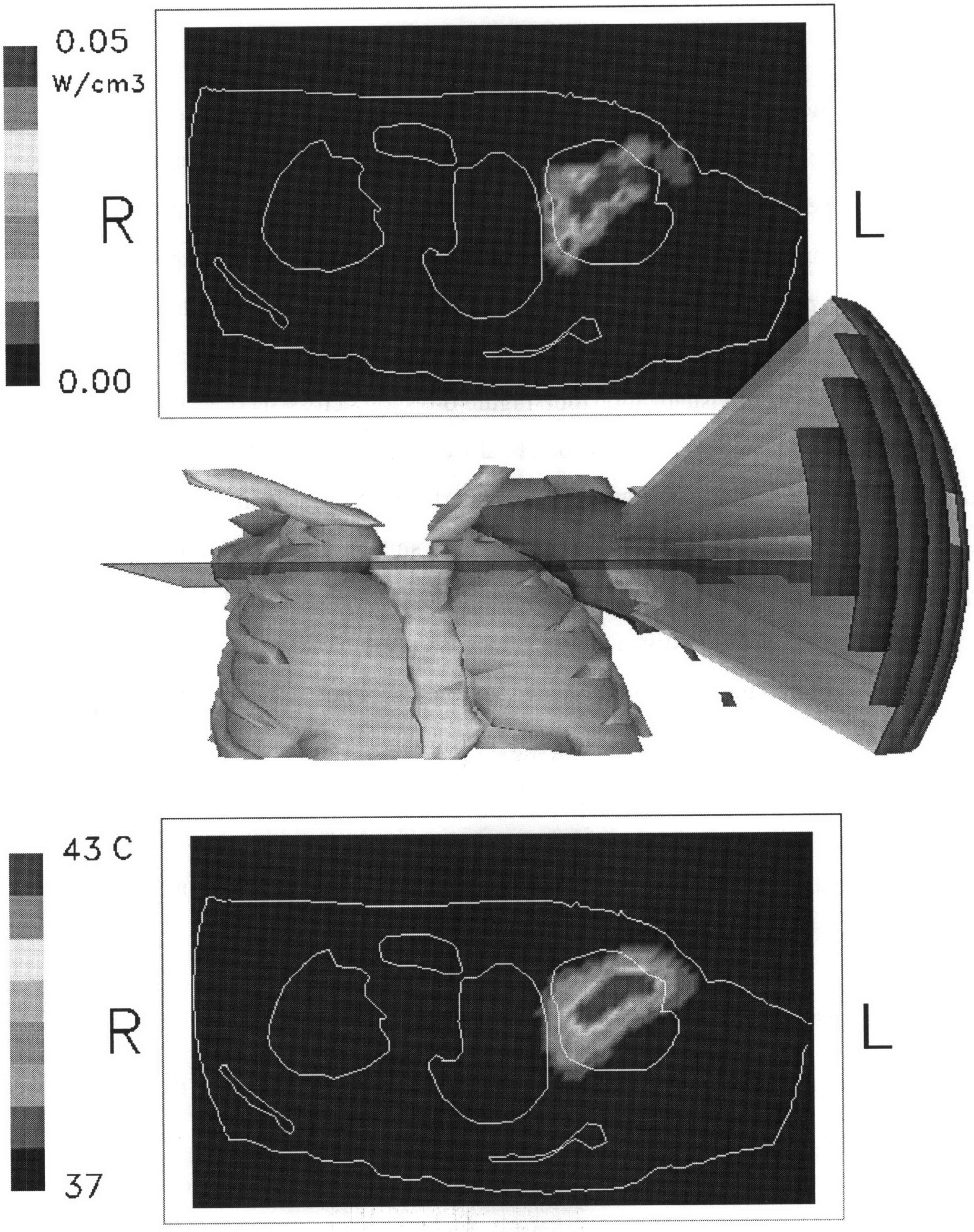

Figure 6-6: Transverse cross-sections of predicted SAR (top) and temperature (bottom) fields using the **Contour** tool.

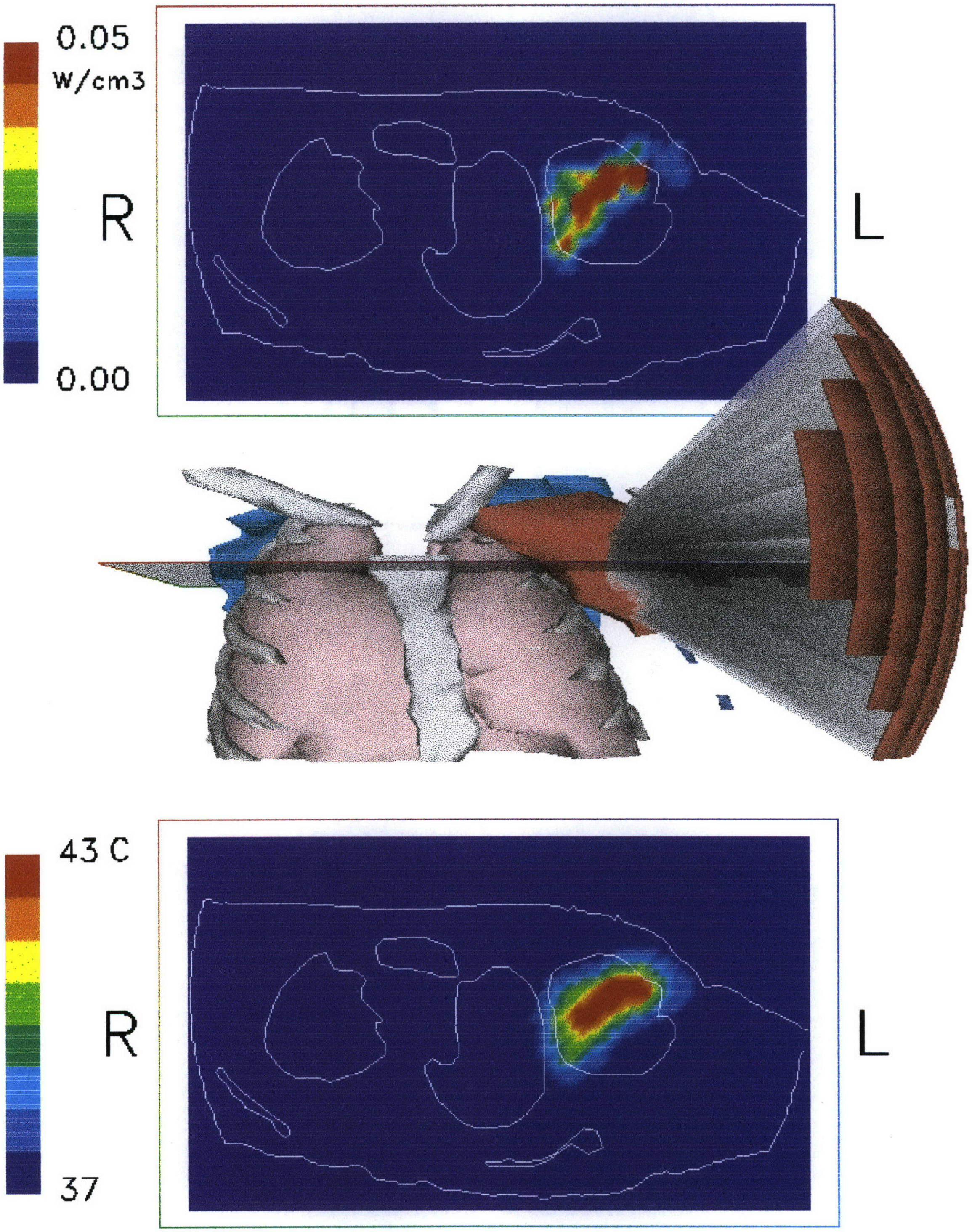

Figure 6-6: Transverse cross-sections of predicted SAR (top) and temperature (bottom) fields using the **Contour** tool, in color.

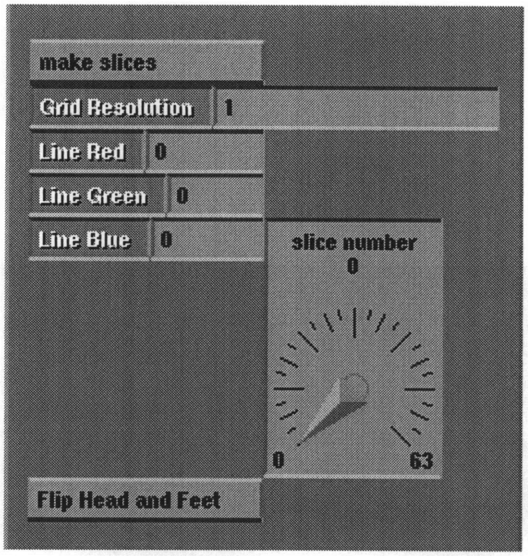

Grid Resolution 1
Line Red 0
Line Green 0
Line Blue 0
slice number 0

Figure 6-7: **Contour** module control panel.

format of the output `AVSfield` is a 2-D field comprising the (x, y) coordinates of the points plotted in the Graph Viewer. The right output port gives output for the SAR, temperature, or temperature elevation field; and when temperature is the input thermal field, the left output port gives output of the thermal dose rate field. Figure 6-8 shows a sample Graph Viewer output, which corresponds to the predicted temperature field in the simulated treatment depicted earlier in Figure 6-6. This module has no control panel.

6.2 Thermal Reconstruction

Thermal reconstruction is performed by fitting to thermal measurements the functional forms of the predicted thermal fields. In this framework, the simplest reconstruction method is to perform a LS fit between measurements and predicted thermal field values at sensor sites. For SAR field reconstruction the most obvious fit is for a constant of proportionality a, *i.e.* the measured SAR field is the product of the fit constant and the predicted SAR field. For temperature field reconstruction, it may be desirable to fit to a constant of proportionality a and an offset b. Thermal reconstruction does not yet follow a specific, well-defined protocol, and it will be the object of future work to determine how best to perform thermal reconstructions. In this section a simple thermal reconstruction AVS module is described, an illustrative SAR field reconstruction

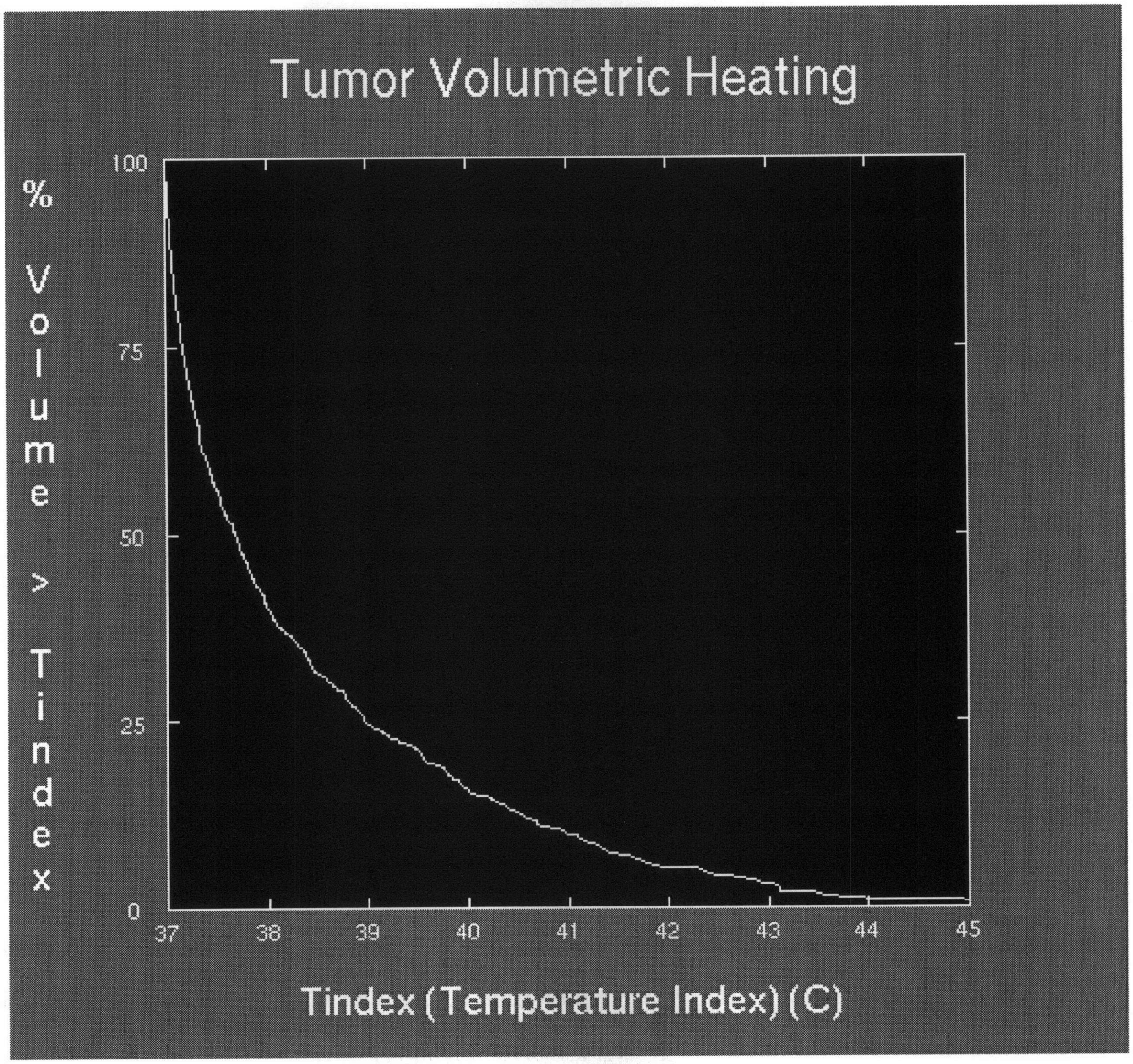

Figure 6-8: Tumor volume fraction above index temperature vs. index temperature.

is performed, and limitations of thermal reconstruction are discussed.

Extract Points

The **Extract Points** module is used to perform rudimentary thermal reconstructions based on a predicted field and thermometric data. The input port takes a thermal `AVSfield`. The control panel of the module, shown in Figure 6-9, consists entirely of a file browser. The selected file contains sets of four numbers, corresponding to the (x, y, z) sensor coordinates (in the patient's reference frame) and measured thermal parameter value of the thermometric sensors. **Extract Points** trilinearly interpolates input field values at the sensor coordinates, and outputs a file with sets of five numbers: (x, y, z) sensor coordinates, sensor measurements, and predicted thermal field value at sensor coordinates.

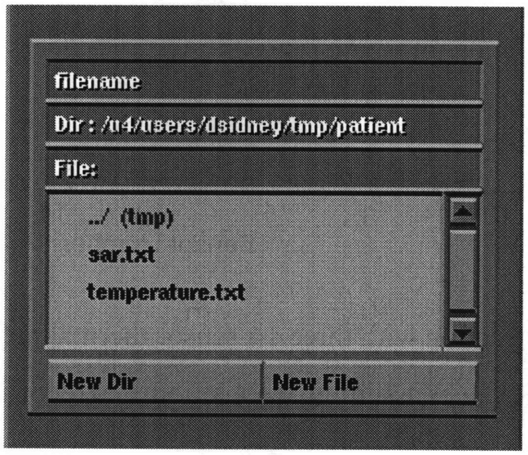
filename

Dir : /u4/users/dsidney/tmp/patient

File:

../ (tmp)
sar.txt
temperature.txt

Figure 6-9: **Extract Points** module control panel.

The interpolated values can be fit by LS to the measured data, and an example of this fitting is given in Figure 6-10. In this particular example, a single constant of proportionality was determined over all sensors to minimize the LS error between measured and predicted SAR values, and the reconstructed SAR field was taken to be the product of that constant of proportionality and the predicted SAR field. Wobulation was used for this particular treatment, but for illustrative purposes reconstructions were performed both with and without the use of wobulation. The agreement between the measured and reconstructed SAR values is not very good, and several aspects of the discrepancies will be used to pedagogical advantage here. Three 14-sensor thermal probes were used. The spacing between adjacent sensors was 5.0 mm for

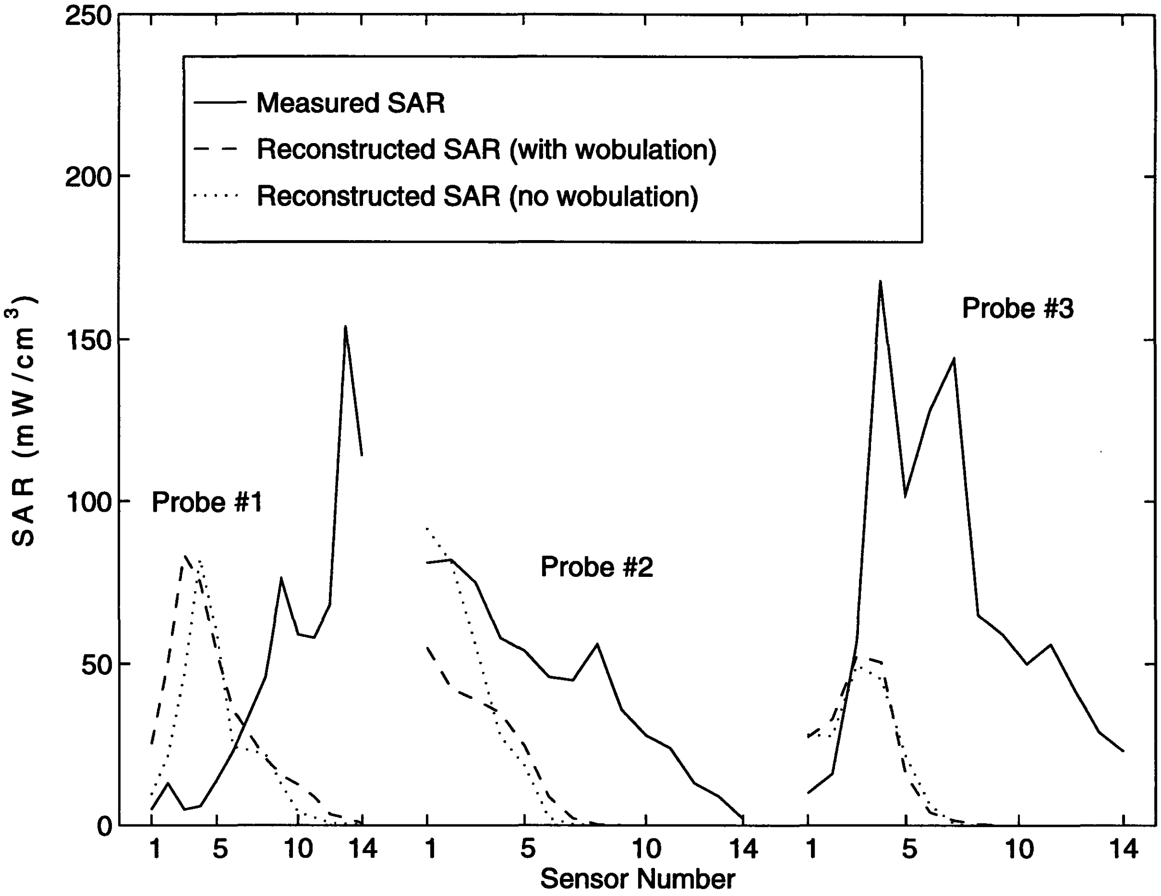

Figure 6-10: SAR reconstruction with three 14-sensor thermal probes, showing measured SAR values, reconstructed SAR values assuming wobulation, and reconstructed SAR values assuming no wobulation.

Probe #1, and 7.5 mm for Probes #2 and #3, so the relative widths of the probes represented in Figure 6-10 are accurate. For the moment ignore the SAR reconstruction without wobulation (dotted lines).

The first observation concerning these reconstructions is that the reconstructed SAR values appear to be translated relative to the probes, particularly for Probes #1 and #2, by what appears to be about 10 sensors (5 cm) for Probe #1 and about 4 sensors (3 cm) for Probe #2. A substantial part of these offsets probably correspond to an error in the relative position and orientation[3] of the FSUM device and the patient. These are significant offsets, assuming the probes are perpendicular to the FSUM acoustic beam; but if the probes are oblique the actual positional

---

[3] In the interest of parsimony, for the remainder of this section "position" will in general be taken to mean "position and orientation."

error between the device and the patient may be considerably less than the apparent offsets, especially if the probes are close to parallel to the beam. These offsets can be used to better estimate the relative position of the device and patient.

These offsets reflect the need to accurately position the patient and applicator, so that treatment administration closely follows the treatment plan; and the need to know the relative position of the patient and applicator, so that thermal reconstruction is accurate. Stereotactic principles [2] are used to locate anatomic structures very precisely (with an accuracy of 1 mm or less) in various cranial radiosurgical and radiotherapeutic procedures, and if they could be applied to hyperthermia it would greatly improve accuracy in patient and device positioning. Unfortunately there are good reasons why stereotaxy has *not* been applied very much to most anatomic sites below the neck: this anatomy is generally soft and movable. Stereotactic radiosurgery and radiotherapy succeeds because head anatomy is relatively fixed, particularly when the skull is oriented in a fixed position by the stereotactic frame. For tumors in the body in general, however, use of a stereotactic frame is impractical and it would be ineffective. In the case hyperthermia treatment of a tumor in the body, the patient moves even when trying to remain still. Even if the patient could control fidgeting for the duration of the treatment, about 30 to 60 min, he or she must still breathe.

Ultrasound heating devices (or extensions of the devices) alter the shape of the patient, pressing against the patient's surface to improve ultrasound transmission. Even if the patient could remain perfectly still, this deformation of the patient can be recognized as a geometric discrepancy between the patient representation (based on the patient image) and the true patient geometry. Furthermore, it is assumed that the patient was in precisely the same anatomic position while imaged as while treated.

Another issue related to patient geometry is that the patient anatomy can actually change between imaging and treatment—*e.g.* some tumors can grow substantially in a matter of a week. If this issue is considered important, of course, the time between imaging and treatment can be shortened (although given the amount of time required to generate organ contours and surfaces, it may not be realistic for imaging and treatment to take place in the same day).

For FSUM treatment, accuracy of the relative position of applicator and patient is a nominal 2 cm. And, for reasons already mentioned associated with patient movement, the error in relative position is not constant during treatment. If probes were inserted prior to imaging, then their location relative to the patient would be fairly accurate.[4] Thus for accurate thermal reconstruction an approach is needed which dynamically and continually reassesses the relative position to obtain the most accurate reconstruction.

Moving beyond issues of treatment geometry, there are certainly other sources of error in thermal reconstruction. For SAR field reconstruction, tissue acoustic absorption is known to about 10% or 20% [35], but this assumes the tissue type is accurately identified. Once the patient and applicator positions are reasonably well established, the acoustic absorption field could be adjusted to decrease error between the predicted and measured SAR values at sensor sites. A likely implementation would assume that absorption is uniform in each organ and each tissue type, but those uniform values could be adjusted independently. For temperature field reconstruction, a similar adjustment could be made with the perfusion field.

For multi-transducer applicators like the FSUM, different transducers may couple to the patient with different efficiencies. This is especially true with odd anatomic geometries. If transducers were excited incoherently then transducer power setting could be related to measured SAR in a linear matrix equation, and the equation could be solved for the efficiency of ultrasound transmission (*i.e.* what fraction of the emitted ultrasound power reached the patient). For the FSUM device, or other devices with coherently excited or phased array transducers, a more difficult non-linear matrix equation would relate transducer power setting to measured SAR. The non-linearities arise because the measured SAR is based on acoustic pressure amplitude, and the acoustic pressure from multiple coherently excited transducers is the *complex* sum of the pressure contributions from each transducer. Solution of this non-linear matrix equation may be difficult.

The acoustic model of the FSUM device has limitations. At this time is does not take into account acoustic reflections, and does not really address acoustic phenomena at soft tissue-bone interfaces. In many treatment geometries these issues may not be important, but in some they will. It may often be possible to choose a treatment geometry such that acoustic interfaces do not significantly affect the acoustic fields.

---

[4] If a probe is substantially oblique or essentially perpendicular to the transverse planes of the patient image, then inaccuracies in probe location along the axial direction of the probe would be on the order of the distance between adjacent image slices—usually 0.5 or 1.0 cm.

Another aspect of the FSUM acoustic model is that it predicts a "smoother" pressure amplitude field than that observed by measurement (*cf.* Figure 4-25, page 136, with Figure 4-27, page 140). This is also reflected in Figure 6-10, in which the measured SAR clearly exhibits local peaks along the probes, whereas the reconstructed SAR values show a single peak each. This observation suggests that it may be advisable to smooth the measured data in some fashion, *e.g.* averaging each measurement with its adjacent neighbors, prior to performing thermal reconstruction. (This may be more relevant for SAR field reconstruction than temperature field reconstruction—see the quote on page 145.)

An interesting observation concerning the SAR profiles along the probes pertains to the differences in the reconstructed fields with and without wobulation. Probes #1 and #3 have remarkably similar profiles, but Probe #2 has an interesting contrast, with a steeper SAR gradient without wobulation. This is expected, given the device design goal that wobulation "smooth out" the thermal fields; but what may be surprising is this phenomenon is only really visible in one of the three probes. This kind of observation has potential consequences for treatment planning, and may help determine when the use of wobulation is desirable.

There is flexibility in the method of calculation of the constant of proportionality a (and offset b, if present). For the results shown in Figure 6-10, a single value of a was calculated throughout the treatment volume. However, there may be appropriate ways to divide up the treatment volume, and fit the reconstructed field to different values of a in different subvolumes. For example, different anatomic structures may be fit to different values of a; or subvolumes around different thermal probes may be fit to different values of a.

Thus far, most of the discussion of thermal reconstruction was either general (for SAR or temperature field reconstruction) or specific for SAR field reconstruction. Temperature field reconstruction has issues all its own, however, the most important of which is how to characterize the perfusion field. Acoustic absorption and thermal conductivity can vary from tissue type to tissue type and from patient to patient, but the variations are still relatively small. Perfusion, in contrast, can vary enormously between different tissue types, different regions of the same organ, different patients, different times at a single location, and in response to heating, pharmaceuticals, *etc.* This points to a need for perfusion measurements and physiologic models of perfusion in order to perform accurate temperature reconstruction.

Chapter 7

Conclusions

> *A good time to finish up old tasks.*
>
> — From a fortune cookie after dinner, April 5, 1997

Conclusions concerning this thesis will fall into two categories: SAR modeling, and clinical integration. Just as results and discussions related to SAR modeling (Chapter 4) preceded those of clinical integration (Chapters 5 and 6), conclusions related to SAR modeling will precede those of clinical integration. Lastly, areas of future related work will be discussed.

7.1 SAR Modeling

The SAR modeling results have interesting implications for both the understanding of the power deposition characteristics of the FSUM applicator in particular, and the design of ultrasound power applicators in general. Du and Breazeale [25] indicated an appreciation of the simple characteristics of the pressure amplitude field of a Gaussian acoustic source, and this simplicity has the potential to go far in acoustic modeling, for several reasons. First, this simplicity facilitated the construction of a parametric model of the acoustic beams of the FSUM transducers (Section 4.2), which, in turn, led to a tremendous increase in the speed of pressure field calculation, compared with solution of the diffraction integral. The potential computational advantage of a parameterized beam is clearly great, Gaussian beam or not; but the complex geometry of the many peaks and troughs typical of the pressure amplitude near fields of uniformly vibrating sources hinders the construction of parametric beam descriptions (although it does not necessarily make it impossible).

Second, a potentially serious drawback in the use of non-Gaussian sources, from the perspective of this thesis, is that a non-Gaussian source (parametrically described or otherwise) might not accommodate the application of the FAM (Section 4.4). Preliminary results with uniformly vibrating sources suggest that the pressure amplitude field may be appropriately transformed by the FAM (although in some cases the acoustic field maintained its general shape, but acoustic peaks shifted position slightly), but the pressure phase field validation of the FAM for these transducers was not performed.

Third, the lack of side lobes (see Footnote 9 on page 73) in the Gaussian acoustic beams makes it easier to control the location of regions of greatest acoustic intensity. In the area of phased arrays, which focus energy by manipulating the relative phase of different source elements instead of using geometric focusing, typically a single focus is desired; however other lesser foci, called grating lobes, are generally observed as well. Grating lobes and side lobes are both essentially regions in which acoustic wave interference is general constructive, and it is possible that the use of Gaussian sources in phased arrays may reduce the size of grating lobes. This strategy is distinct from the one pursued by Hutchinson *et al.* [44, 45], in which linear phased array source elements where constructed in two sizes, and the sizes were arranged in a random pattern. Perhaps for maximal effect, both strategies—Gaussian sources and randomly sized sources—could be used together.

The FSUM is an interesting and difficult device to model acoustically. It is not a phased array, but it is coherently excited; thus it has constructive and destructive interference patterns, like a phased array, but it lacks the electrical focusing ability of a phased array. From the perspective of acoustic modeling, if a multi-element device is not going to be used like a phased array, modeling is simpler if the elements are excited incoherently—*i.e.* by exciting different transducers at different frequencies, or exciting different transducers with different (non-overlapping) duty cycles.

Another unusual feature of the FSUM is its quasi-precessional mode of motion called wobulation (Sections 5.2.2 and B.7). This mode was conceived to extend the focal region from the geometric focus of the spherical shell toward the transducers and to smooth out hot spots that would occur in the absence of wobulation. Conceptually wobulation is not difficult to model, but the current modeling solution—dividing the precessional circuit into n equally spaced discrete positions, and averaging the SAR field from all position—increases the SAR computational burden by a factor of n. Perhaps an extension of the FAM, or a parametric description of the time-averaged acoustic beam of an FSUM transducer undergoing wobulation, could reduce the computation difficulty of SAR field calculation with wobulation.

7.2 Clinical Integration

A newly validated power deposition model of the FSUM device and a previously validated thermal model were integrated with a geometric treatment planner, together forming an interactive, integrated clinical thermal visualization system. This system can be used to investigate thermal reconstruction protocols to better estimate the thermal fields that occur during hyperthermia treatment administration. A number of sources of error in thermal reconstruction were identified, probably the most important of which is inaccuracies in the relative position and orientation of the patient and the power applicator. Other important sources of error include inaccurate values for tissue properties—most notably acoustic absorption (for SAR reconstruction) and perfusion (for temperature reconstruction)—and inconsistent acoustic coupling between the patient and the applicator.

With better thermal reconstruction come powerful system benefits. The relationship between planned thermal fields and reconstructed fields can be investigated; where there are discrepancies, it may be possible to influence treatment planning in such a way that the thermal fields achieved during administration are closer to the planned ones. This closes a clinical loop: planning influences treatment, which then influences planning. Treatment simulations can be used to to provide insight into where and how many thermal probes should be placed in the treatment volume.

3-D thermal modeling opens the door for the use of more quantitative methods in clinical hyperthermia, such as calculation of volumetric treatment descriptors. Quantitative techniques will help make hyperthermia therapy a more scientific, reproducible practice.

And finally, an integrated clinical system can be used to help design treatment devices. In particular, care should be taken to make the applicator as easy as possible to model acoustically. As mentioned in the previous section, Section 7.1, Gaussian acoustic sources have a number of attractive features, from the perspective of modeling. But even with this starting point, there are many variables in transducer geometry and excitation strategy that should be considered in device design, and an integrated system can be used to assist in design evaluation.

7.3 Future Work

An exhaustive list of related future work would be overwhelming, so only a few areas will be touched on here. First, it is clear that more work needs to be done in thermal reconstruction. Of paramount importance is a reasonably automatic way to determine the relative position and orientation of the patient and the applicator. A conceptually simple method that would be relatively straightforward to implement is to repeatedly perturb the position of the applicator about its nominal location and perform the reconstruction; whichever perturbed position gives the best reconstruction (*i.e.* the smallest error between the reconstructed field and measurements at sensor sites) indicates the applicator position.

Second, a worthy goal for the hyperthermia clinic is *real-time* reconstruction, for quantitative, volumetric treatment monitoring. This requires rapid communication between four different systems: the power applicator, thermometric, locating, and modeling systems. (The third listed system, the locating system, is necessary to locate rapidly and accurately the applicator and the thermometric sensors in the patient reference frame.) Real-time thermal reconstruction would allow the clinician to alter hyperthermia administration in the middle of a treatment, giving greater dynamic treatment capability.

And third, the FSUM acoustic model can be improved in several ways. For example, there is a subset of transducers that have not been directly characterized in terms of their modified Gaussian beam parameters. In addition, the current model implementation does not really address acoustic transmission and reflection and soft tissue-air and soft tissue-bone interfaces.

To reiterate what has been accomplished here: A consistent, complete, integrated clinical tool has been developed for hyperthermia treatment planning and evaluation. The next steps, which can be taken in parallel, are to improve the accuracy of the models in this clinical tool, and to apply this tool to improve therapy delivery for maximal patient benefit.

Appendix A

Temporal Oscillation of Temperature for Improved Thermal Dose Deposition

A.1 Abstract

The use of sinusoidal temporal oscillation of tissue temperature elevation was investigated as a hyperthermia treatment strategy. The time-averaged thermal dose rate generally increased with the amplitude of these oscillations. The amplitude of the oscillations was attenuated as they propagated away from heated regions. Hyperthermia treatments were simulated in two idealized simple tumor geometries, with power deposited only in the tumor volume and at the tumor boundary. Different tumor and normal tissue perfusion levels and tumor sizes were investigated. Two comparative dose metrics were conceived to evaluate the theoretical efficacy of oscillating heating in the simulations. The results of the simulations indicated dose deposition can be improved up to 50% (over constant temperature elevation) with oscillating temperature elevation for some of the configurations simulated. The magnitude of improvement was most dependent on and increased with the level of tumor perfusion. Oscillations about a nominal baseline temperature elevation of 44 or 45°C in the tumor most improved dose deposition, with the amplitude of oscillation ranging from 2°C for low tumor perfusion to 3.5 or 4°C for high tumor perfusion. Oscillations about 43°C, in contrast, worsened dose deposition.

A.2 Introduction

The treatment objective in hyperthermia is to deposit power preferentially in tumor tissue, elevating the tumor temperature to therapeutic levels, while trying to minimize temperature elevation in the surrounding normal tissue. Generally heating involves three phases: an initial temperature ramp-up, during which power is deposited principally to raise the tumor temperature; a middle plateau, during which power is administered to maintain tumor temperature elevation and to compensate for conductive and convective power losses in the tumor; and cool-down, during which power deposition is stopped and the tumor cools.

Thermal dose is used to quantify the therapeutic effect of local heating. Dewey *et al.* [23] and Gibbs [34] have suggested metrics for thermal dose for which dose rate is exponentially related to temperature, and both metrics have been used in clinical studies [22, 23, 34, 84, 87].

A hyperthermia treatment strategy in the middle phase of heating is suggested that exploits the positive exponential relationship between dose rate and temperature. By sinusoidally oscillating temperature elevation about a nominal baseline elevation, time-averaged dose rate can be increased, compared to the dose rate achieved by simply maintaining tumor temperature elevation constant at the nominal baseline value. The amplitude of these oscillations is attenuated as they propagate away from the heated volume. This means time-averaged dose rate can be increased in regions of large oscillations (*i.e.* inside the heated volume), whereas the time-averaged dose rate is more modestly increased in regions of small oscillations (*i.e.* outside the heated volume). The potential advantage of oscillatory heating is viewed from two perspectives. First, the dose deposited in the tumor volume, relative to the dose deposited in the normal tissue, may be increased. Second, the heating margin, *i.e.* the spatial extent of the tissue margin around the tumor which receives a thermal dose above a given threshold, may be decreased.

Several groups [50, 70] have recognized that hyperthermia treatment administered by scanned focused ultrasound results in oscillations in temperature elevation, and these oscillations can increase dose deposition. In both cases the effects of these temperature oscillations on dose deposition were investigated in the focal plane only.

Sinusoidal oscillation of power deposition or temperature elevation has also been used for tissue blood perfusion measurement [3, 4, 81]. This class of perfusion measurement device measures the phase lag between power and temperature oscillations, which is related to tissue perfusion, as well as driving frequency of the power deposition and tissue material properties.

Ocheltree and Frizzell [78] investigated the transient power deposition required to ramp up tumor temperature linearly and then maintain it constant. This approach is used here as well. Treatment simulations were performed to investigate the effects of temperature oscillations on dose deposition throughout the tissue volume. Treatment geometry and power deposition were kept simple to allow analytic solution of the heat transfer equations.

A.3 Theory

The simulated patient is divided into a tumor region (signified by the subscript $_\mathrm{t}$) and a normal (non-tumor) region (signified by $_\mathrm{n}$). Tissue properties are considered homogeneous and constant in each region, but need not be the same in both regions.

A temporally oscillating but spatially uniform temperature profile in the tumor is specified, and power is deposited only in the tumor volume and at the tumor boundary. From these considerations, the cyclic steady-state temporal and spatial temperature profile in the normal tissue is determined. In addition, the power deposition necessary to achieve that temperature profile is determined, along with physical constraints on that power deposition. Finally, an analysis is performed of the time-averaged thermal dose rates achieved inside and outside the tumor volume.

The two geometries explored are a Cartesian one-dimensional (1-D) case, in which the tumor is modeled as a slab of finite thickness embedded in an infinitely wide patient (see Figure A-1); and a spherical 1-D case, in which the tumor is a finite sphere in an infinite patient (Figure A-2). In both cases, heat transfer is modeled by the bioheat transfer equation:

$$\frac{1}{\alpha}\frac{\partial \theta}{\partial t} = \nabla^2 \theta - \lambda^2 \theta + \frac{\dot{Q}}{k} \tag{A.1}$$

where θ is temperature elevation above arterial blood temperature, α is tissue thermal diffusivity, t is time, λ is the tissue inverse perfusion length, $\dot{Q}$ is volumetric power deposition, and k is tissue thermal conductivity. $\lambda^2 \equiv w\rho_\mathrm{bl}c_\mathrm{bl}/k$, where w is tissue perfusion, ρ_bl is blood density, and c_bl is blood specific heat capacity. The $\dot{Q}$ term does not include metabolic heat generation explicitly, because Equation A.1 considers temperature elevation above the unheated baseline temperature, and that unheated baseline temperature is determined by basal metabolism.

A.3.1 Temperature Field Solutions

Assume a heating field that produces a spatially uniform tumor temperature elevation $\theta_\text{t}\{t\}$:

$$\theta_\text{t}\{t\} = \theta_1 + \theta_2 \sin \omega t \tag{A.2}$$

(How to actually achieve this heating will be discussed shortly.) Given $\theta_\text{t}\{t\}$, it is desired to determine the cyclic steady-state normal tissue temperature elevation field $\theta_\text{n}\{t\}$, assuming the power deposition in the normal tissue $\dot{Q}_\text{n} = 0$.

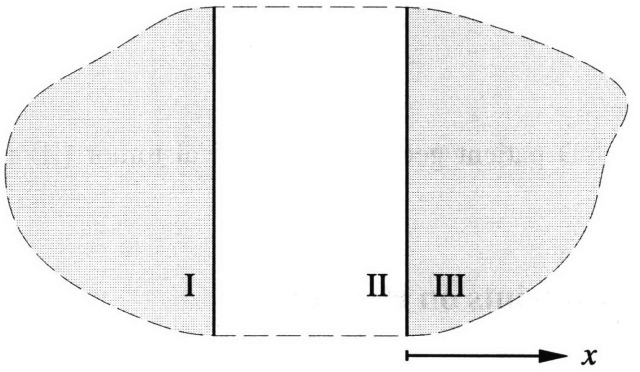

Figure A-1: Cartesian 1-D patient geometry—tumor slab (II) sandwiched between two semi-infinite regions of normal tissue (I and III).

In the Cartesian 1-D geometry, thermal boundary conditions on the normal tissue are:

$$\theta_{\text{n}_\text{c}}\{0,t\} = \theta_\text{t}\{t\} = \theta_1 + \theta_2 \sin \omega t \quad \text{and} \quad \theta_{\text{n}_\text{c}}\{\infty,t\} = 0 \tag{A.3}$$

The solution to the bioheat transfer equation (Equation A.1) with these boundary conditions is:

$$\theta_{\text{n}_\text{c}}\{x,t\} = \theta_1 e^{-\lambda_\text{n} x} + \theta_2 e^{-\beta_1 x} \sin(\omega t - \beta_2 x) \tag{A.4}$$

where $\lambda_\text{n}^2 = w_\text{n} \rho_\text{bl} c_\text{bl} / k_\text{n}$, $\beta_1^2 = \frac{1}{2}\left(\sqrt{\lambda_\text{n}^4 + (\omega/\alpha_\text{n})^2} + \lambda_\text{n}^2\right)$ and $\beta_2^2 = \frac{1}{2}\left(\sqrt{\lambda_\text{n}^4 + (\omega/\alpha_\text{n})^2} - \lambda_\text{n}^2\right)$.

In the spherical 1-D geometry, thermal boundary conditions on the normal tissue are:

$$\theta_{\text{n}_\text{s}}\{R,t\} = \theta_\text{t}\{t\} = \theta_1 + \theta_2 \sin \omega t \quad \text{and} \quad \theta_{\text{n}_\text{s}}\{\infty,t\} = 0 \tag{A.5}$$

The solution to the bioheat transfer equation with these boundary conditions is:

$$\theta_{\text{n}_\text{s}}\{r,t\} = \frac{R}{r}\left\{\theta_1 e^{-\lambda_\text{n}(r-R)} + \theta_2 e^{-\beta_1(r-R)} \sin[\omega t - \beta_2(r-R)]\right\} \tag{A.6}$$

(See Appendix B.8.1 for temperature field derivations.)

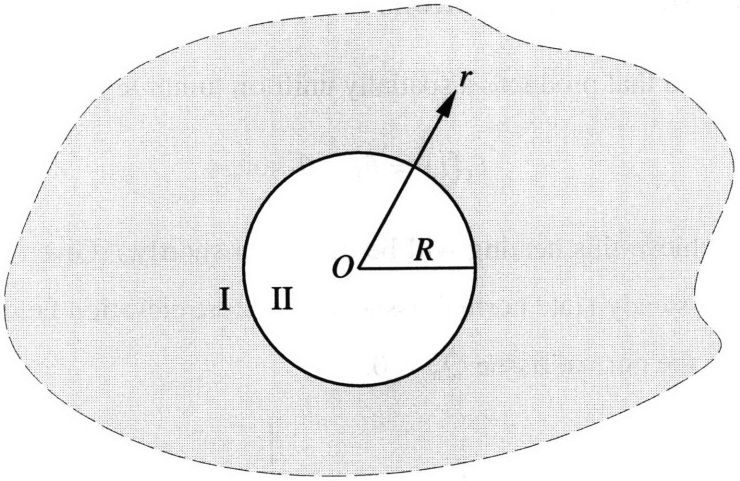

Figure A-2: Spherical 1-D patient geometry—spherical tumor (II) in infinite normal tissue region (I).

A.3.2 Physical Constraints on Heating

The heating necessary to achieve the desired tumor temperature profile can be divided into two components: volumetric power generation throughout the tumor volume, and surface flux at the boundary between the tumor and normal tissues [77, 85]. The first component, the volumetric power $\dot{Q}_{\rm t}$, is necessary to overcome the convective cooling effect of tumor perfusion $w_{\rm t}$, and to change the internal energy of the tumor tissue (in the case of oscillating $\theta_{\rm t}$). The second component, the tumor boundary heat flux $\dot{q}''_{\rm b}$, is necessary to overcome thermal conduction of energy from the tumor into the normal tissue volume.

For the purposes of the current investigation, physical constraints are imposed on $\dot{Q}_{\rm t}$ and $\dot{q}''_{\rm b}$; specifically, they are both constrained to be non-negative, as a violation of either constraint would imply administration of negative thermal energy, or the removal of thermal energy. Though negative $\dot{q}''_{\rm b}$ can be easily performed on the external surface of the patient by surface cooling, the geometries of the idealized simulated patient have no external surface.

Given the tumor temperature $\theta_{\rm t}\{t\} = \theta_1 + \theta_2 \sin \omega t$, the bioheat transfer equation can be solved for the volumetric power deposition $\dot{Q}_{\rm t}\{t\}$:

$$\dot{Q}_{\rm t}\{t\} = k_{\rm t}\left[\lambda_{\rm t}^2\theta_1 + \beta_{\rm t}^2\theta_2 \sin(\omega t + \varphi_{\rm t})\right] \tag{A.7}$$

where $\beta_{\rm t}^2 = \sqrt{\lambda_{\rm t}^4 + (\omega/\alpha_{\rm t})^2}$ and $\tan \varphi_{\rm t} = \frac{\omega/\alpha_{\rm t}}{\lambda_{\rm t}^2}$. Thus $\dot{Q}_{\rm t}$ is found to be a function of ω, and constraining $\dot{Q}_\mathrm{t}$ to be non-negative translates into a constraint on ω:

$$\dot{Q}_\mathrm{t}\{t\} \geq 0 \quad \text{when} \quad \omega \leq \omega_\mathrm{t}^* = \alpha_\mathrm{t}\lambda_\mathrm{t}^2\sqrt{\left(\frac{\theta_1}{\theta_2}\right)^2 - 1} = w_\mathrm{t}\frac{\rho_\mathrm{bl}c_\mathrm{bl}}{\rho_\mathrm{t}c_\mathrm{t}}\sqrt{\left(\frac{\theta_1}{\theta_2}\right)^2 - 1} \qquad \text{(A.8)}$$

where $\lambda_\mathrm{t}^2 = w_\mathrm{t}\rho_\mathrm{bl}c_\mathrm{bl}/k_\mathrm{t}$. ω_t^* is the critical angular velocity which ω cannot exceed without allowing $\dot{Q}_\mathrm{t}$ to become negative, at least during part of its oscillatory cycle. Since ω_t^* is physically constrained to be positive and real, Equation A.8 implies the additional constraint $\theta_1 > \theta_2$. Figure A-3 illustrates how ω_t^* varies as a function of θ_1/θ_2 for various values of w_t spanning the physiological range of perfusion.

Given the temperature field solution (Equation A.4 for the Cartesian 1-D geometry, or Equation A.6 for the spherical 1-D geometry), the tumor boundary heat flux $\dot{q}''_\mathrm{b}\{t\}$ is easily determined. In the Cartesian 1-D case, $\dot{q}''_\mathrm{bC}\{t\}$ is given by

$$\dot{q}''_\mathrm{bC}\{t\} = k_\mathrm{n}\left[\lambda_\mathrm{n}\theta_1 + \beta_\mathrm{C}\theta_2\sin(\omega t + \varphi_\mathrm{C})\right] \qquad \text{(A.9)}$$

where $\beta_\mathrm{C} = \sqrt{\beta_1^2 + \beta_2^2} = \sqrt[4]{\lambda_\mathrm{n}^4 + (\omega/\alpha_\mathrm{n})^2}$ and $\tan\varphi_\mathrm{C} = \beta_1/\beta_2$. In the spherical 1-D case, $\dot{q}''_\mathrm{bS}\{t\}$ is given by:

$$\dot{q}''_\mathrm{bS}\{t\} = k_\mathrm{n}\left[(R^{-1} + \lambda_\mathrm{n})\theta_1 + \beta_\mathrm{S}\theta_2\sin(\omega t + \varphi_\mathrm{S})\right] \qquad \text{(A.10)}$$

where $\beta_\mathrm{S} = \sqrt{(R^{-1} + \beta_1)^2 + \beta_2^2}$ and $\tan\varphi_\mathrm{S} = (R^{-1} + \beta_1)/\beta_2$. Like $\dot{Q}_\mathrm{t}$, $\dot{q}''_\mathrm{b}$ is seen to be a function of ω. Constraining $\dot{q}''_\mathrm{b}$ to be non-negative yields, in the Cartesian 1-D geometry:

$$\dot{q}''_\mathrm{bC}\{t\} \geq 0 \quad \text{when} \quad \omega \leq \omega_\mathrm{bC}^* = \alpha_\mathrm{n}\lambda_\mathrm{n}^2\sqrt{\left(\frac{\theta_1}{\theta_2}\right)^4 - 1} = w_\mathrm{n}\frac{\rho_\mathrm{bl}c_\mathrm{bl}}{\rho_\mathrm{n}c_\mathrm{n}}\sqrt{\left(\frac{\theta_1}{\theta_2}\right)^4 - 1} \qquad \text{(A.11)}$$

and, in the spherical 1-D geometry:

$$\dot{q}''_\mathrm{bS}\{t\} \geq 0 \quad \text{when} \quad \omega \leq \omega_\mathrm{bS}^* = \qquad \text{(A.12)}$$

$$\alpha_\mathrm{n}\left\{\begin{array}{l} B^4 - \lambda_\mathrm{n}^4 + 2R^{-2}(2B^2 + \lambda_\mathrm{n}^2 + R^{-2}) \\ \\ -\,2R^{-1}\sqrt{2B^6 + (5R^{-2} + 2\lambda_\mathrm{n}^2)B^4 + 4R^{-2}(\lambda_\mathrm{n}^2 + R^{-2})B^2 + R^{-4}(2\lambda_\mathrm{n}^2 + R^{-2})} \end{array}\right\}^{\frac{1}{2}}$$

where $B = R^{-1}\sqrt{\left[(1 + R\lambda_\mathrm{n})\,\theta_1/\theta_2\right]^2 - 1}$.

The ultimate constraint on ω is $\omega \leq \omega^*$, where $\omega^* = \omega_\mathrm{C}^* = \min(\omega_\mathrm{t}^*, \omega_\mathrm{bC}^*)$ in the Cartesian 1-D geometry, and $\omega^* = \omega_\mathrm{S}^* = \min(\omega_\mathrm{t}^*, \omega_\mathrm{bS}^*)$ in the spherical 1-D geometry. Usually $\omega_\mathrm{t}^* < \omega_\mathrm{bC}^*$; and $\omega_\mathrm{bC}^* < \omega_\mathrm{bS}^*$ always, with $\lim_{R\to\infty}\omega_\mathrm{bS}^* = \omega_\mathrm{bC}^*$. (See Appendix B.8.2 for derivations concerning heating constraints.)

A.3.3 Comparative Dosimetry

The exponential thermal dose relationship described by Dewey *et al.* [23] was used to perform dosimetry based on the temperature solutions obtained above. Accordingly, dose rate $\dot{D}$ as a function of tissue temperature T is given by:

$$\dot{D}\{T\} = R^{43-T/^{\circ}\mathrm{C}}\ \mathrm{EQ43/min} \quad \text{where} \quad R = \begin{cases} 0.25, & T < 43^{\circ}\mathrm{C} \\ 0.5, & T \geq 43^{\circ}\mathrm{C} \end{cases} \tag{A.13}$$

The units of $\dot{D}$ are equivalent minutes at 43°C per minute, or EQ43/min.

When temperature is constant at $T = T_1$, the dose rate $\dot{D}\{T_1\}$ is simply a function of T_1. When temperature is varied sinusoidally as $T\{t\} = T_1 + T_2 \sin \omega t$, the time-averaged dose rate $\bar{\dot{D}}\{T_1, T_2\}$ is a function of both T_1 and T_2. To simplify nomenclature, $\bar{\dot{D}}$ will imply oscillating heating, and $\dot{D}$ will imply constant heating.

Two comparative metrics are used to compare the dosimetry of the oscillating and non-oscillating heating cases. Both metrics are designed to provide measures of the percent improvement in dose deposition of oscillating heating over non-oscillating heating. The first metric $\mathcal{M}_1$ compares the volume-averaged dose deposition in the normal tissue volume with and without oscillations. Specifically, $\mathcal{M}_1$ is the percent improvement in volume-averaged normalized dose deposition of heating with oscillations over heating without oscillations:

$$\mathcal{M}_1 = \frac{\frac{1}{V}\int_V \frac{\dot{D}_\mathrm{n}}{\dot{D}_\mathrm{t}}\,dV - \frac{1}{V}\int_V \frac{\bar{\dot{D}}_\mathrm{n}}{\bar{\dot{D}}_\mathrm{t}}\,dV}{\frac{1}{V}\int_V \frac{\dot{D}_\mathrm{n}}{\dot{D}_\mathrm{t}}\,dV} \times 100\% = \left(1 - \frac{\dot{D}_\mathrm{t}}{\bar{\dot{D}}_\mathrm{t}} \frac{\int_V \bar{\dot{D}}_\mathrm{n}\,dV}{\int_V \dot{D}_\mathrm{n}\,dV}\right) \times 100\% \tag{A.14}$$

The relevant tissue volume V is the volume of normal tissue in which the time-averaged temperature is greater than 40°C, which is taken to be the nominal threshold for non-trivial thermal damage to tissue. For the metric $\mathcal{M}_1$, dose deposition is normalized to dose deposition in the tumor.

The second metric $\mathcal{M}_2$ compares the width of the margin of heating around the tumor between heating with oscillations and heating without oscillations. For heating without oscillations the margin width d_{50} is defined as the distance outside the tumor at which the dose rate equals half the dose rate of the tumor, *i.e.* $\dot{D}_\mathrm{n}\{d\} = \frac{1}{2}\dot{D}_\mathrm{t}$; for heating with oscillations the margin width $\bar{d}_{50}$ is defined as the distance outside the tumor at which the time-averaged dose rate equals half the time-averaged dose rate of the tumor, *i.e.* $\overline{\dot{D}}_{\mathrm{n}}\{\overline{d}_{50}\} = \frac{1}{2}\overline{\dot{D}}_{\mathrm{t}}$. Then:

$$\mathcal{M}_2 = \frac{d_{50} - \overline{d}_{50}}{d_{50}} \times 100\% = \left(1 - \frac{\overline{d}_{50}}{d_{50}}\right) \times 100\% \tag{A.15}$$

The metrics $\mathcal{M}_1$ and $\mathcal{M}_2$ were both calculated for the cases tumor tissue perfusion $W_{\mathrm{t}} = 10, 20, 40\,\mathrm{ml/min{-}100g}$ (W and w are both measurements of perfusion, related by $\rho W = w$); normal tissue perfusion $W_{\mathrm{n}} = 20, 40\,\mathrm{ml/min{-}100g}$; tumor radius $R = 1, 2, 4, \infty\,\mathrm{cm}$ ($R = \infty$ corresponds to the Cartesian 1-D geometry); $T_1 = 42$ to 46°C in 0.25°C increments; and $T_2 = 0$ to as large as possible in 0.10°C increments. Other tissue properties and blood properties are given in Table A.1. Perfusion is the only tissue property that was allowed to differ between tumor and normal tissue in this analysis. Lastly, ω was set to ω^* to maximally attenuate oscillations in the normal tissue.

Table A.1: Tissue and blood properties.

tissue thermal conductivity	k	5.5 mW/cm–°C
tissue density	ρ	$1.07\,\mathrm{g/cm^3}$
tissue specific heat capacity	c	3.1 J/g–°C
blood density	ρ_{bl}	$1.00\,\mathrm{g/cm^3}$
blood specific heat capacity	c_{bl}	4.18 J/g–°C

T_2 has an upper bound because as T_2 increases, ω^* decreases (see Equations A.8, A.11, and A.12). Although increasing T_2 increases $\overline{\dot{D}}\{T_1, T_2\}$, reducing the time necessary to administer a treatment, ω^* decreases more quickly than $\overline{\dot{D}}\{T_1, T_2\}$ increases. To achieve a total treatment thermal dose D_{TX}, the duration of treatment t_{TX} is given by:

$$t_{\mathrm{TX}} = \frac{2\pi N}{\omega} = \frac{D_{\mathrm{TX}}}{\overline{\dot{D}}\{T_1, T_2\}} \tag{A.16}$$

Here $2\pi/\omega$ is the period of oscillation, and N is the number of cycles of heating. The minimum period of oscillation is $2\pi/\omega^*$. By setting $D_{\mathrm{TX}} \leq 60\,\mathrm{EQ43}$ and $N = 1$, then, T_2 was implicitly constrained.

Time-averaged dose rates were determined by integrating the instantaneous dose rate over one cycle, using the quad8 function in Matlab 4.1 (The Mathworks, Inc., Natick, MA). This function used an "adaptive recursive Newton Cotes 8 panel rule," and performed integrations to an accuracy of 0.1%. $\dot{D}_{\mathrm{n}}$ and $\overline{\dot{D}}_{\mathrm{n}}$ were calculated at 0.01 cm intervals in the normal tissue. To calculate $\mathcal{M}_1$, $\dot{D}_{\mathrm{n}}$ and $\overline{\dot{D}}_{\mathrm{n}}$ were weighted by r^2 (the square of the radial coordinate) and summed. (For the Cartesian 1-D case the weighting was uniform.) To calculate $\mathcal{M}_2$, $\dot{D}_{\mathrm{n}}$ and $\overline{\dot{D}}_{\mathrm{n}}$ were linearly interpolated in the relevant spatial interval.

A.4 Results

Figure A-4 shows a family of curves relating the time-averaged dose rate $\overline{\dot{D}}\{T_1, T_2\}$ to T_2, with each curve corresponding to a different T_1. When $T_2 = 0$ then $T\{t\} = T_1$ is a constant, and $\overline{\dot{D}}\{T_1, 0\} = \dot{D}\{T_1\}$. In general temperature oscillations are seen to increase the time-averaged dose rate $\overline{\dot{D}}\{T_1, T_2\}$, with the exception of oscillations of magnitude $T_2 < 1$°C about a baseline temperature in the range 42.5°C $< T_1 <$ 43.5°C. Furthermore, increasing T_2 generally increases $\overline{\dot{D}}\{T_1, T_2\}$ without limit (with the small exception just noted). A constraint imposed on T_2 during the generation of the curves in Figure A-4 was that $T_1 - T_2 >$ 37°C, ensuring that $T\{t\}$ exceeds the unheated baseline temperature 37°C. (As previously observed, however, T_2 is further constrained in practice.)

Figure A-5 shows the same data as Figure A-4, but $\overline{\dot{D}}\{T_1, T_2\}$ is normalized by $\dot{D}\{T_1\}$; thus Figure A-5 plots $\overline{\dot{D}}\{T_1, T_2\}/\dot{D}\{T_1\}$ as a function of T_2. Again, each curve corresponds to a different T_1. Parts of many of the curves overlap, and all the curves would lie on top of each other if R in Equation A.13 were not a function of temperature. Figure A-6 is an enlargement of the region of small T_2 of Figure A-5. In this region it is seen that all curves with $T_1 <$ 42°C essentially overlap, and all curves with $T_1 >$ 43°C also largely overlap, but curves in the region 42°C $\leq T_1 \leq$ 43°C make the transition between the two extreme curves.

A sample heating profile, obtained using Equation A.6, is given in Figure A-7. For this case, $W_{\mathrm{t}} = 10\,\mathrm{ml/min\text{–}100g}$, $W_{\mathrm{n}} = 20\,\mathrm{ml/min\text{–}100g}$, $R = 2\,\mathrm{cm}$, $T_1 = 44.5$°C, $T_2 = 2$°C, and $\omega = \omega = \omega^* = 7.77 \times 10^{-3}\,\mathrm{rad/s}$. In Figure A-7A, the solid line shows the time-averaged temperature, and the dashed lines bound the temperature oscillations. Note that $r < 2\,\mathrm{cm}$ corresponds to tumor tissue, and $r > 2\,\mathrm{cm}$ to normal tissue. The solid line in Figure A-7B shows the time-averaged tissue dose normalized to the time-averaged tumor dose, $\overline{\dot{D}}_{\mathrm{n}}/\overline{\dot{D}}_{\mathrm{t}}$, as a function of position, for the sinusoidal tumor temperature $T_{\mathrm{t}} = 44.5\text{°C} + 2\text{°C} \sin \omega t$; the dashed line shows tissue dose normalized to tumor dose, $\dot{D}_{\mathrm{n}}/\dot{D}_{\mathrm{t}}$, as a function of position, for the constant tumor temperature profile $T_{\mathrm{t}} = 44.5°\mathrm{C}$. Figure A-7C shows the ratio $\mathcal{R}$ of the normalized time-averaged tissue dose rate with sinusoidal heating $(\overline{\dot{D}_{\mathrm{n}}}/\overline{\dot{D}_{\mathrm{t}}})$ to the normalized tissue dose rate with constant heating $(\dot{D}_{\mathrm{n}}/\dot{D}_{\mathrm{t}})$, $\mathcal{R} = \frac{\overline{\dot{D}_{\mathrm{n}}}/\overline{\dot{D}_{\mathrm{t}}}}{\dot{D}_{\mathrm{n}}/\dot{D}_{\mathrm{t}}}$. The shape of the curve shown (a local minimum in $\mathcal{R}$ near the tumor boundary, a local maximum further from the tumor, and an asymptote with $\lim_{r\to\infty} \mathcal{R} < 1$) is typical when $T_1 > 43.5°\mathrm{C}$, but other variations are possible. When $T_1 = 43°\mathrm{C}$, there is a maximum in $\mathcal{R}$ near the tumor boundary, and the asymptote is $\lim_{r\to\infty} \mathcal{R} > 1$ for small values of T_2 and $\lim_{r\to\infty} \mathcal{R} < 1$ for large T_2. When $T_1 < 42°\mathrm{C}$, the curve decays approximately exponentially from the tumor boundary for small values of T_2, and has a maximum in $\mathcal{R}$ near the tumor and an asymptote $\lim_{r\to\infty} \mathcal{R} < 1$ for large values of T_2.

Figure A-8 shows a set of comparative dose metric curves; Figure A-8A shows $\mathcal{M}_1$, and Figure A-8B shows $\mathcal{M}_2$, and each curve is labeled according to its T_1. These sets of curves exhibit several characteristics found in all the simulations performed in the specified ranges of W_{t}, W_{n}, and R. First, the $T_1 = 43°\mathrm{C}$ curves show poor performance, regardless of T_2. Second, when $T_1 < 43°\mathrm{C}$, the curves have maxima at small values of T_2, and the smaller T_1 is the smaller the value of T_2 at which maximizes the curve; in addition, as T_2 increases the comparative dose metrics go negative. Finally, when $T_1 \geq 44°\mathrm{C}$ the curves nearly coincide, and the curves for lower values of T_1 are able to extend to higher values of T_2, and usually to higher values of the comparative dose metrics as well.

Table A.2 gives the (T_1, T_2) pairs that maximize $\mathcal{M}_1$ and $\mathcal{M}_2$ for all the W_{t}, W_{n}, and R configurations. $R = \infty$ corresponds to the Cartesian 1-D geometry. For $W_{\mathrm{t}} = 10$ ml/min–100g) two maxima are given for $\mathcal{M}_1$ for each W_{t} and R configuration. The one with $T_1 > 44°\mathrm{C}$ is a local maximum, and the one with $T_1 = 42°\mathrm{C}$ is a global maximum within the constraint $42°\mathrm{C} \leq T_1 \leq 46°\mathrm{C}$.

A.5 Discussion

The idiosyncratic behavior exhibited in Figures A-7 and mboxA-8 and in Table A.2 can in large part be attributed to the “kink” at 43°C in the temperature-thermal dose relationship. If in Equation A.13 the base R were constant at $R = 0.5$ over the entire temperature range of interest, then the normalized time-averaged dose rate $\overline{\dot{D}}\{T_1, T_2\}/\dot{D}\{T_1\}$ would be a function of T_2 only, and it would essentially follow the curves associated with $T_1 = 47°\mathrm{C}$ in Figures A-5 and A-6. In this case, oscillating temperatures would improve dose deposition (as measured by comparative dose metrics $\mathcal{M}_1$ and $\mathcal{M}_2$) for any T_1 and T_2, and the larger the value of T_2 the larger the improvement in dose deposition would be. (T_2 would still be constrained by Equation A.16, however, so it could not be arbitrarily large in practice.)

For the regular temperature-thermal dose relationship (Equation A.13), several general conclusions can be drawn from the treatment simulations:

1. The optimal T_1 is in the 44 to 45°C range, nearly independent of W_t, W_n, and R. $\mathcal{M}_2$ is typically maximized at $T_1 = 44°\mathrm{C}$, and $\mathcal{M}_1$ is maximized at slightly higher values of T_1. A potentially significant exception is the simulation configurations for which $W_t = 10\,\mathrm{ml/min–100g}$, for which $T_1 = 42°\mathrm{C}$ maximizes $\mathcal{M}_1$ (but not $\mathcal{M}_2$).
2. A poor choice for T_1, regardless of simulation configuration, is $T_1 = 43°\mathrm{C}$.
3. For the simulation configurations studied, W_t is the most influential parameter over the value of the optimal T_2 and the magnitude of the maximized comparative dose metrics. The larger W_t, the larger the optimal value of T_2, and the larger the values of the metrics.
4. For a given simulation configuration, the maximum value of $\mathcal{M}_2$ registers approximately 50–100% higher than the maximum value of $\mathcal{M}_1$.

Several observations can be made from the heating field solutions presented in Figure A-7. First, temperature rapidly falls off beyond the edge of the tumor, which results in an even more precipitous fall-off in dose rate and time-averaged dose rate. In the case presented in Figure A-7, the margins of heating d_{50} and $\bar{d}_{50}$ are about 0.5 mm, and the margin width was sub-millimeter in all the heating configurations analyzed. This tight margin was possible because the power deposition field was so sharply defined. A more realistic power deposition field will probably not be so sharply defined, so temperature and dose rate and time-averaged dose rate will not fall off from the tumor boundary so quickly. Thus d_{50} and $\bar{d}_{50}$ may increase substantially, although the difference $d_{50} - \bar{d}_{50}$ may not change much; this could lead to reduced values of the comparative dose $\mathcal{M}_2$, compared to the ideal power deposition field. In contrast, $\mathcal{M}_1$ might not change very much.

A second observation from Figure A-7 concerns the ratio $\mathcal{R} = \frac{\overline{\dot{D}_\mathrm{n}}/\overline{\dot{D}_\mathrm{t}}}{\dot{D}_\mathrm{n}/\dot{D}_\mathrm{t}}$. Where $\mathcal{R}$ is less than, equal to, or greater than 1, local dose deposition with oscillatory heating is less than, equal to, or greater than local dose deposition without oscillations, respectively (for the same dose deposition in the tumor). Thus in regions in the normal tissue where dose deposition is significant, the treatment objective is to achieve $\mathcal{R} < 1$. In the case depicted in Figure A-7C, $\mathcal{R} < 1$ near the tumor boundary ($r = 2\,\mathrm{cm}$) and distant from the tumor, but $\mathcal{R} > 1$ in the middle region. Because the vast majority of the dose deposited in the normal tissue occurs in the region nearest the tumor boundary, where $\mathcal{R} > 1$, this heating pattern is a good one. In regions where dose deposition is low, the value of $\mathcal{R}$ is unimportant for practical purposes.

$\mathcal{M}_2$ compares d_{50} and $\overline{d}_{50}$, where local dose deposition is 50% that in the tumor. But if $\mathcal{M}_2$ were based on d_{10} and $\overline{d}_{10}$, for example, where local dose deposition is 10% that in the tumor, the message conveyed by $\mathcal{M}_2$ would change dramatically. Returning to the case shown in Figure A-7C, $d_{50} > \overline{d}_{50}$ yields $\mathcal{M}_2 = 5\%$; but $d_{10} < \overline{d}_{10}$ would yield $\mathcal{M}_2 = -3\%$ —a qualitatively different result. If the administered dose D_TX has a substantial effect on tissue, it is reasonable to assume that $\frac{1}{2}D_\mathrm{TX}$ could have a significant effect as well. $\frac{1}{10}D_\mathrm{TX}$ is quite a bit smaller, however, and may not have much clinical importance. Thus $\mathcal{M}_2$ was based simply on d_{50} and $\overline{d}_{50}$.

For tissue configurations with low tumor perfusion levels (*viz.* $W_\mathrm{t} = 10\,\mathrm{ml/min{-}100g}$), Table A.2 indicates that $T_1 = 42°\mathrm{C}$ gave slightly superior values of $\mathcal{M}_1$ to those obtained when $T_1 > 43°\mathrm{C}$. T_1 was constrained to be between 42 and 46°C in Table A.2. It is possible values for $\mathcal{M}_1$ can be even further increased by allowing $T_1 < 42°\mathrm{C}$, but it cannot be increased by allowing $T_1 > 46°\mathrm{C}$ (unless D_TX is increased). There is a distinct clinical disadvantage to administering hyperthermia treatment with $T_1 \leq 42°\mathrm{C}$: to administer a thermal dose $D_\mathrm{TX} = 60\,\mathrm{EQ43}$ would take three or more hours. Thus heating patterns based on $T_1 < 42°\mathrm{C}$ were excluded from Table A.2, and those with $T_1 = 42°\mathrm{C}$ were included for thoroughness.

The cyclic steady-state and constant steady-state analyses ignored the effects on dose deposition of the transient heating patterns—both the transients associated with the first phase of heating, ramp-up, and the third and final phase, cool-down. The issue of dose deposition during ramp-up can be ignored by essentially injecting a bolus of volumetric thermal energy. The required field of injected volumetric thermal energy is $Q = \rho c \theta_I$, where θ_I is the tissue temperature elevation field at the start of cyclic or constant steady-state temperature elevation. (Note that $t = 0$ does not necessarily correspond to the start of treatment. For example, $\theta_t\{t\} = \theta_1 + \theta_2 \sin \omega t$ indicates $\theta_t\{0\} = \theta_1$, but this is not meant to imply $\theta_I = \theta_1$ in the tumor.) Ocheltree and Frizzell [78] model a bolus injection of thermal energy over the time span of 6 min, but theoretically it could be done essentially instantaneously. For this instantaneous bolus strategy there is no dose deposition at all during ramp-up.

During cool-down local dose deposition largely depends on the phase of the temperature elevation. Generally speaking, if heating is stopped when $\theta_n\{t\}$ near the tumor boundary is close to the minimum of its cycle, relatively little dose will be deposited in that region. The phase of $\theta_n\{t\}$ near the tumor lags slightly behind the phase of $\theta_t\{t\}$ (by $\beta_2 x$ rad and $\beta_2(r - R)$ rad for the Cartesian and spherical 1-D cases, respectively), so if the $\theta_t\{t\}$ is near its baseline θ_1 at the start of cool-down, it is expected there would be less dose deposition in cool-down in the normal tissue near the tumor if the oscillatory heating strategy were used than if it were not.

Scanned focused ultrasound is a popular technique for administering power in hyperthermia treatment. The temperature oscillations induced by this mode of treatment are not sinusoidal, but tend to have an exponential rise and a longer exponential decay in a single oscillatory cycle [50]. For the same time-averaged temperature, this type of oscillation is generally superior to a pure sinusoid, in terms of time-averaged dose deposition, because the difference between the peak and mean temperature elevation is greater than the difference between the mean and minimum temperature elevation. Thus scanned focused ultrasound has the potential to substantially benefit from the temperature oscillations intrinsic to the technique. The longer the scan time (*i.e.* the time to complete one cycle of scanning) is, the greater the size of the temperature fluctuations, and the more significant the potential effect of the temperature oscillations on dose deposition. The magnitude of the temperature fluctuations increases close to linearly with tissue perfusion and scan time. Moros *et al.* [70] calculated theoretical temperature fluctuations from less than 1 to several °C for various tissue perfusion levels and scan times from 5 to 30 s; for tissue perfusion of 30 ml/min–100g and scan time of 30 s, for example, temperature fluctuations (*i.e.* the difference between peak and minimum temperatures) were 3°C. This is comparable to experimental results obtained by Hynynen *et al.* [50], who measured temperature fluctuations of about 5°C in *in vivo* animal experiments.

In these scanned focused ultrasound treatments [50] and simulations[70], the presented temperature fluctuations occurred at locations where the focus passed. Fluctuations at other locations in the heated volume were considerably smaller, however. The comparative dose metrics $\mathcal{M}_1$ and $\mathcal{M}_2$ were used to compare dose when the dose deposition in the tumor volume is uniform, but variations on these metrics could be used for inhomogeneous dose deposition as well. For example, Equation A.14 could be modified by substituting volume-averaged tumor dose rates for $\dot{D}_\mathrm{t}$ and $\overline{\dot{D}}_\mathrm{t}$ (*i.e.* $\dot{D}_\mathrm{t} = \int_{V_\mathrm{t}} \dot{D}\, dV_\mathrm{t}/V_\mathrm{t}$ and $\overline{\dot{D}}_\mathrm{t} = \int_{V_\mathrm{t}} \overline{\dot{D}}\, dV_\mathrm{t}/V_\mathrm{t}$, where V_t is the tumor volume). With such metrics scanning patterns could be simulated and optimized to enhance dose deposition by exploiting the effects of temperature oscillations on time-averaged dose rate.

Table A.2: The optimal comparative dose metrics $\mathcal{M}_1$ and $\mathcal{M}_2$ (%), and the (T_1, T_2) pairs (°C) that achieve them, for all W_t (ml/min–100g), W_n (ml/min–100g), and R (cm) configurations. $R = \infty$ corresponds to the Cartesian 1-D geometry. For $W_\mathrm{t} = 10$ ml/min–100g two solutions are given for $\mathcal{M}_1$, including one at $T_1 = 42$°C.

W_t	R	$W_\mathrm{n} = 20$						$W_\mathrm{n} = 40$					
		$\mathcal{M}_1$	T_1	T_2	$\mathcal{M}_2$	T_1	T_2	$\mathcal{M}_1$	T_1	T_2	$\mathcal{M}_2$	T_1	T_2
10	1	14	44.75	1.9	29	44.00	2.3	15	44.25	2.2	30	44.00	2.3
		15	42.00	1.1				16	42.00	1.2			
	2	15	44.75	1.9	31	44.00	2.3	16	44.25	2.2	32	44.00	2.3
		16	42.00	1.1				17	42.00	1.2			
	4	15	44.75	1.9	32	44.00	2.3	16	44.25	2.2	35	44.00	2.3
		17	42.00	1.1				17	42.00	1.2			
	∞	16	44.25	2.2	33	44.00	2.3	17	44.25	2.2	34	44.00	2.3
		18	42.00	1.1				18	42.00	1.2			
20	1	24	45.00	2.5	40	44.00	3.1	24	44.00	2.8	41	44.25	3.0
	2	26	44.50	2.8	43	44.00	3.1	26	44.25	3.0	44	44.00	3.1
	4	27	44.50	2.8	44	44.00	3.1	27	44.25	3.0	46	44.00	3.1
	∞	28	44.50	2.8	46	44.00	3.1	28	44.25	3.0	46	44.00	3.1
40	1	37	45.00	3.3	52	44.00	3.9	36	44.50	3.6	52	44.25	3.7
	2	39	44.50	3.6	55	44.00	3.9	37	44.50	3.6	54	44.00	3.9
	4	40	44.50	3.6	57	44.00	3.9	38	44.50	3.6	57	44.00	3.9
	∞	42	44.50	3.6	59	44.00	3.9	39	44.50	3.6	57	44.00	3.9

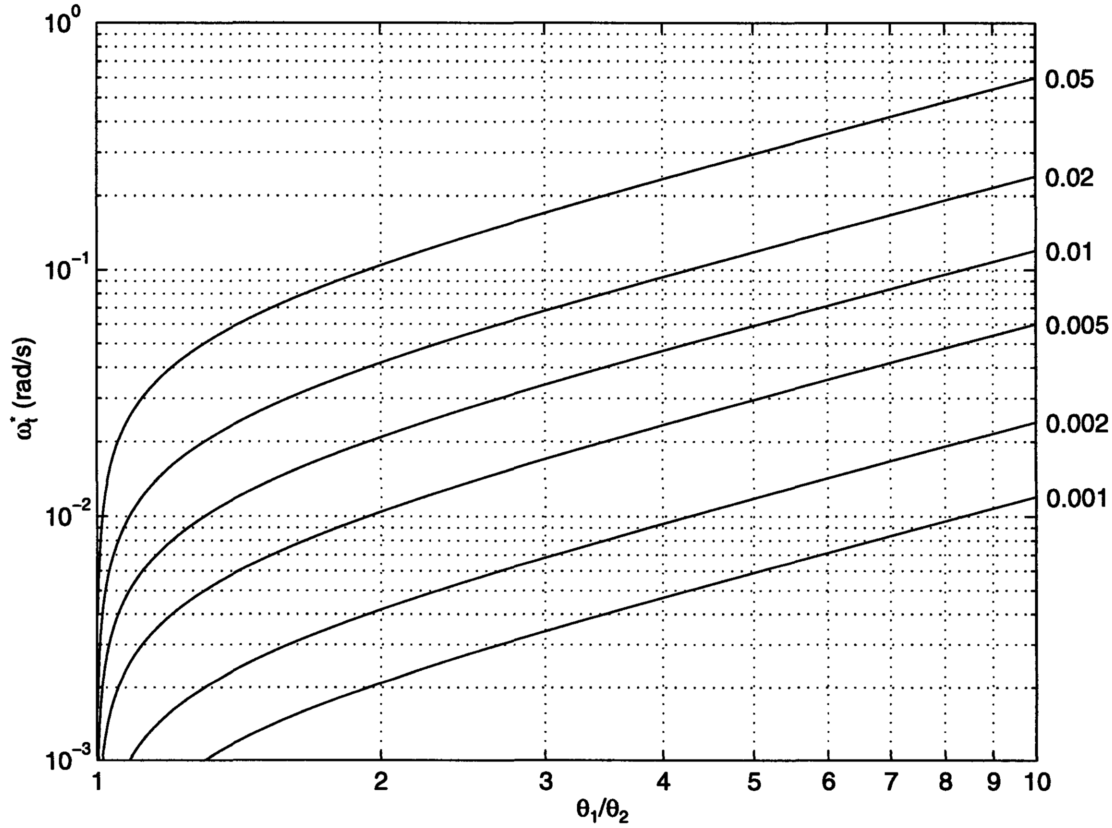

Figure A-3: ω_t^* as a function of θ_1/θ_2. Each curve is labeled according to its w_t (in s^{-1}).

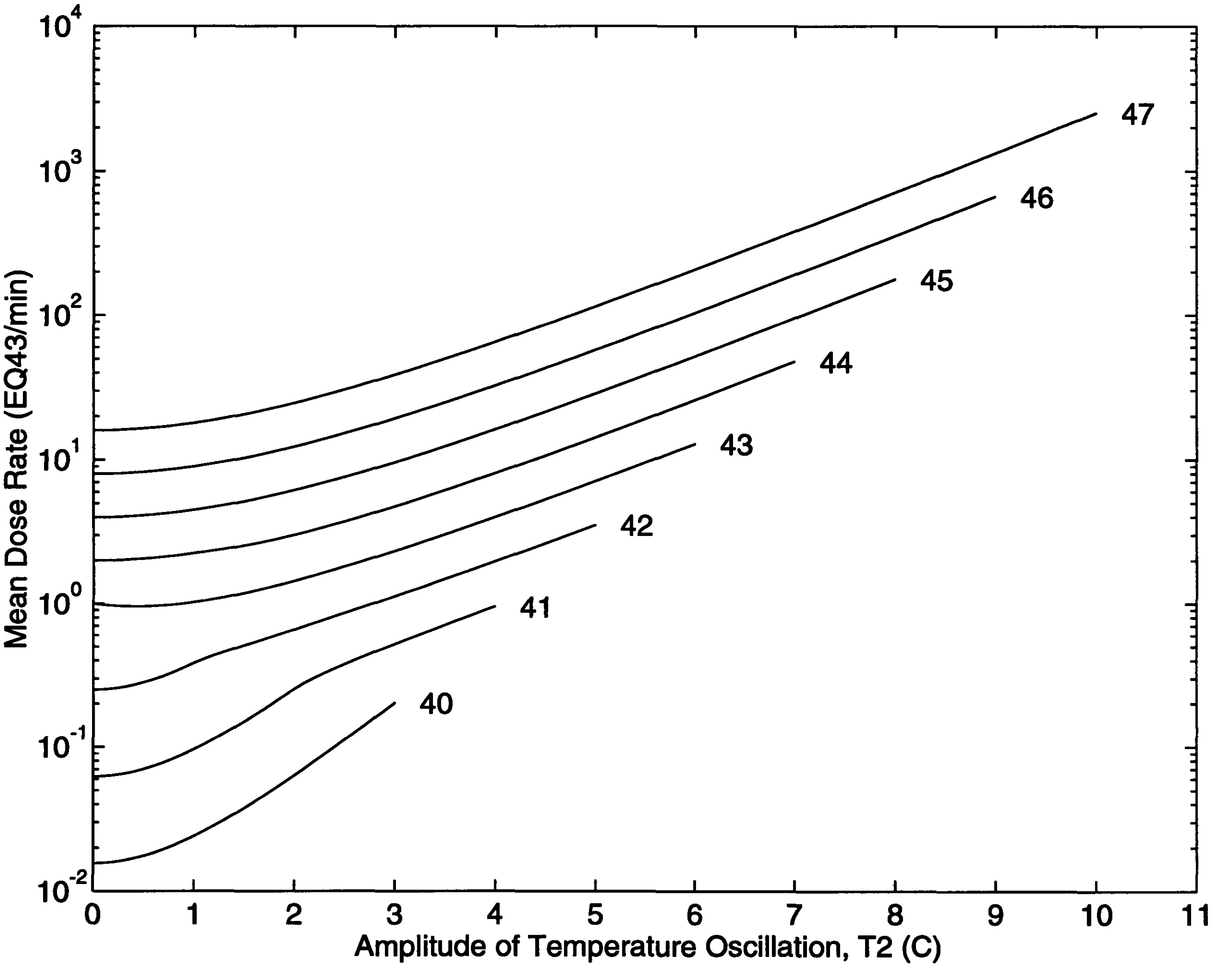

Figure A-4: Time-average dose rate $\overline{\dot{D}}\{T_1, T_2\}$ (EQ43/min) as a function of temperature oscillation amplitude T_2 (°C). Each curve is labeled according to its nominal baseline temperature T_1 (°C).

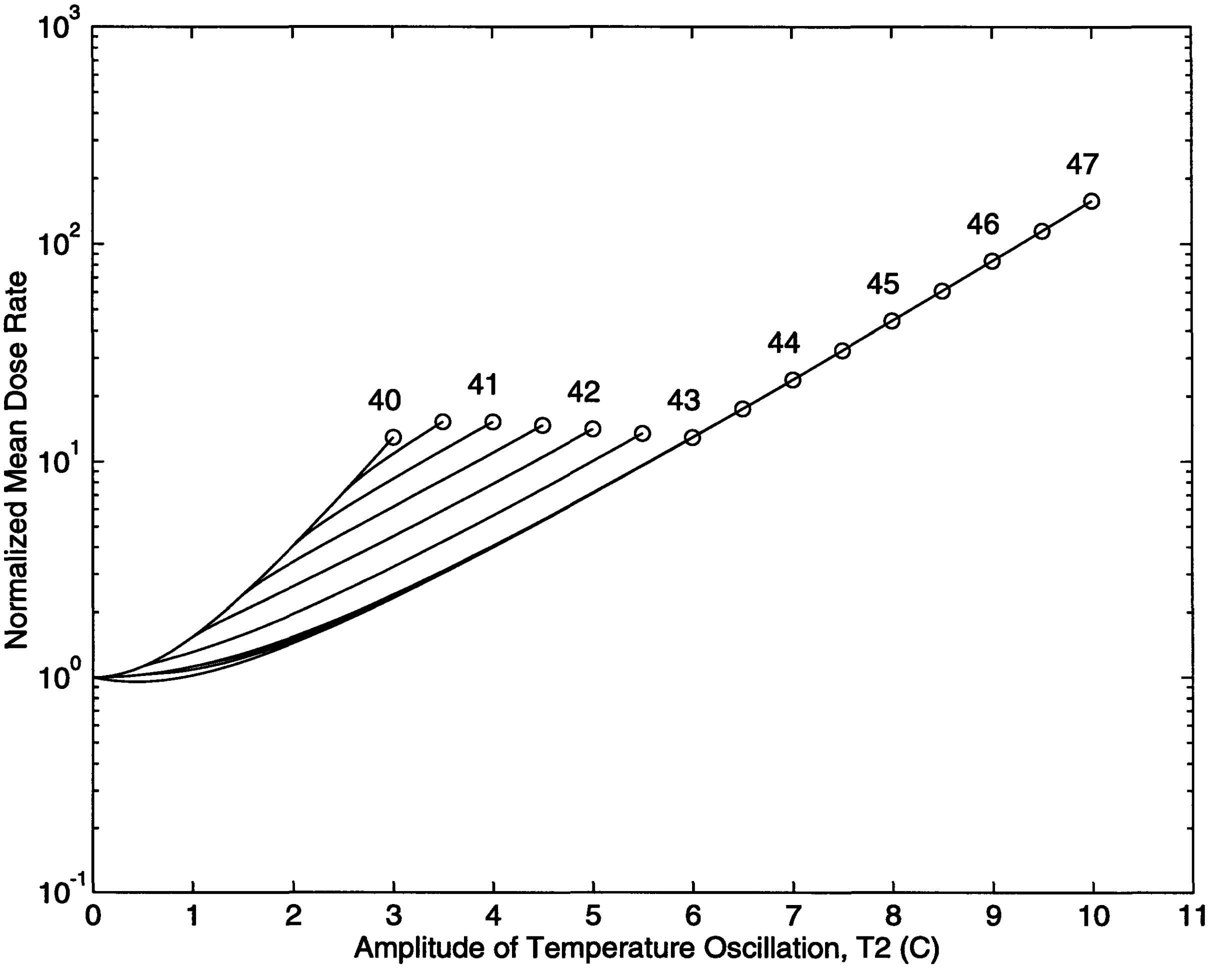

Figure A-5: Normalized time-averaged dose rate $\overline{\dot{D}}\{T_1, T_2\}/\dot{D}\{T_1\}$ as a function of temperature oscillation amplitude T_2 (°C). Each curve is labeled according to its nominal baseline temperature T_1 (°C).

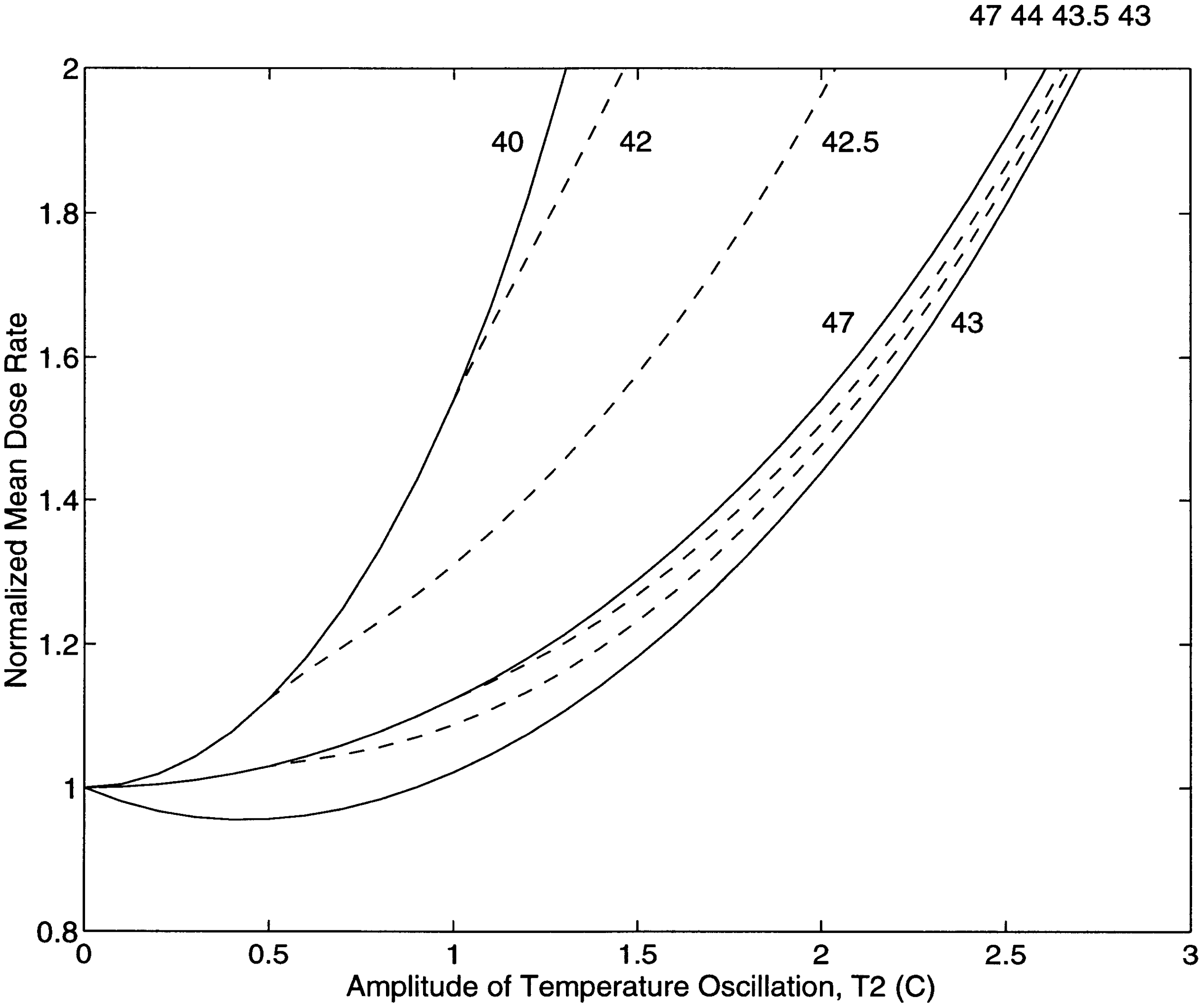

Figure A-6: Enlargement of previous figure—normalized time-averaged dose rate $\overline{\dot{D}}\{T_1, T_2\}/\dot{D}\{T_1\}$ as a function of temperature oscillation amplitude T_2 (°C). Each curve is labeled according to its nominal baseline temperature T_1 (°C).

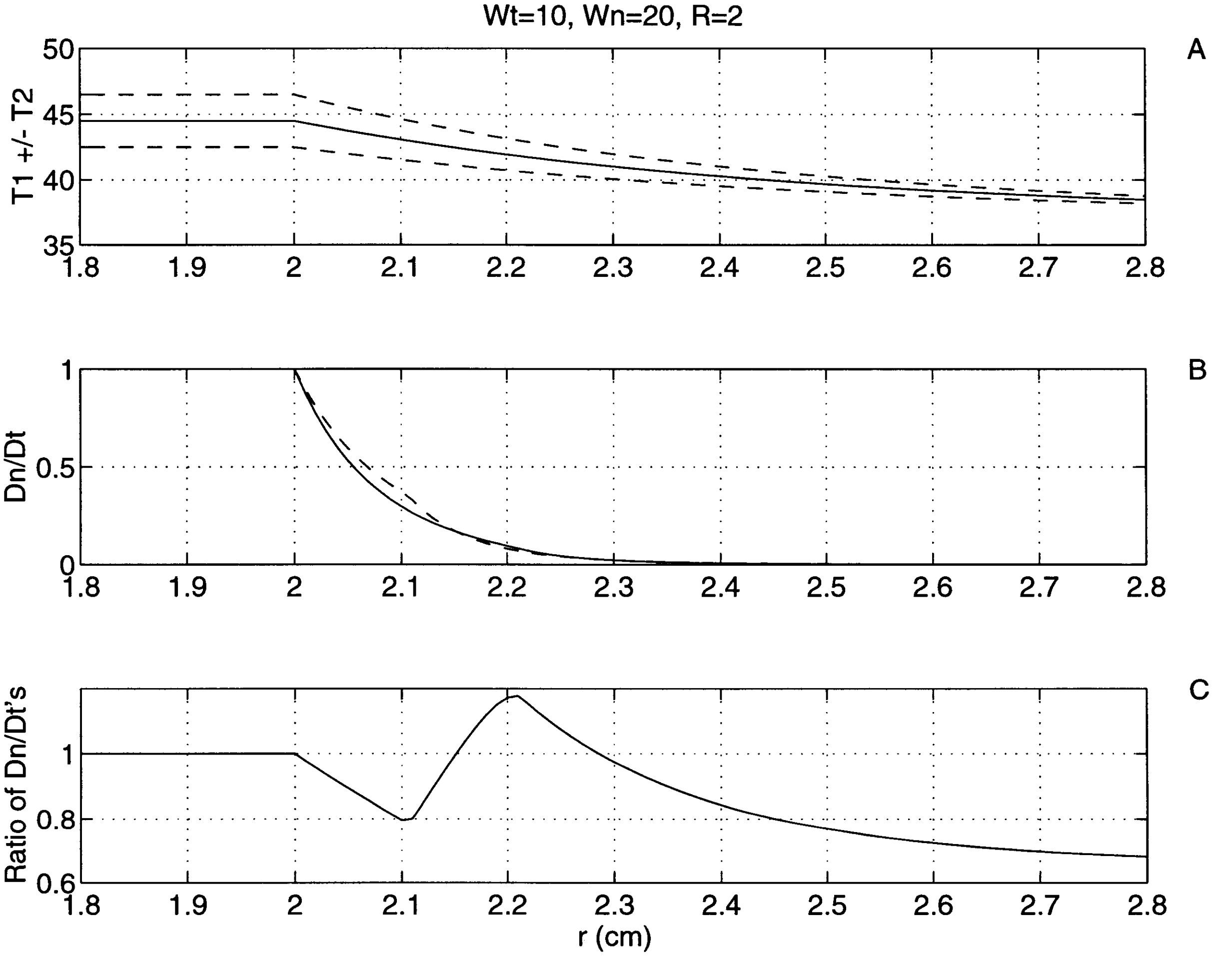

Figure A-7: Temperature and thermal dose profiles in the spherical 1-D case, with $W_t = 10\,\mathrm{ml/min–100g}$, $W_n = 20\,\mathrm{ml/min–100g}$, $R = 2\,\mathrm{cm}$ $T_1 = 44.5°\mathrm{C}$, $T_2 = 2°\mathrm{C}$, and $\omega = \omega^* = 7.77 \times 10^{-3}\,\mathrm{rad/s}$.

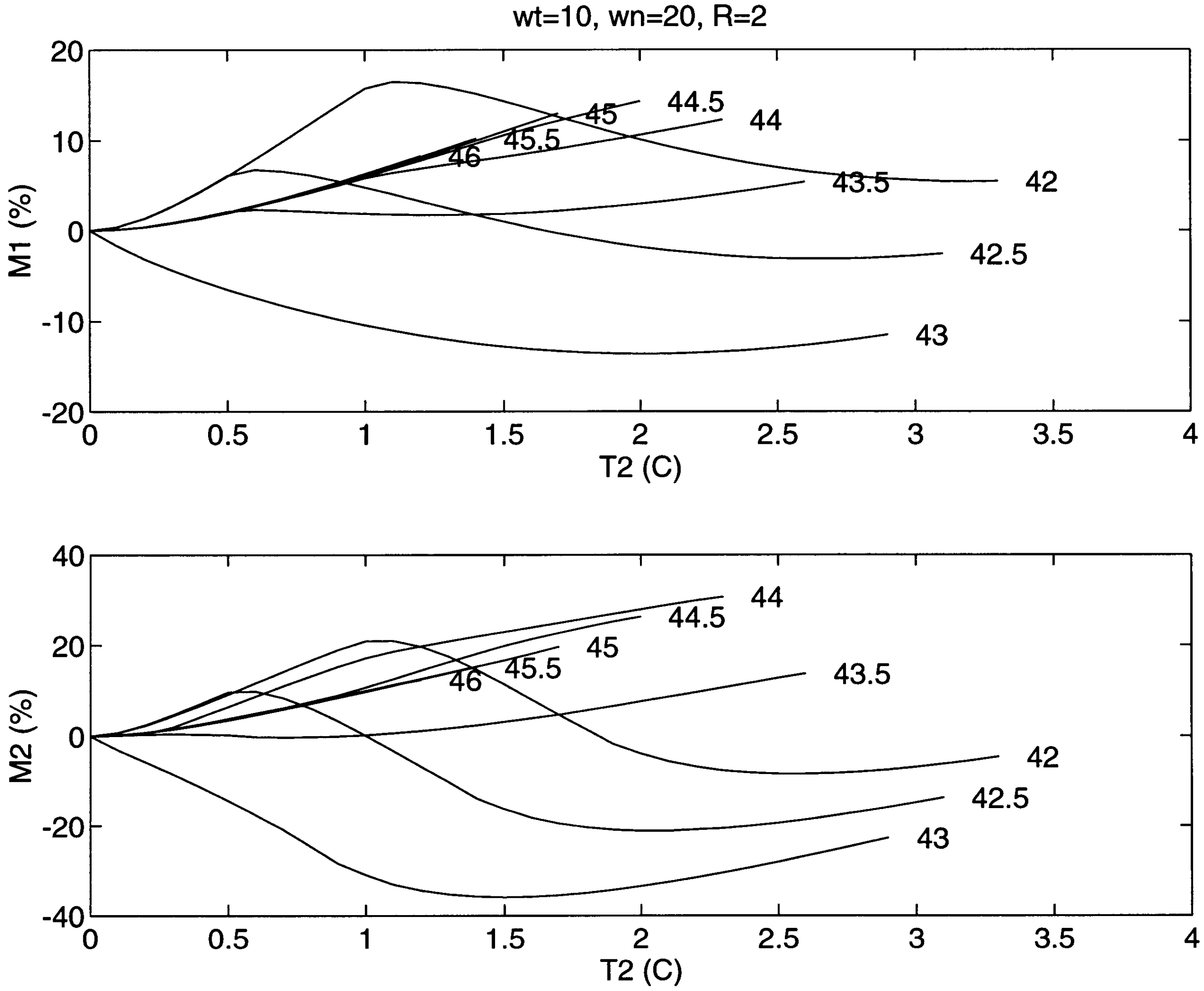

Figure A-8: $\mathcal{M}_1$ and $\mathcal{M}_2$ vs. T_2, for the case where $W_t = 10\,\text{ml/min–100g}$, $W_n = 20\,\text{ml/min–100g}$, and $R = 2\,\text{cm}$. Curves are labeled according to their respective values of T_1.

Appendix B

Supplementary Derivations

This appendix includes a number of derivations meant to supplement the material in the main chapters. These appendicular sections are cited in their respective corresponding areas of the main text, and *vice versa.*

B.1 Geometry and Volumizer

This section describes in detail the method used in Volumizer to determine the equation of a line in a 2-D plane, and the equation of a plane in 3-D space (see Section 2.4.1, page 47). Figure B-1A, taken from Figure 2-5C on page 46, shows a triangle $\triangle PQR$ in the yz-plane. The point P has coordinates $\vec{p} = (p_x, p_y, p_z)$, and likewise for Q and R. Any point (y, z) on the line $\overline{PQ}$ satisfies:

$$y - p_y = \frac{q_y - p_y}{q_z - p_z}\,(z - p_z) \tag{B.1}$$

Rearrangement yields:

$$(q_z - p_z)\,y + (p_y - q_y)\,z = (q_z - p_z)\,p_y + (p_y - q_y)\,p_z \tag{B.2}$$

This equation is in the same form as $A_R\,y + B_R\,z = C_R$, and gives the constants A_R, B_R, and C_R.

By my convention, if a point (y, z) lies inside the projection of $\triangle PQR$, then $A_R\,y + B_R\,z > C_R$. Take the point R as a test point. If $A_R\,r_y + B_R\,r_z > C_R$ the convention holds. If $A_R\,r_y + B_R\,r_z < C_R$, then multiply A_R, B_R, and C_R by -1, and then the convention will hold.

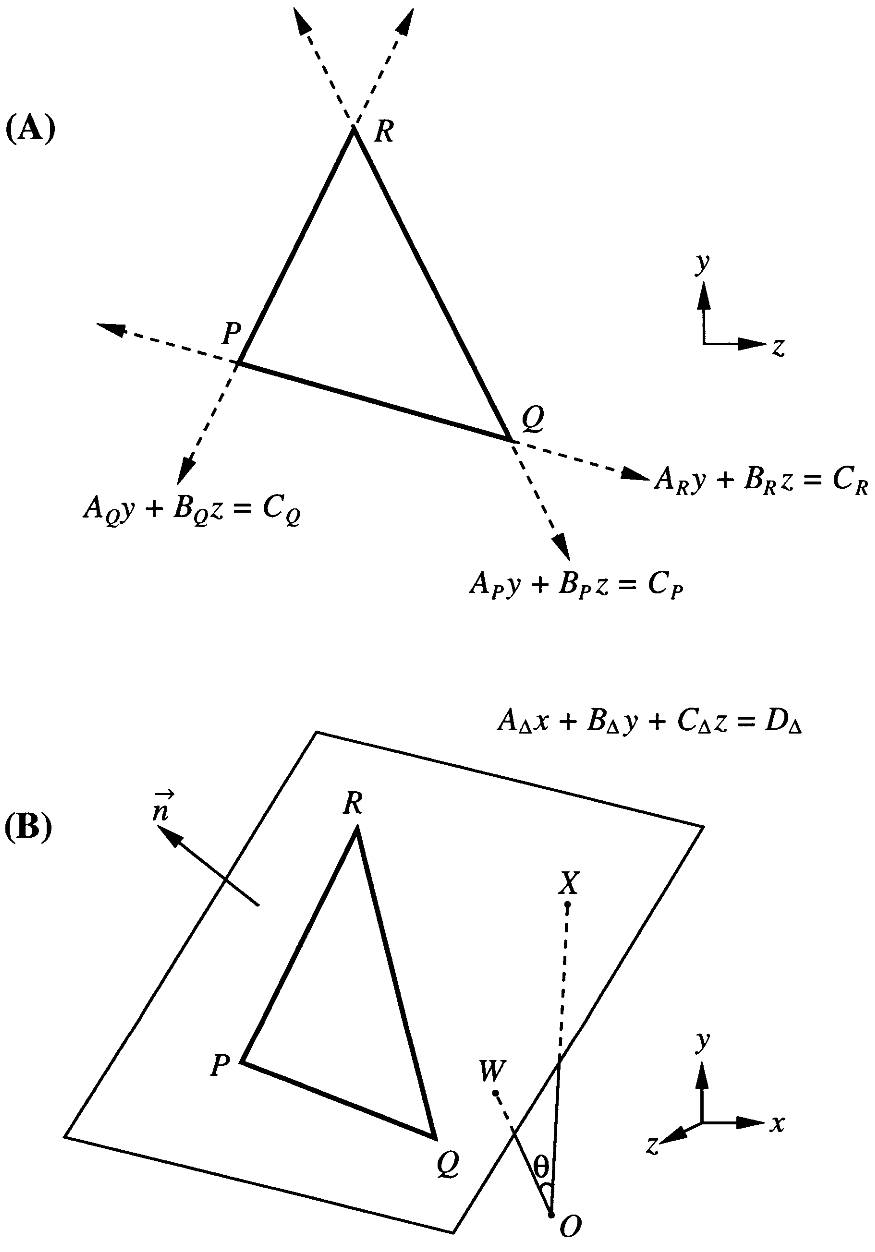

Figure B-1: 2-D and 3-D geometry of triangles.

(If $A_R\, r_y + B_R\, r_z = C_R$, the triangle is degenerate because R is on the line $\overline{PQ}$.) This same procedure is performed for sides $\overline{PR}$ and $\overline{QR}$.

The equation of the plane in which $\triangle PQR$ lies in 3-D space is $A_\triangle\, x + B_\triangle\, y + C_\triangle\, z = D_\triangle$, as shown in Figure B-1B. Let $\vec{n}$ be a vector normal to the plane, O the origin, and W the unique point in the plane closest to the origin. For any point $X \equiv (x, y, z)$ in the plane, the dot product:

$$\vec{n} \cdot \vec{x} = |\vec{n}||\vec{x}| \cos\theta = |\vec{n}||\vec{w}| \tag{B.3}$$

where θ is $\angle WOX$. The important thing to note here is that the final result, $|\vec{n}||\vec{w}|$, is a constant for the plane (as long as we stick with a specific $\vec{n}$), and that constant can be given by $\vec{n} \cdot \vec{p}$, for example. A perfectly reasonable way to calculate $\vec{n}$ is by the cross product $\vec{n} = (\vec{p} - \vec{q}) \times (\vec{p} - \vec{r})$. The equation of the plane, $\vec{n} \cdot \vec{x} = \vec{n} \cdot \vec{p}$, can be expressed by:

$$n_x\, x + n_y\, y + n_z\, z = n_x\, p_x + n_y\, p_y + n_z\, p_z \tag{B.4}$$

which is of the same form as $A_\triangle\, x + B_\triangle\, y + C_\triangle\, z = D_\triangle$. By my convention, if $\vec{x}$ is in the $+x$ direction of the plane, then $A_\triangle\, x + B_\triangle\, y + C_\triangle\, z > D_\triangle$. This is ensured if $A_\triangle > 0$; if $A_\triangle < 0$, then multiply $A_\triangle$, $B_\triangle$, $C_\triangle$, and $D_\triangle$ by -1. (If $A_\triangle = 0$, then the plane is parallel to the x-axis. In this case it is desired that $B_\triangle > 0$. If $B_\triangle = 0$, meaning the plane is parallel to both the x- and y-axes, then it is desired that $C_\triangle > 0$.)

B.2 Rayleigh-Sommerfeld Diffraction Integral

The Rayleigh-Sommerfeld diffraction integral relates the velocity potential Ψ to the velocity of a planar acoustic source embedded in an otherwise infinitely rigid plane (see Section 3.1.3 on page 65). This equation[1] is an important one, and it pervades the literature in ultrasound physics. Despite its ubiquity, however, the author located but a single derivation, in Morse and Ingard [71], and that derivation was difficult, convoluted, and abstract. A shorter and sweeter (more direct and physical) derivation follows.

A hemispherical source is placed on an infinitely rigid plane, and radiates into a semi-infinite medium. By symmetry, the velocity potential in the medium is given by the velocity potential

---

[1] Though called the Rayleigh-Sommerfeld diffraction integral, this term colloquially refers to the entire equation (Equation 3.23, page 65, and Equation B.9, page 235).

solution of a spherical source in an infinite medium, Equation 3.20, which is repeated here:

$$\Psi\{r,t\} = \frac{R}{r}\Psi_{\mathrm{a}}\{R\}e^{j(\omega t-kr)} \tag{B.5}$$

The velocity from a spherical source is also given in Equation 3.20, and it can be solved to find the velocity at the source surface:

$$u_r\{R,t\} = jk(1-j/kR)\Psi_{\mathrm{a}}\{R\}e^{j(\omega t-kR)} \tag{B.6}$$

Equation B.6 can be substituted into Equation B.5 to give:

$$\Psi\{r,t\} = \frac{R}{r}\frac{u_r\{R,t\}}{jk(1-j/kR)}e^{jk(R-r)} \tag{B.7}$$

For sufficiently small values of R ($R \ll \lambda$), the hemispherical source is equivalent to a planar source (located within the rigid plane and radiating into the semi-infinite medium) with the same surface normal velocity ($u_n\{t\} = u_r\{R,t\}$) and surface area ($A = 2\pi R^2$) as the hemispherical source. Taking the limit as $R \to 0$, and letting $A \to dA$, Equation B.7 is transformed into:

$$\Psi\{r,t\} = \frac{u_n}{2\pi r}e^{-jkr}\,dA \tag{B.8}$$

Since the wave equation (Equation 3.8) is a linear homogeneous equation, and the boundary condition is homogeneous (by symmetry $\partial\Psi/\partial n = 0$ everywhere on the planar boundary except at the source location), the solution for Ψ for a non-trivial planar source is the sum (or integral) of Ψ solutions for the simple (or differential) sources that make up the non-trivial planar source:

$$\Psi\{\vec{v},t\} = \int_A \frac{u_n}{2\pi d}e^{-jkd}\,dA \tag{B.9}$$

where A is the source surface, dA is a differential part of A, and d is the distance between the field point of interest and dA. Equation B.9 is the Rayleigh-Sommerfeld diffraction integral.

B.3 Visibility of Cylindrical Wedge Source from Field Point

Figure B-2 illustrates which parts of the cylindrical wedge are visible to a given field point, with the case of the convex radiator (*i.e.* sound waves radiate outward from the source, in the direction of increasing r) in Figure B-2A, and the concave radiator in Figure B-2B (see Section 4.1.5 on page 108). This figure shows the projections of the cylindrical wedge (heavy, solid circular arc) and field point on the xy- and $r\theta$-plane. To avoid certain special cases, the constraints $0 < \sigma_\theta \leq \pi$ and $-\pi < \theta_p \leq \pi$ are made. Tangent lines from the shown circle (on which the projection of the cylindrical wedge lies) to the field point intersect the circle at the angles $\theta_p \pm \beta$, where $\cos\beta = R/r_p$.

For there to be a line of sight between the cylindrical wedge and the field point in the case of a convex source (Figure B-2A), $r_p > R$ by necessity. If this condition is met, then the visible radiating surface extends through the interval $\theta_{\text{min}} < \theta < \theta_{\text{max}}$, where $\theta_{\text{min}} = \max(-\sigma_\theta/2, \theta_p - \beta)$ and $\theta_{\text{max}} = \min(\sigma_\theta/2, \theta_p + \beta)$. (*N.B.*: The conditions $\sigma_\theta - \beta \leq -\pi$ and $\sigma_\theta + \beta > \pi$ can occur and are allowed.) It is possible this interval does not exist at all, *e.g.* in the case $(r_p, \theta_p) = (2R, \pi)$; in such cases no portion of the cylindrical wedge is visible to the field point, so the entire cylindrical wedge does not contribute to the sound pressure field at the field point.

The story is somewhat more complicated in the concave case (Figure B-2B). If $r_p \leq R$ the field point is visible to the entire cylindrical wedge, *i.e.* $\theta_{\text{min}} = -\sigma_\theta/2$ and $\theta_{\text{max}} = \sigma_\theta/2$. If $r_p > R$, what happens depends on which of five intervals around the circle contains θ_p. If $-\sigma_\theta/2 \leq \theta_p \leq \sigma_\theta/2$, no portion of the cylindrical wedge is visible to the field point. If $\theta_p < -\sigma_\theta/2 - \pi/2$ or $\theta_p > \sigma_\theta/2 + \pi/2$, the entire cylindrical wedge is visible to the field point. In the remaining two intervals, r'_p is defined as the length of the part of the ray $\theta = \theta_p$ up to the intersection of the ray with the tangent on the circle at $\pm\sigma_\theta/2$. (If $-\sigma_\theta/2 - \pi/2 \leq \theta_p \leq -\sigma_\theta/2$, $\cos(-\sigma_\theta/2 - \theta_p) = R/r'_p$; if $\sigma_\theta/2 \leq \theta_p \leq \sigma_\theta/2 + \pi/2$, $\cos(\theta_p - \sigma_\theta/2) = R/r'_p$. These two expressions can be combined into a single expression for r'_p: $r'_p = R/\cos(|\theta_p| - \sigma_\theta/2)$.) In these two intervals, if $r_p < r'_p$ the entire cylindrical wedge is visible to the field point. Otherwise, if $-\sigma_\theta/2 - \pi/2 \leq \theta_p \leq -\sigma_\theta/2$, as in Figure B-2B, $\theta_{\text{min}} = -\sigma_\theta/2 + 2[(\theta_p + \beta) - -\sigma_\theta/2] = 2(\theta_p + \beta) + \sigma_\theta/2$, and $\theta_{\text{max}} = \sigma_\theta/2$; and if $\sigma_\theta/2 \leq \theta_p \leq \sigma_\theta/2 + \pi/2$, $\theta_{\text{min}} = -\sigma_\theta/2$ and $\theta_{\text{max}} = \sigma_\theta/2 - 2[\sigma_\theta/2 - (\theta_p - \beta)] = 2(\theta_p - \beta) - \sigma_\theta/2$. Table B.1 summarizes how to determine which part of the cylindrical wedge is visible to the field point.

Table B.1: Determination of the interval $\theta_{\min} < \theta < \theta_{\max}$, the portion of the cylindrical wedge visible to the field point. If $\theta_{\min} \geq \theta_{\max}$, or $\theta_{\min}$ and $\theta_{\max}$ are given as —, there is no visible part of the cylindrical wedge to the field point. If the r_p condition is given as —, $r_p \geq 0$; if the θ_p condition is given as —, $-\pi < \theta_p \leq \pi$. $0 < \sigma_\theta \leq \pi$, $\cos\beta = R/r_p$, and $r'_p = R/\cos(|\theta_p| - \sigma_\theta/2)$.

r_p condition	θ_p condition	$\theta_{\min}$	$\theta_{\max}$
convex radiator			
$0 \leq r_p \leq R$	—	—	—
$r_p > R$	—	$\max(-\sigma_\theta/2, \theta_p - \beta)$	$\min(\sigma_\theta/2, \theta_p + \beta)$
concave radiator			
$0 \leq r_p \leq R$	—	$-\sigma_\theta/2$	$\sigma_\theta/2$
$r_p > R$	$-\sigma_\theta/2 \leq \theta_p \leq \sigma_\theta/2$	—	—
—	$-\pi < \theta_p < -\sigma_\theta/2 - \pi/2$	$-\sigma_\theta/2$	$\sigma_\theta/2$
—	$\sigma_\theta/2 + \pi/2 < \theta_p \leq \pi$	$-\sigma_\theta/2$	$\sigma_\theta/2$
$R < r_p < r'_p$	$-\sigma_\theta/2 - \pi/2 \leq \theta_p \leq -\sigma_\theta/2$	$-\sigma_\theta/2$	$\sigma_\theta/2$
$r_p \geq r'_p$	"	$2(\theta_p + \beta) + \sigma_\theta/2$	$\sigma_\theta/2$
$R < r_p < r'_p$	$\sigma_\theta/2 \leq \theta_p \leq \sigma_\theta/2 + \pi/2$	$-\sigma_\theta/2$	$\sigma_\theta/2$
$r_p \geq r'_p$	"	$-\sigma_\theta/2$	$2(\theta_p - \beta) - \sigma_\theta/2$

B.4 Mathematical Adjustment of Coordinates of FSUM Transducers

This appendicular section details the determination of the FSUM transducer coordinates (see Section 4.3.1, page 133). The objective here is to rotate an FSUM transducer about its center C so that the central axis of its beam passes through O', the *observed* point of peak pressure in the focal plane, instead of through O, the *designed* point of peak pressure in the focal plane, and the origin of the canonical FSUM coordinate system (see Figure 4-23 on page 133).

Figure B-3 depicts the geometry. The prime symbol ($'$) will denote quantities related to the observed geometry, and the lack of prime symbol to quantities related to the designed geometry. The coordinates of the center of a transducer $\vec{c}$ (in the FSUM reference frame) are determined from the coordinates of the corners of the transducer. From the geometry of the FSUM, the ideal ultrasound beam axis is a ray from $\vec{c}$ through $\vec{0}$ (the origin of the FSUM coordinate system), so the normal vector of the ideal transducer surface is given by $\vec{n} = -\vec{c}$. For the real beam axis, which is a ray from $\vec{c}$ through $\Delta\vec{c} = (x_{\text{off}}, y_{\text{off}}, 0)$, the vector normal vector of the real transducer surface is given by $\vec{n}' = -\vec{c} + \Delta\vec{c}$.

The best (but not only) way to rotate the transducer about its center so that its surface normal is transformed from $\vec{n}$ to $\vec{n}'$ is to rotate the transducer about the line $\overline{CD}$, which is perpendicular to both $\overline{CO}$ and $\overline{CO'}$. The direction of this line is given by $\vec{e}_2 = \vec{n} \times \vec{n}'$. $\vec{e}_3 = \vec{n} \times \vec{e}_2$ is perpendicular to both $\vec{n}$ and $\vec{e}_2$, and rounds out a non-canonical local coordinate system $(\hat{n}, \hat{e}_2, \hat{e}_3)$ related to the designed transducer geometry. Similarly, $\vec{e}_3' = \vec{n}' \times \vec{e}_2$ is perpendicular to both $\vec{n}'$ and $\vec{e}_2$, and rounds out a non-canonical local coordinate system $(\hat{n}', \hat{e}_2, \hat{e}_3')$ related to the observed transducer geometry. The matrix transformations G_e (for going from the $(\vec{n}, \vec{e}_2, \vec{e}_3)$ to the FSUM coordinate systems) and $G_{e'}$ (for going from the $(\vec{n}', \vec{e}_2, \vec{e}_3')$ to the FSUM coordinate systems) are then given by:

$$G_e = \begin{vmatrix} \hat{n} & 0 \\ \hat{e}_2 & 0 \\ \hat{e}_3 & 0 \\ -\vec{c} & 1 \end{vmatrix} \quad \text{and} \quad G_{e'} = \begin{vmatrix} \hat{n}' & 0 \\ \hat{e}_2 & 0 \\ \hat{e}_3' & 0 \\ -\vec{c} & 1 \end{vmatrix} \tag{B.10}$$

where $\hat{x} \equiv \vec{x}/||\vec{x}||$ is the unit vector in the $\vec{x}$ direction.

Finally, the desired rotation of an arbitrary point, *e.g.* a transducer corner vertex, from

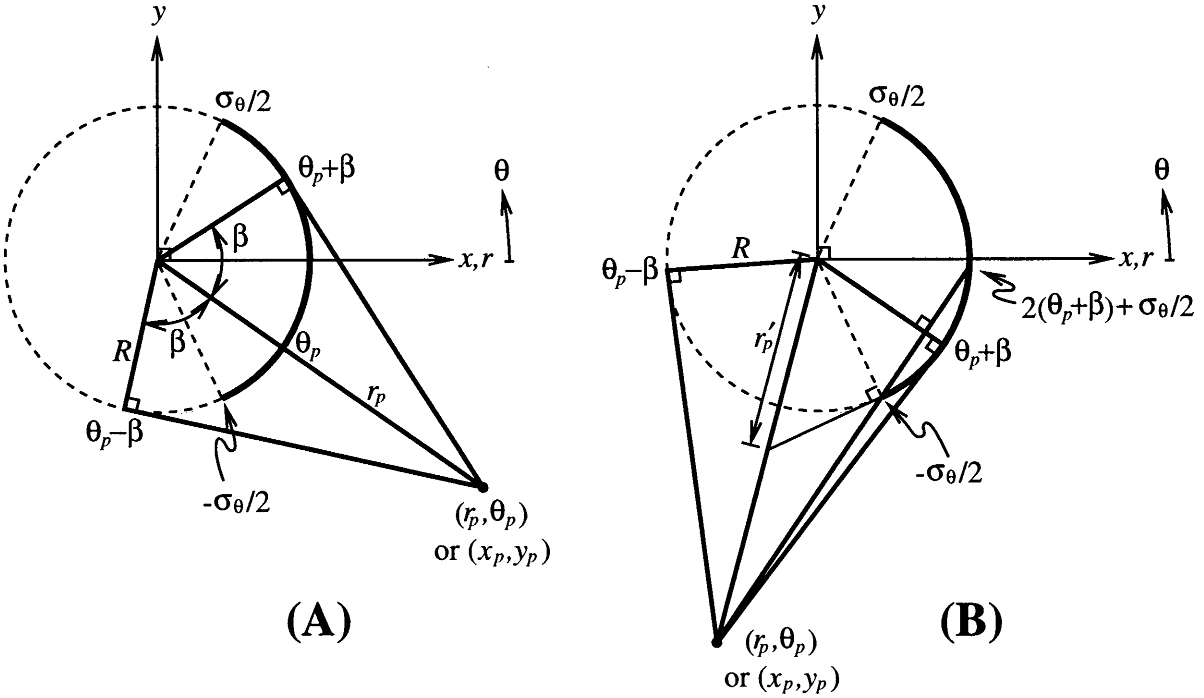

Figure B-2: Projected cylindrical wedge and field point in the $r\theta$- and xy-plane. (A) illustrates the convex radiator case, (B) the concave radiator case.

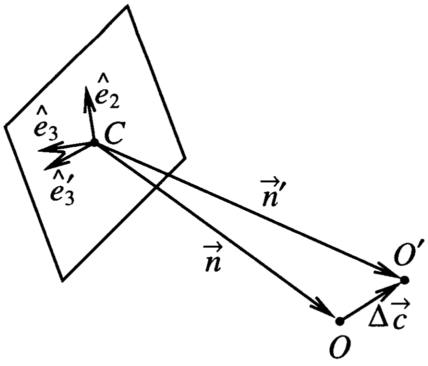

Figure B-3: Geometry of transducer rotation about the transducer center.

designed coordinates to observed coordinates is accomplished by:

$$\vec{x}' = \vec{x}G_e^{-1}G_{e'} \tag{B.11}$$

B.5 Trilinear Interpolation

This appendicular section presents the ubiquitous trilinear interpolation algorithm (see Section 4.4.1, page 147, and Section 4.4.2, page 147). Trilinear interpolation, as its name suggests, is essentially a linear interpolation technique, except it is applied to 3-D instead of 1-D geometries. It is a pervasive method for interpolating field values between grid points on a rectilinear lattice, with known field values at each lattice point. A lattice point (i, j, k) is associated with the location $(x\{i\}, y\{j\}, z\{k\})$, or equivalently (x_i, y_j, z_k). Similarly, the field f is given at each lattice point by $f\{i, j, k\}$ or $f\{x_i, y_j, z_k\}$.

Figure B-4 illustrates how to find $f\{\vec{p}\}$, the trilinearly interpolated field value at the arbitrary location P. First the voxel, or cell, in the lattice that contains P must be identified. (For cases in which P lies on the boundary between two or more voxels, any one of these voxels can be chosen.) In the figure, the voxel (i, j, k) is observed to contain P.

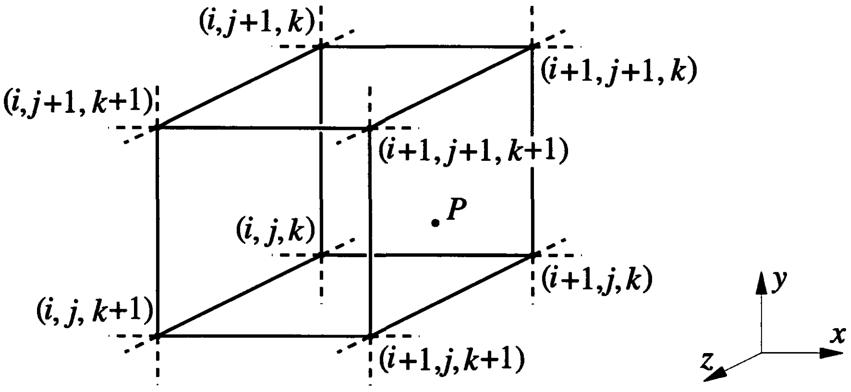

Figure B-4: A voxel, or cell, in a rectilinear lattice.

An arbitrary p_x value between x_i and x_{i+1} can be linearly interpolated as follows: $p_x\{t_x\} = \text{lin}(x_i, x_{i+1}, t_x)$, where $\text{lin}(x_0, x_1, t) \equiv x_0 + (x_1 - x_0)t$, where $0 \leq t_x \leq 1$. ($p_x\{0\} = x_i$ and

$p_x\{1\} = x_{i+1}$.) Analogous equations can be expressed in the y and z coordinates, giving:

$$\begin{aligned} p_x &= x_i + (x_{i+1} - x_i)t_x \\ p_y &= y_i + (y_{i+1} - y_i)t_y \qquad \text{where} \quad 0 \le t_x, t_y, t_z \le 1\,. \\ p_z &= z_i + (z_{i+1} - z_i)t_z \end{aligned} \tag{B.12}$$

Thus given the coordinates of P and the relevant lattice points, the vector $\vec{t} = (t_x, t_y, t_z)$ can be found.

Seven linear interpolations are then required to perform the trilinear interpolation:

$$\begin{aligned} 1:&\ f_{\text{back bottom}} = \text{lin}(f\{i, j, k\}, f\{i+1, j, k\}, t_x) \\ 2:&\ f_{\text{back top}} = \text{lin}(f\{i, j+1, k\}, f\{i+1, j+1, k\}, t_x) \\ 3:&\ f_{\text{back}} = \text{lin}(f_{\text{back bottom}}, f_{\text{back top}}, t_y) \\ 4:&\ f_{\text{front bottom}} = \text{lin}(f\{i, j, k+1\}, f\{i+1, j, k+1\}, t_x) \\ 5:&\ f_{\text{front top}} = \text{lin}(f\{i, j+1, k+1\}, f\{i+1, j+1, k+1\}, t_x) \\ 6:&\ f_{\text{front}} = \text{lin}(f_{\text{front bottom}}, f_{\text{front top}}, t_y) \\ 7:&\ f\{\vec{p}\} = \text{lin}(f_{\text{back}}, f_{\text{front}}, t_z) \end{aligned} \tag{B.13}$$

Trilinear interpolation fits the field within the voxel to the functional form:

$$f\{x, y, z\} = (a_1 + a_2 x)(a_3 + a_4 y)(a_5 + a_6 z) \tag{B.14}$$

or, equivalently:

$$f\{x, y, z\} = b_1 + b_2 x + b_3 y + b_4 z + b_5 xy + b_6 xz + b_7 yz + b_8 xyz \tag{B.15}$$

where $a_1, \ldots, a_6$ and $b_1, \ldots, b_8$ are constants.

B.6 Geometry of Validation Conditions

Two geometries associated with are investigated in this appendicular section: spherical and planar (see Section 4.4.2 on page 161). In particular, a ray is cast from the origin through a field point of interest. In the spherical geometry, we would like to know the distance from the origin to both points of intersection (if they exist) of the ray with the sphere. In the planar geometry, we would like to know how to transform the equation of the plane by rotation and translation, and also the distance from the origin to the intersection (if it exists) of the ray with the plane.

B.6.1 Spherical Geometry

The sphere geometry is shown in Figure B-5A. The sphere has radius r and center Q. O is the origin, and P is the field point of interest. If the ray $\overline{OP}$ intersects the surface of the sphere at S and T, we would like to know the lengths $a_1 = \left|\overline{OS}\right|$, $a_2 = \left|\overline{OT}\right|$, and $b = \left|\overline{ST}\right| = a_2 - a_1$. Figure B-5B shows a 2-D cross-section of the 3-D geometry in the plane containing O, P, and Q. For simplicity, define $p = \left|\overline{OP}\right|$ and $q = \left|\overline{OQ}\right|$. θ, the angle $\angle POQ$, is given from the dot product: $pq \cos\theta = \vec{P} \cdot \vec{Q}$. If $r \geq q \sin\theta$ then $\overline{OP}$ intersects the circle, but if $r < q \sin\theta$ then it does not. If there is intersection, then using the law of cosines and the quadratic formula:

$$a_1, a_2 = q\cos\theta \pm \sqrt{r^2 - (q\sin\theta)^2} \tag{B.16}$$

and:

$$b = \mathrm{Re}(a_2 - a_1) = \begin{cases} 2\sqrt{r^2 - (q\sin\theta)^2} \ , & r > q\sin\theta \\ 0 \ , & r \leq q\sin\theta \end{cases} \tag{B.17}$$

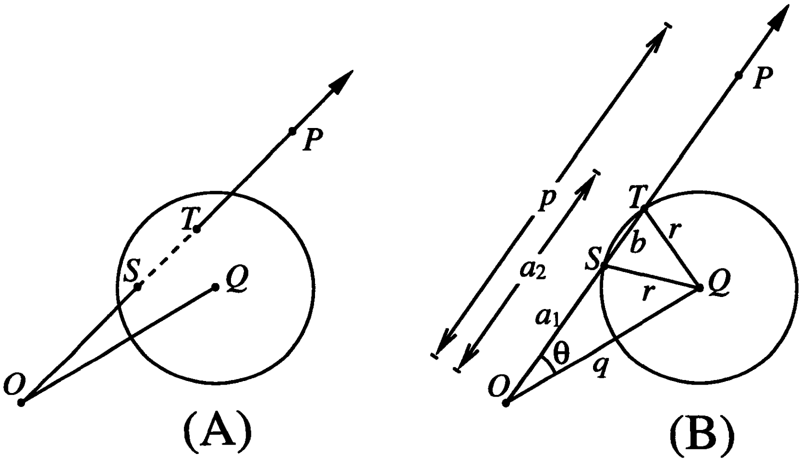

Figure B-5: 3-D and 2-D geometry of a sphere intersected by a ray.

B.6.2 Planar Geometry

A plane is defined by $Ax + By + Cz = D$ (see Equation B.4). This equation can be expressed in matrix form:

$$\begin{vmatrix} x & y & z & 1 \end{vmatrix} \begin{vmatrix} A \\ B \\ C \\ -D \end{vmatrix} = 0 \tag{B.18}$$

or symbolically:

$$\vec{x}\vec{a}^T = 0 \tag{B.19}$$

where $\vec{x} = |x \; y \; z \; 1|$ is an arbitrary vector that falls in the plane, and $\vec{a} = |A \; B \; C \; -D|$ is a 4-D vector that defines the plane.

If the coordinate system is transformed by G, then $\vec{x}$ is transformed to $\vec{x}' = \vec{x}G$, and $\vec{a}$ is transformed to $\vec{a}'$. Now:

$$\vec{x}\vec{a}^T = \vec{x}GG^{-1}\vec{a}^T = \vec{x}'G^{-1}\vec{a}^T = \vec{x}'\vec{a}'^T = 0 \tag{B.20}$$

which easily demonstrates $\vec{a}'^T = G^{-1}\vec{a}^T$.

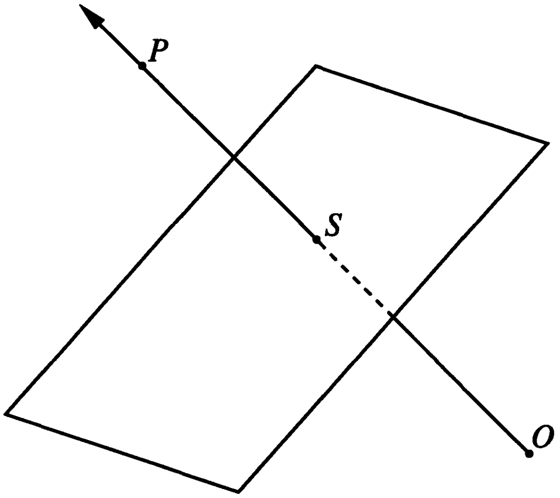

Figure B-6: Geometry of a plane intersected by a ray.

The planar geometry is shown in Figure B-6. The equation describing the plane is $Ax + By + Cz = D$. Once again, O is the origin, and P is the field point of interest. The ray $\overline{OP}$ intersects the plane at S. In this reference frame, with origin O, $\vec{s}$ and $\vec{p}$ are proportional to each other—*i.e.* $\vec{s} = \sigma\vec{p}$, where σ is simply a scaling factor. Recognizing that (s_x, s_y, s_z) satisfies the equation of the plane:

$$\sigma = \frac{D}{Ap_x + Bp_y + Cp_z} \tag{B.21}$$

If the denominator of Equation B.21 equals zero then the line $\overline{OP}$ is parallel to the plane, lying entirely in the plane if $D = 0$, and not intersecting the plane at all otherwise. If $0 \leq \sigma \leq 1$ then the infinite line $\overline{OP}$ intersects the plane on the line segment $\overline{OP}$, if $\sigma > 1$ it intersects beyond P, and if $\sigma < 0$ it intersects beyond O.

B.7 FSUM Coordinate Transformation Under Wobulation

The object of this section is to determine how to transform coordinates between the FSUM rigid housing and spherical shell reference frames, given the angular position of wobulation, $\theta_{\text{wob}} = \omega_{\text{wob}} t$. The geometry of the problem is given in Figure B-7, which is borrowed with minor changes from Figure 5-2 on page 176. (See Section 5.2.2 on page 174 for background.)

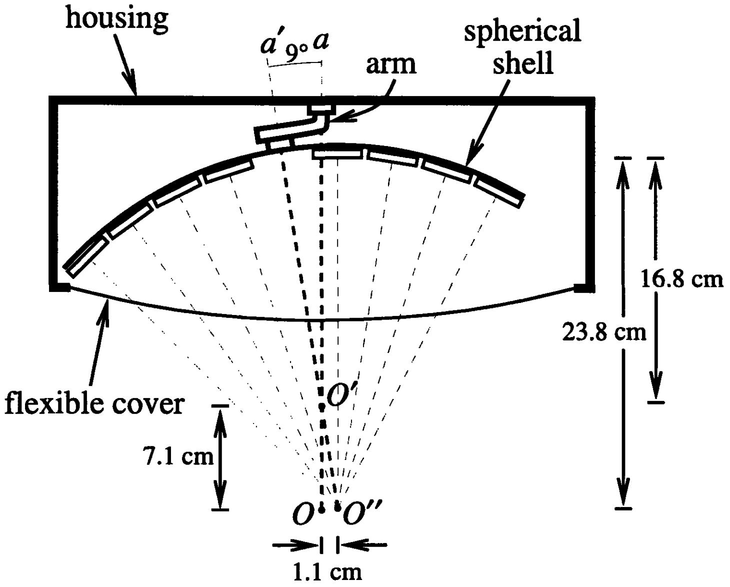

Figure B-7: Geometry of wobulation mode of FSUM.

A number of coordinate transformations will be made. All reference frames considered will have the z direction either straight down in Figure B-7, or tilted at 9°, depending on the specific reference frame. There are also three relevant reference frame origins to consider, labeled O, O', and O''. The necessary transformations necessary to go from the housing reference frame to the spherical shell reference frame are:

1. Start in the housing reference frame, rotate by $+\theta_{\text{wob}}$ around the a-axis (the $\overline{OO'}$ line) to transform to the arm reference frame (this transformation is symbolized by G_1).

2. Tilt by 9° around O' to transform to the *un*counterrotated spherical shell reference frame (G_2).

3. Rotate by $-\theta_{\text{wob}}$ around the a'-axis (the $\overline{O'O''}$ line) to transform to the *counterrotated* spherical shell reference frame (G_3).

The term counterrotation here denotes the dynamic that, while the arm is rotating relative to the housing, the spherical shell is rotating relative to the arm at the same speed in (essentially) the opposite direction. The combined transformation matrix $G_{\mathrm{rh}\rightarrow\mathrm{ss}}$ from the rigid housing reference frame to the spherical shell reference frame is given by $G_{\mathrm{rh}\rightarrow\mathrm{ss}} = G_1 G_2 G_3$.

Now G_1 and G_3 can be obtained in a straightforward manner, as they are simple rotations about the z-axis in the relevant reference frame:

$$G_1 = \begin{vmatrix} \cos\theta_{\mathrm{wob}} & +\sin\theta_{\mathrm{wob}} & 0 & 0 \\ -\sin\theta_{\mathrm{wob}} & \cos\theta_{\mathrm{wob}} & 0 & 0 \\ 0 & 0 & 1 & 0 \\ 0 & 0 & 0 & 1 \end{vmatrix} \quad \text{and} \quad G_3 = \begin{vmatrix} \cos\theta_{\mathrm{wob}} & -\sin\theta_{\mathrm{wob}} & 0 & 0 \\ +\sin\theta_{\mathrm{wob}} & \cos\theta_{\mathrm{wob}} & 0 & 0 \\ 0 & 0 & 1 & 0 \\ 0 & 0 & 0 & 1 \end{vmatrix}$$

G_2 requires a little more work, however. This is because the origin of the housing reference frame is O and the origin of the spherical shell reference frame is O'', but the tilting associated with G_2 is about O'. This tilting can be broken down into three simple transformations:

A. Translate 7.1 cm from the O origin to the O' origin ($G_{2\mathrm{A}}$).

B. Tilt by 9° about O' ($G_{2\mathrm{B}}$).

C. Translate 7.1 cm from the O' origin to the O'' origin ($G_{2\mathrm{C}}$).

Then G_2 is given by $G_2 = G_{2\mathrm{A}} G_{2\mathrm{B}} G_{2\mathrm{C}}$, and:

$$G_{2\mathrm{A}} = \begin{vmatrix} 1 & 0 & 0 & 0 \\ 0 & 1 & 0 & 0 \\ 0 & 0 & 1 & 0 \\ 0 & 0 & +7.1 & 1 \end{vmatrix}, \quad G_{2\mathrm{B}} = \begin{vmatrix} \cos 9^\circ & 0 & +\sin 9^\circ & 0 \\ 0 & 1 & 0 & 0 \\ -\sin 9^\circ & 0 & \cos 9^\circ & 0 \\ 0 & 0 & 0 & 1 \end{vmatrix}, \text{ and } \quad G_{2\mathrm{C}} = \begin{vmatrix} 1 & 0 & 0 & 0 \\ 0 & 1 & 0 & 0 \\ 0 & 0 & 1 & 0 \\ 0 & 0 & -7.1 & 1 \end{vmatrix}$$

Observations concerning the component transformations of $G_{\mathrm{rh}\rightarrow\mathrm{ss}}$ include $G_1 = G_3^{-1}$, $G_{2\mathrm{A}} = G_{2\mathrm{C}}^{-1}$, and G_1 and G_3 depend on θ_{wob} but G_2 does not.

B.8 Oscillatory Heating

This appendicular section is actually a rare appendix to an appendix! Specifically, the derivations presented refer to various sections of Appendix A, page 212.

B.8.1 Temperature Field Solutions

These derivations expand on discussions and derivations in Section A.3.1 (page 215).

B.8.1.1 Steady-State Solution in Cartesian 1-D Geometry

In this case the objective is to determine the steady-state solution for $\theta_{\mathrm{nc}}\{x,t\}$ in the Cartesian 1-D geometry, with $\theta_{\mathrm{t}}\{t\} = \theta_1$, where θ_1 is a constant. With no volumetric power deposition, the bioheat transfer equation in the Cartesian 1-D geometry becomes:

$$\frac{1}{\alpha_{\mathrm{n}}}\frac{\partial\theta_{\mathrm{nc}}}{\partial t} = \nabla^2\theta_{\mathrm{nc}} - \lambda_{\mathrm{n}}^2\theta_{\mathrm{nc}} = \frac{\partial^2\theta_{\mathrm{nc}}}{\partial x^2} - \lambda_{\mathrm{n}}^2\theta_{\mathrm{nc}} \tag{B.22}$$

In the steady-state, this reduces to:

$$0 = \frac{d^2\theta_{\mathrm{nc}}}{dx^2} - \lambda_{\mathrm{n}}^2\theta_{\mathrm{nc}} \tag{B.23}$$

This equation, taken with the boundary conditions:

$$\theta_{\mathrm{nc}}\{0,t\} = \theta_{\mathrm{t}}\{t\} = \theta_1 \quad \text{and} \quad \theta_{\mathrm{nc}}\{\infty,t\} = 0 \tag{B.24}$$

easily yields the steady-state solution:

$$\theta_{\mathrm{nc}}\{x,t\} = \theta_1 e^{-\lambda_{\mathrm{n}}x} \tag{B.25}$$

B.8.1.2 Cyclic Steady-State Solution in Cartesian 1-D geometry

In this case the objective is to determine the cyclic steady-state solution for $\theta_{\mathrm{nc}}\{x,t\}$ in the Cartesian 1-D geometry, with $\theta_{\mathrm{t}}\{t\} = \theta_2 \sin\omega t$, where θ_2 is a constant. For this case, the boundary conditions are:

$$\theta_{\mathrm{nc}}\{0,t\} = \theta_{\mathrm{t}}\{t\} = \theta_2 \sin\omega t \quad \text{and} \quad \theta_{\mathrm{nc}}\{\infty,t\} = 0 \tag{B.26}$$

If the normal tissue were unperfused (meaning $w_{\mathrm{n}} = 0$, and consequently $\lambda_{\mathrm{n}} = 0$), the regular heat diffusion equation would prevail:

$$\frac{1}{\alpha_{\mathrm{n}}}\frac{\partial\theta_{\mathrm{nc}}}{\partial t} = \nabla^2\theta_{\mathrm{nc}} = \frac{\partial^2\theta_{\mathrm{nc}}}{\partial x^2} \tag{B.27}$$

The cyclic steady-state solution of this equation given the oscillating boundary condition is well-known:

$$\theta_{\mathrm{nc}}\{x,t\} = \theta_2 e^{-\beta_{\mathrm{n}} x}\sin(\omega t - \beta_{\mathrm{n}} x) \tag{B.28}$$

where $\beta_{\mathrm{n}}^2 = \omega/2\alpha_{\mathrm{n}}$.

In the perfused case, a solution of the form:

$$\theta_{\mathrm{nc}}\{x,t\} = \theta_2 e^{-\beta_1 x}\sin(\omega t - \beta_2 x) \tag{B.29}$$

is assumed. Substitution of this form into the bioheat transfer equation (Equation A.1) demonstrates this is a valid solution, with $\beta_1^2 = \frac{1}{2}\left(\sqrt{\lambda_{\mathrm{n}}^4 + (\omega/\alpha_{\mathrm{n}})^2} + \lambda_{\mathrm{n}}^2\right)$ and $\beta_2^2 = \frac{1}{2}\left(\sqrt{\lambda_{\mathrm{n}}^4 + (\omega/\alpha_{\mathrm{n}})^2} - \lambda_{\mathrm{n}}^2\right)$.

B.8.1.3 Cyclic Steady-State Solution with Offset in Cartesian 1-D Geometry

In this case the objective is to determine the cyclic steady-state solution for $\theta_{\mathrm{nc}}\{x,t\}$ in the Cartesian 1-D geometry, but now with $\theta_{\mathrm{t}}\{t\} = \theta_1 + \theta_2 \sin\omega t$, where θ_1 and θ_2 are constants. For this case, the boundary conditions are:

$$\theta_{\mathrm{nc}}\{0,t\} = \theta_{\mathrm{t}}\{t\} = \theta_1 + \theta_2 \sin\omega t \quad \text{and} \quad \theta_{\mathrm{nc}}\{\infty,t\} = 0 \tag{B.30}$$

Since the bioheat transfer equation is homogeneous, and the boundary conditions in the steady-state (Equation B.24) and simple cyclic steady-state (Equation B.26) sum up to the current boundary conditions, the current solution is given by the sum of the steady-state and simple cyclic steady-state solutions (Equation B.25 and Equation B.29):

$$\theta_{\mathrm{nc}}\{x,t\} = \theta_1 e^{-\lambda_{\mathrm{n}} x} + \theta_2 e^{-\beta_1 x}\sin(\omega t - \beta_2 x) \tag{B.31}$$

B.8.1.4 Cyclic Steady-State Solution with Offset in Spherical 1-D Geometry

In this case the objective is to determine the cyclic steady-state solution for $\theta_{\mathrm{ns}}\{x,t\}$ in the spherical 1-D geometry, with $\theta_{\mathrm{t}}\{t\} = \theta_1 + \theta_2 \sin\omega t$, where θ_1 and θ_2 are constants. With no volumetric power deposition, the bioheat transfer equation in the spherical 1-D geometry becomes:

$$\frac{1}{\alpha_{\mathrm{n}}}\frac{\partial\theta_{\mathrm{ns}}}{\partial t} = \nabla^2\theta_{\mathrm{ns}} - \lambda_{\mathrm{n}}^2\theta_{\mathrm{ns}}\frac{\partial^2\theta_{\mathrm{ns}}}{\partial r^2} + \frac{2}{r}\frac{\partial\theta_{\mathrm{ns}}}{\partial r} - \lambda_{\mathrm{n}}^2\theta_{\mathrm{ns}} \tag{B.32}$$

With the substitution $\phi_{\mathrm{n}} = r\theta_{\mathrm{ns}}$, the spherical 1-D bioheat transfer equation (Equation B.32) is transformed into:

$$\frac{1}{\alpha_{\mathrm{n}}}\frac{\partial \phi_{\mathrm{n}}}{\partial t} = \frac{\partial^2 \phi_{\mathrm{n}}}{\partial r^2} - \lambda_{\mathrm{n}}^2 \phi_{\mathrm{n}} \tag{B.33}$$

which has the same form as the Cartesian 1-D bioheat transfer equation (Equation B.22). The boundary conditions for the spherical 1-D problem are:

$$\theta_{\mathrm{ns}}\{R,t\} = \theta_{\mathrm{t}}\{t\} = \theta_1 + \theta_2 \sin\omega t \quad \text{and} \quad \theta_{\mathrm{ns}}\{\infty, t\} = 0 \tag{B.34}$$

Expressed in terms of ϕ_{n}, the boundary conditions become:

$$\phi_{\mathrm{n}}\{R,t\} = R(\theta_1 + \theta_2 \sin\omega t) \quad \text{and} \quad \phi_{\mathrm{n}}\{\infty, t\} = 0 \tag{B.35}$$

(The second boundary condition on ϕ_{n}, *i.e.* $\phi_{\mathrm{n}}\{\infty, t\} = 0$, is determined as follows: Although r increases linearly with r, $\theta_{\mathrm{ns}}\{r,t\}$ decays exponentially, so $\phi_{\mathrm{n}}\{\infty,t\} = \lim_{r\to\infty} r\theta_{\mathrm{ns}}\{r,t\} = 0$.)

Using the solution in Equation B.31, and making the substitution $\theta_{\mathrm{ns}} = \phi_{\mathrm{n}}/r$, the spherical 1-D solution is obtained:

$$\theta_{\mathrm{ns}}\{r,t\} = \frac{R}{r}\left\{\theta_1 e^{-\lambda_{\mathrm{n}}(r-R)} + \theta_2 e^{-\beta_1(r-R)} \sin[\omega t - \beta_2(r-R)]\right\} \tag{B.36}$$

B.8.2 Constraints on Heating

These derivations expand on discussions and derivations in Section A.3.2 (page 217).

B.8.2.1 Tumor Volumetric Heating

In the tumor volume the bioheat transfer equation (Equation A.1) is:

$$\frac{1}{\alpha_{\mathrm{t}}}\frac{\partial \theta_{\mathrm{t}}}{\partial t} = \nabla^2\theta_{\mathrm{t}} - \lambda_{\mathrm{t}}^2\theta_{\mathrm{t}} + \frac{\dot{Q}_{\mathrm{t}}}{k_{\mathrm{t}}} \tag{B.37}$$

where $\lambda_{\mathrm{t}}^2 = w_{\mathrm{t}}\rho_{\mathrm{bl}}c_{\mathrm{bl}}/k_{\mathrm{t}}$. For the specified heating pattern, $\theta_{\mathrm{t}} = \theta_1 + \theta_2 \sin\omega t$, $\partial\theta_{\mathrm{t}}/\partial t = \omega\theta_2\cos\omega t$, and $\nabla^2\theta_{\mathrm{t}} = 0$. With substitution and rearrangement, this yields:

$$\begin{aligned} \dot{Q}_{\mathrm{t}}\{t\} &= k_{\mathrm{t}}\left[\lambda_{\mathrm{t}}^2\theta_1 + \theta_2\left(\lambda_{\mathrm{t}}^2 \sin\omega t + \frac{\omega}{\alpha_{\mathrm{t}}}\cos\omega t\right)\right] \\ &= k_{\mathrm{t}}\left[\lambda_{\mathrm{t}}^2\theta_1 + \beta_{\mathrm{t}}^2\theta_2 \sin(\omega t + \varphi_{\mathrm{t}})\right] \end{aligned} \tag{B.38}$$

where $\beta_{\mathrm{t}}^2 = \sqrt{\lambda_{\mathrm{t}}^4 + (\omega/\alpha_{\mathrm{t}})^2}$ and $\tan\varphi_{\mathrm{t}} = \frac{\omega/\alpha_{\mathrm{t}}}{\lambda_{\mathrm{t}}^2}$. To ensure $\dot{Q}_{\mathrm{t}}\{t\} \geq 0$ it is necessary that $\lambda_{\mathrm{t}}^2\theta_1 \geq (\beta_{\mathrm{t}}\{\omega\})^2\theta_2$. Solving this inequality results in the constraint on ω:

$$\dot{Q}_{\mathrm{t}}\{t\} \geq 0 \quad \text{when} \quad \omega \leq \omega_{\mathrm{t}}^* = \alpha_{\mathrm{t}}\lambda_{\mathrm{t}}^2\sqrt{\left(\frac{\theta_1}{\theta_2}\right)^2 - 1} = w_{\mathrm{t}}\frac{\rho_{\mathrm{bl}}c_{\mathrm{bl}}}{\rho_{\mathrm{t}}c_{\mathrm{t}}}\sqrt{\left(\frac{\theta_1}{\theta_2}\right)^2 - 1} \tag{B.39}$$

B.8.2.2 Tumor Boundary Heating in Cartesian 1-D Geometry.

The tumor boundary heat flux is easily given by $\dot{q}''_{\mathrm{bC}}\{t\} = -k_{\mathrm{n}}\nabla\theta_{\mathrm{nC}}|_{\mathrm{b}} = -k_{\mathrm{n}}\partial\theta_{\mathrm{nC}}/\partial x|_{x=0^+}$. ($\nabla\theta_{\mathrm{nC}}|_{\mathrm{b}}$ refers to the gradient of θ_{nC} at the boundary, and $\partial\theta_{\mathrm{nC}}/\partial x|_{x=0^+}$ refers to the first derivative of θ_{nC} in the limit as x goes to 0 from the positive (*i.e.* $x > 0$) direction.) Given $\theta_{\mathrm{nC}}\{x, t\}$ from Equation A.4:

$$\begin{aligned} \dot{q}''_{\mathrm{bC}}\{t\} &= k_{\mathrm{n}}\left[\lambda_{\mathrm{n}}\theta_1 + \theta_2\left(\beta_1\sin\omega t + \beta_2\cos\omega t\right)\right] \\ &= k_{\mathrm{n}}\left[\lambda_{\mathrm{n}}\theta_1 + \beta_{\mathrm{C}}\theta_2\sin(\omega t + \varphi_{\mathrm{C}})\right] \end{aligned} \tag{B.40}$$

where $\beta_{\mathrm{C}} = \sqrt{\beta_1^2 + \beta_2^2} = \sqrt[4]{\lambda_{\mathrm{n}}^4 + (\omega/\alpha_{\mathrm{n}})^2}$ and $\tan\varphi_{\mathrm{C}} = \beta_1/\beta_2$. As above, $\dot{q}''_{\mathrm{b}}\{t\} \geq 0$ when $\lambda_{\mathrm{n}}\theta_1 \geq \beta_{\mathrm{C}}\{\omega\}\theta_2$, which yields:

$$\dot{q}''_{\mathrm{bC}}\{t\} \geq 0 \quad \text{when} \quad \omega \leq \omega_{\mathrm{bC}}^* = \alpha_{\mathrm{n}}\lambda_{\mathrm{n}}^2\sqrt{\left(\frac{\theta_1}{\theta_2}\right)^4 - 1} = w_{\mathrm{n}}\frac{\rho_{\mathrm{bl}}c_{\mathrm{bl}}}{\rho_{\mathrm{n}}c_{\mathrm{n}}}\sqrt{\left(\frac{\theta_1}{\theta_2}\right)^4 - 1} \tag{B.41}$$

B.8.2.3 Tumor Boundary Heating in Spherical 1-D Geometry.

Now $\dot{q}''_{\mathrm{bS}}\{t\} = -k_{\mathrm{n}}\nabla\theta_{\mathrm{nS}}|_{\mathrm{b}} = -k_{\mathrm{n}}\partial\theta_{\mathrm{nS}}/\partial r|_{r=R^+}$. With the same analysis as performed for the Cartesian 1-D geometry, in the spherical 1-D case:

$$\begin{aligned} \dot{q}''_{\mathrm{bS}}\{t\} &= k_{\mathrm{n}}\left\{(R^{-1} + \lambda_{\mathrm{n}})\theta_1 + \theta_2\left[(R^{-1} + \beta_1)\sin\omega t + \beta_2\cos\omega t\right]\right\} \\ &= k_{\mathrm{n}}\left[(R^{-1} + \lambda_{\mathrm{n}})\theta_1 + \beta_{\mathrm{S}}\theta_2\sin(\omega t + \varphi_{\mathrm{S}})\right] \end{aligned} \tag{B.42}$$

where $\beta_{\mathrm{S}} = \sqrt{(R^{-1} + \beta_1)^2 + \beta_2^2}$ and $\tan\varphi_{\mathrm{S}} = (R^{-1} + \beta_1)/\beta_2$. Again, $\dot{q}''_{\mathrm{bS}}\{t\} \geq 0$ when $(R^{-1} + \lambda_{\mathrm{n}})\,\theta_1 \geq \beta_{\mathrm{S}}\{\omega\}\theta_2$, which yields:

$$\dot{q}''_{\mathrm{bS}}\{t\} \geq 0 \quad \text{when} \quad \omega \leq \omega_{\mathrm{bS}}^* = \tag{B.43}$$

$$\alpha_{\mathrm{n}}\left\{\begin{array}{l} B^4 - \lambda_{\mathrm{n}}^4 + 2R^{-2}(2B^2 + \lambda_{\mathrm{n}}^2 + R^{-2}) \\ \\ \quad - 2R^{-1}\sqrt{2B^6 + (5R^{-2} + 2\lambda_{\mathrm{n}}^2)B^4 + 4R^{-2}(\lambda_{\mathrm{n}}^2 + R^{-2})B^2 + R^{-4}(2\lambda_{\mathrm{n}}^2 + R^{-2})} \end{array}\right\}^{\frac{1}{2}}$$

where $B = R^{-1}\sqrt{[(1 + R\lambda_{\mathrm{n}})\,\theta_1/\theta_2]^2 - 1}$.

B.8.2.4 Demonstration that $\omega^*_{\mathrm{bc}} > \omega^*_{\mathrm{t}}$ Usually

(See Equations B.39 and B.41, respectively, for definitions of ω^*_{t} and ω^*_{bc}.) Combining Equations B.39 and B.41 yields:

$$\omega^*_{\mathrm{bc}} = \omega^*_{\mathrm{t}} \frac{w_{\mathrm{n}}}{w_{\mathrm{t}}} \frac{\rho_{\mathrm{t}} c_{\mathrm{t}}}{\rho_{\mathrm{n}} c_{\mathrm{n}}} \sqrt{\left(\frac{\theta_1}{\theta_2}\right)^2 + 1} \tag{B.44}$$

Tissue material properties (*viz.* ρ and c) are typically very similar in normal and tumor tissue, w_{t} is rarely significantly larger than w_{n}, and $\sqrt{(\theta_1/\theta_2)^2 + 1} > \sqrt{2}$.

B.8.2.5 Demonstration that $\omega^*_{\mathrm{bs}} > \omega^*_{\mathrm{bc}}$ Always

(See Equations B.41 and B.43, respectively, for definitions of ω^*_{bc} and ω^*_{bs}.) Equation B.40 provides an expression for $\dot{q}''_{\mathrm{bc}}\{t\}$, and Equation B.42 for $\dot{q}''_{\mathrm{bs}}\{t\}$. Rearranging the latter equation, substituting the former, and noting that $\theta_{\mathrm{t}}\{t\} > 0$ (because $\theta_1 > \theta_2$) yields:

$$\begin{aligned}
\dot{q}''_{\mathrm{bs}}\{t\} &= k_{\mathrm{n}} \Big\{ (R^{-1} + \lambda_{\mathrm{n}})\theta_1 + \theta_2 \Big[(R^{-1} + \beta_1) \sin\omega t + \beta_2 \cos\omega t \Big] \Big\} \\
&= k_{\mathrm{n}} \Big\{ [\lambda_{\mathrm{n}}\theta_1 + \beta_{\mathrm{C}}\theta_2 \sin(\omega t + \varphi_{\mathrm{C}})] + R^{-1}(\theta_1 + \theta_2 \sin\omega t) \Big\} \\
&= \dot{q}''_{\mathrm{bc}}\{t\} + k_{\mathrm{n}} R^{-1} \theta_{\mathrm{t}}\{t\} > \dot{q}''_{\mathrm{bc}}\{t\} \qquad \text{(B.45)}
\end{aligned}$$

If $\omega = \omega^*_{\mathrm{bc}}$, then $\dot{q}''_{\mathrm{bs}} > \dot{q}''_{\mathrm{bc}} = 0$. This implies ω can exceed ω^*_{bc} while maintaining $\dot{q}''_{\mathrm{bs}} \geq 0$, so $\omega^*_{\mathrm{bs}} > \omega^*_{\mathrm{bc}}$.

Appendix C

Power Deposition and Thermal Model Parameters

This appendix contains two tables related to power deposition and thermal modeling. Table C.1 provides nominal tissue property values for power deposition and thermal models, *viz.* acoustic absorption, thermal conductivity, and blood perfusion. (This table contains most of the information in the file designated by the `$HoTPES_tissueProperties` Unix shell variable—see Section 6.1). Table C.2 comprises data associated with the geometry and acoustic power characteristics of FSUM transducers. (See Sections 4.3.2, 4.3.3, and B.4 for related material.)

Table C.1: Nominal acoustic absorption α, thermal conductivity k, and blood perfusion W values of different tissue types.

Tissue Type	α	k	W
Bladder	0.05 Np/cm	5 mW/cm–°C	10 ml blood/min–100 ml tissue
Bone	2.5	5	1
Bowel	9.0	5	10
External Volume	0.05	5	10
Heart	0.05	5	150
Implant	0.0	6	1
Kidney	0.05	5	200
Liver	0.05	5	110
Lung	4.5	5	10
Prostate	0.05	5	10
Rectum	9.0	5	10
Stomach	0.05	5	50
Tumor	0.05	5	9

Table C.2: Various data associated with the transducers of the FSUM. The columns are transducer number (#), normalized maximum pressure amplitude p_{max}, x and y offsets (cm), and Gaussian beam width σ_{b} (cm) in the focal plane of the device. p_{max}, x, and y data are courtesy of Jørgen L. Hansen.

#	p_{max}	Δx	Δy	σ_{b}
0	.877	-0.5	2.0	0.75
1	.946	0.9	0.0	0.76
2	.738	1.7	2.0	0.77
3	.536	-0.9	1.9	0.74
4	.562	-0.5	1.2	0.79
5	.865	0.0	1.4	0.84
6	.769	0.7	0.8	0.80
7	.0			
8	.674	-0.7	0.5	0.68
9	.713	-0.5	0.2	0.80
10	.771	-0.2	0.5	0.73
11	.771	0.0	0.5	0.90
12	.604	0.5	-0.3	0.72
13	.778	0.4	-0.2	0.75
14	.768	0.5	-0.1	0.72
15	.853	0.0	0.0	0.75
16	.700	-2.1	0.0	0.76
17	.947	-1.2	0.0	0.78
18	.702	-0.4	0.1	0.78
19	.697	0.4	0.0	0.78
20	.813	0.5	0.2	0.79
21	.723	1.0	-0.3	0.75
22	.0			
23	.670	1.7	-0.1	0.66
24	.801	0.0	0.3	0.67
25	1.	-1.3	0.0	
26	.909	-1.0	-0.3	
27	.695	-0.3	-0.6	0.74
28	.800	0.5	0.0	0.75
29	.545	1.0	-0.8	0.88
30	.639	1.5	-0.2	0.80
31	.916	0.0	0.0	0.75
32	.917	-2.3	-0.3	0.80
33	.570	-0.5	-0.3	0.83
34	.870	-1.2	-0.8	0.86
35	.650	-0.6	-0.6	0.80
36	.707	-0.3	-0.5	0.77
37	.805	0.0	-0.8	
38	.525	0.2	-1.0	
39	.720	1.2	-1.0	
40	.864	1.5	-0.8	
41	.894	-1.2	-0.6	
42	.916	-0.5	-0.5	
43	.911	-0.6	-1.0	
44	.886	-0.3	-1.1	
45	.758	0.0	-1.0	
46	.853	0.6	-1.2	
47	.725	1.0	-1.1	
48	.836	-1.0	-1.2	
49	.600	-0.9	-1.1	
50	.852	-0.5	-1.1	
51	.532	-0.5	-1.1	
52	.719	0.8	-1.2	
53	.941	-1.0	-3.4	
54	.644	-0.1	-2.0	
55	.738	0.4	-2.3	

Appendix D

Hyperthermia Therapy Systems

What follows are short descriptions of several hyperthermia treatment systems that have a history of clinical use. All of these systems have been reported in the literature within the last seven years, with the exception of the Steered, Intensity Modulated, Focused Ultrasound (SIMFU) hyperthermia system, which appeared earlier. This list is not meant to be comprehensive.

- The HTS-100 (Tokyo Keiki Co., Ltd.) is a relatively low frequency (430 MHz) microwave heating device that uses a lens to focus power deep in the patient [67, 68]. Treatment planning is minimal with this system, as is feedback of thermal measurements during treatment. Nevertheless the system has been used clinically in Japan.

- The Dartmouth MIMO Adaptive Hyperthermia Controller, a system that is not yet used clinically, learns adaptively how to control each power transducer to optimize the temperature elevations measured during treatment administration [40, 41]. This type of system has several advantages. First, it is a relatively simple system, both in terms of computer hardware and software and treatment planning. Second, it is flexible in that it can use different types and numbers of power transducers and thermometric instrumentation. And third, it has the potential to deal easily with patient movement. An obvious criticism, however, is that it gives the desired heating only at the thermal measurement sites, and the heating that is achieved elsewhere is not known.

- Helios (Varian Associates) is a commercial ultrasound hyperthermia system designed for deep heating [76]. This system uses ultrasound for imaging as well as power deposition.

Hynynen *et al.* have developed an intracavitary ultrasound hyperthermia system that takes advantage of both ultrasound functional modalities as well [49]. The on-line imaging capability of these systems ensures the power transducers are well situated for reasonably accurate power deposition over the anatomy of interest, and it is conducive to quick treatment planning and preparation. But without thermal modeling the temperature field that results in treatment is not well known.

- Scanned focused ultrasound (SFUS) describes systems that focus ultrasound, generally through the use of multiple geometrically focused power transducers, and move the focal point through the patient target volume by translating and rotating the transducers together. The Sonotherm 6500 (Labthermics Technologies Inc.) is a 6-transducer SFUS system typical of the genre [37]. It has an ultrasound imaging transducer located at the center of the gantry carrying the power transducers. The path the transducers follow is defined prior to treatment, and it can be modified within treatment by the system operator based on invasive temperature measurements taken during treatment. A genealogically related SFUS system uses more sophisticated planning procedures to predict the SAR and temperature fields that would result from a given transducer excitation pattern, and to determine the optimal trajectory of the transducer gantry [60]. Both systems have seen clinical use.
- The Stanford 3D Hyperthermia Treatment Planning System (S3DHTPS) is based on the Sigma-60 Applicator of the BSD-2000 Hyperthermia System (BSD Medical Corp.), a microwave device for hyperthermia treatment [92]. In treatment planning the predicted SAR field is determined on a patient-specific basis, and it can be displayed on CT slices of patient anatomy as iso-SAR contours or in pseudocolor. This 2-D visualization is probably one of the most sophisticated uses of patient visualization in clinical hyperthermia today, but it still lacks the benefits of 3-D visualization. In addition, knowledge of the SAR field is not an end in itself, but rather a means to obtain knowledge of the temperature field; thus the S3DHTPS is limited in clinical prospective planning because it does not predict temperature field. Another potential problem with this system is the difficulty in gauging the accuracy of its predicted SAR field. This difficulty exists because the SAR field that was actually achieved in treatment is not measured.

- The Steered, Intensity Modulated, Focused Ultrasound (SIMFU) system was used to treat hundreds of cancer patients in the MIT Hyperthermia Center [58, 59]. This system could be categorized as a SFUS device, although it lacks ultrasound imaging capability, and it uses a lens to focus ultrasound from a single transducer (in contrast to multiple transducers focused by their geometric arrangement). To control treatment, multiple thermal probes are used with a protocol that results in copious measurement sites, but thermal modeling and thermal visualization are not used. The SIMFU system requires considerable support staff to operate, but treatment results were superior.

- The Focused Segmented Ultrasound Machine (FSUM) (Labthermics Technologies Inc.) was designed for heating of deep tumors in the DFCI hyperthermia clinic [38]. It uses 56 independently controllable ultrasound transducers arranged on a spherically focused gantry. It is similar to standard SFUS systems, but it heats a region by adjusting the size and shape of the diffuse focus rather than moving a sharp focus through a trajectory. Although treatment planning involves patient 3-D visualization through HYPER/Plan, thermal modeling has not yet been incorporated into treatment planning or evaluation procedures. Nevertheless, the 3-D patient anatomic visualization by itself distinguishes this treatment system from the other systems mentioned above.

References

[1] S. I. Aanonsen, T. Barkve, J. N. Tjøtta, and S. Tjøtta. Distortion and harmonic generation in the nearfield of a finite amplitude sound beam. *Journal of the Acoustical Society of America*, 75(3):749–768, 1984.

[2] E. Alexander, III, J. S. Loeffler, and L. D. Lunsford, editors. *Stereotactic Radiosurgery*. McGraw-Hill, Inc., New York, 1993.

[3] R. L. Anderson and J. W. Valvano. Self-heated thermistor measurements of perfusion. *IEEE Transactions on Biomedical Engineering*, 39(9):877–885, 1992.

[4] R. L. Anderson and J. W. Valvano. A small artery heat transfer model for self-heated thermistor measurements of perfusion in the kidney cortex. *Journal of Biomechanical Engineering*, 116:71–78, 1994.

[5] J. A. Archer-Hall and D. Gee. A single integral computer method for axisymmetric transducers with various boundary conditions. *NDT International*, 13(3):95–101, 1980.

[6] T. A. Balasubramaniam and H. F. Bowman. Thermal conductivity and thermal diffusivity of biomaterials: a simultaneous measurement technique. *Journal of Biomechanical Engineering*, 99:148–154, 1977.

[7] C. R. Barrett, W. D. Nix, and A. S. Tetelman. *The Principles of Engineering Materials*. Prentice Hall, Inc., Englewood Cliffs, NJ, 1973.

[8] G. C. Bentel. *Radiation Therapy Planning*. McGraw-Hill, Inc., New York, 1993.

[9] B. Blad, B. Persson, and K. Lindström. Quantitative assessment of impedance tomography for temperature measurements in hyperthermia. *International Journal of Hyperthermia*, 8(1):33–43, 1992.

[10] H. F. Bowman. The bio-heat transfer equation and discrimination of thermally significant vessels. *Annals of the New York Academy of Sciences*, 335:155–160, 1980.

[11] H. F. Bowman. Estimation of tissue blood flow. In A. Shitzer and R. C. Eberhart, editors, *Heat Transfer in Medicine and Biology*, volume 1, chapter 9, pages 193–230. Plenum Publishing Corporation, 1984.

[12] H. F. Bowman. Thermal dosimetry. In L. J. Anghileri and J. Robert, editors, *Hyperthermia in Cancer Treatment*, volume 2, chapter 9, pages 155–177. CRC Press, Inc., Boca Raton, FL, 1986.

[13] H. F. Bowman, E. G. Cravalho, and M. Woods. Theory, measurement, and application of thermal properties of biomaterials. *Annual Review of Biophysics and Bioengineering*, 4:43–80, 1975.

[14] H. F. Bowman, W. H. Newman, M. G. Curley, S. C. Summit, S. Kumar, G. T. Martin, J. Hansen, and G. K. Svensson. Tumor hyperthermia: dense thermometry, dosimetry, and effects of perfusion. In J. J. McGrath, editor, *Advances in Biological Heat and Mass Transfer*, HTD-volume 189/BED-volume 18, pages 23–31. ASME, 1991.

[15] M. A. Breazeale and D. Huang. Gaussian ultrasonics: theory and practice. In Proceedings of the *1995 IEEE Ultrasonics Symposium*, pages 577–580, 1995.

[16] P. C. P. Carvalho and P. R. Cavalcanti. Point in polyhedron testing using spherical polygons. In A. W. Paeth, editor, *Graphics Gems V*, chapter II.2, pages 42–49. AP Professional, Boston, 1995.

[17] C. K. Charny, S. Weinbaum, and R. L. Levin. An evaluation of the Weinbaum-Jiji bioheat equation for normal and hyperthermic conditions. *ASME Journal of Biomechanical Engineering*, 112:80–87, 1990.

[18] J. C. Chato, J. J. Eckburg, and E. Hurlburt. Comparison of three bioheat transfer models using finite difference techniques. In R. B. Roemer, J. J. McGrath, and H. F. Bowman, editors, *Bioheat Transfer—Applications in Hyperthermia, Emerging Horizons in Instrumentation and Modeling*, HTD-volume 126/BED-volume 12, pages 17–21. ASME, 1989.

[19] M. M. Chen and K. R. Holmes. Microvascular contributions in tissue heat transfer. *Annals of the New York Academy of Sciences*, 335:137–151, 1980.

[20] M. Chive. Use of microwave radiometry for hyperthermia monitoring and as a basis for thermal dosimetry. In M. Gautherie, editor, *Methods of Hyperthermia Control*, chapter 3, pages 113–128. Springer-Verlag, Berlin, Germany, 1990.

[21] B. J. Davis and P. P. Lele. A theoretical study of rapid hyperthermia by using scanned, focused ultrasound. In R. B. Roemer, J. J. McGrath, and H. F. Bowman, editors, *Bioheat Transfer—Applications in Hyperthermia, Emerging Horizons in Instrumentation and Modeling*, HTD-volume 126/BED-volume 12, pages 51–66. ASME, 1989.

[22] W. C. Dewey. Interaction of heat with radiation and chemotherapy. *Cancer Research*, 44 (Supplement):4714s–4720s, 1984.

[23] W. C. Dewey, I. E. Hopwood, S. A. Sapareto, and L. E. Gerweck. Cellular responses to combination of hyperthermia and radiation. *Radiology*, 123:463–474, 1977.

[24] C. J. Diederich and K. Hynynen. The development of intracavitary ultrasonic applicators for hyperthermia: a design and experimental study. *Medical Physics*, 17(4):626–634, 1990.

[25] G. Du and M. A. Breazeale. The ultrasonic field of a Gaussian transducer. *Journal of the Acoustical Society of America*, 78(6):2083–2086, 1985.

[26] E. S. Ebbini and C. A. Cain. Optimization of the intensity gain of multiple-focus phased-array heating patterns. *International Journal of Hyperthermia*, 7(6):953–973, 1991.

[27] D. S. Ellis and W. D. O'Brien, Jr. The monopole-source solution for estimating tissue temperature increases for focused ultrasound fields. *IEEE Transactions on Ultrasonics, Ferroelectrics, and Frequency Control*, 43(1):88–97, 1996.

[28] F. J. Fahy. *Sound Intensity*. Elsevier Science Publishing Co., Inc., New York, 1989.

[29] X. Fan and K. Hynynen. The effect of wave reflection and refraction at soft tissue interfaces during ultrasound hyperthermia treatments. *Journal of the Acoustical Society of America*, 91(3):1727–1736, 1992.

[30] X. Fan and K. Hynynen. The effects of curved tissue layers on the power deposition patterns of therapeutic ultrasound beams. *Medical Physics*, 21(1):25–34, 1994.

[31] J. D. Foley and A. van Dam. *Fundamentals of Interactive Computer Graphics*. Addison-Wesley Publishing Company, Inc., Reading, MA, 1984.

[32] J. D. Foley, A. van Dam, S. K. Feiner, J. F. Hughes, and R. L. Phillips. *Introduction to Computer Graphics*. Addison-Wesley Publishing Company, Inc., New York, 1990.

[33] A. Freedman. Sound field of a rectangular piston. *Journal of the Acoustical Society of America*, 32(2):197–209, 1960.

[34] F. A. Gibbs, Jr. Regional hyperthermia: a clinical appraisal of noninvasive deep-heating methods. *Cancer Research*, 44 (Supplement):4765s–4770s, 1984.

[35] S. A. Goss, L. A. Frizzell, and F. Dunn. Ultrasonic absorption and attenuation in mammalian tissues. *Ultrasound in Medicine and Biology*, 5:181–186, 1979.

[36] E. Haines. Point in polygon strategies. In P. S. Heckbert, editor, *Graphics Gems IV*, chapter I.4, pages 24–46. Academic Press, Inc., Boston, 1994.

[37] J. W. Hand, C. C. Vernon, and M. V. Prior. Early experience of a commercial scanned focused ultrasound hyperthermia system. *International Journal of Hyperthermia*, 8(5):587–607, 1992.

[38] J. L. Hansen, B. A. Bornstein, G. K. Svensson, W. H. Newman, G. T. Martin, D. A. Sidney, and H. F. Bowman. A quantitative, integrated, clinical focused ultrasound system for deep hyperthermia. In L. J. Hayes, editor, *Advances in Biological Heat and Mass Transfer*, HTD-volume 322/BED-volume 32, pages 155–163. ASME, 1995.

[39] Y. Harima, M. Nishizawa, K. Nagata, K. Harima, and Y. Tanaka. P53 expression in stage IIIb cervical carcinoma after radiotherapy with or without hyperthermia. In C. F. Arcangeli and R. Cavaliere, editors, *Hyperthermic Oncology 1996, Proceedings of the 7th International Congress on Hyperthermic Oncology*, volume 2, pages 218–220, Rome, 1996.

[40] A. Hartov, T. A. Colacchio, and J. W. Strohbehn. Detailed evaluation of the Dartmouth MIMO Adaptive Hyperthermia Controller. In *Program and Abstracts of the 42nd Annual Meeting of the Radiation Research Society and the 14th Annual Meeting of the North American Hyperthermia Society*, page 110, Nashville, 1994.

[41] A. Hartov, T. A. Colacchio, J. W. Strohbehn, T. P. Ryan, and P. J. Hoopes. Performance of an adaptive MIMO controller for a multiple-element ultrasound hyperthermia system. *International Journal of Hyperthermia*, 9(4):563–579, 1993.

[42] T. S. Herman, B. A. Teicher, M. Jochelson, J. Clark, G. Svensson, and C. N. Coleman. Rationale for use of local hyperthermia with radiation therapy and selected anticancer drugs in locally advanced human malignancies. *International Journal of Hyperthermia*, 4(2):143–158, 1988.

[43] T. F. Hueter and R. H. Bolt. *Sonics—Techniques for the Use of Sound and Ultrasound in Engineering and Science*. John Wiley & Sons, Inc., New York, 1962.

[44] E. B. Hutchinson, M. T. Buchanan, and K. Hynynen. Design and optimization of an aperiodic ultrasound phased array for intracavitary prostate thermal therapies. *Medical Physics*, 23(5):767–776, 1996.

[45] E. B. Hutchinson, M. T. Buchanan, and K. Hynynen. Evaluation of an aperiodic phased array for prostate thermal therapies. *Proceedings of the 1996 IEEE Ultrasonics Symposium*, 2:1601–1604, 1996.

[46] K. Hynynen. Induction of local hyperthermia using ultrasound. In B. R. Paliwal, F. W. Hetzel, and M. W. Dewhirst, editors, *Biological, Physical, and Clinical Aspects of Hyperthermia*, pages 152–166. American Institute of Physics, Inc., New York, 1988.

[47] K. Hynynen. Biophysics and technology of ultrasound hyperthermia. In M. Gautherie, editor, *Methods of External Heating*, chapter 2, pages 61–115. Springer-Verlag, New York, 1990.

[48] K. Hynynen. The role of nonlinear ultrasound propagation during hyperthermia treatments. *Medical Physics*, 18(6):1156–1163, 1991.

[49] K. Hynynen, D. Anhalt, J. Catone, and H. Fosmire. An intracavitary ultrasound hyperthermia system with B-scan imaging. In *Program and Abstracts of the 42nd Annual Meeting of the Radiation Research Society and the 14th Annual Meeting of the North American Hyperthermia Society*, page 123, Nashville, 1994.

[50] K. Hynynen, R. Roemer, E. Moros, C. Johnson, and D. Anhalt. The effect of scanning speed on temperature and equivalent thermal exposure distributions during ultrasound hyperthermia *in vivo*. *IEEE Transactions on Microwave Theory and Techniques*, MTT-34(5):552–559, 1986.

[51] L. M. Jiji, S. Weinbaum, and D. E. Lemons. Theory and experiment for the effect of vascular microstructure on surface tissue heat transfer. Part I: Anatomical foundation and model conceptualization. *ASME Journal of Biomechanical Engineering*, 106:321–330, 1984.

[52] L. M. Jiji, S. Weinbaum, and D. E. Lemons. Theory and experiment for the effect of vascular microstructure on surface tissue heat transfer. Part II: Model formulation and solution. *ASME Journal of Biomechanical Engineering*, 106:331–341, 1984.

[53] L. E. Kinsler, A. S. Frey, A. B. Coppens, and J. V. Sander. *Fundamentals of Acoustics*. John Wiley & Sons, Inc., New York, 3 edition, 1982.

[54] H. Kooy. Algorithm design—the photon model. JCRT, Boston, 1988.

[55] H. M. Kooy, L. A. Nedzi, J. S. Loeffler, E. Alexander, C. W. Cheng, E. G. Mannarino, E. J. Holupka, and R. L. Siddon. Treatment planning for stereotactic radiosurgery of intracranial lesions. *International Journal of Radiation Oncology, Biology, Physics*, 21(3):683–693, 1991.

[56] G. Kossoff. Analysis of focusing action of spherical curved transducers. *Ultrasound in Medicine and Biology*, 5(4):359–365, 1979.

[57] P. P. Lele. Thresholds and mechanisms of ultrasonic damage to "organized" animal tissues. In D. G. Hazzard and M. L. Litz, editors, *Proceedings of a Symposium of Biological Effects and Characterizations of Ultrasound Sources*, pages 224–239, Boston, 1977. DHEW (FDA) 78-8048.

[58] P. P. Lele. Physical aspects and clinical studies with ultrasound hyperthermia. In F. K. Storm, editor, *Hyperthermia in Cancer Therapy*, chapter 16, pages 333–367. G. K. Hall & Co., 1983.

[59] P. P. Lele. Ultrasonic hyperthermia. In J. G. Webster, editor, *Encyclopedia of Medical Devices and Instrumentation*, volume 3, pages 1599–1612. John Wiley & Sons, 1988.

[60] W.-L. Lin, R. B. Roemer, E. G. Moros, and K. Hynynen. Optimization of temperature distributions in scanned, focused ultrasound hyperthermia. *International Journal of Hyperthermia*, 8(1):61–78, 1992.

[61] J. C. Lockwood and J. G. Willette. High-speed method for computing the exact solution for the pressure variations in the nearfield of a baffled piston. *Journal of the Acoustical Society of America*, 53(5):736–741, 1973.

[62] X.-Q. Lu, E. C. Burdette, B. A. Bornstein, J. K. Hansen, and G. K. Svensson. Design of an ultrasonic therapy system for breast cancer treatment. *International Journal of Hyperthermia*, 12(3):375–399, 1996.

[63] W. Lutz. Radiation physics for radiosurgery. In Alexander, III, E., and Loeffler, J. S. and Lunsford, L. D., editor, *Stereotactic Radiosurgery*, chapter 2, pages 7–15. McGraw-Hill, Inc., New York, 1993.

[64] E. L. Madsen, M. M. Goodsitt, and J. A. Zagzebski. Continuous waves generated by focused radiators. *Journal of the Acoustical Society of America*, 70(5):1508–1517, 1981.

[65] G. T. Martin. *A Thermal Model for Rapid Hyperthermia Therapy Planning and Evaluation*. PhD thesis, Massachusetts Institute of Technology, June 1995.

[66] G. T. Martin, W. H. Newman, and H. F. Bowman. Formulation and validation of the Finite Basis Element Method for rapid temperature field calculations in tissue. In preparation.

[67] T. Matsuda, M. Kikuchi, Y. Tanaka, M. Hiraoka, Y. Nishimura, K. Akuta, M. Takahashi, M. Abe, N. Fuwa, and K. Morita. Clinical research into hyperthermia treatment of cancer using a 430 MHz microwave heating system with a lens applicator. *International Journal of Hyperthermia*, 7(3):425–440, 1991.

[68] T. Matsuda, S. Takatsuka, Y. Nikawa, and M. Kikuchi. Heating characteristics of a 430 MHz microwave heating system with a lens applicator in phantoms and miniature pigs. *International Journal of Hyperthermia*, 6(3):685–696, 1990.

[69] J. Milan and R. E. Bentley. The storage and manipulation of radiation dose data in a small digital computer. *British Journal of Radiology*, 47:115–121, 1974.

[70] E. G. Moros, R. B. Roemer, and K. Hynynen. Simulations of scanned focused ultrasound hyperthermia: the effects of scanning speed and pattern on the temperature fluctuations at the focal depth. *IEEE Transactions on Ultrasonics, Ferroelectrics, and Frequency Control*, 35(5):552–560, 1988.

[71] P. M. Morse and K. U. Ingard. *Theoretical Acoustics*. Princeton University Press, Princeton, NJ, 1986.

[72] P. Munro, R. P. Hill, and J. W. Hunt. The development of improved ultrasound heaters suitable for superficial tissue heating. *Medical Physics*, 9(6):888–897, 1982.

[73] W. H. Newman. Temperature field calculation algorithm for hyperthermia treatment planning using basis elements. In *Program and Abstracts of the 41st Annual Meeting of the Radiation Research Society and the 13th Annual Meeting of the North American Hyperthermia Society*, Dallas, 1993.

[74] W. H. Newman, P. P. Lele, and H. F. Bowman. Limitations and significance of thermal washout data obtained during microwave and ultrasound hyperthermia. *International Journal of Hyperthermia*, 6(4):771–784, 1990.

[75] W. H. Newman, G. T. Martin, and D. A. Sidney. Evaluation and application of the Basis Element Method: A rapid 3-D algorithm for bioheat transfer calculations. In L. J. Hayes, editor, *Advances in Biological Heat and Mass Transfer*, HTD-volume 322/BED-volume 32, pages 49–54. ASME, 1995.

[76] G. H. Nussbaum, W. L. Straube, M. D. Drag, G. L. Melson, B. Emami, V. Sathiaseelan, E. Seppi, and E. Shapiro. Potential for localized, adjustable deep heating in soft-tissue environments with a 30-beam ultrasonic hyperthermia system. *International Journal of Hyperthermia*, 7(2):279–299, 1991.

[77] K. B. Ocheltree and L. A. Frizzell. Determination of power deposition patterns for localized hyperthermia: a steady-state analysis. *International Journal of Hyperthermia*, 3(3):269–279, 1987.

[78] K. B. Ocheltree and L. A. Frizzell. Determination of power deposition patterns for localized hyperthermia: a transient analysis. *International Journal of Hyperthermia*, 4(3):281–296, 1988.

[79] K. B. Ocheltree and L. A. Frizzell. Sound field calculation for rectangular sources. *IEEE Transactions on Ultrasonics, Ferroelectrics, and Frequency Control*, 36(2):242–248, 1989.

[80] H. T. O'Neil. Theory of focusing radiators. *Journal of the Acoustical Society of America*, 21(5):516–526, 1949.

[81] A. T. Patera, G. Eden, B. B. Mikić, and H. F. Bowman. Prediction of tissue perfusion from measurement of the phase shift between heat flux and temperature. In M. K. Wells, editor, *Advances in Bioengineering*, pages 187–188. ASME, 1979.

[82] H. H. Pennes. Analysis of tissue and arterial blood temperature in the resting human forearm. *Journal of Applied Physiology*, 1(2):93–122, 1948.

[83] A. Penttinen and M. Luukkala. The impulse response and pressure nearfield of a curved ultrasonic radiator. *Journal of Physics D: Applied Physics*, 9:1547–1557, 1976.

[84] C. A. Perez and S. A. Sapareto. Thermal dose expression in clinical hyperthermia and correlation with tumor response/control. *Cancer Research*, 44 (Supplement):4818s–4825s, 1984.

[85] R. B. Roemer. Optimal power deposition in hyperthermia. I. The treatment goal: the ideal temperature distribution: the role of large blood vessels. *International Journal of Hyperthermia*, 7(2):317–341, 1991.

[86] R. B. Roemer, E. G. Moros, and K. Hynynen. A comparison of bio-heat transfer and effective conductivity equation predictions to experimental hyperthermia data. In R. B. Roemer, J. J. McGrath, and H. F. Bowman, editors, *Bioheat Transfer—Applications in Hyperthermia, Emerging Horizons in Instrumentation and Modeling*, HTD-volume 126/BED-volume 12, pages 11–15. ASME, 1989.

[87] S. A. Sapareto and W. C. Dewey. Thermal dose determination in cancer therapy. *International Journal of Radiation Oncology, Biology, Physics*, 10:787–800, 1984.

[88] R. Sedgewick. *Algorithms*. Addison-Wesley, Reading, MA, 1983.

[89] D. A. Sidney, W. H. Newman, G. T. Martin, J. L. Hansen, G. K. Svensson, and H. F. Bowman. Characterization of acoustic pressure field of ultrasound heating device for hyperthermia treatment of cancer. In the proceedings of the 1997 Summer ASME Bioengineering conference, Sun River, OR, 1997.

[90] M. I. Skolnik. *Introduction to Radar Systems*. McGraw-Hill Book Company, Inc., New York, 1962.

[91] P. K. Sneed and T. L. Phillips. Combining hyperthermia and radiation: how beneficial? *Oncology*, 5(3):99–108, 1991.

[92] D. M. Sullivan, R. Ben-Yosef, and D. S. Kapp. Stanford 3D hyperthermia treatment planning system. Technical review and clinical summary. *International Journal of Hyperthermia*, 9(5):627–643, 1993.

[93] W. Swindell. Ultrasonic hyperthermia. In J. H. Hand and J. R. James, editors, *Physical Techniques in Clinical Hyperthermia*, chapter 6, pages 288–326. John Wiley & Sons, Inc., New York, 1986.

[94] W. Swindell, R. B. Roemer, and S. T. Clegg. Temperature distributions caused by dynamic scanning of focused ultrasound transducers. In *Proceedings of the 1982 IEEE Ultrasound Symposium*, pages 750–753, 1982.

[95] Tharp, H. S. Optimal power deposition with finite-sized, planar hyperthermia applicator arrays. *IEEE Transactions on Biomedical Engineering*, 39(6):569–579, 1992.

[96] Umemura, S.-I., and Cain, C. A. Analysis of temperature responses to diffused ultrasound focal fields produced by a sector-vortex phased array. *International Journal of Hyperthermia*, 6(3):641–655, 1990.

[97] Valdagni, R. et al. International consensus meeting on hyperthermia: final report. *International Journal of Hyperthermia*, 6(5):839–877, 1990.

[98] J. W. Valvano, J. T. Allen, and H. F. Bowman. The simultaneous measurement of thermal conductivity, thermal diffusivity, and perfusion in small volumes of tissue. *Journal of Biomechanical Engineering*, 106:187–191, 1984.

[99] J. van der Zee, D. Gonzalez Gonzalez, G. C. van Rhoon, J. D. P. van Dijk, W. L. J. van Putten, A. A. M. Hart, P. C. M. Koper, G. A. de Wit, and F. T. de Charro. Results of additional hyeprthermia in inoperable pelvic tumours. In C. F. Arcangeli and R. Cavaliere, editors, *Hyperthermic Oncology 1996, Proceedings of the 7th International Congress on Hyperthermic Oncology*, volume 2, pages 215–217, Rome, 1996.

[100] D. F. Watson. *Contouring—A Guide to the Analysis and Display of Spatial Data*. Pergamon Press, New York, 1992.

[101] P. N. T. Wells. *Biomedical Ultrasonics*. Academic Press, Inc., New York, 1983.

[102] L. X. Xu, M. M. Chen, K. R. Holmes, and H. Arkin. The theoretical evaluations of the Pennes, the Chen-Holmes and the Weinbaum-Jiji bioheat transfer models in the pig renal cortex. In J. J. McGrath, editor, *Advances in Biological Heat and Mass Transfer*, HTD-volume 189/BED-volume 18, pages 15–21. ASME, 1991.

[103] J. Zemanek. Beam behavior within the nearfield of a vibrating piston. *Journal of the Acoustical Society of America*, 49(1):181–191, 1971.

[104] Y. Zhang, T. V. Samulski, W. T. Joines, J. Mattiello, R. L. Levin, and D. LeBihan. On the accuracy of noninvasive thermometry using molecular diffusion magnetic resonance imaging. *International Journal of Hyperthermia*, 8(2):263–274, 1992.

Biography

Lightning, mercurial, meteoric—all words I would not use to describe my MIT graduate career, which spanned less than a decade. But though I've been here seemingly forever, most of my life was lived elsewhere. I was born in New Haven and raised in Storrs, home to UConn. My junior year at the local Edwin O. Smith High School my swim team voted me "most likely to cerebrate." I graduated in 1984, and then returned to my place of birth for college. Four years later I emerged from Yale with a B.A. in Molecular Biophysics and Biochemistry, and considerably more skilled at foosball. I did not pass "GO," I did not collect $200, but I instead proceeded directly to MIT. (This is not meant to imply that MIT is "Jail." But then again. . . .) In 1992 I received my M.S. in Mechanical Engineering, and in 1997 I received my Ph.D. in Medical Engineering.

And now I subject the reader to a barrage of disjoint experiences from my tenure at MIT, because, on some abstract level, these pieces make up the man. I overcame addictions to *Northern Exposure* and *Melrose Place*, and I still nurse addictions to *Seinfeld* and *Friends*. (On a related subject, I wrote a *Seinfeld* teleplay, much to the amusement of family and friends. But don't look for it on TV, my friend—it ain't there.) I met my favorite sci-fi author, James P. Hogan, after he contacted me out of the blue, seven years after I sent him fan mail, to say he was coming to Boston and he'd like to get together. I ran the 1997 Boston Marathon in the leisurely yet painful unofficial time of 4:57:36. I hit a home run with my first MIT at-bat. I enjoyed traveling around the country and around the world. And I got my Ph.D.